

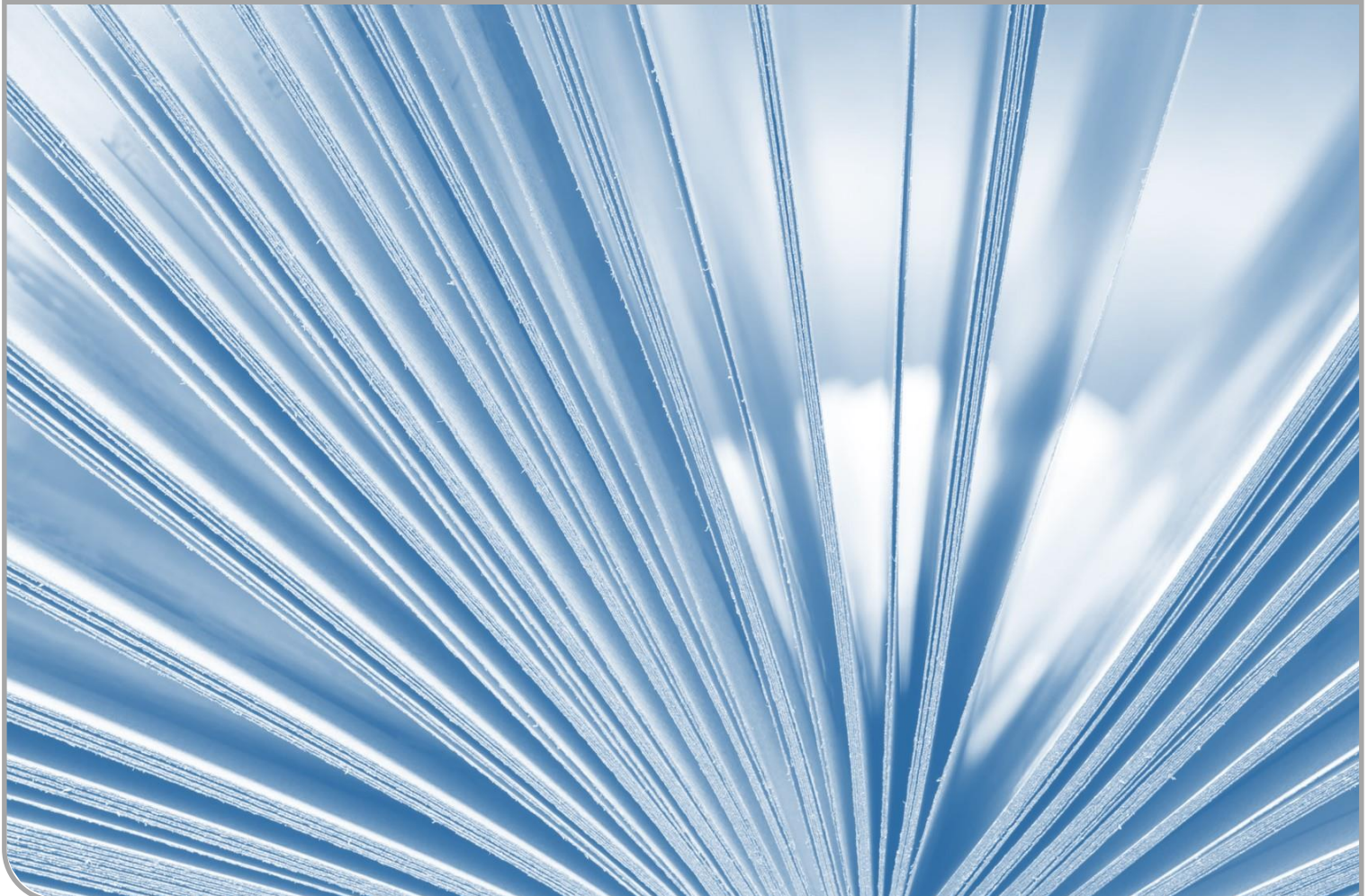
Annual Report 2020/21

Institute for Nuclear Waste Disposal

By H. Geckeis, M. Altmaier, S. Fanghänel (Eds.)

INE SCIENTIFIC WORKING DOCUMENTS

06



Institut für Nukleare Entsorgung (INE)

Hermann-von-Helmholtz-Platz 1
76344 Eggenstein-Leopoldshafen
www.ine.kit.edu

Impressum

Karlsruher Institut für Technologie (KIT)
www.kit.edu



This document is licensed under the Creative Commons Attribution – Share Alike 4.0 International License (CC BY-SA 4.0): <https://creativecommons.org/licenses/by-sa/4.0/deed.en>

2022

URL: <http://www.ine.kit.edu/53.php>

ISSN: 2701-262X

DOI: 10.5445/IR/1000143439

Foreword

This bi-annual report summarizes main activities, achievements and research highlights performed over the last two years, in 2020 and 2021 at KIT-INE.

A main challenge during the last years was certainly to cope with the impact of the global Covid-19 pandemic. INE was fortunate to keep largely operative and also to maintain the possibility to work in the conventional laboratories but also in the controlled area of the institute and the INE-operated beamlines at the KIT Light Source. This is also owing to a huge effort from the side of all persons working at INE and especially of the respective infrastructure staff at INE who strictly implement all relevant safety regulations and enabled us to successfully mitigate this crisis.

In October 2021, INE was organizing a symposium at KIT Campus North related to the 40th anniversary of the foundation of the institute. The “Symposium Nukleare Entsorgungsforschung – Zukunftsperspektiven“ was built around several high level invited oral contributions from key organisations and experts involved in nuclear waste disposal on several levels, both in Germany but also internationally. It became clear, that nuclear waste disposal research is a pronounced interdisciplinary topic with many technical, fundamental aspects in various fields of natural sciences but also social sciences. Respective activities are clearly future oriented and required to support the energy transition project with regard to the safe phase-out of nuclear policy in Germany.

In order to plan for future research strategies, it is also necessary to provide state-of-the-art instrumentation. INE was receiving additional opportunities to further develop the analytical and technical infrastructure within the HOVER project, funded by BMBF and the Helmholtz Association. By offering, e.g., funding to establish an Accelerator Mass Spectrometry lab at INE as well as advanced spectro/microscopy techniques, this will open new lines of nuclear waste disposal research not available before. HOVER is also providing new laboratory infrastructures for “pre-disposal” issues: Within a dedicated laboratory it will be possible to investigate spent nuclear fuel cladding behaviour under extended interim storage conditions. Establishment of virtual laboratories and notably a Building Information Modelling (BIM) laboratory will enhance KIT research on the optimization of decommissioning processes significantly. The realisation of HOVER is ahead of schedule, quite advanced and many facilities will start operation in 2022.

Past efforts on the development of advanced analytical tools in the field of synchrotron-based X-ray spectroscopy at INE contributed to the ERC grant ‘The Actinide Bond’ awarded to Dr. Tonya Vitova. By combining state-of-the-art high-resolution XAFS techniques and advanced quantum chemistry methods, this project likewise opens up new perspective for internationally outstanding fundamental research on actinides and other radionuclides at INE.

As new structures are established in Germany to organize the site selection process for a high-level nuclear waste repository, several activities by INE researchers were performed in this context. For instance, INE researchers contributed to several events organized in Germany to discuss options and facts regarding waste disposal with the interested public and key institutional stakeholders. Providing scientific understanding and expertise is clearly at the core of decision-making and offers important feedback options to our research activities. Ongoing efforts at INE to train students and early career researchers in the field of nuclear waste disposal importantly contribute to the availability of highly trained experts in the field.

Research at KIT-INE goes beyond nuclear waste disposal topics. The challenging task of rebuilding the energy system in Germany requires a broad variety of technologies. Geoenergy can play an important role in respective systems. KIT has proposed two major research infrastructures, in order to study relevant processes under realistic conditions: The GeoLab facility aims at integrating German research activities in a large underground research laboratory. The second facility DeepStor is planned to be established at the KIT-CN site and aims at developing high-temperature heat storage technologies. Both projects do not only concentrate on technical issues with cutting-edge research tools but also consider close interaction with the public and decision makers.

In all KIT-INE activities, we are looking back to numerous excellent scientific results, successfully finished laboratory projects, master- and doctoral theses, and important newly acquired third party funded projects.

Prof. Dr. Horst Geckeis

Director of the Institute for Nuclear Waste Disposal

Table of contents

1	Introduction to the Institute for Nuclear Waste Disposal (INE)	1
2	Education and training	5
3	National and international cooperation, conferences and workshops	7
3.1	National and international cooperation	7
3.2	Colloquium celebrating the 40 th anniversary of the foundation of the Institute for Nuclear Waste Disposal at KIT and TransRet2020 workshop	13
4	Fundamental studies: Process understanding on a molecular scale	15
4.1	Chemistry and thermodynamics of actinides and fission products in aqueous solution	15
4.2	Sorption on mineral surfaces	21
4.3	Retention of radionuclides by secondary phase formation.....	28
5	Applied studies: Radionuclide behavior in the multi-barrier system	35
5.1	Highly radioactive waste forms.....	35
5.2	Geo-engineered barrier materials	40
5.3	Colloid impact on radionuclide migration.....	42
5.4	Diffusion.....	46
5.5	Reactive transport modelling.....	49
6	Coordination chemistry	53
7	Deconstruction and decommissioning of conventional and nuclear buildings	57
7.1	Development of the department of deconstruction and decommissioning of conventional and nuclear buildings	57
7.2	Robotic systems for decontamination in hazardous environments	59
7.3	Stakeholders based analysis of research for decommissioning	61
8	Development of radionuclide speciation methods	63
8.1	R&D projects conducted at the INE-Beamline and the ACT station of the KIT Light Source	63
8.2	Development of a new software for LIBD analysis	69
8.3	Microscopy and surface analytics	71
8.4	NMR spectroscopy at INE.....	74
8.5	Accelerator mass spectrometry (AMS)	76
8.6	Computational chemistry.....	78
9	(Radio-)chemical analysis	83
10	Radiation protection research	87
10.1	Age-dating of young Cf sources by means of g-spectroscopy	87
10.2	Impact of neutron slowing down on radiation fields for spent nuclear fuel waste disposal.....	89
11	Geoenergy	93
12	Publications	99

1 Introduction to the Institute for Nuclear Waste Disposal (INE)

The **Institute for Nuclear Waste Disposal (INE)**, at the Karlsruhe Institute of Technology **KIT** performs R&D focusing on

- (i) **Long-term safety research for nuclear waste disposal (key focus of INE research),**
- (ii) **Radiation protection**
- (iii) **Decommissioning of nuclear facilities**
- (iv) **Geoenergy.**

All R&D activities of INE are integrated into the program Nuclear Safety Research within the KIT-Energy Center and the program Nuclear Waste Management, Safety and Radiation Research (NUSAFE) within the Helmholtz Association. INE contributes to German provident research for the safety of nuclear waste disposal, which is the responsibility of the Federal Government.

Following the decision taken by Germany to phase out the use of nuclear energy, the safe disposal of long-lived nuclear waste remains as a key topic of highest priority. Projections based on scheduled operation times for nuclear power plants (Amendment to German Atomic Energy Act, August 2011) in Germany indicate that about a total of 17,770 tons of spent nuclear fuel will be generated. About 6,670 tons have been shipped to France and the UK until 2005 for reprocessing, to recover plutonium and uranium. Consequently, two types of high level, heat producing radioactive waste (HLW) have to be disposed of safely: spent nuclear fuel and vitrified high level waste from reprocessing (HLW glass). The disposal of low- and intermediate level waste present in much larger quantities likewise needs to be addressed.

Over the last decades, a consensus within the international scientific/technical community was established, clearly emphasizing that disposal in deep geological formations is the safest way to dispose of high level, heat producing radioactive waste. Disposal concepts with strong inherent passive safety features ensure the effective protection of the population and the biosphere against radiation exposure over very long periods of time. The isolation and immobilization of nuclear waste in a repository is ensured by the appropriate combination of redundant barriers (multi-barrier system).

Long term safety research for nuclear waste disposal at INE develops geochemical expertise and models to be used in the nuclear waste disposal Safety Case, focusing primarily on the detailed scientific description of aquatic radionuclide chemistry in the geochemical environment of a repository. Work concentrates on the disposal of spent nuclear fuel and HLW-glass in the relevant potential host rock formations currently considered: rock salt, clay and crystalline rock formations. Actinides

and long-lived fission and activation products play a central role, as they dominate HLW radiotoxicity and risks over long periods of time. Long-lived anionic fission and activation products are likewise investigated as significant contributors to the maximum radiation dose projected for relevant scenarios.

Relevant long-term scenarios for nuclear repositories in deep geological formations have to take into account possible radionuclide transport via the groundwater pathway. Possible groundwater intrusion into emplacement caverns may cause waste form corrosion and eventually radionuclide release. Radionuclide mobility is then determined by the various geochemical reactions in complex aquatic systems: i.e., dissolution of the nuclear waste form (HLW glass, spent nuclear fuel), radiolysis phenomena, redox reactions, complexation with inorganic and organic ligands, colloid formation, surface reactions at mineral surfaces, precipitation of solid phases and solid solutions.

Prediction and quantification of all these processes require fundamental thermodynamic data and comprehensive process understanding at the molecular scale. Radionuclide concentrations in relevant aqueous systems typically lie in the nano-molar range, which is exceedingly small in relation to main groundwater components. Quantification of chemical reactions occurring in these systems require the application and development of advanced tools and experimental approaches, to provide insight into the chemical speciation of radionuclides at trace concentrations. Innovative laser and X-ray spectroscopic techniques are continuously developed and applied to this end. A specialized working group performing state-of-art quantum chemical calculations for radionuclide chemistry supports both interpretation of experimental results and optimized experiment design.

The long-term safety of a nuclear waste repository must be demonstrated by application of modelling tools on real natural systems over geological time scales. Geochemical models and thermodynamic databases are developed at INE as basis for the description of radionuclide geochemical behavior in complex natural aquatic systems. The prediction of radionuclide migration in the geosphere necessitates coupled modelling of geochemistry and transport. Transferability and applicability of model predictions are examined by designing dedicated laboratory experiments, field studies in underground laboratories and by studying natural analog systems. This strategy allows to identify and analyze key uncertainties and continuously optimize the developed models.

The R&D topic **radiation protection** at INE focuses on the assessment of radiation exposures of

humans by estimating doses from external radiation fields. The strategy driving this work is to provide techniques and models for an individualized dosimetry, which goes beyond the current approach of applying reference models in dose assessment. Both the specific anatomical and physiological features of the exposed individual and the specific effective radiation fields are considered in the frame of an individualized dosimetry. Work is performed in close cooperation with the KIT safety management SUM.

The R&D topic **decommissioning of nuclear and conventional facilities** at INE expands the existing activities at the Institute of Technology and Management in Construction (KIT-TMB). Research in this field is focusing on a better understanding of the complete decommissioning process in Germany as well as on a global level.

For the environmentally-friendly use and monitoring of deep geothermal resources, the topic **geoenergy** at INE focusses on the development and testing of novel and integrative concepts for the management of the deep underground and of geophysical monitoring methods. Against this background, reservoir properties and processes and their influence on geophysical fields that are used for exploration and monitoring are crucial. To investigate this, experiments on different scales, from laboratory to reservoir scale, are carried out.

INE laboratories are equipped with all necessary infrastructures to perform radionuclide/actinide research, including a shielded box line enabling the investigation of spent nuclear fuel and nuclear waste glass, alpha glove boxes, inert gas alpha glove boxes and radionuclide laboratories. State-of-the-art analytical instruments and methods are applied for analysis and speciation of radionuclides and radioactive materials. Advanced spectroscopic tools exist for the sensitive detection and analysis of radionuclides. Trace element and isotope analysis is made by instrumental analytical techniques such as atomic absorption spectroscopy (AAS), ICP-atomic

emission spectroscopy (ICP-AES) and ICP-mass spectrometry (Quadrupole-ICP-MS and high resolution ICP-MS). Methods available for surface sensitive analysis and characterization of solid samples include X-ray diffraction (XRD), atomic force microscopy (AFM) and laser-ablation coupled with ICP-MS. A modern X-ray photoelectron spectrometer (XPS) and an environmental scanning electron microscope (ESEM) are installed. Laser spectroscopic techniques are developed and applied for sensitive actinide and fission product speciation such as time-resolved laser fluorescence spectroscopy (TRLFS), laser-induced breakdown detection (LIBD) and Raman spectroscopy. Insight into structural and electronic properties of radionuclide species is obtained by X-ray absorption fine structure (XAFS) spectroscopy and related techniques available at the INE-Beamline and the ACT experimental station at the KIT synchrotron source KARLA. INE's beamlines, in close proximity to INE controlled area laboratories, represent in combination with the other analytical methods a unique experimental infrastructure, which both profits from and contributes to INE's leading expertise in the field of actinide chemistry and spectroscopy. A 400 MHz-NMR spectrometer adapted to measuring radioactive liquid samples adds to the analytical and speciation portfolio of INE. Quantum chemical calculations are performed on INE's computing cluster, which is equipped with 17 nodes and 76 processors. The INE CAD workstations enable construction and planning of hardware components, process layout and flow sheets. The institute workshop is equipped with modern machine tools to manufacture components for specific experimental and analytical devices in hot laboratories.

In 2020 and 2021, the **Institute for Nuclear Waste Disposal** had around **90 employees** working in the four departments and two clusters, which reflect the R&D and organizational tasks of the institute (Fig. 1).

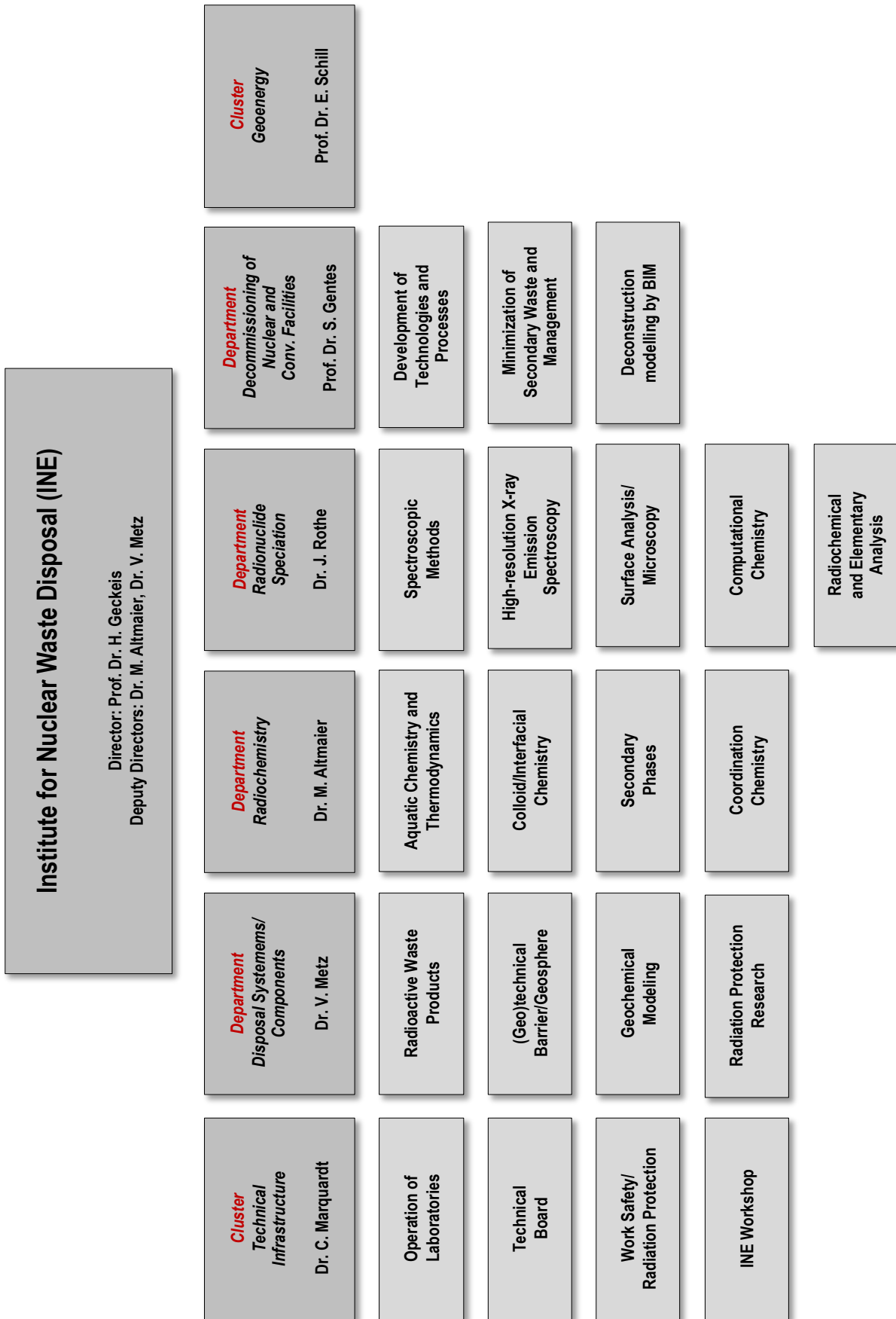


Fig. 1: Organizational chart of the Institute for Nuclear Waste Disposal (INE)

2 Education and training

Teaching of students and promotion of young scientists is of fundamental importance to ensure high-level competence and to maintain a leading international position in the fields of nuclear and radiochemistry. INE scientists are strongly involved in teaching at KIT Campus South and the Universities of Heidelberg and Strasbourg as well as the TU Darmstadt.

Prof. Dr. **Horst Geckeis**, director of INE, holds a professorship for radiochemistry at KIT, Department of Chemistry and Biosciences. He teaches fundamental and applied radiochemistry for chemistry students in bachelor and master courses. A radiochemistry module consisting of basic and advanced lectures on nuclear chemistry topics and laboratory courses has been set up for master students in Karlsruhe. In addition, Dr. **Marcus Altmaier**, head of the department radiochemistry, gives a lecture concerning the chemistry of f-elements.

Prof. Dr. **Sascha Gentes** head of the department decommissioning of nuclear and conventional facilities holds a professorship at the Institute for Technology and Management in Construction at the KIT-Department of Civil Engineering, Geo and Environmental Sciences and gives lectures in the field of decommissioning of nuclear facilities, environmentally-friendly Recycling and Disassembly of Buildings, Machinery and Process Engineering as well as construction technology.

Prof. Dr. **Petra Panak**, heading a working group on coordination chemistry at INE, holds a professorship of radiochemistry at the Heidelberg University. A basic course in radiochemistry is offered for bachelor and/or master students. An advanced course comprised of the chemistry of f-elements and medical applications of radionuclides is also offered. The advanced radiochemistry lectures are supplemented by scientific internships at the INE radioactive laboratories.

Around 50 students from Karlsruhe and Heidelberg participated in three 3-week radiochemistry laboratory courses in 2020 and 2021 held at KIT Campus North in the FTU radiochemistry and the hot laboratories at INE. Some students are intensifying their knowledge in nuclear/radiochemistry topics during scientific internships at INE. Obviously, students are very interested in nuclear chemistry topics and appreciate the various semester courses.

Dr. **Tonya Vitova** gives lectures at KIT, Department of Chemistry and Biosciences, in the field of instrumental analytics and Prof. Dr. **Eva Schill** at the Department of Civil Engineering, Geo and Environmental Sciences in the field of geothermal energy as well as at the university of Darmstadt. Dr. **Volker Metz** and Prof. Dr. **Ron Dagan** give lectures at the Department of Mechanical Engineering in the field of nuclear fuel cycle. Lectures and practical units taught by Dr. **Frank Heberling** and Dr. **Volker Metz** at KIT, Department of Civil Engineering, Geo and Environmental Sciences, focused in 2020 and 2021 on “environmental geology: radio- and chemotoxic elements”.

Dr. **Andreas Geist** gives lectures at the École européenne de chimie, polymères et matériaux in Strasbourg concerning the Solvent Extraction of Metal Ions.

Moreover, INE was involved in many schools and workshops concerning the education and teaching of students and young scientists.

Through this close cooperation with universities, students are educated in the field of nuclear and actinide chemistry, which most universities can no longer offer. Hence, INE makes a vital contribution to the intermediate and long perspective of maintaining nuclear science competence. Moreover, INE is involved in the education of trainees (chemical lab technicians, industrial mechanics and product designers) as well as student internships like BORS and BOGY.

PhD students

In 2020 and 2021, around 20 doctoral students worked at INE on their dissertations; five doctoral students were awarded their doctorate in 2020/2021.

Topics of the current doctoral students:

1. Influence of carbonate on the radium uptake by barite
2. Determination of geothermal relevant parameters in high temperature and superheated reservoirs with gravimetric and magnetotelluric methods
3. Aqueous chemistry of technetium in the presence of inorganic and organic ligands
4. Investigation of the diffusion of U(IV), Np(IV), Pu(IV), and Am(III) at ultra-trace levels through natural clay with accelerator mass spectrometry
5. Sorption of low molecular weight organics on C-S-H, AFM-phases, ettringite, CEM I and their effect on radionuclide uptake
6. Electromagnetical und Eigenpotential monitoring of fluid injections in crystalline rock
7. Fundamental investigation of Zr(IV) solubility and surface processes in alkaline systems: a combined solubility, spectroscopic and theoretical study
8. Investigation of the radionuclide inventory and chemical interactions at the interface between nuclear fuel and zircaloy cladding of irradiated light water reactor fuel rod samples
9. Joint inversion of magnetotelluric and gravity data from Mt. Viilarica area (S-Chile)
10. Speciation of actinides and fission products by mass spectrometric methods
11. Investigations of Np, Tc, and Se structural properties applying in situ high-energy resolution X-ray emission/absorption spectroscopy

12. Influence of heterogeneity of natural claystones on radionuclide sorption and migration
13. Impact of the degradation products of an ion exchange resin (UP2) on the uptake of radionuclides by cement
14. Sorption of An(III) and An(IV) on cement phases and bentonite: influence of competitive ligands and kinetic effects"
15. Investigations of actinide structural properties in solid, liquid and gas state applying high-energy resolution X-ray emission/absorption spectroscopy
16. Accurate neutron scattering based Monte Carlo Simulations of Radiation Fields and Dosimetry imposed by stored High-Level Nuclear Fuel Waste
17. Kinetics and interfacial processes in recrystallization of calcite and barite, and influence on radionuclide incorporation

Topics of the completed dissertations:

1. Retention of Iodine by the iron secondary phases green rust and magnetite
2. Assessment of the fate and behavior of naturally occurring thorium and uranium in the environment of central Sri Lanka
3. Spectroscopic investigation of the complexation of actinides and lanthanides with organic ligands
4. Steel corrosion and actinides sorption by iron corrosion products under saline conditions
5. Extraction and speciation studies for the optimization of the EURO-GANEX process

3 National and international cooperation, conferences and workshops

3.1 National and international cooperation

INE R&D involves numerous national and international collaborations and projects. These are described in the following.

National

INE is involved in various bi- and multilateral collaborations with national research centers, universities and industrial partners on different topics. The projects are partly supported by the German Federal Ministry for Economics and Technology (BMWt), the Federal Ministry for Education and Research (BMBWF), the Federal Ministry for the Environment, Nature Conservation, Building and Nuclear Safety (BMU), the Federal Company for Radioactive Waste Disposal (BGE), the German Research Foundation (DFG) and the Helmholtz Association (HGF).

In the framework of measures for retrieval of radioactive waste and decommissioning of the **Asse II salt mine**, provisions for emergency preparedness are taken. The operator of Asse II, the Federal Company for Radioactive Waste Disposal (BGE), performed an exploration drilling in the overlying sedimentary rocks of the salt diapir and coordinates studies with respect to the near-field of the radioactive waste. INE contributes both to the studies on radionuclide retention by rocks of the overlying sediments as well as to studies on the geochemical milieu and radionuclide solubility in the near-field of the radioactive waste. Based on the experimental results, sorption coefficients are derived, which are important input parameters for the assessment of the radionuclide retention capability. With respect to the near field of the waste within Asse II, INE performs experimental studies to improve the basis for assessing radionuclide transport and source terms.

In the collaborative project **EIKE**, funded by BMWt, aims at developing an inhibitor combination that helps increase the availability and sustainability of geothermal power. The economic efficiency of geothermal plants is often impaired by depositions of secondary minerals or corrosion damage. A promising countermeasure is the use of inhibitors, which can thereby improve the sustainability and economic use of geothermal plants. Geothermal plants in the North German Basin (NDB) extract highly saline thermal water from porous aquifers. Because of the small pore sizes (<100 μm), the flow parameters of such aquifers are sensitive to secondary mineral formation. If mineral deposition occurs near the injection well, the injectivity decreases. In geothermal plants, which extract thermal water from fractured aquifers - such as in the Upper Rhine Graben (ORG) - commercially available inhibitors are currently used in testing operation. In the long term, the harmlessness to water management as well as an expansion of the application to lower

injection temperatures will be essential, in order to enable sustainable and economic long-term operation. In EIKE we develop an inhibitor combination from available basic chemicals. Compared to commercial products, the combination of pure substances of known composition enables a systematic selection process and targeted studies on the thermal and chemical stability of the product mixture as well as a targeted adjustment to the respective geological and hydrological conditions.

Goal of the **f-Char** project is to deepen the understanding of the coordination chemistry of actinide and lanthanide ions with so-called soft donor ligands. In particular, the subtle differences in the interaction of soft donor ligands with the chemically similar actinide vs. lanthanide ions are further characterized and quantified. An essential aspect is the training and promotion of young scientists in the field of nuclear safety research and nuclear chemistry in general and in actinide chemistry in particular. Thus, the project makes an important contribution to the establishment, further development and maintenance of scientific-technical competence in nuclear safety research.

Geothermal energy will be a crucial element of the German *Energiewende*, in particular of the heat transition. The geothermal development faces a number of drawbacks resulting from immature technological development in early prototypes. Although major technological developments have been made, the related major setback, the low acceptability of deep geothermal technology by the society, remains. This is where the inter- and transdisciplinary project **GECKO** comes in. GECKO aims at involving the public in a co-design process that is linked to the establishment of deep geothermal infrastructures for heat production and storage at the KIT Campus North. The campus is located on the largest known thermal anomaly in Germany with approx. 170 °C at a depth of 3 km. At INE, different scenarios of utilization and their respective consequences were established using numerical modelling to provide the co-design process with the consequences of criteria decisions and alternatives in the design.

The **GRaZ II** project deals with the migration of radionuclides in the near field of a repository for radioactive waste in clay formations with focus on the hyperalkaline water-cement-system. KIT-INE investigates the retention of actinides and lanthanides by clay minerals in presence of relevant inorganic and organic ligands. The project focusses on carbonate, and cement additives (e.g. plasticizer and superplasticizer) like gluconate and citrate. The impact of these ligands on the sorption and solubility of actinides is studied in a wide pH range up to hyperalkaline pH values. One important aim of the project is the consistent thermodynamic modelling of experimental solubility, complexation,

and sorption data. The project provides basic knowledge and thermodynamic data needed in the frame of a long-term safety analysis of different repository concepts.

The **Helmholtz Climate Initiative** involves research on climate mitigation and adaptation. In the *ZeroNet-Zero-2050* Cluster, strategies and new approaches to achieve rapid and far-reaching reductions in emissions from all greenhouse gases including removal from the atmosphere and permanent storage or turning into high energy-density chemical energy carriers by renewable energy are scientifically examined and evaluated in four projects with regard to the German framework. In addition, two case studies are carried out with external stakeholders. The *Climate Neutral City*, is placed at the city of Karlsruhe. In the project *Potential and Integration of Subsurface Storage Solutions*, INE contributes to the topic of high-temperature heat storage. Forecasting chemical processes and related changes in reservoir condition over the operation time was carried out using thermo-hydraulic and chemical modelling. Results were coupled to the district heating model of the campus.

The collaborative project **iCross** is jointly funded by HGF and BMBF. Goal of the project is to progress towards a more realistic description of waste disposal systems, i.e. to reduce the need for conservative assumptions in model predictions of radionuclide migration through the near- and far field around nuclear waste repositories. In order to demonstrate significant progress within the three years funding period, the iCross consortium agreed to focus on two aspects of this very general task: 1) radionuclide migration through the evolving near-field (i.e. multi-barrier system), with a special focus on the canister-bentonite interface, and 2) the influence of heterogeneities in the host rock on radionuclide migration, from the micro- to the regional scale. Investigations involve laboratory- as well as underground research laboratory experiments (mainly in Mt. Terri, Switzerland), and modelling exercises from quantum chemical simulations through pore-scale modelling, continuum-scale modelling to regional scale THMC models. Experimental results and small-scale models are integrated into a reactive transport model chain, representing radionuclide transport from the near- to the farfield. The iCross consortium combines competences from the HGF program NUSAFE / research field “Energy”, with the HGF research field “Earth and Environment”, with the goal to become the cornerstone for a “Helmholtz Competence Centre for Nuclear Waste Repository Research”.

Detailed knowledge of metallic corrosion processes is important input for the Safety Case of a nuclear waste repository. The project **IMKORB** aims to provide an improved understanding of metallic corrosion processes for conditions representative of clay-based disposal sites for heat generating waste. Modern microscopic and spectroscopic techniques are applied to decipher the underlying processes and their associated kinetics in dedicated experiments carried out in the laboratory. These experiments are complemented by in situ

experiments under undisturbed conditions in underground research laboratory (see below). The ultimate goal is to identify the corrosion products likely to be present in the long-term and which may act as chemical barrier and reduce the radionuclide mobility.

The **KOLLORADO-e3** project aims at a profound mechanistic understanding of the processes that can lead to compromise the integrity of the bentonite engineered barrier system and the consequent colloid-mediated radionuclide transport. In particular, such processes are investigated under natural, repository relevant conditions present in fractured granitic host rock. The project, funded by BMWi, comprises three partners (KIT-INE, FSU and GRS). KIT-INE, together with FSU, perform laboratory scale experiments in the controlled area of KIT-INE, as well as *in situ* tests at the generic underground research lab of the Grimsel Test Site (Switzerland) in the frame of the international collaboration of the CFM project. The experimental research focuses on the fundamental mechanisms of bentonite erosion and colloid formation especially at the interface between the saturated bentonite and the crystalline rock, the speciation of the radionuclides, their tendency to sorb onto the colloids and the interactions between colloid-bound or dissolved radionuclides with the surface of the crystalline rock. To address these studies, a variety of analytical methods are employed at KIT-INE, including radiation detection (gamma- and alpha- spectrometry), mass spectrometry (ICP-MS and AMS), surface/solid state analysis and microscopy (XRD and SEM). The obtained experimental data are then merged with modelling results in order to acquire performance-assessment information concerning the influence of bentonite colloids on radionuclide migration and retardation, and finally to gain knowledge on the long-term safety of geological repositories in granitic host rock.

The mechanical and chemical stability of steel containers containing nuclear waste play an important role in performance assessment of disposal sites. The project **KORSO** aims at improving the understanding of steel corrosion in saline environments under conditions representative of disposal sites for heat generating waste. Microscopic and spectroscopic techniques are applied to identify the underlying corrosion mechanisms and their kinetics in dedicated experiments in saline, anoxic and elevated temperature conditions. The second aim is to investigate the retention of radionuclides by secondary phases identified in corrosion experiments by applying spectroscopic and chemical methods. The ultimate goal is to reduce uncertainties concerning interaction mechanisms between radionuclides and corrosion products, and thereby improve confidence in the long-term prediction of radionuclide mobility. The project was successfully finalized in 2020.

The research topic of the collaborative project **KRIMI** relates to non-site-specific scenarios for safety assessments for deep geologic repositories for highly radioactive nuclear waste, where waste packages get into contact with groundwater. This will result in corrosion and potentially in failure of canisters and release

of radionuclides. Assuming such conditions, long-term simulations will be necessary to demonstrate repository safety. Essential parameters for the description of the mobility of radionuclides in such simulations are solubility limits and sorption coefficients of involved radionuclides under the respective geochemical conditions. An intermediate between sorption and precipitation is the incorporation of radionuclides into solid-solutions. In solid-solutions the whole mineral volume may be effective towards radionuclide retention. Thus, solid-solutions have a high potential for radionuclide sequestration compared to pure surface adsorption processes. Nevertheless, despite their retention potential, solid-solutions are nowadays rarely included in safety assessment simulations. This is due to the lack of necessary model parameters, which may serve to reliably describe the thermodynamics and especially also the kinetics of solid-solution formation. Scientific goal of KRIMI is the investigation of thermodynamics and formation kinetics of repository-relevant solid-solutions. Systems investigated within KRIMI include the radionuclides: TC(IV), Pu(III), Se(IV), Np(V), and Ra(II) and the host minerals magnetite, calcite and barite. Studies include atomistic simulations, experimental studies, and investigation of natural analogue samples. An overarching societal goal of KRIMI is to contribute to the build-up and retention of competence in the field of radio-geochemistry. KRIMI is funded by BMBF.

The joint project **NaMaSK** is a promising approach to reduce the amount of secondary waste generated by waterjet abrasive suspension cutting (WASS) in the context of nuclear power plant decommissioning. In this project, which is funded by the German Federal Ministry of Education and Research (BMBF), an existing pilot separation device will be optimized and upgraded to provide proof of concept for radioactive operations. For this purpose, a separation device adapted to a glovebox will be installed and operated in the KIT-INE control area. Another focus of the project is the scientific investigation of suitable corrosion inhibitors for the application of the separation device to low-alloy steels, especially under the influence of ionizing radiation.

The overall objective of the **SEPAM** project is the scientific investigation and further development of extraction processes as well as the basic chemistry for the separation of americium from highly radioactive wastes. Due to the international orientation of the project (Lomonosov Moscow State University being partner to the project), current developments abroad are taken into account. Thus, the project makes an important contribution to the establishment, further development and maintenance of scientific-technical competence in nuclear safety research.

SMILE is a project dealing with reactive transport modeling (Smart-Kd in long term safety-assessment – applications). The main goals of SMILE are the extension of the concept developed up till now towards inclusion of redox-reaction, to corroborate the chemical description of interfacial reactions via more fundamental insight in structure, stoichiometry and thermodynamic parameters of relevant surface complexes, to compare

state of the art surface complexation in the evaluation of available experimental data, to extend the experimental data basis via batch- and column experiments on laboratory systems, to calculate smart Kd-martrices for selected redox-systems, and to apply the concept and verify the concept via experiments and modeling for systems that are closer to environmental systems in a critical manner. This is supposed to pave a fundamental basis allowing to transfer the smart-Kd-concept to various geological settings. Additionally, this will allow for the coupling of the concept to geochemical reactive transport codes to be initiated.

The collaborative project **SPIZWURZ** focuses on experimental and theoretical studies on the behaviour of hydrogen in fuel rod cladding materials and the stress state of Zircaloy-4 cladding in contact with high burn-up spent nuclear fuel to assess the impact on cladding integrity under dry interim storage conditions. For this purpose, long-term and detailed studies on non-irradiated cladding materials and samples will be performed by other project partners within workpackage 1. In workpackage 2, KIT-INE will determine the geometry of an irradiated nuclear fuel rod segment by means of a laser scan micrometre before and after removal of the fuel. The variation of the cladding geometry allows to determine the hoop stress in the cladding, exerted by the fuel pellet. The experimental work is further supported by simulations and theoretical modelling performed by the German Association for Plant and Reactor Safety (GRS). Moreover, the Company for Interim Storage (BGZ) is involved in the project as an observer.

Within the **THEREDA** project, KIT-INE provides thermodynamic data – complex formation constants, solubility data – for selected radionuclides from experiments and literature. The data are incorporated into a centrally managed and administered database of evaluated thermodynamic parameters after passing an evaluation process. This database is open for registered user. Thermodynamic data are required for environmental applications in general and radiochemical issues in particular. THEREDA, funded by the the Federal Company for Radioactive Waste Disposal (BGE), is developed as a national (reference) standard and basis for future Safety Assessments for a national nuclear waste repository.

The **ThermAc** project (01.03.2015 to 30.04.2020) aimed at extending the chemical understanding and available thermodynamic database for actinides, long-lived fission products and relevant matrix elements in aquatic systems at elevated temperatures. To this end, a systematic use of estimation methods, new experimental investigations and quantum-chemistry-based information is intended. The project is funded by the German Federal Ministry for Education and Research (BMBF) and is coordinated by KIT-INE. The ThermAc project is developed in order to improve the scientific basis for assessing nuclear waste disposal scenarios at elevated temperature conditions. The project was successfully finalized in 2020.

The collaborative project **TRANSENS**, funded by BMWi, is the first large-scale project in Germany for

transdisciplinary research into the disposal of spent nuclear fuel and vitrified high-level radioactive waste. TRANSENS aims to evaluate technical, safety related and procedural aspects of disposal strategies for high-level radioactive waste from the perspective of all scientific disciplines involved, such as natural sciences, engineering, law, and social sciences. A key objective of this transdisciplinary research project is the interaction between scientists from different disciplines and citizen scientists. In doing so, citizens, actors from practice and other non-academic stakeholders are included in the research process. Within the project, KIT-INE is responsible for a work package on developing criteria for decisions at critical points or “switch points” for recertifications on the route from interim storage to deep geological disposal of highly radioactive waste. At KIT-INE, interdependencies between interim storage and final disposal and their implications are investigated. Thereby, a multidimensional "landscape" results from the consideration of (procedural) technical steps, technical alternatives, interdependences, and resulting constraints. In the decades-long process, intended and unforeseen hold points have to be taken into account, these have to be foreseen and analyzed, and decision criteria for the course of action have to be developed.

The work of KIT-INE within **VESPA II** (initiated in September 2017 and ongoing until mid-2022) is highlighting the key relevance of geochemical research for evaluating radionuclide retention and mobilization in the frame of nuclear waste disposal. Based upon new systematic experimental studies, a significant increase of understanding regarding the behavior of long-lived fission and activation products, i.e. ^{99}Tc , ^{79}Se and ^{129}I , has been obtained. Fundamental site- and host-rock independent thermodynamic data derived within VESPA allow a better modeling and prediction of radionuclide chemistry in aquatic systems. The retention of radionuclides on several relevant mineral phases is analyzed and quantified. As a result of the work performed by KIT-INE within VESPA II, the long-term safety of different repository concepts and scenarios can be assessed on a decisively improved scientific level.

International

The international Colloid Formation and Migration (**CFM**) project focuses on the stability of the bentonite buffer/backfill in contact with water conducting features and the influence of colloids on radionuclide migration in crystalline host rocks coordinated by NAGRA (National Cooperative for the Disposal of Radioactive Waste, Switzerland). The project uses the experimental set-up in the controlled zone at the Grimsel Test Site (Switzerland). Additional partners involved are from Japan (JAEA, NUMO, CRIEPI), South Korea (KAERI), Finland (POSIVA Oy and Helsinki University), Switzerland (NAGRA, PSI-LES), Spain (CIEMAT), Sweden (SKB, KTH), United Kingdom (NDA RWMD) and United States (LANL). INE plays a decisive role in the laboratory program and is mainly carries out the field activities.

KIT-INE is also partner in the Material Corrosion Test (**MaCoTe**), which is a project carried out at the Grimsel Test Site and coordinated by NAGRA. Additional partners involved in this project are KIGAM (South Korea), RWM (United Kingdom), NWMO (Canada), NUMO (Japan), SURAO (Czech Republic) and BASE (Germany). KIT-INE performs non-heated experiments to study in situ the corrosion of selected candidate canister materials embedded in bentonite. The aims are to provide confirmation on the long-term anaerobic corrosion rate in compacted bentonite under repository relevant conditions and to identify the associated corrosion processes.

Horizon 2020 and EJP

The overall objective of the Horizon 2020 project **BEACON** is to develop and test the tools necessary for the assessment of the mechanical evolution of an installed bentonite barrier and the resulting performance of the barrier. This will be achieved by cooperation between design and engineering, science and performance assessment. The evolution from an installed engineered system to a fully functioning barrier will be assessed. This will require a more detailed understanding of material properties, of the fundamental processes that lead to homogenization via water saturation, of the role of scale effects and improved capabilities for numerical modelling. The goal is to verify the performance of current designs for buffers, backfills, seals and plugs. For some repository designs mainly in crystalline host rock, the results can also be used for the assessment of consequences of mass loss from a bentonite barrier in long-term perspective.

The goal of the H2020 project **DEEPEGS** is to demonstrate the feasibility of enhanced geothermal systems (EGS) for delivering energy from renewable resources in Europe. Testing of stimulating technologies for EGS in deep wells in different geologies will deliver new innovative solutions and models for wider deployments of EGS reservoirs across Europe. DEEPEGS will demonstrate advanced technologies for widespread exploitation of high enthalpy heat (i) beneath existing hydrothermal field at Reykjanes (volcanic environment) with temperature up to 550°C and (ii) very deep hydrothermal reservoirs in France with temperatures up to 220°C. The focus on business cases will demonstrate advances in bringing EGS derived energy (TRL6-7) to market exploitation. We seek to understand and address social concerns about EGS deployments. We will through risk analysis and hazard mitigation plans ensure that relevant understanding and minimization of the risks will be implemented as part of the RTD business case development. The project was successfully finalized in April 2020.

Within the European Commission Horizon 2020 frame, the study of modern spent nuclear fuel dissolution and chemistry in failed container conditions is included in the **DISCO** collaborative project. The aims of this project are, first, to enhance the understanding of spent fuel matrix dissolution under conditions representative of failed containers in reducing repository environments and, second, to assess whether novel types

of fuel (MOX, UO₂ doped with additives such as Cr, Gd) behave like the conventional ones (UO₂). INE provides results on the dissolution of MOX fuel under reducing conditions and, in addition, is the leader of work package 3 “Spent fuel dissolution experiment” supervising the spent nuclear fuel dissolution experiments performed by the different partners within the project. INE also contributed also to work package 2 “Preparation and characterization of samples and experimental systems”.

Understanding the electronic structure and chemical bonding properties of the early actinide (An) elements (Th-Cm) poses a great challenge and scientific frontier in fundamental chemistry and physics. A deep insight into the An electronic structure and bond formation is also essential for developing innovative spent nuclear fuel conditioning strategies, to understand actinide environmental behaviour - e.g., in contaminated legacy sites or the context of underground nuclear waste repositories - as well as for developing advanced pharmaceutical compounds for targeted cancer treatment. The ERC funded project „**The Actinide Bond**“ focuses on the link between covalency and strength of the chemical bond of the An elements in gas, liquid and solid state materials. The scientific challenges of these materials are tackled by combining highly innovative experimental setups, advanced synchrotron based X-ray spectroscopy methods and state-of-the-art quantum chemical computations. X-ray based methodologies with high potential for a breakthrough in efforts will be developed, e.g., to select An materials or complexing agents with specific characteristics for the aforementioned application fields. Of essential importance for the success of the “The Actinide Bond” project are the ACT (CAT-ACT beamline) and X-Spec experimental stations at the KIT synchrotron source (KARA storage ring), situated within 10 minutes walking distance from the INE institute with its state of the art radiochemical laboratories.

The European Joint Programme on Radioactive Waste Management (**EURAD**) is a large scale integrated research programme dealing with various aspects of safe management of nuclear waste (www.ejpurad.eu/). Within EURAD, KIT-INE is strongly involved in EURAD and contributes to four workpackages: Cement-Organic-Radionuclide-Interactions (CORI), Fundamental understanding of radionuclide retention (FUTuRE), Spent Fuel Characterisation and Evolution Until Disposal (**SFC**) and Uncertainty Management multi-Actor Network (**UMAN**).

INE is coordinating the WP **CORI**. CORI aims to develop an in-depth understanding of the interaction of cementitious materials with organic matter and radionuclides. Organic materials are present in some nuclear waste and as admixtures in cement-based materials and can potentially influence the performance of a geological disposal system, especially in the context of low and intermediate level waste disposal. The potential effect of organic molecules on radionuclide migration is related to the formation of complexes in solution with

some radionuclides of interest (actinides and lanthanides) which can increase the radionuclide solubility and decrease the radionuclide sorption. INE is active in all WPs of CORI, performing two separate studies in cooperation with EMPA (Switzerland) and with SKB (Sweden).

FUTURE aims at realizing a step change in quantitative mechanistic understanding of radionuclide retention in the repository barrier system. Work in **FUTURE** concerns the identification of constraints and the increase in predictability of radionuclide migration properties in “real” clay and crystalline rocks, quantifying the influence of key parameters of the heterogeneous rock/water system such a rock structure, redox interfaces, water saturation, reversibility etc.. Work of INE focusses on the investigation of radionuclide retention processes on clay materials, using a large set of modern analytical tools.

The **SFC** workpackage aims mainly to establish beyond state-of-the-art quantification of the characteristics and chemical processes of spent nuclear fuel assemblies from discharge of nuclear reactors, during interim storage until (pre-)disposal activities. Within SFC, KIT-INE contributes with experimental and numerical studies to improve determination of radionuclide inventories of spent nuclear fuel rods and to assess chemical interaction between spent nuclear fuel pellets and cladding within the fuel rods. KIT-INE reviewed and improved measurements methods to analyse radionuclide inventories of spent nuclear fuel samples. They allow a considerable enhanced reliability, estimated at about 5 to 10%. On the numerical side the governing codes in KIT-INE (MCNP, CINDER and NUCLEONICA) are validated by dedicated benchmarks. The encouraging results allows for future accurate estimation of the material composition of and characterization of the fuel pellet and in particular of the cladding. The cladding properties are of immense importance of the fuel integrity and hence the safety of the disposal site.

The **UMAN** workpackage is dedicated to the management of uncertainties possibly relevant at different stages of radioactive waste management and programs. It aims at exchange of views, practices and uncertainty management options as well as the review of existing strategies, approaches and tools. Moreover, **UMAN** tries to foster the interaction of various types of actors and also the civil society. The workpackages tries to identify remaining and emerging issues associated with uncertainty management, that could be addressed then in subsequent waves of EURAD, by reviewing past and present EU, IAEA and NEA projects. KIT-INE is involved in various subtasks dealing with uncertainty management of spent nuclear fuel. Furthermore, KIT-INE leads the core group on compiled and reviewed information about possible management options for uncertainties related to spent nuclear fuel.

With the **PREDIS** project funded by the European Commission, INE contributes to WP7 which is aiming to provide innovations in cemented waste handling and pre-disposal storage. The **PREDIS** project started 1.9.2020 with four years duration. **PREDIS** high-level

objectives are to develop solutions (methods, processes, technologies and demonstrators) for future treatment and conditioning of waste, improving safety during next waste management steps or improve existing solutions with safer, cheaper or more effective alternative processes where they bring measurable benefits to several Member States. In WP7, INE KIT contributes in to adapt and demonstrate digital twin technology. In this context, INE uses advanced analytical techniques for the characterization of cement-based waste packages for calibration / validation of geochemical and mechanical models.

The **GEMex** project is a EU-Mexico joint effort in development of Enhanced Geothermal Systems (EGS) and Superhot Geothermal Systems (SHGS) at Aco-culco and Los Humeros that bases on three pillars:

1 – Resource assessment of these geothermal sites by understanding the tectonic evolution, fracture distribution and hydrogeology and predicting in-situ stresses and temperatures at depth.

2 – Reservoir characterization including novel geophysical and geological methods to be advanced for the specific condition. Accompanying high-pressure/ high-temperature laboratory experiments will provide the input parameters.

3 – Concepts for site development will include definition of drill paths, a design for well completion including suitable material selection, and optimum stimulation and operation procedures for safe and economic exploitation. In these steps, we will address issues of public acceptance and outreach as well as the monitoring and control of environmental impact. The project was successfully finalized in May 2020.

A follow-up of the FP7 project SACSESS, **GENIORS** focuses on actinide separations related to future multiple recycling strategies. GENIORS is expected to provide the EU with science-based strategies for nuclear fuel management and contribute significantly to its energy independence. In the longer term, the project's results will facilitate radioactive waste management by reducing its volume and radiotoxicity, and support a more efficient utilization of natural resources. 24 Partners from 10 countries contribute to GENIORS; a formal collaboration with US-DOE is established. The project is coordinated by CEA; KIT is in charge of the

hydrometallurgy domain. The project was successfully finalized in May 2021.

The European Horizon-2020 project **SANDA** (Supplying Accurate Nuclear Data for energy and non-energy Applications) is combining experimental and theoretical efforts to produce reliable nuclear data libraries for safety authorities, research institutions, the nuclear energy industry, health organizations, other non-energy applications and the EU society. KIT-INE investigates nuclear data needs, which arise in connection with nuclear plant decommissioning and waste disposal operations. In this sense, the governing nuclear data needs concern decay heat, mobility of radioactive nuclides and the absorption and scattering characteristics of the walls within the disposal gallery. Beyond the analysis of the data themselves, KIT-INE investigates the uncertainties of the data by means of covariance's data introduction into random files, from which the deviation from the mean value is illuminated.

VESTA is a collaborative research project on high-temperature heat storage in the deep underground. It involves five German partners from industry and science as well as the international partners GeoEnergie Suisse, Lawrence Berkeley National Laboratory (LBNL) and Idaho National Laboratory (INL). For thermal energy storage on a large scale and in the higher temperature range required for feeding into district heating networks and for industrial processes, novel high-temperature storage (HTS) systems in the deep subsurface are an option. However, many technical, regulatory, legal, environmental, and economic challenges need to be resolved to enable broader application of HTS. Within the scope of the VESTA project, it is planned to scientifically investigate the implementation of HTS systems by means of demonstration projects. Overarching goals of VESTA are to 1) demonstrate HTS at selected pilot sites including DeepStor, 2) evaluate technical and non-technical barriers, 3) support development and implementation of commercial projects by providing process understanding, modeling and monitoring techniques, and optimized component design, 4) support agencies with scientific and technical knowledge as a basis for advancing regulatory provisions. The new Helmholtz research infrastructure DeepStor is one of the demonstrators of VESTA.

3.2 Colloquium celebrating the 40th anniversary of the foundation of the Institute for Nuclear Waste Disposal at KIT and TransRet2020 workshop

In 2020 the Institute for Nuclear Waste Disposal (INE) at the Campus North of KIT turned 40. The basic and applied research in the fields of radio/geo-chemistry and material sciences carried out at INE is focused on safety aspects of a future underground repository for highly radioactive, heat producing waste forms from decades of nuclear energy generation in Germany. In addition, research at INE was recently extended to the medium-term behavior of irradiated fuel elements during interim storage until their final emplacement in an underground storage facility, which is - according to the current site selection process - not to be expected before the middle of the century. Further activities at INE are related to geothermal energy generation and the dismantling of nuclear facilities.

Nuclear waste related safety research on Campus North goes back to the early days of the research facility in the 'Hardtwald' forest near Eggenstein-Leopoldshafen. A first expert group to elucidate the possibilities of deep geological storage of nuclear waste was established in 1964 by the KIT predecessor organization 'Gesellschaft für Kernforschung mbH'. In 1974 the scientific working group Treatment of Radioactive Waste (ABRA) was separated from the Department for Decontamination Operations ('Hauptabteilung Dekontaminationsbetriebe', today KTE Karlsruhe) at the former Nuclear Research Center Karlsruhe (KfK). From this entity, INE emerged in 1980, initially as the Institute for Nuclear Waste Disposal Technology. Finally, this was abbreviated to Institute for Nuclear Waste Disposal in the era of the 'Forschungszentrum Karlsruhe GmbH' (FZK). The renaming took the increasingly basic character of research at INE into account, i.e., a distinct focus on molecular process understanding when describing the long-term evolution of a nuclear waste repository.

To celebrate the 40th anniversary of INE's foundation - due to the COVID-19 pandemic one year late - on October 11, 2021, experts and invited guests came together for a colloquium in the Aula of the Training Center for Technology & Environment (FTU) on KIT Campus North. Participants included representatives of the Helmholtz (HGF) Centers involved in Germany's nuclear repository safety research (HZDR, FZJ, UFZ, GFZ and KIT), the Helmholtz program NUSAFE, the Federal Company for Radioactive Waste Disposal (BGE) in charge of the site selection process, the Fed-

eral Office for the Safety of Nuclear Waste Management (BASE) as the national supervisory authority, the responsible federal and state ministries, the National Advisory Committee (NBG) for the search of a repository site and representatives of European repository research programs. The event was opened with a greeting from KIT President Prof. Dr. Holger Hanselka and a video message from HGF President Prof. Dr. Otmar Wiestler. As a special challenge for the organizers, the symposium was held in a hybrid format with about 80 participants attending onsite and many more connected online from their offices at KIT or abroad.

The INE symposium was followed by the two-day scientific workshop TransRet2020 – Workshop on Processes Influencing Radionuclide Transport and Retention – on October 12-13, 2021, held at the same venue. TransRet2020 – as well postponed from 2020 due to the restrictions imposed by the pandemic – was the seventh meeting in the series of the Karlsruhe Geochemical Workshops (co-)organized by INE. The first workshop was held in 1997 at the KIT predecessor Forschungszentrum Karlsruhe (FZK). Its main topic was *Geochemical modelling – radiotoxic and chemical toxic substances in natural aquatic systems*. The second meeting was held in 1999 in Speyer, focusing on *Mineral/water interactions close to equilibrium*. TRePro 2002 held in Karlsruhe dealt with *Modelling of coupled Transport Reaction Processes*. SoPro 2005 held again in Karlsruhe treated *Sorption Processes on oxide and carbonate minerals*. TRePro II 2009 was again more focusing on contaminant transport aspects. TRePro III 2014 took up the ideas of TRePro 2002 and TRePro II 2009. The intention of the workshops has always been to enhance the discussion between experimentalists and modelers from different domains – a goal achieved as well for TransRet2020, although the meeting had to be organized in hybrid format with about 40 participants attending onsite at KIT-FTU and about the same number following online. For the accompanying poster session with 30 contributions, all authors (onsite or online) were given the opportunity for a four minute flash presentation of their work summarized in two slides. All posters were available as downloads for registered participants and later (online) discussion. A compilation of TransRet2020 abstracts will be published in the KITopen Series *INE Scientific Working Documents* at <https://www.ine.kit.edu/english/53.php>.

4 Fundamental studies: Process understanding on a molecular scale

In order to develop fundamental scientific understanding on a molecular scale and ensure the reliable quantitative prediction of key processes in aquatic chemistry, several R&D studies on radionuclide chemistry and geochemistry are performed at KIT-INE. Aiming at a comprehensive assessment of radionuclide behavior and mobility in aquatic systems relevant for nuclear waste disposal, experimental studies with actinides, long-lived fission and activation products and selected non-radioactive elements of interest are performed. The investigated aqueous systems cover from dilute solutions to highly saline salt brine systems and establish essential site-independent data and process understanding. Work is focusing both on detailed experimental investigations using the unique facilities available at KIT-INE, and subsequently developing reliable chemical models and consistent thermodynamic data. This combined approach allows a systematic and reliable evaluation of key processes such as radionuclide solubility, radionuclide speciation, radionuclide retention and transport processes in relevant near- and far-field scenarios.

The fundamental studies summarized in this section is related to the (i) chemistry and thermodynamics of actinides and fission products in aqueous solution, (ii) radionuclide sorption on mineral phases, and (iii) retention of radionuclides by secondary phase formation. The studies aim at identifying relevant radionuclide retention/retardation mechanisms on a molecular level and their robust thermodynamic quantification in support of the Nuclear Waste Disposal Safety Case. The fundamental studies on aqueous radionuclide chemistry described in Chapter 4 are supporting the applied studies (see Chapter 5) performed at KIT-INE.

4.1 Chemistry and thermodynamics of actinides and fission products in aqueous solution

M. Altmaier, M. Böttle, N. Cevirim-Papaioannou, K. Dardenne, N. DiBlasi, D. Fellhauer, X. Gaona, Y. Jo, J.-Y. Lee, R. Polly, T. Prüßmann, J. Rothe, D. Schild

In co-operation with:

B. de Blochouse^a, K. Garbev^b, O. Walter^c

^a ONDRAF/NIRAS, Sint-Joost-ten-Node, Belgium; ^b Institute for Technical Chemistry, Karlsruhe Institute of Technology, Karlsruhe, Germany; ^c European Commission, DG Joint Research Centre, Directorate G - Nuclear Safety and Security, 2340, D-76125 Karlsruhe, Germany

Introduction

Research activities developed at KIT-INE within the field of *Aquatic chemistry and thermodynamics of actinides and fission products* mainly focus on systems relevant for nuclear waste disposal, and aim at contributing to the safety and performance assessment of repositories designed for the disposal of such wastes. Source term estimations and geochemical calculations require complete and correct chemical, thermodynamic and ion-interaction (activity) models, which are preferably based on sound and systematic experimental investigations. This section highlights the fundamental and applied research performed at KIT-INE in the period 2020–2021 within this topic.

In addition to the experimental R&D activities described in this chapter, KIT-INE contributes to several national and international projects, *e.g.* providing support and expert judgement to BGE with regard to geochemical or radiochemical processes, participating in the development of the national thermodynamic reference database for actinides and fission products (THEREDA project) or contributing to several volumes of the OECD NEA-TDB thermodynamic series.

Solubility, hydrolysis and solid phase formation of Np(V) in alkaline NaCl solutions

Systematic investigations of Np(V) solubility, hydrolysis and solid phase formation have been a continuous research topic at KIT-INE over the last decade and covered several relevant electrolyte systems, *e.g.* NaCl [1,2], CaCl₂ [3] and MgCl₂ [4]. One of the first chemical and thermodynamic models describing the solubility and hydrolysis of Np(V) in Na⁺-dominated solutions was provided by Neck *et al.* [1]. It is based on the results of solubility experiments performed with binary NpO₂OH(am) as a function of pH and salt concentration. In subsequent studies it became more and more evident that NpO₂OH(am) is actually only metastable over wide pH ranges in alkaline Na⁺-dominated solutions towards transformation into ternary Na-Np(V)-OH solid phases [2]. Depending on the solution conditions, several structurally different phases were identified based on diffraction data and XAFS information. Preliminary solubility data indicated a great stability (low solubility) of these ternary Na-Np(V)-OH phases, but did not allow for a quantitative evaluation of thermodynamic solubility constants. To overcome this

fact, additional experiments were performed in the present work. Two different crystalline Na-Np(V)-OH solid phases were (i) synthesized, (ii) chemically and structurally characterized, and (iii) their thermodynamic stability determined within a solubility study.

Experiments were performed under inert argon atmosphere in an alpha-tight glove box. Aliquots of an oxidation state pure $^{237}\text{NpO}_2^+$ stock solution were equilibrated in 0.1 and 1.0 M NaOH solutions under mild hydrothermal conditions for several weeks resulting in the formation of crystalline Na-Np(V)-OH solid compounds. The latter were comprehensively characterized by various methods including scanning electron microscopy (SEM-EDX), quantitative chemical and oxidation state analysis, powder and single crystal X-ray diffraction (XRD). The solubility behavior of both solids was independently studied in 1.02 m NaCl solutions as a function of $\text{pH}_m = -\log m_{\text{H}^+} = 8.5\text{--}13$ at $T = (22 \pm 2)^\circ\text{C}$. ^{237}Np concentration in the samples were routinely determined by mass spectrometry (ICP-MS) and/or liquid scintillation counting (LSC) after phase separation by 10 kD ultrafiltration. The Np oxidation state distribution was analyzed by a solvent extraction procedure using HDEHP. The pH_m values were measured with combination glass electrodes.

The results of the solid phase characterization confirmed that both reaction conditions lead to the formation of two different, pure Na-Np(V)-OH crystalline solid phases. Stoichiometries and structural models were revealed by single crystal XRD analysis at JRC Karlsruhe. In 0.10 m NaOH the so far not described $\text{Na}_{0.5}[\text{NpO}_2(\text{OH})_{1.5}] \cdot 0.5\text{H}_2\text{O}(\text{cr})$ (**A**) was obtained. It crystallizes in the monoclinic space group and appears as bulky platelets. In 1.0 m NaOH, hexagonal $\text{Na}[\text{NpO}_2(\text{OH})_2](\text{cr})$ (**B**) formed which was previously reported by Almond *et al.* [5]. SEM pictures of (**A**) and (**B**) are shown in Fig. 1.

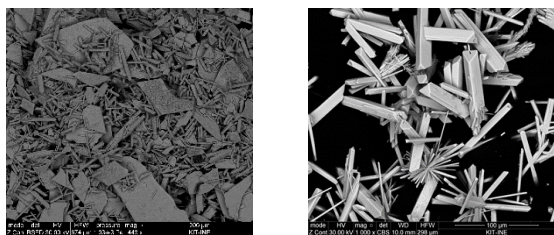


Fig. 1: Scanning electron microscope pictures of $\text{Na}_{0.5}[\text{NpO}_2(\text{OH})_{1.5}] \cdot 0.5\text{H}_2\text{O}(\text{cr})$ (left) and $\text{Na}[\text{NpO}_2(\text{OH})_2](\text{cr})$ (right).

The experimental solubility, $\log [\text{Np}(\text{V})]$ vs. pH_m , of solids (**A**) and (**B**) are displayed in Fig. 2. Both are less soluble compared to binary $\text{NpO}_2\text{OH}(\text{am})$ under the same experimental conditions, *i.e.* the two Na-Np(V)-OH solid phases are thermodynamically more stable. Furthermore, and as indicated by the intersecting solubility curves of (**A**) and (**B**), the former holds a greater stability at $\text{pH}_m < \approx 10.5$ and the latter at $\text{pH}_m > \approx 10.5$. This behavior is in clear accordance with the different hydroxide contents of both phases.

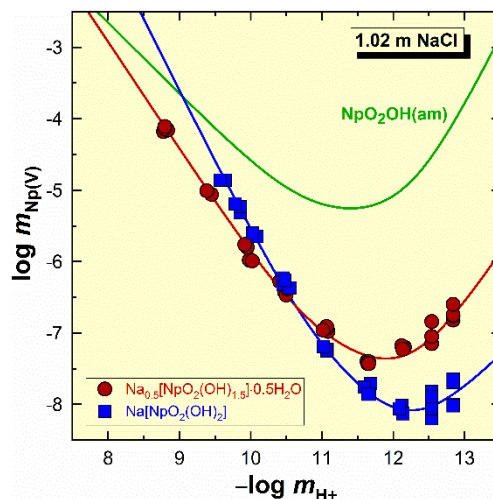
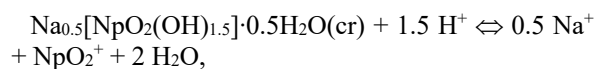
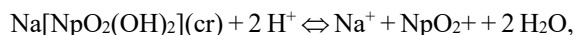


Fig. 2: Experimental and calculated (SIT) solubility of $\text{Na}_{0.5}[\text{NpO}_2(\text{OH})_{1.5}] \cdot 0.5\text{H}_2\text{O}(\text{cr})$, $\text{Na}[\text{NpO}_2(\text{OH})_2](\text{cr})$ and $\text{NpO}_2\text{OH}(\text{am})$ in alkaline 1.02 m NaCl solutions.

Up to $\text{pH}_m \approx 11$, an equilibrium between the Na-Np(V)-OH solid phases and the NpO_2^+ cation controls the Np(V) solubility,



and



leading to a rather steep decrease in $\log [\text{Np}(\text{V})]$ with increasing pH_m (slopes ≈ -1.5 to -2). At $\text{pH}_m > \approx 11$, the hydroxo complexes $\text{NpO}_2(\text{OH})_n^{1-n}$ with $n = 1\text{--}3$ are dominating the aqueous Np(V) speciation. This results in a flattening of the solubility curves, and finally in an enhancement of the solubility of (**A**) and (**B**) with increasing pH_m . From both data sets, new solubility constants $\log K_{s,0}$ and a set of consistent Np(V) hydrolysis constants $\log \beta_n$ with $n = 1\text{--}3$ were derived.

By systematic combination of sophisticated structural and well-established thermodynamic investigations, a superior understanding of the chemical equilibria that can control the solubility and hydrolysis of Np(V) in alkaline Na^+ -containing solutions was obtained. The results highlight the relevance of ternary M-Np(V)-OH solid phases as a sink for Np(V) in alkaline solutions, reveal details about their structural characteristics and stability, and provide chemical and thermodynamic models to be implemented into geochemical databases.

Impact of gluconate on the solubility and redox chemistry of Tc

^{99}Tc is one of the main fission products of ^{235}U and ^{239}Pu in nuclear reactors. Due to its long half-life ($t_{1/2} \sim 2.1 \cdot 10^5$ a), redox sensitive character and large inventory in spent nuclear fuel, ^{99}Tc is of great relevance in the context of safety assessment of repositories for radioactive waste. Tc is expected as the sparingly soluble

$\text{Tc}^{\text{IV}}\text{O}_2(\text{am, hyd})$ under the reducing conditions foreseen in deep-underground repositories. Under oxidizing and redox-neutral conditions, $\text{Tc}(\text{VII})$ is the predominating oxidation state forming the soluble and mobile pertechnetate anion, TcO_4^- . Gluconic acid (GLU, $\text{C}_6\text{H}_{12}\text{O}_7$) is a polyhydroxycarboxylic acid commonly used as additive in cement formulations. It is known to form strong complexes with hard Lewis acids such as tetravalent actinides, $\text{An}(\text{IV})$ [6]. In the field of medicine, gluconate has been described to stabilize other oxidation states of technetium beyond the “conventional” +IV and +VII prevailing in aqueous systems in the absence of complexing ligands [7-8]. This study aims at obtaining a better understanding of both fundamental processes at the molecular level and an improved quantitative thermodynamic model description of $\text{Tc}(\text{IV})$ systems in the presence of gluconate using the concepts of established solution thermodynamics.

Experiments were performed at $T = (22 \pm 2)^\circ\text{C}$ in Ar gloveboxes with < 2 ppm O_2 . The impact of gluconate on the solubility of Tc was investigated from under- and oversaturation conditions with $\text{TcO}_2(\text{am, hyd})$ and (in-situ reduction of) $\text{Tc}(\text{VII})$, respectively. Solubility samples were prepared in 0.1–5.0 M NaCl solutions with $9 \leq \text{pH}_m \leq 14$ and $10^{-4} \text{ M} \leq [\text{GLU}]_{\text{tot}} \leq 0.5 \text{ M}$. Reducing conditions were chemically set for each independent sample with $\text{Na}_2\text{S}_2\text{O}_4$, $\text{Sn}(\text{II})$, hydrazine or Fe powder, except for a limited number of samples that remained redox-unbuffered.

Concentration of Tc, pH_m and E_h values were monitored at regular time intervals, and thermodynamic equilibrium was assumed after repeated measurements with constant $[\text{Tc}]$ and pH_m . After attaining equilibrium conditions, the redox speciation of technetium in the aqueous phase of selected samples was investigated by L_3 - and K -edge XANES measurements. Solid phases of selected solubility experiments were characterized by XRD, SEM-EDS as well as EXAFS analysis. XAFS spectra were recorded at the INE- and ACT-Beamlines at KIT Synchrotron (formerly ANKA), KIT Campus North, in Karlsruhe (Germany).

The presence of gluconate significantly enhances the solubility of $\text{TcO}_2(\text{am, hyd})$ compared to GLU-free conditions (Fig. 3). The experimental solubility curve in the presence of gluconate shows also a different slope in the pH_m -range 10–14, providing indirect evidence on the change in the aqueous speciation, which is dominated by $\text{TcO}(\text{OH})_3^-$ under reducing conditions but absence of gluconate. Tc L_3 -edge XANES and K -edge EXAFS measurements of selected samples support the predominance of $\text{Tc}(\text{IV})$ -GLU aqueous species in the very reducing conditions defined by $\text{Sn}(\text{II})$, but the predominance of a $\text{Tc}(\text{V})$ -GLU complex in the absence of $\text{Sn}(\text{II})$ (Fig. 4). These novel findings are also analyzed by complementary theoretical calculations. Preliminary chemical and thermodynamic models are derived based on the combination of solubility data, solid phase characterization and spectroscopic observations (see red line in Fig. 3).

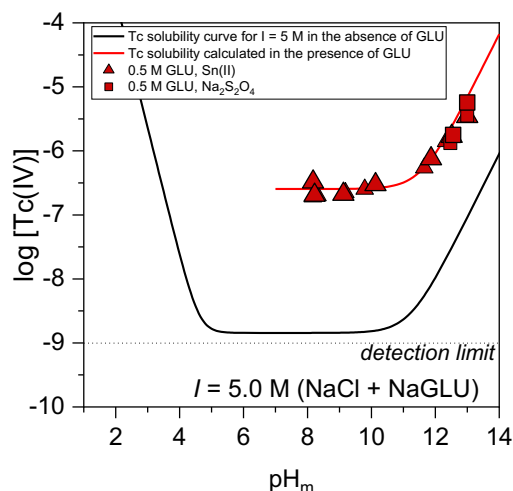


Fig. 3: Experimental solubility data of $\text{Tc}(\text{IV})$ in 5.0 M NaCl–NaGLU solutions with $[\text{GLU}] = 0.5 \text{ M}$. Red and black solid lines corresponds to the solubility of $\text{TcO}_2 \cdot 0.6\text{H}_2\text{O}(\text{am})$ in 5.0 M NaCl in the presence and absence of gluconate. Model calculations performed using thermodynamic data derived in this work or reported in [9], respectively.

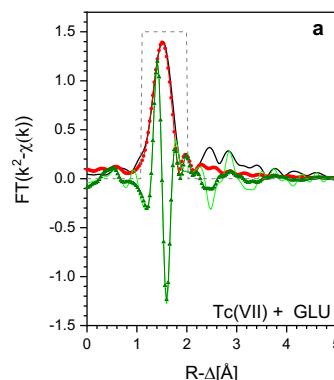


Fig. 4: Tc K -EXAFS of $\text{Tc}(\text{VII})$ samples containing gluconate in (a) absence and (b) presence of $\text{Sn}(\text{II})$ as reducing chemical. Fourier transform (FT) magnitude and imaginary part of k^2 -weighted $\chi(k)$ (black and light green solid lines, respectively) and corresponding R -space fit results (red line with filled circles and dark green line with filled triangles, respectively). Windows for forward FT and fit range are indicated by dashed lines.

This work highlights the potential of a combined approach including classical wet-chemistry methods (measurements of pH , E_h , $[\text{Tc}]$), advanced spectroscopic techniques (K -, L_3 -edge XAFS) and theoretical methods for the characterization of Tc aqueous systems of potential relevance in the context of nuclear waste disposal and other environmental applications [10-11].

Solubility of niobium(V) in hyperalkaline systems containing Ca: characterization of the solubility-controlling solid phases in cementitious environments

^{94}Nb is a long-lived activation product ($t_{1/2} = 2 \cdot 10^4 \text{ a}$) generated in nuclear reactors by neutron activation of stable ^{93}Nb present in structural components, e.g. Inconel alloy and stainless steel. Niobium is predominantly found in the +V oxidation state within the stability field of water, whereas the formation of $\text{Nb}(\text{III})$

is only expected under very acidic and reducing conditions. $\text{Nb}_2\text{O}_5(\text{s})$ is the solid phase controlling the solubility of Nb(V) in acidic to weakly alkaline pH conditions. The solubility of $\text{Nb}_2\text{O}_5(\text{s})$ is significantly enhanced in alkaline to hyperalkaline systems due to the formation of $\text{Nb}(\text{OH})_6^-$, $\text{Nb}(\text{OH})_7^{2-}$ or polyniobates at $[\text{Nb}]$ above ≈ 1 mM. In NaCl-NaOH systems, the formation of highly soluble Na-polyniobate solid phases, e.g. $\text{Na}_8\text{Nb}_6\text{O}_{19} \cdot 13\text{H}_2\text{O}(\text{s})$, has been described in the literature [12]. In contrast to pure Na-systems, dissolved Nb concentrations significantly drop in cement pore water solutions containing calcium ($[\text{Nb}] \approx 10^{-7} - 10^{-8}$ M) [13], although a conclusive characterization of the solid phase/s controlling the solubility of Nb(V) in these conditions is still missing.

All preparation, treatment, and handling of samples were conducted in an Ar-glove box ($\text{O}_2 < 1$ ppm) at $T = (22 \pm 2)^\circ\text{C}$. The initial concentration of Nb(V) in the solubility samples was varied between $1 \cdot 10^{-5}$ M and $5 \cdot 10^{-4}$ M, with $10 < \text{pH}_m < 12$ and $5 \cdot 10^{-3}$ M $< [\text{Ca}] < 0.03$ M. An additional experimental solubility series was prepared in 1 M CaCl_2 . An artificial cement pore water representative of the degradation stage I of cement was prepared with $\text{pH} = 13.5$, $[\text{Na}] = 0.14$ M, $[\text{K}] = 0.37$ M, $[\text{Ca}] = 3.5 \cdot 10^{-4}$ or $1.4 \cdot 10^{-3}$ M, and $[\text{CO}_3^{2-}]_{\text{tot}} = 3.4 \cdot 10^{-4}$ M (young cement pore water containing Ca, i.e. YCWCa) [14]. After contact times of 32, 57, and 200 days, an aliquot of the supernatant solution of each sample was taken, and potential colloids or suspended particles were removed by 10 kDa ultrafiltration. The dissolved concentration of Nb was quantified by ICP-MS. Nb solid phases were characterized after attaining equilibrium conditions. Solid phases were washed with ethanol 3 to 5 times and dried under Ar-atmosphere before characterization by powder X-ray diffraction (XRD), scanning electron microscopy with energy dispersive spectroscopy (SEM-EDS) and quantitative chemical analysis (after dissolution with a mixture of 2% HNO_3 and 0.1% HF).

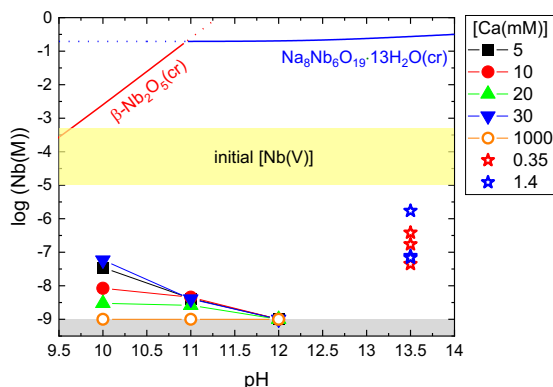


Fig. 5: Nb(V) solubility determined in alkaline to hyperalkaline systems with varying Ca concentrations. Symbols at pH 13.5 and $[\text{Ca}] = 1.4$ mM show the concentrations of Nb in YCWCa. Dashed lines delimit the range of initial Nb concentrations in the experiments. Solid lines display the calculated solubility of $\beta\text{-Nb}_2\text{O}_5(\text{cr})$ and $\text{Na}_8\text{Nb}_6\text{O}_{19} \cdot 13\text{H}_2\text{O}(\text{cr})$ in 0.1 M and 0.3 M NaClO_4 solutions, respectively [12]. Grey area represents the detection limit of ICP-MS in the conditions of this study.

In contrast to the stable stock solution in pure NaCl-NaOH system ($[\text{Nb}(\text{V})] = 1.2 \cdot 10^{-3}$ M, $\text{pH} = 12.3$), a clear drop of the initial concentration of niobium is observed in all samples prepared in Na-Ca-Nb(V)-Cl- H_2O systems, with $[\text{Nb}(\text{V})]_{\text{eq}} < 2 \cdot 10^{-6}$ M, see Fig. 5. A significant decrease of the initial Nb concentration is also observed in the YCWCa, with $[\text{Nb}] \approx 7 \cdot 10^{-8} - 2 \cdot 10^{-6}$ M. These observations support the formation of sparingly soluble Nb(V) solid phases, expectedly in the form of ternary solid phases containing Ca.

The results of the quantitative chemical analysis of Nb solid phases dissolved in $\text{HNO}_3 + \text{HF}$ confirm that all solid phases contain Ca and Nb, whilst disregarding any significant contribution of Na. XRD pattern collected for the sample equilibrated in YCWCa is exemplarily displayed in Fig. 6, which shows a good agreement with the patterns reported for the cubic pyrochlore $\text{Ca}_2\text{Nb}_2\text{O}_7(\text{cr})$.

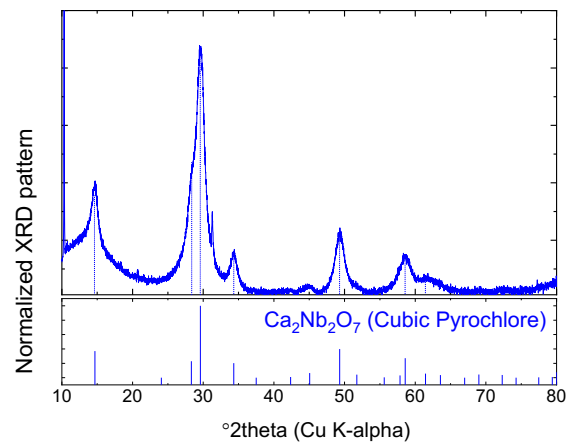


Fig. 6: XRD pattern of Nb(V) solid phase equilibrated in YCWCa ($\text{pH} 13.5$, $[\text{Ca}] = 1.4 \cdot 10^{-3}$ M) and reference patterns reported for $\text{Ca}_2\text{Nb}_2\text{O}_7(\text{cr})$.

These observations confirm the low solubility of Nb(V) in hyperalkaline pH conditions containing Ca, representative of cementitious systems. Quantitative chemical analysis and XRD unequivocally support the key role of Ca in the formation of the solid phases controlling the solubility of Nb(V) under the investigated boundary conditions. These results provide also upper Nb concentration limits to be considered in the study of sorption processes controlling the retention of niobium in cement systems.

Be(II) solubility, hydrolysis and carbonate complexation in dilute to concentrated saline systems

Beryllium is a chemotoxic element used in nuclear reactors as reflector or moderator due to its low thermal neutron absorption cross section and its specific chemical / structural properties. Therefore, it is expected in specific waste forms to be disposed of in repositories for radioactive waste. The amphoteric behavior of Be(II) involving the formation of anionic hydrolysis species ($\text{Be}(\text{OH})_3^-$ and $\text{Be}(\text{OH})_4^{2-}$) in alkaline conditions was only investigated in a few experimental studies but it is widely accepted in the literature [15-16].

The formation of strong complexes of Be(II) with carbonate is also expected, although so far most of the available studies investigating this system have focused on acidic to weakly alkaline pH conditions [17–18].

This study investigates the solubility of Be(II) under alkaline to hyperalkaline pH conditions in the absence and presence of carbonate. The main objectives are the development of comprehensive thermodynamic and activity models for the system $\text{Be}^{2+}\text{--Na}^+\text{--K}^+\text{--Ca}^{2+}\text{--H}^+\text{--Cl}^-\text{--OH}^-\text{--H}_2\text{O(l)}$, and the assessment of the impact of carbonate on the solubility in alkaline systems representative of cementitious systems.

Sample preparation and handling were performed in Ar-gloveboxes at $T = (22 \pm 2)^\circ\text{C}$. Solubility experiments were conducted with $\text{Be(OH)}_2(\text{s})$ obtained by precipitating a $\approx 0.35\text{ M}$ BeSO_4 stock solution at $\text{pH} \approx 10.5$. Solubility samples were prepared by contacting 0.5–5 mg of solid phase (per sample) with the following systems: (i) 0.1–5.0 M NaCl--NaOH ($5 \leq \text{pH}_m \leq 14.5$); (ii) 0.1–4.0 M KCl--KOH ($9 \leq \text{pH}_m \leq 14.3$); (iii) 0.05–3.5 M CaCl_2 ($9 \leq \text{pH}_m \leq 12$); (iv) 0.01–4.0 M NaOH ; (v). 0.01–4.0 M KOH . Two series of solubility experiments were prepared in the presence of carbonate: (i) in 0.5 M NaCl solutions at $9 \leq \text{pH}_m \leq 13$ with $C_{\text{tot}} = [\text{HCO}_3^-] + [\text{CO}_3^{2-}] = 0.01$ and 0.1 M, and (ii) in 5.0 M NaCl solutions at $9 \leq \text{pH}_m \leq 13$ with $C_{\text{tot}} = 0.1$ and 0.4 M. Total concentrations of Be(II) in the aqueous phase were quantified by ICP–MS after ultra-filtration with 10 kD ($\sim 2\text{--}3\text{ nm}$) filters. Solid phases in selected solubility experiments were characterized by XRD, SEM–EDX and quantitative chemical analysis, whereas ^9Be NMR was used for the characterization of the speciation of beryllium in the aqueous phase.

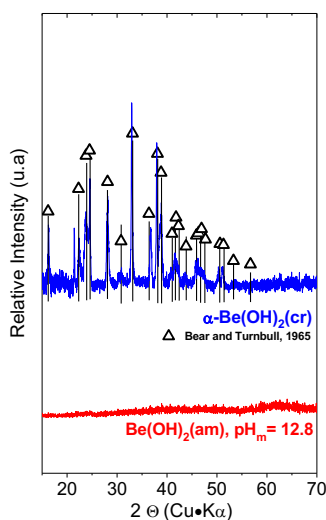


Fig. 7: XRD patterns of the $\text{Be(OH)}_2(\text{s})$ solid phase synthesized in this work after 14 (red) and 600 days (blue) of equilibration time. Reference patterns shown by triangle data points correspond to $\alpha\text{-Be(OH)}_2(\text{cr})$ as reported in Bear and Turnbull, 1965 [19].

Fig. 7 shows the diffractograms of the $\text{Be(OH)}_2(\text{s})$ solid phase after 14 (red) and 600 (blue) days of equilibration time. The freshly precipitated solid shows an amorphous character, whereas the patterns of the aged

phase are in excellent agreement with reference data for $\alpha\text{-Be(OH)}_2(\text{cr})$. This observation reflects the transformation of the amorphous material into a crystalline phase, following the well-known Ostwald ripening process.

Fig. 8 shows selected Be(II) solubility data in 0.5 M NaCl (a, absence and presence of carbonate), 3.5 M CaCl_2 (b, absence of carbonate). Solubility data in NaCl systems and absence of carbonate confirm the amphoteric behaviour of Be(II) with a solubility minimum at $\text{pH}_m \approx 9.5$, regardless of the ionic strength. Slope analysis of the solubility data under alkaline to hyperalkaline conditions in combination with ^9Be NMR support the predominance of the monomeric hydrolysis species $\text{Be(OH)}_2(\text{aq})$, Be(OH)_3^- and Be(OH)_4^{2-} above $\text{pH}_m \approx 8$. A relatively weak impact of carbonate in the solubility is observed in alkaline conditions with C_{tot} up to 0.1 M (Fig. 8a), thus highlighting that carbonate cannot outcompete hydrolysis within the boundary conditions expected in cementitious systems.

The solubility of Be(II) in dilute, alkaline CaCl_2 solutions is very similar to analogous experiments in dilute, alkaline NaCl and KCl solutions (data not shown). However, in concentrated CaCl_2 solutions, Be(II) solubility is significantly enhanced above $\text{pH}_m \approx 9$ with a slope ($\log [\text{Be(II)}]$ vs. pH_m) of $\approx +2$ (Fig. 8b). These observations point towards an earlier stabilization of the moiety Be(OH)_4^{2-} , most likely due to the strong interaction with Ca^{2+} .

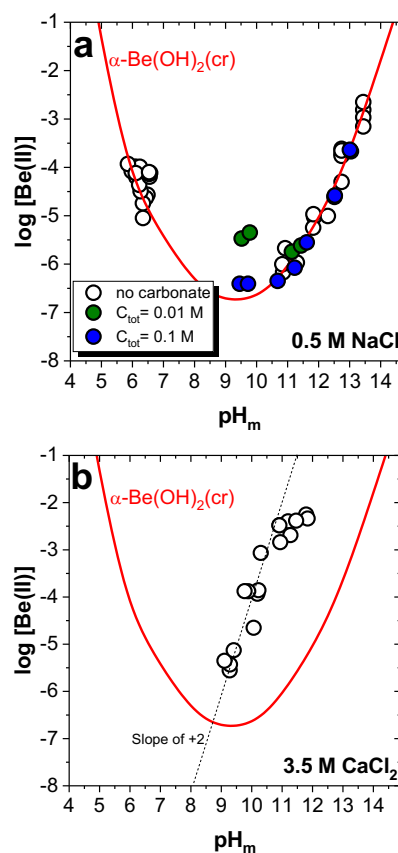


Fig. 8: Solubility $\alpha\text{-Be(OH)}_2(\text{cr})$ in (a) 0.5 M NaCl solutions in the absence and presence of carbonate (b) 3.5 M CaCl_2 solutions. Solubility curve (red line) calculated for $I = 0.5\text{ M}$ NaCl using thermodynamic data based upon thermodynamic and activity models derived in this work.

The extensive solubility dataset collected within this study allows the development of complete chemical, thermodynamic and activity (SIT) models for the system $\text{Be}^{2+}\text{-Na}^+\text{-K}^+\text{-H}^+\text{-Cl}^-\text{-OH}^-\text{-H}_2\text{O(l)}$ [20-21]. These models can be implemented in thermodynamic databases and used in geochemical calculations of relevance in the context of nuclear waste disposal.

References

- [1] Neck, V., et al., *Radiochim. Acta*, 56, 25-30, (1992).
- [2] Petrov, V. G., et al., *Radiochim. Acta*, 105, 1-20, (2017).
- [3] Fellhauer, D., et al., *Radiochim. Acta*, 104, 355-379, (2016).
- [4] Fellhauer, D., et al., *Book of abstracts, ABC Salt Workshop Ruidoso*, (2016).
- [5] Almond, P. M., et al., *Chem. mater.*, 19, 280-285, (2007).
- [6] Gaona, X., et al., *Journal of Contaminant Hydrology*, 102, 217-227, (2008).
- [7] Mazzi U., et al., *Technetium in Medicine. In Technetium-99m Pharmaceuticals*, Springer: Berlin, Heidelberg, (2007).
- [8] Mendez-Rojas, M. A., et al., *J. Coord. Chem.*, 59, 1-63, (2006).
- [9] Yalcintas, E., et al., *Dalton. Trans.*, 45, 8916-8936, (2016).
- [10] Duckworth, S., PhD thesis, KIT (2021)
- [11] Dardenne et al., *Inorg. Chem.*, 60, 16, 12285-12298, (2021).
- [12] Peiffert, C., et al., *J. Solution Chem.*, 39, 197-218, (2010)
- [13] Talerico, C., et al., *Mat. Res. Soc. Symp. Proc.*, 824, 443-448, (2004).
- [14] Cachoir, C. et al., *IW.W&D.0099*, 1-8, (2006).
- [15] Gilbert, R. A., Garrett, A. B., *J. Am. Chem. Soc.*, 78, 5501-5505 (1956).
- [16] Green, R.W., Alexander, P.W., *Aust. J. Chem.*, 18, 651 (1965).
- [17] Bruno, J. et al., *J. Chem. Soc. Dalton Trans.*, 2439-2444 (1987).
- [18] Bruno, J. et al., *J. Chem. Soc. Dalton Trans.*, 2445-2449 (1987).
- [19] Bear, I. J., Turnbull, A.G., *J. Phys. Chem.*, 69, 2828-2833 (1965).
- [20] Cevirim-Papaioannou, N. et al., *Applied Geochemistry*, 117, 104601 (2020).
- [21] Grambow, B. et al., *Applied Geochemistry*, 112, 104480, (2020).

4.2 Sorption on mineral surfaces

M. Altmaier, I. Androniuk, N. Cevirim-Papaioannou, X. Gaona, T. Gil-Diaz, F. Heberling, J. Lützenkirchen, M. Marchetti, N. Ait Mouheb, A. Skerencak-Frech, A. Tasi, A. Thumm

In co-operation with:

J. Bruno^a, E. Colàs^a, S. Gaboreau^b, M. Haisf, S. Han^c, D. Jara-Heredia^e, K. Källström^d, J. Linké, H.-M. Ludwig^g, T. Schäfer^e, T. Sowoidnich^g, W. Um^c

^a Amphos²¹ Consulting S.L., Passeig Garcia i Faria, 49-51, 1-1a, 08019 Barcelona, Spain; ^b BRGM Bureau de Recherches Géologiques et Minières, Orleans, France, ^c Division of Advanced Nuclear Engineering (DANE), Pohang University of Science and Technology (POSTECH), Pohang, Gyeongbuk, South Korea, ^d Svensk Kärnbränslehantering AB, Avd. Låg-och medelaktivt Avfall, Evenemangsgatan 13 Box 3091, 169 03 Solna, Sweden, ^e Friedrich-Schiller-Universität Jena, Institute of Geosciences, Burgweg 11, 07749 Jena, Germany, ^f Leibniz University Hannover, Institute for Building Materials Science, Appelstraße 9a, 30167 Hannover, Germany, ^g Bauhaus University Weimar, Coudraystrasse 11, 99423 Weimar, Germany

Introduction

The interaction mechanisms with mineral surfaces are key processes for the retention of radionuclides within the Safety Case of a nuclear waste repository. For their thorough quantification and implementation in safety performance calculations, a detailed mechanistic understanding of these processes is essential. This requires an in-depth knowledge of the mineral-water interfaces, and a reliable thermodynamic description of the sorption reactions.

The sorption of radionuclides on different relevant solid phases needs to be studied under systematic variation of experimental conditions, i.e., radionuclide concentration, pH values, composition and concentration of the electrolyte solution, and presence of other radionuclides and/or complexing aqueous ligands, which may both be able to compete/interfere during sorption onto the surface.

Besides classic batch and solubility studies, a variety of modern spectroscopic speciation techniques with a high analytical sensitivity are applied to study the sorption processes on a molecular level. In combination with a subsequent description by thermodynamic surface complexation models and molecular dynamic simulations, comprehensive information on the retention processes is determined, which is of high importance for the Safety Case.

In the present bi-annual report, various aspects of the interaction of different compounds with mineral surfaces are considered.

- A new code for sorption and speciation calculations (SINFONIA) was developed.
- The sorption of different elements (Cs, Be, Eu, Pu) on different mineral phases (halite, bentonite, cement and CSH phases) was studied.
- Special focus was put on the impact of competing organic ligands (oxalate, EDTA, isosaccharinate) and dilute to high ionic strength conditions of NaCl and CaCl₂.

Development of a new code for sorption and speciation simulations in narrow pores (open access SINFONIA)

Detailed knowledge on aquatic chemistry and mineral-solution interaction is necessary to understand and better predict radionuclide transport through and fate in narrow pore systems in the containment providing rock zone of high-level waste (HLW) repositories. Surface speciation and electrostatic effects of single mineral surfaces can be accounted for via Surface Complexation Models (SCMs) [1], whereas overlapping of electric double layers (EDL) at interacting surfaces are most efficiently accounted for by calculating the electric field inside the pore space via Charge Regulation (CR) [2]. This model concept implies that surface speciation, interfacial charges and potentials are adjusted in accordance with the distance between the surfaces based on generally valid intrinsic equilibrium constants and mean-field type Poisson-Boltzmann (PB) theory, which considers ions as point charges and water as a continuous dielectric medium. Currently, commercial (geo-)chemical speciation codes (e.g., PHREEQC, ECOSAT, FITEQL, Visual MINTEQ) do not include surface interactions through CR, and other codes that do, are not publicly available.

KIT-INE developed the speciation code SINFONIA (Speciation and INter-particle FORces for Nanoscale InterActions) [3] that enables CR type simulations and extends SCMs to a four-layer model (FLM) involving interactions of both, equal or unequal surfaces, with a numerical solution for the PB equation for arbitrary electrolytes. As part of the results, the simulations provide the speciation of the involved mineral surfaces and their changes as a function of separation distance as well as the corresponding osmotic pressure build-up between surfaces and the resulting electrostatic interaction forces. The code provides a self-consistent coupling between surface chemistry and mechanical properties (MC), and thus provides a major tool lacking in many reactive transport models. Examples of the code are available in GitHub (<https://github.com/T-G-D>) and collaborations with Helmholtz Centre for Environmental Research - UFZ (Leipzig) are in progress to couple SINFONIA to OpenGeoSys (i.e., an open ac-

cess reactive transport model, not considering yet electrostatic interactions nor mechanical properties in narrow pores).

One of the ubiquitous radioisotopes in HLW repositories is ^{79}Se ($t_{1/2} = 3.27 \cdot 10^5$ y), expected to be potentially released on the very long-term from both matrix and instant release fractions towards the overburden, contributing to the estimated total cumulative radioactive dose [4].

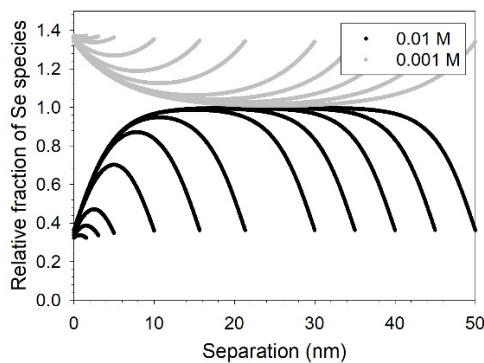


Fig. 1: Profiles of relative fractions of total aqueous Se in interstitial pore water compared to bulk solution between goethite surfaces at different separation distances for pH 9 and two ionic strengths (NaCl).

Calculations using SINFONIA to simulate adsorption from a $2.5 \cdot 10^{-4}$ M Se solute onto goethite at pH 9 (i.e., close to the isoelectric point), based on thermodynamic constants described in [5], show that a change in the ionic strength of the narrow pore solution from 0.01 M to 0.001 M will shift the transport pore regime from anion exclusion (fraction < 1) to enhanced anion migration (fraction > 1, Fig. 1). The strongest effects occur in the smallest pores (e.g., < 20 nm) where the mid-plane composition is modified by the overlapping EDL.

At a given separation, e.g., 3 nm, the presence or absence of adsorbed Se species onto goethite (Fig. 2) influences the osmotic pressure developed between the surfaces, showing characteristic behaviours for each pH along the ionic strength gradient.

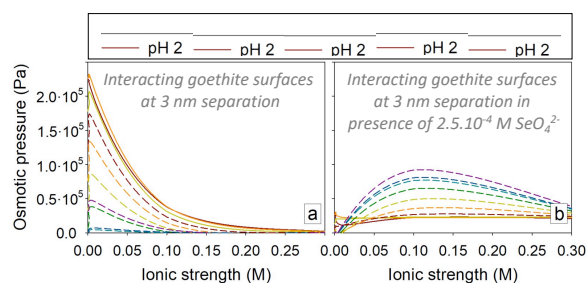


Fig. 2: Examples of variations in the osmotic pressure developed between equal goethite surfaces for a wide pH range at different ionic strengths in NaCl (a) without and (b) in presence of selenium.

These examples imply that changes in the ionic strength of a porous media occurring over time due to

mineral precipitation or input/mixing with renewed solution (e.g., glacial melt water) could entail enormous shifts in the transport regime of the geological system. In turn, a change in the osmotic pressure in a nanopore (e.g., due to sediment compaction/decompression, fractures, or anthropogenic remobilization) may affect surface and solution chemistry, which will eventually also impact the inherent transport of ions through the pore space. This variability in the system should be assessed and accounted for in dual/multi-porosity transport models, undoubtedly improving current predictions on the radionuclide release from geological repositories.

Sorption of $^{137}\text{Cs(I)}$ in Halite

Studies concerning the retention mechanisms of radionuclides on salt rocks are scanty [6], notwithstanding the fact that bedded salt deposits are considered as possible host formation for waste disposal [7-8]. Generally, salt rocks show a low sorption capacity for many radionuclides, although some nuclides (e.g., Am, Eu) should display stronger sorption [6]. Nevertheless, a low sorption capacity can also lead to a significant retention of poorly soluble radionuclides over long time-scales, which are characteristic for a deep geological repository. In addition to the nature of the radionuclide, the retention capacity of natural salt rocks might be strongly increased by the co-presence of different mineral phases and impurities.

This work aims at studying the sorption kinetics of $^{137}\text{Cs(I)}$ on halite by considering three successive experiments designed to observe the influence of increasing impurities content on the retention capacity:

- Sorption of $^{137}\text{Cs(I)}$ on ultrapure NaCl_s in saturated NaCl solution
- Sorption of $^{137}\text{Cs(I)}$ on ultrapure NaCl_s , added with 1 wt % of impurities (e.g., CaSO_4) in saturated NaCl solution
- Sorption of $^{137}\text{Cs(I)}$ on three natural salt rocks (see Fig. 3), collected from the Heilbronn salt mine in Germany

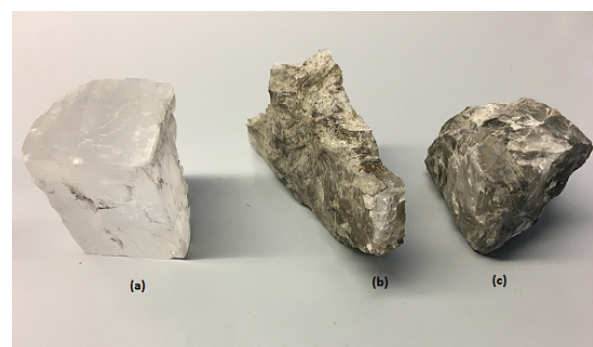


Fig. 3: Halite samples collected from the Heilbronn salt mine in Germany. (a) Halite with low impurities content (mainly Al, K, Ca and Zn) (b) Halite with moderate amount of impurities consisting mainly of quartz, muscovite and chamosite phases (c) Halite with a high amount of impurities consisting mainly of quartz, dolomite, chamosite and biotite phases.

The impurities content and the additional phases of the three salt rocks acquired from the Heilbronn salt mine

were analyzed by means of Inductively Coupled Plasma Mass Spectrometry (ICP-MS) and X-ray diffraction (XRD) analysis. The X-ray diffractogram was acquired with a Bruker D8 (Cu $K\alpha$ radiation, 40 mV/40 mA) from 0° to 70° with step width of 0.02 and 0.05 s/step.

The diffractogram in Fig. 4, corresponding to the sample in Fig. 3(c), was obtained after washing a powdered sub-sample and centrifuging at 6000 rpm for 10 min. The rock in Fig. 3(a) contains low amount of impurities consisting mainly of Al, K, Ca and Zn, while the rocks in Fig. 3(b) and (c) highlight the coexistence of quartz, muscovite and chamosite phases (rock in Fig. 3(b)), or quartz, dolomite, chamosite and biotite for the rock in Fig. 3(c).

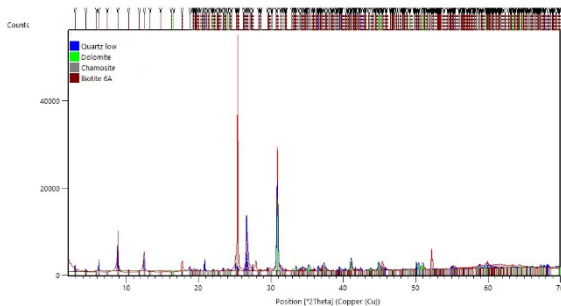


Fig. 4: X-ray diffractogram of the salt rock depicted in figure 1(c). The analysis was performed by using HighScore Plus (PANalytical) 3.0 d.

Herein, the result of the sorption of Cs(I) on pure NaCl_s are presented. The experiments were performed by means of batch experiments, performed under argon atmosphere: 3.33 ± 0.16 kBq of $^{137}\text{Cs(I)}$ were added to 20 mL of a NaCl saturated solution (6.16 M) containing 20 mg or 200 mg or 2 g of NaCl (99.99 % purity), resulting in solid/liquid ratios of 1, 10 and 100 g L⁻¹. A $\text{pH}_m = 6.60$ was measured, correcting for the effect of the high salt concentration on the liquid junction potential of the electrode. Aliquots of the samples solution were taken after 7, 24, and 42 days and centrifuged at 50 000 rpm for 1 h. A defined aliquot of the supernatant was withdrawn and measured via HPGe gamma spectrometry in the same attenuation and geometrical conditions as the calibration solution.

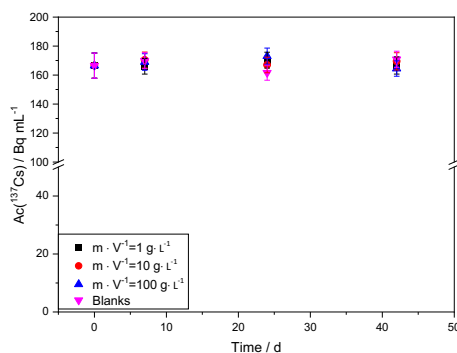


Fig. 5: Sorption kinetics of $^{137}\text{Cs(I)}$ on ultrapure NaCl_s measured $^{137}\text{Cs(I)}$ activity concentration at days 7, 24 and 42 for blanks and three different solid-to-liquid ratios, namely 1, 10 and 100 g L⁻¹.

Fig. 5 shows the $^{137}\text{Cs(I)}$ activity concentration [9] at the studied time-steps: for all samples and blanks no significant change of the concentration of $^{137}\text{Cs(I)}$ is observed, with the small variation being well within the error range of the data. Hence, $^{137}\text{Cs(I)}$ does neither sorb to ultrapure NaCl_s nor to the container walls over the studied time period. These results are in very good agreement with the results obtained by Carlsen and Platz in [6].

In future work, the effect of the impurities and different coexisting phases (e.g. quartz, dolomite) of natural salt rock on the sorption of $^{137}\text{Cs(I)}$ and further radionuclides (e.g. Pu, Am, Cl, I, etc.) will be investigated. On the one hand, the impact of the impurities on the sorption capacity of the natural salt rock will be quantified. On the other hand, the retention mechanism of the radionuclides in a system that is more representative of reality will be studied.

Sorption of Oxalate and EDTA onto Bentonite and CSH-Phases

Cement and bentonite are considered as potential geotechnical barriers in certain nuclear waste repository concepts.[10,11] Both materials are able to adsorb certain radionuclides (e.g. actinides, lanthanides) For cement, the sorption properties are primarily governed by CSH phases, which are the main components of cement. The high sorption capacity of bentonite is mainly due to its high content of montmorillonite (80 - 84).[12] Organic ligands are present in a nuclear waste repository either directly as part of the waste (e.g. decontamination agents) or as additives in commercial cement mixtures (e.g. superplasticizers and their degradation products). Information on the impact of these organic compounds on the sorption behavior of radionuclides are scarce, in particular at increased ionic strengths. Hence, the sorption behavior of different radionuclides on CSH phases and bentonite in the presence of organic compounds under varying ionic strength conditions must be studied. An in-depth understanding of these systems requires prior investigation of the sorption properties of the organic compounds itself to the aforementioned phases.

In the present work, sorption of EDTA and oxalate on CSH phases and bentonite was studied at different concentrations of NaCl and CaCl₂. The CSH phases were prepared at different C/S-ratios according to L'Hopital *et al.* [13] The used MX80 bentonite was purchased from Süd Chemie AG Werk Duisburg. It originates from Wyoming (USA), reflecting a naturally occurring Na-bentonite. It was crushed and sieved to a particle size of < 1 mm.[14]

The investigations were performed using batch sorption experiments. The organic ligands were added as Na₂-EDTA and Na₂-Oxalate, respectively. For both solid phases, a fixed solid to liquid ratio of 1 g/L was used. The ionic strength for the NaCl system was set to 1 m and for CaCl₂ to 0.1 m. The ligand concentrations were fixed to 0.001 M for both organic ligands. The pH-value was varied in the range of 3 to 12 in case of the bentonite-system For the CSH phases, different C/S

ratios of 0.6, 0.83, 1.0, 1.1, 1.2, and 1.3 were investigated. The pH varied between 9 and 12, depending on the C/S-ratio. All the experiments were performed under argon atmosphere with an equilibration time of five days after addition of the organic compounds. The concentration of the organic ligands in the aqueous phase was determined with NPOC. A speciation analysis was performed with the geochemical modelling software PHREEQC, using the SIT-database for ionic strength corrections.

The determined NPOC concentration for the oxalate-bentonite system are given in Fig. 6 as function of the pH_m in NaCl and CaCl₂ electrolyte solutions. In 1.0 m NaCl (blue), the NPOC concentration increases from acidic to almost neutral pH (pH_m 3 – 6). In the neutral to alkaline region, a constant NPOC of about $5 \cdot 10^{-4}$ mol/L is observed, corresponding to the total oxalate concentration. This effect is explained as follows: the surface of the bentonite is positively charged for $pH_m < 4.1$ and negatively charged for $pH_m > 4.1$. In the acidic region the aqueous speciation is dominated by the negatively charged species $H(Ox)^-$, which is able to sorb to the positive surface via ion exchange. In the slightly acidic to alkaline region, the deprotonated oxalate species are repelled from the negatively charged surface, leading to a strong decrease in their adsorption.

Fig. 6 also shows the analogous results in a 0.1 m CaCl₂ solution (green). In comparison with the respective NaCl-system, the NPOC concentrations are much lower. Also, no clear pH-dependence is visible. This may be explained by general precipitation of a Ca(Ox)_s solid phase over the entire pH range.

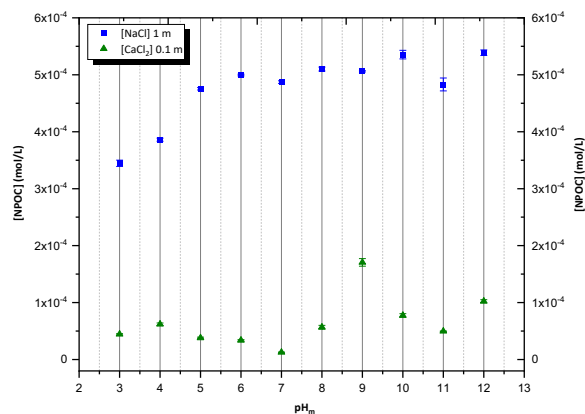


Fig. 6: Oxalate sorption onto bentonite MX80 in NaCl (1 m, blue) and CaCl₂ (0.1 m, green) electrolyte solutions as function of the pH_m . The NPOC concentrations are shown as carbon concentration (mol/L). $[NPOC]_{total} = 5 \cdot 10^{-4}$ mol/L.

For the EDTA-bentonite system the NPOC concentration are shown in Fig. 7. For both electrolytes, no clear pH-dependence is observable and the NPOC concentrations remain close to the total amount of EDTA. The slightly lower NPOC concentrations at pH_m 3 to 5 in NaCl solution, should not be over-interpreted as this effect is within the scattering range of the data. These points towards a high stability of the Na/Ca-EDTA species in the aqueous phase and a negligibly adsorption.

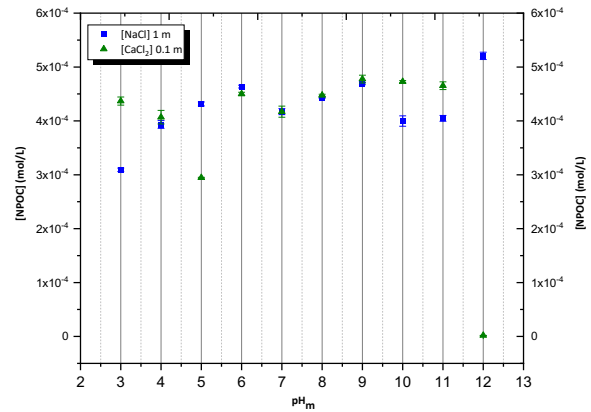


Fig. 7: EDTA sorption onto bentonite MX80 in NaCl (1 m, blue) and CaCl₂ (0.1 m, green) electrolyte solutions as function of the pH_m . The NPOC concentration is shown as carbon concentration (mol/L). $[NPOC]_{total} = 5 \cdot 10^{-4}$ mol/L.

The NPOC results for the binary CSH-oxalate system are given in Fig. 8 as function of the C/S ratios in NaCl and CaCl₂ solutions. The NPOC concentrations for the different C/S-ratios do not differ significantly for a defined background electrolyte. However, for CaCl₂ slightly lower NPOC concentrations were determined, compared to the NaCl solution. Also, all NPOC concentrations are lower, compared to the bentonite system. These findings may be explained by a general precipitation of a solid Ca(Ox)_s phase, due to the omnipresence of Ca²⁺ ions in the presence of CSH phases.

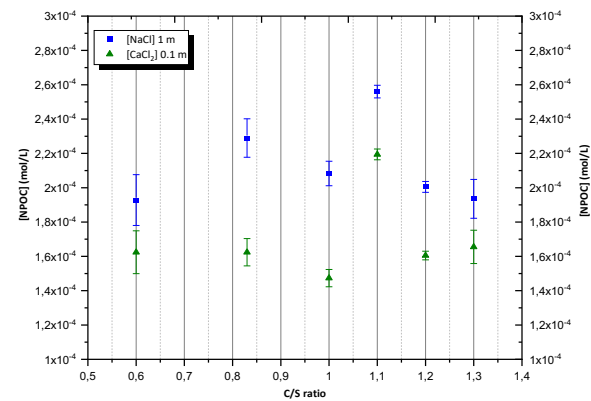


Fig. 8: Oxalate sorption onto CSH-Phases in NaCl (1 m, blue) and CaCl₂ (0.1 m, green) electrolyte solutions as function of the C/S ratio. The NPOC concentration is shown as carbon concentration (mol/L) at the C/S ratios of 0.6, 0.83, 1.0, 1.1, 1.2, and 1.3. $[NPOC]_{total} = 5 \cdot 10^{-4}$ mol/L

The analogous results for the EDTA-CSH system are given in Fig. 9.

In NaCl, the NPOC concentration is rather constant around $[NPCO]_{total} = 5 \cdot 10^{-4}$ mol/L over the entire studied range of C/S ratios. For CaCl₂ solution some variation are observable at low C/S ratios (0.6 to 0.83). However, for C/S ratios above 1.1 the NPOC concentrations are again constant around $5 \cdot 10^{-4}$ mol/L. These results indicate that EDTA is not adsorbed by the CSH phases under the studied conditions. This is explained as follows: The surface of CSH phases is negatively charged for $C/S < 1.3$ and positively for $C/S > 1.3$. [15]

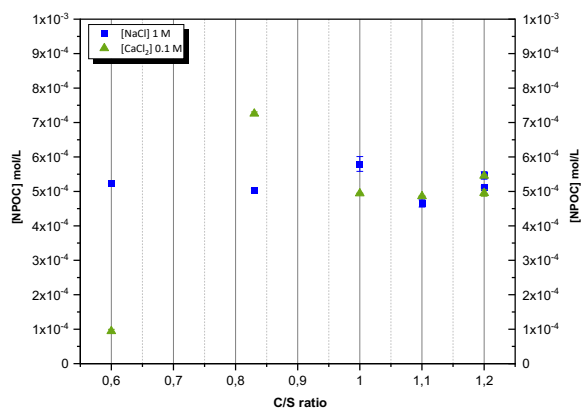


Fig. 9: EDTA sorption onto CSH-Phases in NaCl (1 m, blue) and CaCl₂ (0.1 m, green) electrolyte solutions. The NPOC concentration is shown as carbon concentration (mol/L) with the C/S ratios of 0.6, 0.83, 1.0, 1.1, 1.2, and 1.3. $[NPOC]_{total} = 5 \cdot 10^{-4}$ mol/L.

Under the alkaline pH_m of the samples, EDTA is present either as deprotonated species or as a Ca(II) complex, which both are negatively charged. Hence, EDTA is repelled from the surface and the adsorption is minimized.

Based on these data, future studies will focus on the the sorption of trivalent actinides and lanthanides on MX80 bentonite and CSH phases in the presence if oxalate and EDTA diluted to concentrated NaCl and CaCl₂ solutions.

Retention of Plutonium by cement in the presence of alpha-isosaccharinic acid

Cementitious materials are of high importance in the context of final disposal of low- and intermediate-level radioactive waste (L-/ILW) in deep geological formations. Hydrated cementitious phases represent a main sink for radionuclides and small organic molecules often determining the mobility of hazardous metal ions in the near-field of a repository. Although plutonium is not highly abundant in L-/ILW, it may also contribute to the long-term risk of repositories for such wastes due the long half-life of ²³⁹Pu [16]. Cellulose-based materials are present in large quantities within L-/ILW, which, under the developing alkaline, reducing conditions, will degrade into isosaccharinic acids [17]. The α -D-isosaccharinate (ISA) is identified to be the most relevant hydrolytic degradation product capable of simulating the complexation effect of cellulose leachates imposed on trivalent and tetravalent actinides and lanthanides [18].

Uptake of plutonium by Portland cement in degradation stage II ($[Ca(II)]_{tot} \sim 0.02$ M, $pH \sim 12.5$) was investigated in the absence and presence of ISA under reducing conditions set by hydroquinone (HQ), Sn(II) or Na₂S₂O₄ ($0 \leq (pe + pH_c) \leq 9$). Sorption experiments were performed at initial concentrations of plutonium: $\log [Pu]_{in} = -6$ to -9 , $\log [ISA]_{tot} = -6$ to -2 and with solid to liquid ratios (S:L) of 0.1 to 50 g·dm⁻³. Special focus was dedicated to assess the reversibility and the kinetic effects related to the order of addition of the individual components within the ternary Pu-ISA-cement system.

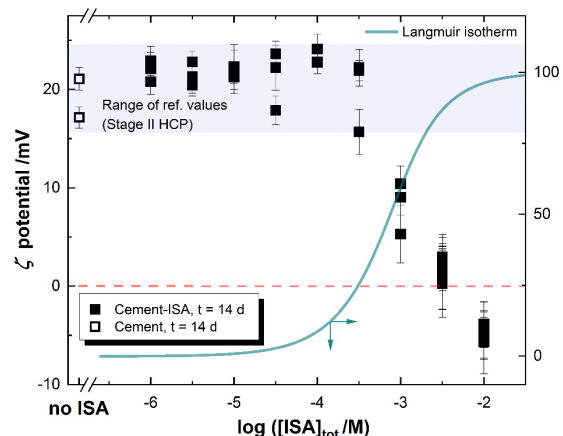


Fig. 10: Zeta-potentials (ζ) measured on suspended colloidal cement particles (at $pH_c = 12.50 - 12.63$) in the absence (opened symbols) and in the presence of ISA (filled symbols) with $-6 \leq \log ([ISA]_{tot} /M) \leq -2$ in equilibrium with HCP at $S:L = 4$ g·dm⁻³ after a contact time of $t = 14$ d. Solid cyan line represents the surface coverage percentage of the cement solid phase by ISA as calculated from the two-site Langmuir isotherm established in the present work.

In the absence of ISA, uptake of Pu by cement in degradation stage II is substantial under reducing conditions. Determined distribution ratios are in line with data available in the literature for tetravalent actinides.

ISA has high affinity towards cement and the likely surface-mediated process can be empirically described by a two-site Langmuir isotherm. Approaching the saturation of sorption sites, above ~ 25 % of ISA-coverage i.e. $\log ([ISA]_{tot} /M) \geq -3.5$ at $S:L = 4$ g·dm⁻³, the process imposes a charge inversion in the zeta potential values of suspended cement particles (see Fig. 10).

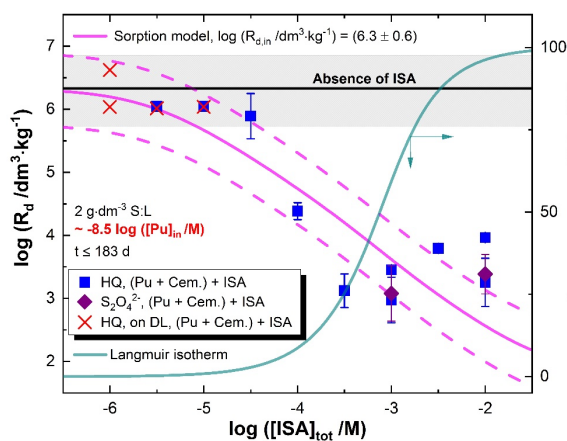


Fig. 11: Distribution ratios (R_d , dm³ kg⁻¹) of Pu in HQ- (blue) and dithionate-buffered (purple symbols) HCP – pore water systems with $\log ([Pu]_{in} /M) \approx -8.5$, and $-6 \leq \log ([ISA]_{tot} /M) \leq -2$ at $S:L = 2$ g·dm⁻³ for the order of addition of individual components: “(Pu + Cement) + ISA”. Solid black line and gray shaded area indicate the expected R_d values (and uncertainty) in the absence of ISA. Violet solid (and dashed) line shows the calculations of the simplified sorption model for the conditions of this experiment (and associated uncertainties). Solid cyan line represents the surface coverage percentage of the cement solid phase by ISA.

The adsorption of Pu onto the hydrated cement is significantly impacted by ISA above $\log ([ISA]_{\text{tot}} / M) \approx -4.5$ regardless of the reducing agent underlining the expected stabilization of the +4-oxidation state by the ligand (Fig. 11). The uptake of Pu slowly increases above $\log ([ISA]_{\text{tot}} / M) \approx -3.5$ owing to the surface complexation of Pu(IV) with ISA correlating with the evolution of zeta-potential values in the system.

Remarkable differences are found between the order of addition sequences “(Pu + Cement) + ISA” and “(Pu + ISA) + Cement”. Long-term sorption experiments ($t \leq 490$ days) and desorption experiments confirm the significantly longer contact time required for the sequence (Pu + ISA) + Cement to attain equilibrium.

A simplified sorption model was derived on the basis that the decrease in the uptake of Pu by cement is only caused by the formation of Ca(II)–Pu(IV)–OH–ISA aqueous complexes. Model predictions qualitatively agree well with the trend in experimental data over a wide parameter-range, whilst overestimating the effect of ISA at high surface coverage. This study provides a significantly improved understanding on interactions driving sorption processes of actinides on hydrated cement phases in the presence of organic ligands [19].

Sorption of beryllium in cementitious systems relevant for nuclear waste disposal

Beryllium has applications in fission and fusion reactors, and it is present in specific streams of radioactive waste. Accordingly, the environmental mobility of beryllium needs to be assessed in the context of repositories for nuclear waste. Although cement is widely used in these facilities, the uptake of Be(II) by cementitious materials was not previously investigated and was hence assumed negligible [20]. In the context of studies performed within the EC funded collaborative project “Cement-based materials, properties, evolution, barrier functions” (CEBAMA), this study aimed at a comprehensive investigation of beryllium uptake by cementitious systems. Beyond the quantitative experimental investigation of the uptake on the basis of sorption kinetics, sorption isotherms and distribution ratios, the use of molecular dynamics provides a very accurate description of the surface processes driving the uptake of beryllium at molecular scale. This work complements and further extends the study on the solubility, hydrolysis and thermodynamics of Be(II) in alkaline to hyperalkaline conditions relevant for cementitious systems (see Chapter 4.1 and reference [21]).

Sample preparation and handling were conducted in Ar-glove boxes at $t = (22 \pm 2)^\circ\text{C}$. Sorption experiments were performed with ordinary Portland cement in the degradation stage I and II, low pH cement and C-S-H phases with Ca:Si ratio 0.6, 1.0 and 1.6, as well as with TiO₂. Pore water solutions were characterized by $10 \leq \text{pH}_m \leq 13$, as imposed by the equilibrium with portlandite, C-S-H phases and Na/K hydroxides. Batch sorption samples were prepared with solid-to-liquid ratios of 0.2–50 g/L and $10^{-6} \text{ M} \leq [\text{Be(II)}]_0 \leq 10^{-3} \text{ M}$, considering the solubility limit of $\alpha\text{-Be(OH)}_2(\text{cr})$ at the investigated pH conditions. Total concentration of Be(II) in

the aqueous phase was quantified by ICP–MS after ultrafiltration with 10 kD filters. Solid and aqueous phases in selected samples were characterized by XRD, SEM-EDX and quantitative chemical analysis. Classical molecular dynamics (MD) simulations were conducted to identify typical sorption sites and surface complexes of Be(OH)_3^- and Be(OH)_4^{2-} species on the (001) surface of C-S-H. The ClayFF force field [22] was used with modified parameters for Ca and Be [23]. The simulation model was initially equilibrated for 5 ns in the *NPT* ensemble, then for 5 ns in *NVT* ensemble. The main MD production run was performed for 10 ns (*NVT*) at ambient conditions.

Based on first ever direct experimental evidence, a strong uptake of Be(II) ($5 \leq \log R_d \leq 7$, with R_d in $\text{L}\cdot\text{kg}^{-1}$) is quantified for the investigated cementitious systems (Fig. 12). Sorption isotherms show a linear behavior with slope of $\approx +1$ ($\log [\text{Be(II)}]_{\text{solid}}$ vs. $\log [\text{Be(II)}]_{\text{aq}}$) over four orders of magnitude ($10^{-8} \text{ M} \leq [\text{Be(II)}]_{\text{aq}} \leq 10^{-4} \text{ M}$) (data not shown), which confirm that the uptake is controlled by sorption processes and that solubility phenomena do not play any role within the considered boundary conditions. The analogous behavior observed for cement and C-S-H phases (Fig. 12) support that the latter are the main sink of beryllium in cementitious systems. The two step sorption kinetics is explained by a fast surface complexation process, followed by the slow incorporation of Be(II) in C-S-H. The different behavior observed for the uptake by TiO₂ (Fig. 12) supports the incorporation in C-S-H as main mechanism for Be(II) uptake.

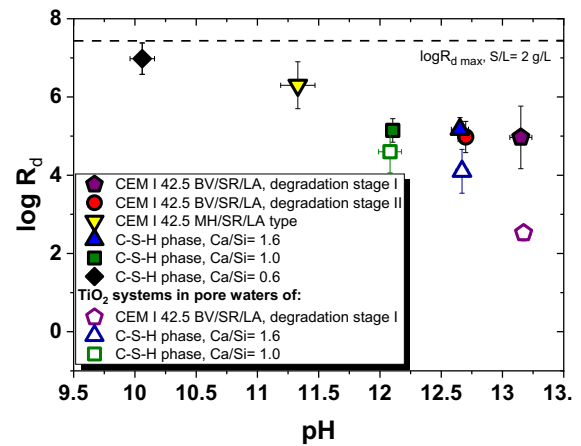


Fig. 12: $\log R_d$ values determined for the uptake of Be(II) by C-S-H (0.6, 1.0 and 1.6), HCP (deg. Stages I and II), “low pH” cement and TiO₂.

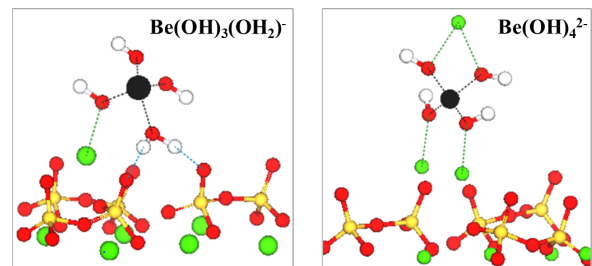


Fig. 13: The simulation snapshots of surface complexes of beryllium on the (001) surface of C-S-H (colour scheme: Si – yellow; Ca – green; O – red; H – white; Be – black).

MD analysis of the time-averaged local structures on the C-S-H/solution interface showed that $\text{Be}(\text{OH})_3^-$ and $\text{Be}(\text{OH})_4^{2-}$ are sorbed to the (001) surface through Ca-bridges (Fig. 13). Also, it was found that the most stable are the surface complexes of beryllium hydroxides that coordinate multiple Ca^{2+} ions.

This work provides a comprehensive quantitative and mechanistic description of the uptake of beryllium by cementitious material which so far was considered negligible in the view of lacking experimental studies. This new information is of high relevance and allows to better quantify the retention of beryllium in the context of the Safety Case for deep underground repositories for nuclear waste. It provides also a thorough scientific basis for the future development of more detailed thermodynamic / geochemical models, e.g. in the form of aqueous-solid solution models [24].

References

- [1] J. Lützenkirchen, *J Colloid Interf Sci*, **217**: 8 (1999)
- [2] B.W. Ninham, V.A. Parsegian, *J Theor Biol*, **31**: 405 (1971)
- [3] T. Gil-Díaz et al. *Adv Colloid Interfac*: 102469 (2021)
- [4] ANDRA, Dossier 2005 Argile (2005)
- [5] Z. Nie et al., *Environ Sci Tech*, **51**: 3751 (2017)
- [6] L. Carlsen, Lars, and D. Platz. , *European Applied Research Reports: Nuclear Science and Technology Section 7.4* , 539-575, (1986).
- [7] G. Bidoglio, and A. De Plano. *Nuclear Technology*, **74(3)**, 307-316, (1986).
- [8] E.A.Voudrias et al. *Chemosphere*, **26(10)**, 1753-1765. (1993)
- [9] J. J. M. De Goeij and M. L. Bonardi, *J. Radioanal. Nucl. Chem.*, **263(1)**, 13-18. (2005).
- [10] V. Häußler, S. Amayri, A. Beck, T. Platte, T. A. Stern, T. Vitova, T. Reich, *Applied Geochemistry* 2018, **98**, 426-434; I. Pointeau, B. Piriou, M. Fedoroff, M.-G. Barthes, N. Marmier, F. Fromage, *Journal of Colloid and Interface Science* 2001, **236**, 252-259.
- [11] N. Guo, J. Yang, R. Zhang, Y. Ye, W. Wu, Z. Guo, *Journal of Radioanalytical and Nuclear Chemistry* 2015, **303**, 2185-2192.
- [12] C. Hurel, N. Marmier, *Journal of radioanalytical and nuclear chemistry* 2010, **284**, 225-230.
- [13] E. L'Hôpital, B. Lothenbach, D. Kulik, K. Scrivener.
- [14] L. Delavernhe, A. Steudel, G. Darbha, T. Schäfer, R. Schuhmann, C. Wöll, H. Geckeis, K. Emmerich, *Colloids and Surfaces A: Physicochemical and Engineering Aspects* 2015, **481**, 591-599.
- [15] T. Iwaida, S. Nagasaki, S. Tanaka, *Radiochimica Acta* 2000, **88**, 483-487.
- [16] Svensk Kärnbränslehantering AB, SKB R-08-130, Stockholm, Sweden (2008).
- [17] Glaus, M.A., Van Loon, L.R., *Environ Sci Technol* **42**, 2906-2911, (2008).
- [18] Van Loon, L.R., Glaus, M.A., PSI Bericht 98-07, Paul Scherrer Institute, Villigen, Switzerland (1998).
- [19] Tasi, A. et al., *Applied Geochemistry*, **126**, 104862, (2021).
- [20] Wieland, E., Nagra Technical Report 14-08, (2014).
- [21] Cevirim-Papaioannou, N. et al., *Applied Geochemistry*, **117**, 104601, (2020).
- [22] Cygan, R.T. et al. *J. Phys. Chem. B* **108**, 1255-1266, (2004)
- [23] Li, P.F. et al., *J. Chem. Theory Comput.* **10(1)**, 289-297, (2014).
- [24] Cevirim-Papaioannou, N. et al., *Chemosphere*, **282**, 131094, (2021).

4.3 Retention of radionuclides by secondary phases formation

M. Alzaydan, N. Finck, N. Gill, F. Heberling, V. Metz, N. Morelovà, T. Platte, R. Polly, D. Schild, F. Steegborn, M. Vogt, L. Zunftmeister, H. Geckeis.

In co-operation with:

S. Mangold,

Institute for Photon Science and Synchrotron Radiation (IPS), Karlsruhe Institute of Technology (KIT), Hermann-von-Helmholtz-Platz 1, 76344 Eggenstein-Leopoldshafen.

Introduction

The final disposal in a deep geological repository (DGR) is a generally accepted strategy for dealing with long-lived high-level radioactive waste (HLW). The design of deep repositories involves the use of several natural and engineered barriers capable to retard and/or to prevent groundwater contact with the waste matrix, subsequent mobilization of radionuclides, and their transport into the biosphere. Potential intrusion of groundwater results in various alteration and corrosion processes, followed by the formation of secondary phases. E.g., metallic corrosion will limit the canister service lifetime, but on the other hand side the neoformation of secondary phases will provide a new chemical barrier able to scavenge radionuclides (RNs), which may be released upon waste matrix alteration.

Various molecular scale processes can result in radionuclide immobilization, ranging from surface adsorption to structural incorporation by formation of a solid solution. Among these mechanisms, incorporation within the bulk structure may occur when RNs are present during growth or recrystallization of secondary phases and may result in very effective retention. In order to be implemented in the Safety Case, kinetic and thermodynamic models of RNs immobilization need to be developed. The development of such models usually relies on the application of complementary advanced microscopic and spectroscopic techniques combined with computational studies. This strategy is applied at KIT-INE to develop models describing the immobilization of key RNs by relevant secondary phases. Examples of ongoing studies performed within national and international projects are present in the following.

Barite transformation to witherite in presence of carbonate and its impact on radium retention

Ra-226 is a critical radionuclide with respect to the long-term safety of various types of radioactive waste repositories. Due to its relatively short half-life ($1.6 \cdot 10^3$ years), Ra-226 will be in secular equilibrium with its parent nuclide U-238. Thus, migration of radium through the repository system will strongly depend on uranium release from the radioactive waste and will last for long time spans. Barium isotopes belong to the most abundant fission products in nuclear reactors and will occur in HLW in concentrations of some grams per kg waste.

As sulfate containing groundwater contacts the waste, barite (BaSO_4) formation is expected. Ra uptake by barite occurs when dissolved Ra reacts with barite, leading to Ra retention in a $(\text{Ba,Ra})\text{SO}_4$ solid-solution [1]. On the other hand, the reaction of barite with aqueous carbonate at elevated pH, as it may originate from alteration of cementitious material inside a waste repository, is expected to lead to the transformation of barite into witherite (BaCO_3) [2]. It is likely that carbonate alters the chemical behavior of barite surfaces, either by mixing at the surface or through formation of a witherite layer at the barite surface through the mechanism of interface-coupled dissolution-precipitation reactions [3]. The long-term goal of the study is to investigate the effect of carbonate on the Ra retention by barite / witherite. Here we present results of experiments on barite transformation into witherite, so far performed in the absence of Ra.

Barite suspensions were contacted with carbonate solutions (1-100 mM, pH 7-11). Barite particles reacted with carbonate and witherite formed as hexagonal rod-like shapes as displayed in Figure 1.

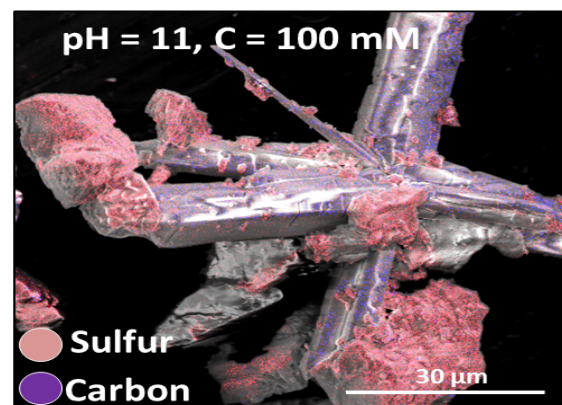


Fig. 1: SEM image showing barite powder (Androvo mine, Bulgaria) reacted with carbonate, evidencing witherite formation.

X-ray diffractograms (XRD) showed shifts of reflection in batches with pH values of 9-11 and carbonate concentrations of 10-100 mM, indicating a potential witherite-barite solid-solution formation on the carbonate rich end of the solid-solution series [3].

Reaction rates depend on the type of barite used. In general, reactions slow down after about 10 days, likely

due to surface passivation through a witherite layer covering barite and preventing further recrystallization [4] as shown in Figures 2 and 3.

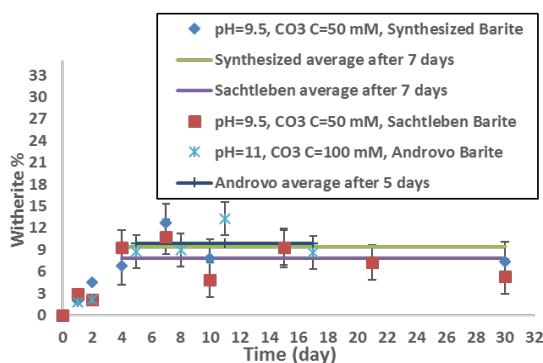


Fig. 2: Kinetic batches for different types of barite where witherite formation is the highest between 7th-10th days, followed by a slowing down of the reactions probably due to surface passivation.

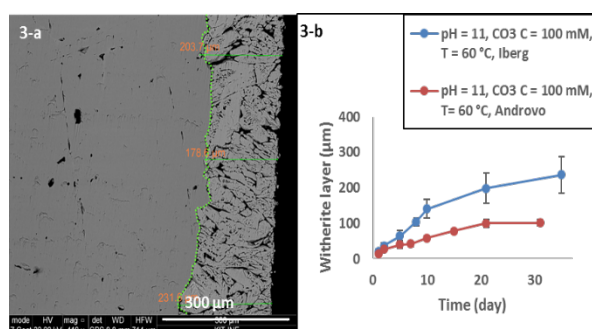


Fig. 3: (a) Porous witherite layer formed around a cube of barite and (b) Witherite layer thickness of Iberg barite (Harz mountains, Germany) and Androvo barite.

To have insight into the progress and mechanism of the recrystallization process, natural barite was cut into cube like shapes (weighing ~ 120 mg) and reacted with 100 mM carbonate solutions at pH 11. As a result, a porous witherite layer of $272 \pm 32 \mu\text{m}$ formed. Witherite layer growth tends to slow down after around 15 days (cf. Figure 3).

The work will be continued, including studies on the interactions with Ra.

Recrystallization kinetics of barite and calcite and the interrelation with ion incorporation

In natural geological systems, mineral phases are often close to the solubility equilibrium. Nonetheless, dynamic dissolution and reprecipitation processes (recrystallization) can be expected in the time periods relevant to nuclear waste disposal. If the solubility equilibria are disturbed in the area of material transitions in the near field of a repository (e.g. in a multi-barrier system of a repository in claystone, the transitions: steel / bentonite, bentonite / cement, cement / clay), the result is increased reactivity and thus increased material turnover related to dissolution and reprecipitation reactions.

The incorporation of radionuclides in mixed crystals (e.g. calcite and barite), which is the focus of the

KRIMI project (KRIMI = Kinetics of recrystallization of mineral phases, relevant for nuclear waste disposal), offers great potential for radionuclide retention. In contrast to sorption reactions, which only take place on mineral surfaces, the entire crystal volume can contribute to the retention of radionuclides through ion incorporation. Understanding the reversibility of the RN incorporation and the associated potential for remobilization are of great importance.

The heterogeneity in the distribution of the incorporated radioisotope depends on the nature of the crystal surface, and the distribution and size of pores. A quantitative description of these dependencies is necessary to characterize the retention potential of the respective crystal phases.

Comparative studies on calcite and barite samples of different origins, as a function of synthesis conditions, or as a function of solution parameters (pH, anion / cation ratio) are ongoing. The aim is to identify parameters that significantly control the recrystallization kinetics. Recrystallization rates are accessed through tracer-uptake (^{133}Ba and ^{45}Ca) in isotope exchange experiments. The so generated experimental data will be complemented by quantum chemical calculations (DFT). The energetic landscape of a surface, where ions (e.g. Ra^{2+} or Ba^{2+}) are attached to different sites present at kinks of the (001) barite surface, will be examined. At this point, these sites have been characterized and an appropriate supercell has been set up.

Reaction products of previous long-term recrystallization experiments, where aragonite recrystallizes to its thermodynamically more stable polymorph calcite in the presence of ^{237}Np and selenite (SeO_3^{2-}) are being characterized.

Several XRD studies were carried out for the solid phase and the proportion of calcite after 2886 days ranged from 1.7% (in NaCl solutions) to 6.3% in KCl solution. Partition coefficients of 2.3 (NaCl) and 3.5 (KCl) for the incorporation of ^{237}Np into calcite were in the range of those reported in the literature [5].

Experiments on the selenite-calcite system were carried out in a similar fashion. Solid/liquid ratio was set to 2 g/L with a total volume of 50 mL. 0.1 M NaCl was added and the selenite concentration varied from 0-100

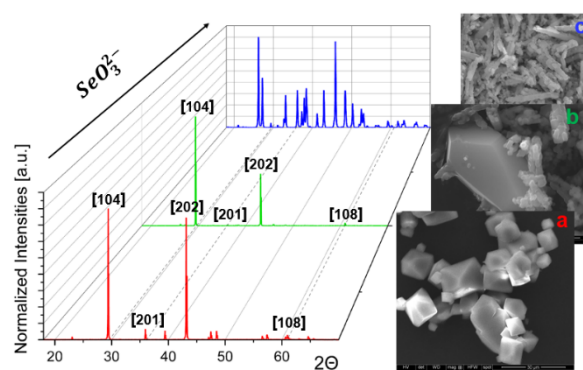


Fig. 4: XRD spectra and SEM images (a: $90 \times 90 \mu\text{m}$; b/c: $15 \times 15 \mu\text{m}$) after recrystallization from aragonite to calcite at different SeO_3^{2-} concentrations (red: 10, green: 40 and blue: $100 \mu\text{M}$)

μM . The presence of selenite inhibited the recrystallization from aragonite to calcite, while at the same time selenite was incorporated into the growing calcite ($D \approx 0.02$). Up to a Se-concentration of $20 \mu\text{M}$, 100% of the aragonite recrystallized into calcite. At higher concentrations, more and more aragonite remained in suspension. X-ray data suggest a strong dominance of (104) and (202) crystal surfaces that seem to increase with the selenium concentration as shown in Figure 4. One possible explanation is the inhibition of growth on other surfaces through Se-adsorption (and incorporation), forcing the calcite into a thermodynamically less stable habit. At selenite concentrations between $20\text{-}60 \mu\text{M}$ the supersaturation ($SI=0.14$) is not sufficient for calcite to grow [6].

Interaction of iodide with green rust and magnetite

The long-lived fission product ^{129}I ($t_{1/2} \approx 15.7 \text{ Ma}$) is a dose determining nuclide in many safety analyses for nuclear waste repositories [7]. It is expected to prevail as anionic species in repositories and thus be poorly retained by geological and engineered barriers such as bentonite. In contrast, layered double hydroxides (LDH) have high affinity for anions. Green rust (GR) is a mixed-valent iron-bearing LDH and can form as corrosion product of steel canisters upon contact with groundwater. However, GR may not be thermodynamically stable on the long-term and convert into more stable magnetite. The interaction of iodide with chloride GR and magnetite was investigated in this study. Two different series of retention experiments were performed. In a first series, chloride GR (GR-Cl) was prepared in the presence of iodide (solid solution) using $\text{Fe}(\text{OH})_2$ as a precursor phase (Figure 5). In a second series of experiments, pre-synthesized GR or magnetite was contacted with I^- in suspension. Experimental parameters such as ionic strength, concentration of halides (Cl^- , I^-), pH and reaction time were varied in both series of the experiments. Results showed that the sorption equilibrium is attained quickly. Analyses of samples involved among others XRD and X-ray absorption spectroscopy (XAS) at the KIT synchrotron light source, as well as ICP-MS and gamma spectrometry (use of I-125 as tracer).

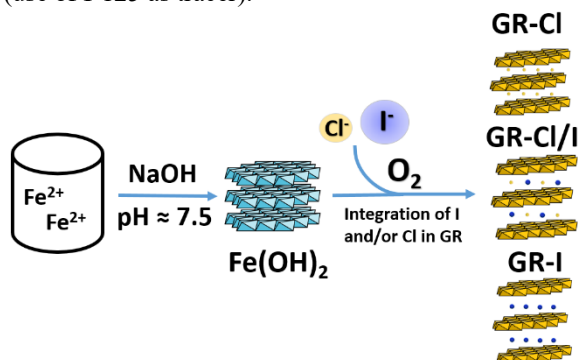


Fig. 5: Synthesis of GR in the presence of chloride and iodide considering various Cl:I ratios.

In the first series of experiments, GR was prepared at constant ionic strength of halide and considering various Cl:I ratios, from the chloride to the iodide endmember. Samples analysis showed that the interlayer composition had the same Cl:I ratio as it is in the starting suspension. GR-Cl and GR-I are isostructural, only the height of the interlayer gallery differs because both anions have different ionic radii.

In this study, data revealed a progressive increase of basal spacing (d_{003}) with iodide content from 7.7 \AA for GR-Cl to 8.3 \AA for GR-I (Figure 6). No phase separation or interstratification was detected and no preferential uptake of one anion over the other could be detected. This suggests a random distribution of both anions in the interlayer. Furthermore, the Fe K-edge and I L_{3} -edge were probed by XAS. No significant change in Fe or I speciation could be evidenced. Further details can be found in the corresponding publication [8].

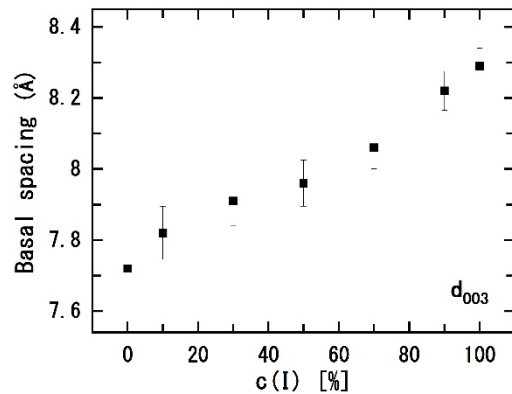


Fig. 6: Basal spacing of GR as function of the proportion of iodide in the starting suspension

In the second series of experiments, iodide was contacted with preformed GR-Cl. In these experiments, sorption equilibrium was reached fast and the uptake decreased with increasing ionic strength. Experimental data may suggest that iodide is retained by GR-Cl via ion exchange. At low ionic strength ($[\text{Cl}^-] < 0.1 \text{ M}$) the sorption constant was $R_d = 0.19 \text{ L/g}$ and decreased to zero with increasing iodide concentration in the range $0.8 \mu\text{mol/L}$ to 150 mmol/L . Within the pH range $7.5 - 8.5$ there were no changes in the solid solution composition. The iodine K-edge was probed by XAS, data evidenced the presence of six neighboring oxygen atoms which indicates a chemical environment comparable to that of hydrated I^- in solution. This result hints at a relatively weak interaction with GR octahedral sheet. Finally, iodide-containing GR samples were transformed into magnetite and the uptake was quantified. Separately, iodide was contacted with preformed magnetite in suspension. No significant iodide uptake could be evidenced in both types of experiments with magnetite. Findings suggest that the formation of magnetite as steel canister corrosion product will not contribute to substantial retention of iodide within the HLW-repository near-field.

Actinide sorption by steel corrosion products under saline conditions

Some countries consider salt rock as potential host rock for a nuclear waste repository, among those being Germany and the US. In case of unlikely case of groundwater intrusion, the conditions in this repository type are expected to evolve into reducing and mildly alkaline with groundwater containing high salt content. The interaction of trivalent americium and europium as a chemical analogue to trivalent plutonium, prevalent under very reducing conditions, with iron corrosion products is described here. Strong sorption capacity of RNs/pollutants and reducing power of Fe(II) containing minerals have been reported for low ionic strength conditions [9-12]. However, there is clearly a lack of sorption data for RNs under highly saline conditions for relevant Fe corrosion products.

Relevant secondary phases (magnetite, iron(II) hydroxychloride, trevorite (NiFe_2O_4) and chromium oxide (Cr_2O_3)) have been identified previously in dedicated corrosion studies [13]. Here, potential corrosion products were synthesized and thoroughly characterized before performing Eu batch sorption experiments. The Eu uptake was investigated in dilute to concentrated NaCl and MgCl_2 brines at room temperature under anoxic conditions considering different Eu concentrations (5.1×10^{-10} M, 1×10^{-7} M, 1×10^{-5} M).

For magnetite, data showed a strong Eu uptake with the formation of a tridentate surface complex at pH_M of 8.0, with no significant ionic strength effect in dilute to concentrated NaCl brines independent of the Eu concentration [14]. In dilute to concentrated MgCl_2 a small reduction in Eu uptake was observed and attributed to Mg and Eu competition for the surface sites compared to NaCl brine with identical ionic strength.

Europium uptake by iron(II) hydroxychloride exhibits a strong reduction with increasing ionic strength in MgCl_2 brines, especially at elevated pH_M . Uptake above 90 % was observed for $\text{pH}_M \leq 8.0$ in dilute to concentrated NaCl brines, with Eu concentration of 1×10^{-7} M and at a solid to liquid ratio of 1 g/L. For identical Eu concentration and solid to liquid ratio, the

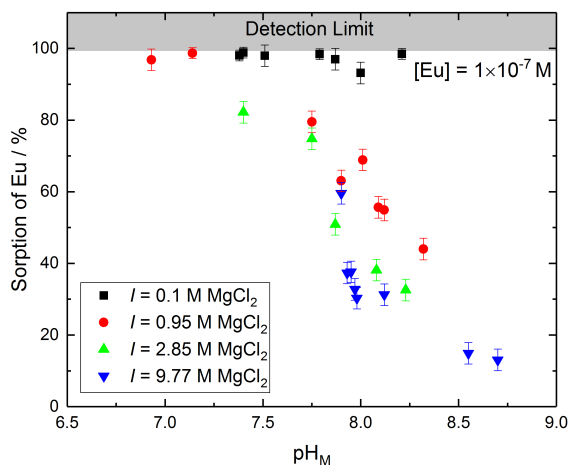


Fig. 7: Sorption of europium $[\text{Eu}] = 5.1 \cdot 10^{-7}$ M as percentage uptake on iron hydroxychloride (1 g/L) as a function of pH_M and at different ionic strengths of MgCl_2 .

uptake in dilute MgCl_2 brine was also above 90 % for $\text{pH}_M \geq 8.0$, but in concentrated (3.26 M) MgCl_2 brine, the uptake was only 30 % for $\text{pH}_M = 8.0$ (Figure 7).

The reason for this sorption reduction is not yet clear. Possible explanations range from possible conversion of the Fe solid phase to mixed Fe/Mg phases in MgCl_2 brines, with each phase having different sorption properties, to Mg competition for surface sites.

For trevorite and chromium oxide in dilute to concentrated NaCl brines, data showed a retention capability comparable to that of magnetite, with a pH_M dependent uptake behavior at Eu concentration of $1 \cdot 10^{-5}$ M and no significant ionic strength effect independent of Eu concentration.

Overall, the investigated corrosion products have a significant retention potential for trivalent actinides, thus contributing to the immobilization of these RNs in a repository near-field. The extent of retention seems only marginally affected in dilute to concentrated NaCl brines, while the reduction in uptake is limited in MgCl_2 brines.

Influence of the heterogeneity of the sandy facies Opalinus Clay on radionuclide retention

In the process of finding a suitable host rock for a final nuclear waste repository, one of the candidates is natural clay rock. The advantage of choosing clay rock lays in its swelling capacity, which enables a self-healing of formed cracks in the presence of water and in its retention capabilities towards radionuclides. The Opalinus Clay (OPA) is the considered host rock for the Swiss repository system. Here, samples from the Underground Rock Laboratory (URL) Mont Terri are investigated.

The clay formations in Southern Germany are also considered as potential host rock, alongside the lower cretaceous clays in northern Germany, and further tertiary clay formations. The OPA can be subdivided into different facies, differing in composition and properties. These facies range from shaly over carbonate rich-sandy to sandy. While the shaly facies shows a homogeneous distribution of its constituents, the sandy facies is quite heterogeneous. Due to this similarity to the lower cretaceous clay, studies made on the heterogeneity of the sandy facies OPA can also yield important information for the safety assessment of the before mentioned potential clay host rock.

To attribute possible differences in radionuclide retention properties to the heterogeneity and the resulting differences in composition, a thorough characterization of the bore core BMB-A7 (sandy facies OPA, Mont Terri) was performed. XRF measurements were performed at the terrachem GmbH Mannheim and at GFZ Potsdam. This yielded SiO_2 concentrations of 65.2 ± 0.5 wt.% which is higher than what was previously reported [15,16]. The Al_2O_3 and CaO concentrations are 9.59 ± 0.1 wt.% and 6.86 ± 0.1 wt.%, respectively, this indicates a higher quartz and a lower clay mineral content in this bore core compared to the previously analyzed samples. To validate this assumption, XRD measurements were performed. In addition to

powder measurements, samples treated with ethylene glycol vapor and samples treated at 550°C were measured to gather information on the amount of swellable clay minerals present (Fig. 8).

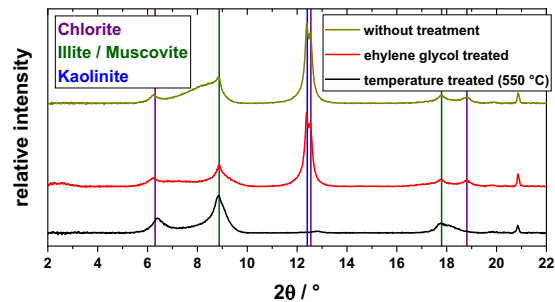


Fig. 8: Diffractogram of the clay mineral area of 2–22° 2 θ . Relative intensity of the differently conditioned samples shown in greenish (without further treatment), red (ethylene glycol treated) and black (temperature treated).

The resulting diffractograms were evaluated and quantified with Rietveld analysis using the program code TOPAS-64 V6, yielding a composition of quartz 50.7 \pm 2.6 wt.%, calcite 13.1 \pm 0.8 wt.% and clay minerals 22.4 \pm 1.0 wt.%, which is in good agreement with the XRF data. The clay minerals are further divided into 48 \pm 5 wt.% illite/muscovite, 39 \pm 4 wt.% kaolinite and 13 \pm 1 wt.% chlorite. Thermal analysis confirmed the established mineral composition. Further analytical methods used were BET, XPS, SEM-EDX, MIP (mercury intrusion porosimetry) and Mössbauer spectroscopy.

To investigate the influence of the heterogeneity on the radionuclide retention, multiple powder samples were prepared, differing in amount of clay minerals and sand lenses present. 100 mg of each of these samples were analyzed with a N/C 2100S from Analytic Jena GmbH for their carbon contents. While the TOC remained steady across all samples with 0.6–0.7 \pm 0.1 wt.%, the TIC varied greatly from 1.7–4.4 \pm 1.2 wt.%. This is an indication, that the TOC is distributed evenly, while the TIC and thereby mostly the calcite content is distributed heterogeneously. Furthermore, this proves that the samples in fact have different mineralogical compositions. The determination of the CEC was performed with two different methods, the compulsive exchange method and the Cu-Triene method. The resulting CEC was 5.8 \pm 0.4 cmol/kg, for the clay rich sample and 2.2 \pm 1.4 cmol/kg for the sand lenses rich sample with both methods.

Batch sorption experiments were conducted to investigate the retention potential of the different samples. 50 mg of each sample was contacted with 5 mL of pore water ($I = 0.2$ mol/L, pH 7.2 [17]). Afterwards they were spiked with a tracer solution to reach a concentration of $2 \cdot 10^{-7}$ mol/L and an activity of 1000 Bq/mL of Cs-137, Co-60 and Eu-152 respectively. After 7 days of equilibration, the samples were centrifuged (90.000 rpm, 30 min) and the supernatant analyzed via γ -spectroscopy. The resulting distribution coefficients (R_d in L/kg) of the samples are reported in Fig. 9.

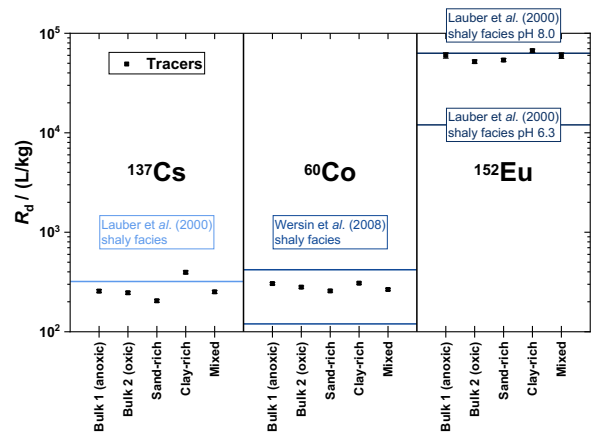


Fig. 9: Distribution coefficients of the batch experiments of sandy facies OPA (10 g/L) in synthetic pore water ($I = 0.2$ mol/L, pH 7.2 [17]) with $2 \cdot 10^{-7}$ mol/L tracer concentrations.

Although the samples did show differences in their TIC concentrations and CEC, only minor differences are visible in the retention behavior. Firstly, the samples ground under atmospheric and anoxic conditions show no differences across all three tracer solutions. The clay-rich samples show in general the highest retention and the sand lenses rich samples show the lowest. This effect is most pronounced for Cs⁺. R_d -values for all investigated samples are within the range of the retention behavior described in literature.

To further investigate the influence of the heterogeneity, more samples of smaller size (down to 1 cm³) were prepared and are currently being investigated.

References

- [1] Heberling, F. et al., *Geochim. Cosmochim. Acta*, **232**, 124-139 (2018).
- [2] Rendón-Angeles, JC, et al., *J. Mater. Sci.*, **43**, 2189-2197 (2008).
- [3] Putnis, A. and Putnis C.V., *J. Solid State Chem.*, **180**, 1783-1786 (2007).
- [4] Prieto, M. et al., *Elements* **9**, 195-201 (2013).
- [5] Heberling, F. et al., *Environ. Sci. Technol.*, **42**, (2), 471-476 (2008).
- [6] Heberling, F. et al., *Geochim. Cosmochim. Acta*, **134**, 16-38 (2018).
- [7] Hou, X. et al., *Anal. Chim. Acta* **632**, 181 (2009).
- [8] Platte, T. et al., *Inorg. Chem.*, **60**, 10585 (2021).
- [9] Geckeis, H. et al., *Chem. Rev.*, **113**, 1016-1062 (2013).
- [10] Li, D. and Kaplan, D. (2012). *J. Hazard. Mater.*, **243**, 1-18 (2013).
- [11] Martín Cabañas, B. et al., *J. Colloid Interface Sci.*, **360**, 695-700 (2011).
- [12] Wang, G. et al., *J. Hazard. Mater.*, **364**, 69-77 (2019).
- [13] Finck, N. et al. Korrosions- und Sorptionsprozesse an Stahloberflächen bei hohen Temperaturen und Drücken im anaeroben salinaren Milieu (KORSO) Abschlussbericht Teilprojekt B, KIT-INE. INE Scientific Working Documents 03 (2021). DOI: 10.5445/IR/1000130282

- [14] Morelovà, N. et al. *J. Colloids Interface Sci.*, **561**, 708-718 (2020).
- [15] Pearson, C.J. et al., Geochemistry of Water in the Opalinus Clay Formation at the Mont Terri Rock Laboratory, Office fédéral des eaux et de la géologie, Switzerland, 2003.
- [16] Kaufhold, A. et al., *Engineering Geology*, **156**, 111–118 (2013).
- [17] Gimmi, T. et al., *Geochim. Cosmochim. Acta*, **152**, 373–393 (2014).

5 Applied studies: Radionuclide retention in the multi-barrier system

Long-term safety of a deep geological repository for nuclear waste depends on a multi-barrier system which consists of technical and geo-technical barriers such as the waste form, the canister, backfilling and sealing of the mined openings as well as on the natural barrier function of the host rock. Currently, a series of applied studies on various subsystems with respect to potential multi-barrier systems in argillaceous or crystalline host-rocks are performed. These experimental and numerical studies cover a variety of components of the multi-barrier systems such as spent nuclear fuel as waste form, bentonite as geo-engineered barrier material and the interface between an iron-based canister and bentonite. Experiments are conducted on migration of radionuclides within bentonite emplaced in granodiorite and radionuclide diffusion in Jurassic clay stone (i.e. Opalinus Clay, Switzerland). Moreover, the distribution of natural organic matter in Oligocene clay (i.e. Boom Clay, Belgium) and uranium speciation in soils of a former uranium mine (i.e. Rophin mine, France) are analysed. In the context of dry interim storage of spent nuclear fuel in surface facilities, the integrity of the cladding of fuel rods as technical barrier is investigated.

5.1 Highly radioactive waste forms

M. Herm, E. Bohnert, M. Böttle, R. Dagan, L. Iglesias-Peréz, T. König, M. Marchetti, V. Metz, A. Walschburger

Chemical analysis of fuel-cladding interfaces of irradiated UO_x fuel rod segments

Introduction

In Germany, the current waste management concept foresees the direct disposal of spent nuclear fuel (SNF) assemblies in deep geological repositories (DGR). After discharge from a nuclear power reactor, the SNF is cooled for several years in SNF pools within the reactor building and subsequently loaded into dual-purpose casks (e.g., CASTOR[®], GNS) for transport and dry interim storage in surface facilities. However, due to several delays in the site selection process, as well as the estimated time for geological exploration, construction and commissioning of a DGR in Germany, a prolongation of dry interim storage is inevitable [1].

Tab. 1: Characteristics and irradiation data of the examined fuel rod specimen [5, 6]:

Reactor	PWR Gösgen, Switzerland
Fuel data	UO _x fuel with 3.8% enrichment of ²³⁵ U
	Pellet length = 11 mm
	Pellet radius = 9.11 mm
	Initial O/U ratio = 2.002 Density = 10.41 g/cm ³
Cladding data	Zircaloy-4 Initial wall thickness: 0.725 mm
	Average burn-up: 50.4 GWd/t _{HM} Number of cycles: 4
Irradiation data	Average linear power: 260 W/cm
	Date of discharge: 27.05.1989
	Full power days: 1226 days
	Fission gas release: 8.3%

The integrity of the irradiated cladding tubes is the most crucial aspect regarding the safe handling and latter conditioning as well as relocating of the fuel rods for ultimate disposal. Already during reactor operation, the chemical and physical properties of the nuclear fuel and cladding are significantly altered. The nuclear fuel rods will experience an elongation phenomenon due to the harsh irradiation conditions intertwined with a creep of the cladding under external pressure [2].

To some extent, the pellet structure will fracture due to the steep thermal gradient between pellet centre and the inner surface of the cladding displaying a pathway for volatile fission products to be segregated to the pellet's rim zone. Furthermore, the cladding is impaired by hydrogen involving effects e.g. the dissolution and precipitation of hydrides into the zirconium matrix as well as a hydride induced embrittlement and delayed hydride cracking [2, 3].

The fuel pellets are subject to a swelling effect owed to the constant build-up of fission products during irradiation, which ultimately results in the closing of the pellet-cladding gap and the pellet being in contact with the cladding. This leads to the formation of an interaction layer between the nuclear fuel pellet and the cladding, which displays an interface for chemically assisted degradation processes [3]. Moreover, the cladding is damaged by continuous irradiation of alpha-emitters near the pellet periphery [4].

In this study, we present results on the chemical composition and possible enrichment effects of fuel-cladding interface layers occurring between irradiated Zircaloy-4 cladding and nuclear fuel. The insights and outcomes of this study are aimed at improving the knowledge on chemically assisted degradation processes, which are suspected to occur during (prolonged) dry interim storage.

Materials and irradiation history

The examined fuel fragments and Zircaloy-4 cladding segments were sampled from a high burn-up UO_x fuel

in ownership of KIT-INE. Fuel characteristics and irradiation history are given in Table 1. The fuel was irradiated in a light water reactor (LWR) during the 1980s with a cooling time of approximately 32 years.

Experimental and analytical methods

Samples of the SNF were obtained by dry cutting an approximately 2 mm thick disk using a low speed saw (IsoMet, 11-1180, Buehler Ltd.) equipped with a diamond wavering blade (IsoMet, 15LC, Buehler Ltd.) and selectively defueling of the specimens by means of a piston. Figure 1 depicts exemplarily the cutting process and the partly defueled high burn-up UO_x fuel disk. From the defueled Zircaloy-4 disk, fragments originating from the closed gap were taken for radiochemical inventory determination. Masses and dose rates of the specimens were determined with an analytical balance (Entris 623-1S, Sartorius, Göttingen, Germany) and a gamma probe (6150AD-15/E, Automation und Messtechnik, Ladenburg, Germany) located inside the hot cell connected with a dose rate meter (6150AD, Automation und Messtechnik, Ladenburg, Germany). For inventory analysis of the UO_x fuel, two-millimetre sized fragments from the closed gap with a contact dose rate of approximately 6 mSv/h and a weight of 0.028 ± 0.001 g and 0.031 ± 0.001 g (see figure 2) were digested in a mixture of 30% H_2O_2 and saturated $(NH_4)_2CO_3$ as described in [7]. Digestion of the UO_x fragments was carried out for five days in either a flask or an autoclave for additional gas phase analysis and the (radio-)nuclide inventory was determined by various analytical methods.

Determination of fission gases, Kr and Xe in the gas phase was carried out by means of a gas-sampling cylinder (SS-4CS-TW-50, Swagelok, USA) which was connected to the autoclave from the backside of the hot cell. Measurements were performed with a gas mass spectrometer (GAM400, InProcess Instruments, Bremen, Germany) equipped with a secondary electron multiplier for low concentration measurements.

For γ -emitting fission products and minor actinides e.g. $^{134/137}Cs$, ^{241}Am , $^{154/155}Eu$, ^{125}Sb and ^{129}I , measurements were conducted utilising a high-resolution γ -

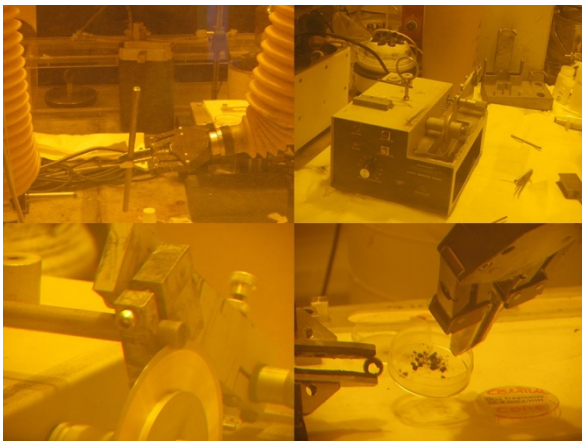


Fig. 1: Cutting of 2mm UO_x fuel disk and defueled cladding specimen.

spectrometer (GX3018, Canberra Industries Inc., USA) equipped with an extended range coaxial Ge detector. Calibration of the device was performed with a certified multi-nuclide standard (Mixed Gamma 7600, Eckert & Ziegler, Strahlen- und Medizintechnik, Berlin, Germany) and evaluation of the obtained data was carried out with the Genie 2000 software (Canberra Industries Inc., USA). Aliquots of one millilitre were sampled from the digestion liquors prior and after chemical separation of other radionuclides and measured in APEX screw-cap microcentrifuge tube vials (2 mL, polypropylene, Alpha Laboratories Ltd., UK) with a relative efficiency of the device in the range of $\geq 30\%$.

For β -emitting activation and fission products such as ^{36}Cl , ^{129}I or ^{90}Sr , liquid scintillation counting (LSC) measurements were performed after separation from interfering radionuclides. LSC analysis was performed by mixing up to 3 mL of sample solution with 10 mL scintillation cocktail (ProSafe HC+, Meridian Biotech-

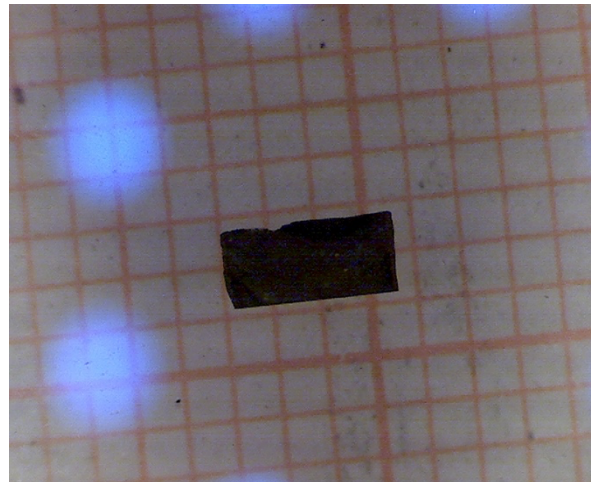


Fig. 2: Selected UO_x fragment from the closed gap for inventory analysis.

nologies Ltd., Tadworth UK or Ultima Gold LLT/XR, PerkinElmer, USA) in Polyvials (HDPE, Zinsser Analytic, Eschborn, Germany). Measurements were performed with an ultra-low-level spectrometer (Quantulus 1220, Wallac Oy, PerkinElmer, USA).

In addition, the actinide inventory e.g. $^{235/238}U$, ^{237}Np , $^{238/239/240/241/242}Pu$, $^{241/243}Am$, ^{244}Cm , of the obtained solutions was determined by means of sector field inductive-coupled plasma mass spectrometry (ELEMENT XR, ThermoFisher Scientific, USA). At this, samples were diluted by a factor of 1000 with 2% HNO_3 .

The applied separation techniques in this study include extraction chromatography for e.g. ^{36}Cl and ^{90}Sr [8, 9], precipitation of caesium isotopes with ammonium molybdophosphate [9], as well as separation by liquid-liquid extraction for ^{129}I [9]. Ultimately, the radiochemical inventory was compared to theoretical results obtained by MCNP/CINDER and webKORIGEN calculations [10, 11].

Results and discussion

Table 2 shows the experimentally determined inventories of various fission products derived from the analysis of the alkaline digestion liquor of UO_x fuel fragments originating from the closed gap in comparison to the calculated inventories. In general, a good agreement of both values, experimentally determined and theoretically calculated (E/C), can be seen. The deviation between both values can be explained to some extent by the sampling process of the SNF fragment, as the thickness of the rim layer is only about 100 µm as stated by Grambow and co-workers [11].

For ¹²⁹I (and to some extent for ¹³⁷Cs) a possible rim enrichment is apparent, resulting from the possible migration of iodine from the pellet centre to the pellet periphery and precipitation as CsI during irradiation. In case of the uranium isotopes and various minor actinides an enrichment in ^{241/243}Am can be seen as table 3 depicts. For ²⁴¹Am the decay of non-fissioned ²⁴¹Pu, which had been segregated to the rim, has to be taken into account as described in Grambow et al. [11]. Table 4 shows the fission gas inventory of an UO_x fuel fragment from the closed gap in mol/gUO₂. For the xenon isotopes, a good agreement with the calculated values is depicted, yet due to a possible contamination of the argon gas with krypton traces, the results for the krypton concentration might be skewed.

Summary and conclusion

So far, the aim of this study is to provide further insight in possible enrichment effects of fission products and minor actinides within the fuel-cladding interface layer of irradiated LWR fuel with respect to the integrity of SNF under the conditions of dry interim storage. Since some fission and activation products such as ³⁶Cl, ¹²⁹I and the caesium isotopes are able to embrittle the Zircaloy cladding via a stress corrosion cracking mechanism, a profound knowledge on their speciation and distribution within the fuel-cladding interaction layer is of great importance.

Experimental results for the radionuclide inventory are in general in good accordance to the theoretical

obtained values by means of MCNP/CINDER and webKORIGEN calculations.

In case of ¹²⁹I, which is expected to be present as CsI, an enrichment effect in the pellet periphery and cladding adherent region is observed.

Determination of the irradiation damage produced in the cladding by the actinide's alpha-decay in thirty years

Introduction

In the context of the Spent Nuclear Fuel (SNF) structural integrity studies, it is pivotal to consider that high burnup fuels at discharge have pellets fully in contact with the cladding. The consequence of this phenomenon is the determination of chemical and mechanical interactions between the pellet and the cladding, which increase the stress the cladding has to withstand during dry cask interim storage and beyond.

The pellet-cladding contact, moreover, exposes the inner surface of the cladding to the actinide's alpha decays, which produce irradiation damage and may contribute to deteriorating the cladding physical and mechanical properties.

Irradiation damage during dry interim storage is particularly important if one considers that the temperature decreases and may reach 313.15 K after forty years and even room temperature after 100 years of storage [12]; hence thermal annealing is not expected.

The accumulation of irradiation damage during about thirty years of storage was investigated along radial positions between the inner and the outer diameter of an irradiated Zircaloy-4 cladding in terms of displacements per atom (dpa).

Materials and Methods

The considered cladded UO_x pellet belongs to a PWR fuel rod segment having an average burnup at discharge of 50.4 GWd t⁻¹_{HM} (Table 1).

Displacements per atom (dpa) were calculated by means of FLUKA-2020.0.10 Monte Carlo code together with FLAIR 2.3-0 advanced graphical interface [13–15].

Tab. 2: Comparison of experimental and theoretical fission product inventory in the rim zone of alkaline digested UO_x fuel.

	⁹⁰ Sr [Bq/g _{HM}]	¹²⁹ I [Bq/g _{HM}]	¹³⁷ Cs [Bq/g _{HM}]	¹⁵⁴ Eu [Bq/g _{HM}]	¹⁵⁵ Eu [Bq/g _{HM}]
experimental	2.00(±0.46)×10 ⁹	2.40(±0.26)×10 ³	3.40(±0.14)×10 ⁹	3.03(±0.03)×10 ⁷	3.25(±0.04)×10 ⁶
calculated	2.04×10 ⁹	2.70×10 ³	4.16×10 ⁹	5.73×10 ⁷	3.32×10 ⁶
ratio (E/C)	0.98 ± 0.23	0.89 ± 0.10	0.82 ± 0.05	0.53 ± 0.05	0.98 ± 0.10

Tab. 3: Comparison of experimental and theoretical uranium and various minor actinides inventory in the rim zone of alkaline digested UO_x fuel.

	²³⁵ U [Bq/g _{HM}]	²³⁸ U [Bq/g _{HM}]	²⁴¹ Am [Bq/g _{HM}]	²⁴³ Am [Bq/g _{HM}]
experimental	3.52(±0.20)×10 ²	1.16(±0.05)×10 ²	2.71(±0.07)×10 ⁸	3.32(±0.40)×10 ⁶
calculated	3.34×10 ²	1.15×10 ²	4.17×10 ⁸	4.77×10 ⁶
ratio (E/C)	1.03 ± 0.06	1.01 ± 0.04	0.65 ± 0.07	0.70 ± 0.1

Tab. 4: Comparison of experimental and theoretical fission gas inventory in the rim zone of alkaline digested UO_x fuel.

	Kr _{total} [mol/gUO ₂]	Xe _{total} [mol/gUO ₂]
experimental	3.25(±0.04)×10 ⁻⁵	4.51(±0.03)×10 ⁻⁵
calculated	4.84×10 ⁻⁶	4.85×10 ⁻⁵
ratio (E/C)	6.71 ± 0.08	0.93 ± 0.01

The geometry used is depicted in Fig. 3, where a pellet of irradiated UO₂ (11.5 mm of height) is surrounded by Zircaloy-4 cladding (inner diameter is 9.28 mm and outer diameter is 10.75 mm). The radioactive source possesses a cylindrical geometry and is in contact with the cladding.

The actinides are selected by using the ISOTOPE option in the BEAM card and the radioactive decay is followed by means of a Monte Carlo semi-analogue mode: the decay times and the type of decay are randomly sampled according to the radionuclide specific decay-probability.

The considered time interval is 1.01×10^9 s, which correspond to about 32 years elapsed from the end of irradiation in May 1989.

The dpa calculations are based on the modified Kinchin-Pease damage model and implement a correction factor derived from molecular dynamics, which considers the higher damage recombination probability when the primary knock-atom kinetic energy increases [16].

The dpa obtained per 1 Bq are successively normalised on the basis of the actinide's activity at the periphery of the pellet.

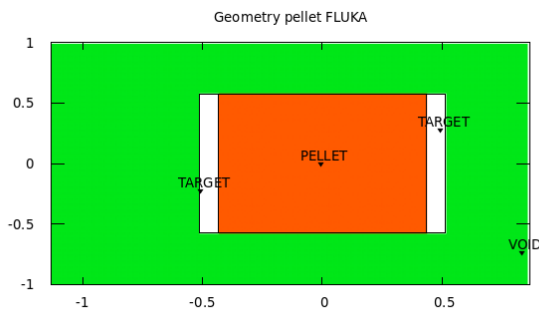


Fig. 3: Schematic of the pellet which represents the geometry created with FLAIR 2.3-0. The target represents the Zircaloy cladding while the orange area is the uranium dioxide pellet. The green area illustrates the void around the pellet.

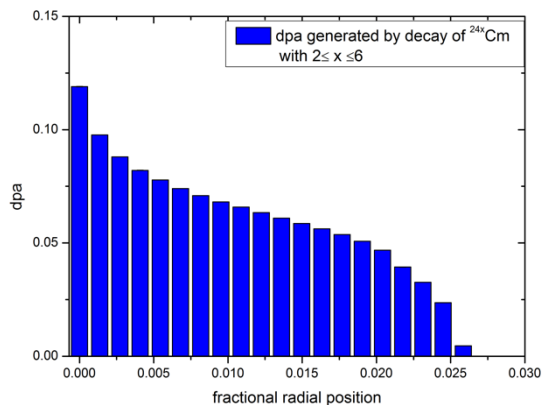


Fig. 4: Displacements per atom produced by the Cm isotopes (²⁴²Cm–²⁴⁶Cm) inside the Zircaloy-4 cladding. The positions are indicated as fractional radial position starting from the inner surface.

Results and discussion

According to the calculations, ²⁴¹Am and ²⁴³Am produce less than 8×10^{-5} dpa, while the Pu isotopes (²³⁸Pu–²⁴²Pu) produce about 5×10^{-3} dpa on the inner surface of the cladding. More important contribution to the displacements per atom derives from the Cm isotopes (²⁴²Cm–²⁴⁶Cm): on the cladding inner surface the dpa are more than 1×10^{-1} dpa (see Fig. 4). The displacements per atom produced by the Cm isotopes penetrate more in depth and reach the 0.025 fractional radial position (in comparison with 0.022 of Am and Pu isotopes).

Summary and conclusion

The results obtained highlight how the irradiation damage occurs mainly on the inner surface of the cladding and does not penetrate more than 3% in depth (as expected considering the short range of the alpha particles in matter).

However, this region corresponds to the area where interactions between the pellet and the cladding are established and the impact on the physical and mechanical properties (together with the effect of the hydrides) needs to be singled-out.

Leaching of irradiated MOX fuel in bicarbonate water and hydrogen overpressure

Introduction

In safety assessments for disposal of spent nuclear fuel in a deep geological repository, water access, consecutive failure of canisters and loss of integrity of fuel cladding is considered in the long-term. In this context, it is indispensable to evaluate the contribution of fission products and gases to the instant release fraction (IRF). This fraction consists of mobile radionuclides with low retention tendency and contributes significantly to the calculated doses arising from release in an deep underground repository.

Materials and irradiation characteristics

In the present study, irradiated mixed oxide fuel (MOX) pellets with cladding were sampled from a fuel rod segment, which was irradiated in the pressurized water reactor Obrigheim (Germany) during the 1980s. The fuel rod achieved an average burn-up of 38.0 GWd t⁻¹HM and an average linear heat generation rate of 200 W·cm⁻¹. The fuel was initially enriched with 3.2% Pu. Static leaching experiments under 40 bar Ar/H₂ overpressure (p(H₂) = 3.2 bar) were performed with a cladded pellet and decladded fragments of the sampled spent MOX fuel in bicarbonate water (19 mM NaCl + 1 mM NaHCO₃). The experiments were periodically sampled and solution aliquots and gas phases were analyzed for IRF. The cumulative release of the fission gases (Kr + Xe) as well as the release of ⁹⁰Sr, ¹³⁷Cs, ¹²⁹I, ⁹⁹Tc and ²³⁸U were determined over a period of > 1000 days of leaching under anoxic/strongly reducing conditions.

Results and discussion

A relatively fast release of volatile radionuclides such as ^{137}Cs and ^{129}I , compared to predominately matrix bound elements such as ^{90}Sr and ^{99}Tc , possibly due to fast dissolving ^{137}Cs and ^{129}I bearing fraction in irradiated MOX samples, is seen in Fig. 5. All fission products approach towards a so-called concentration plateau after about 200 days of leaching. The data obtained in the present study is in good agreement with data obtained for high burn-up spent UO_2 fuel also leached in bicarbonate water and argon/ H_2 atmosphere [17].

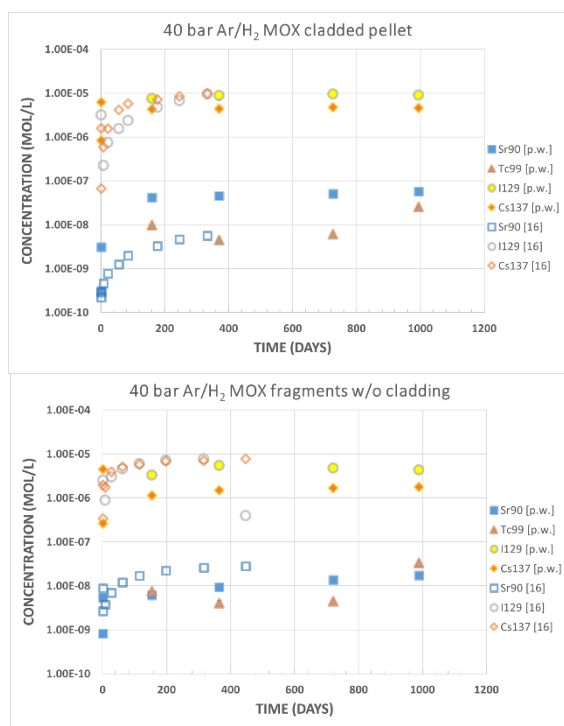


Fig. 5: Molar concentration of fission products released into aqueous solution from spent MOX fuel compared with data obtained for spent UO_2 fuel [17].

References

- [1] Abschlussbericht der Kommission Lagerung hoch radioaktiver Abfallstoffe, K-Drs. 268, Berlin, Germany (2016).
- [2] H. Bailly, D. Ménessier, C. Prunier: The nuclear fuel of pressurized water reactors and fast reactors: design and behaviour, Lavoisier Publishing, Paris (1999).
- [3] D. Olander: Nuclear fuels – Present and future, J. Nucl. Mat. **389**, 1 – 22 (2009).
- [4] R. Ewing: Long-term storage of spent nuclear fuel, Nat. Mater. **14**, 252 – 257 (2015).
- [5] E. González-Robles, V. Metz, D.H. Wegen, M. Herm, D. Papaioannou, E. Bohnert, R. Gretter, N. Müller, R. Nasyrow, W. de Weerd, W., B. Kienzler: Determination of fission gas release of spent nuclear fuel in puncturing test and in leaching experiments under anoxic conditions. Journal of Nuclear Materials **479**, 67-75 (2016).
- [6] Kernkraftwerk Gösgen: Technik und Betrieb – Technische Hauptdaten (2010).
- [7] C. Soderquist, B. Hanson: Dissolution of spent nuclear fuel in carbonate-peroxide solution, J. Nucl. Mat. **396**, 159 – 162 (2010).
- [8] A. Zulauf, S. Happel, M. Mokili, A. Bombard, H. Jungclas: Characterization of an extraction chromatographic resin for the separation and determination of ^{36}Cl and ^{129}I , J. Nucl. Mat. **286**, 539 – 546 (2010).
- [9] H. Geckeis, D. Degering, A. Goertzen, F. W. Geyer, P. Dressler: Langzeitsicherheit nuklearer Endlager: Radiochemische Analytik von Proben aus Brennstoffauslaugungsexperimenten. FZKA 5650, Forschungszentrum Karlsruhe (FZK), Karlsruhe, Germany (1996).
- [10] E. González-Robles, M. Herm, N. Müller, M. Böttle, E. Bohnert, V. Metz, in H. Geckeis, M. Altmaier, S. Fanghänel (eds.): INE-Annual Report 2017, KIT-Scientific Reports (2018).
- [11] B. Grambow, A. Loida, P. Dressier, H. Geckeis, J. Gago, I. Casas, J. de Pablo, J. Giménez, M. E. Torrero: Chemical reaction of fabricated and high burn-up spent UO_2 fuel with saline brines, European commission report, EUR 17111 (1997).
- [12] K.-T. Kim, Nucl. Eng. Technol., **52**, 1486–1494, (2020).
- [13] A. Fasso et al., *tech. rep.*, CERN-2005-10, (2005).
- [14] T. Böhlen et al., Nucl. Data sheets, **120**, 211–214, (2014).
- [15] V. Vlachoudis, Proc. Int. Conf. on Mathematics, Computational Methods & Reactor Physics, Saratoga Springs, New York, (2009).
- [16] A. Fasso et al., *PNST*, 769–775, (2011).
- [17] E. González-Robles, M. Lagos, E. Bohnert, N. Müller, M. Herm, V. Metz, B. Kienzler : Leaching experiments with clad pellet and fragment of high burn-up nuclear fuel rod segment under argon/ H_2 atmosphere in *Final workshop proceedings of the collaborative project “Fast/Instant release of safety relevant radionuclides from spent nuclear fuel”*, (Eds. B. Kienzler, V. Metz, A. Valls), KIT Scientific Publishing, SR-7716, 2014.

5.2 Geo-engineered barrier materials

Y. Kouhail, H. Geckeis, F. Geyer, V. Metz, F. Quinto, D. Schild, E. Soballa

In co-operation with:

T. Schaefer^a, M. Andrew^b, I. Blechschmidt^b, R. Schneeberger^b

^aFriedrich-Schiller-University (FSU), Institute for Geosciences (IGW), Applied Geology, Jena, Germany; ^bNAGRA (National Cooperative for the Disposal of Radioactive Waste), Wetingen, Switzerland

Introduction

Natural bentonite is envisaged to be used as engineered barrier for deep geological repositories (DGR) of high-level radioactive waste in, e.g., crystalline or argillaceous rocks [1-3]. In these type of host rocks, emplacement of iron-based canisters containing spent nuclear fuel rods or vitrified high level waste products are planned, with bentonite surrounding the canisters as a backfill and buffer material. In some scenarios of safety assessment studies for DGR in crystalline rocks, these canisters are considered to be sealed tight for some thousands of years before an intrusion of glacial melt water through fractures in the host rock is expected to increase their corrosion. Following to corrosion of the canisters, radionuclides would be released from the waste package into the bentonite. Moreover, the intrusion of groundwater would lead to the swelling and the erosion of the bentonite [4], with consecutive formation of bentonite colloids that would act as carrier for radionuclides, increasing their mobility. Therefore, there is a need to study the processes of radionuclide diffusion through the bentonite, bentonite erosion and the colloid-associated radionuclide migration in order to assess its long-term barrier function.

Long term bentonite erosion experiments in an artificial fracture: Radionuclides diffusion in FEBEX bentonite

At the KIT-INE laboratories, FEBEX bentonite erosion experiments have been conducted in an artificial horizontal fracture set-up (mock-up experiments) to simulate the intrusion of groundwater in the near-field of a repository with bentonite as geo-engineered barrier. A ring of compacted bentonite (40 mm inner diameter, 80 mm outer diameter, 25 mm height) was emplaced between two Plexiglas plates spaced by a 1 mm height aperture to simulate a parallel fracture around the bentonite. Groundwater of the Grimsel Test Site, pumped through the fracture at a flow rate of 50 $\mu\text{L}/\text{min}$, led to bentonite swelling and formation of a gel in the aperture [5]. Coarse grains of accessory minerals of various colors were visible in this gel and sampled for SEM-EDX and XRD analysis. Some minerals that were originally present in the bentonite (i.e. gypsum) were not identified, suggesting a dissolution of these minerals – in agreement with SO_4 concentrations in the collected water samples – while some other secondary phases were formed in the ring (i.e. pyrite as seen in Fig. 1).

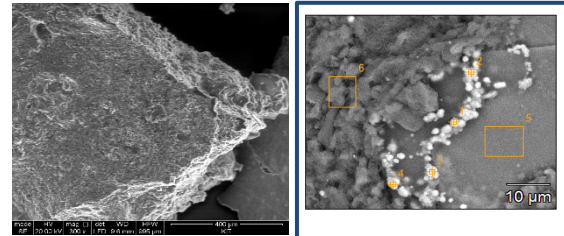


Fig. 1: Formation of pyrite in the bentonite gel evidenced by SEM-EDX.

A similar experiment was performed with Zn-labelled montmorillonite, a cocktail of radionuclide tracers (containing $^{241}\text{Am}(\text{III})$, $^{137}\text{Cs}(\text{I})$, $^{242}\text{Pu}(\text{III})$, $^{45}\text{Ca}(\text{II})$, $^{75}\text{Se}(\text{IV})$, $^{99}\text{Tc}(\text{VII})$, $^{233}\text{U}(\text{VI})$, $^{237}\text{Np}(\text{V})$) and a conservative tracer, Amino-G, that were mixed with a bentonite slurry and inserted in open glass vials within the bentonite. This experiment was carried out in an argon glove box. In the collected effluent, analysis of colloids, elemental composition and radionuclide breakthrough were carried out [3]. The Plexiglas box containing this radioactive mock-up test was opened after ca. 5 years from the end of the experiment for post mortem analysis. The bentonite ring and gel were preserved as two samples of the same size that adhere onto the two Plexiglas plates (top and bottom plates of the Plexiglas box as seen in Fig. 2).

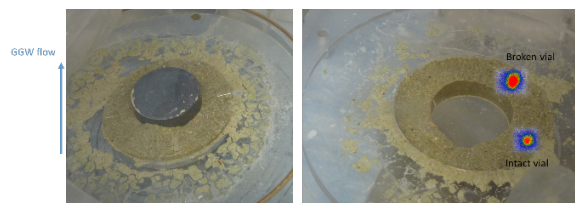


Fig. 2: Post mortem picture of the FEBEX experiment containing the radioactive tracer cocktail. Autoradiography of the bentonite ring on the right.

Two of the vials were found intact and the two others broken due to the pressure rise during the experiment. Autoradiography was performed on the ring to detect gamma emitters radionuclide tracers (namely ^{241}Am and ^{137}Cs). Two different types of diffusion distances were identified as shown in Fig. 2. For the intact vial, the radionuclides were still mostly contained in the vial, with a diffusion at a millimeter scale around the vial. In the case of the broken vial, the radionuclides were diffusing further away from the source at a centi-meter scale. Cutting of the sample into ca. 100 μm

slices by abrasive peeling and desorption of the radionuclides with concentrated nitric acid will be performed in order to investigate with (SF)ICP-MS the diffusion profiles of the radionuclides through the bentonite.

Radionuclides mobility and diffusion in FEBEX bentonite

The results of the mentioned mock-up experiments in artificial fracture can be compared to the ones of the Long-term In situ Test (LIT) experiment that was performed at the Grimsel Test Site in Switzerland. The LIT experiment started in 2014 and ended in 2018 and consisted of compacted bentonite (FEBEX and Zn-labelled montmorillonite) spiked with glass vials containing the same radionuclide tracer cocktail than the laboratory experiments. The compacted bentonite rings were emplaced into the granodiorite host rock in a water-conductive migration shear zone. Three dedicated boreholes were used to monitor the transport of radionuclides and the results are described in Chapter 5.4 of this report.

For the post mortem analysis of the experiment, the granodiorite containing the bentonite rings was overcored and cut into slices. The first LIT sample, which consists of a disk of the granodiorite core (30 cm diameter and 3 cm thick, taken 15cm from the bentonite rings spiked with the radionuclide tracers) and contains a bentonite ring was used to test the sampling procedure for the analysis of the active LIT samples. The bentonite ring was cut out from the granodiorite using an oscillating multi-tool saw. Samples were then drilled from the bentonite ring to obtain fine powder specimens. Investigation of the mineralogical composition with SEM-EDX and XRD showed the presence of minerals containing copper and sulfur in addition to similar minerals present in the mock up experiment. The powder bentonite samples were successively digested with hydrofluoric acid and aqua regia and submitted to (SF)ICP-MS for elemental composition analysis. Some residues left undissolved after the digestion were analyzed using SEM-EDX and showed that they are mainly composed of $ZrSiO_4$ and TiO_2 , known to be refractory minerals. In the dissolved fraction of the bentonite samples, the actinide tracers were always below the detection limit of (SF) ICP-MS, equal to ~ 10 fg/ml. The elemental composition of these LIT samples was then compared to pristine bentonite that was not used in the experiment. The main difference observed is linked to the copper, manganese and vanadium con-

centration (Table 1). These elements had a higher concentration in the bentonite sample 2 taken in the vicinity of the carbon steel mandrel – at ca. 3 mm – compared to sample 1 taken in the middle of the bentonite ring – at ca. 1 cm from the carbon steel mandrel – as well as to the pristine bentonite sample, suggesting a diffusion of these elements from the carbon steel through the bentonite.

Table 1: Concentrations of copper, iron, manganese and vanadium in two LIT bentonite samples and in pristine bentonite determined by (SF)ICP-MS after digestion in hydrofluoric acid and aqua regia. Sample 1 was taken in the middle of the bentonite ring when sample 2 was taken in the vicinity of the carbon steel mandrel.

C $\mu\text{g/g}$ of bentonite	Pristine Bentonite	Sample 1 (ca. 10 mm from the carbon steel mandrel)	Sample 2 (ca. 3 mm from the carbon steel mandrel)
V	17.1 \pm 0.3	12.8 \pm 0.4	33.2 \pm 0.2
Mn	324.1 \pm 3.2	208.8 \pm 2.1	854.5 \pm 2.9
Fe	30205.7 \pm 205.4	22944.8 \pm 160.6	37070.9 \pm 189.1
Cu	15.3 \pm 0.7	15.1 \pm 0.6	43.4 \pm 0.3

This LIT sample was also be used to refine the abrasive peeling procedure that will be used to cut the spiked bentonite into thin sections of ca. 100 μm in order to obtain diffusion profiles of the radionuclide tracers.

These results will allow for a comprehensive understanding of the mechanisms of radionuclide mobility through a bentonite geotechnical barrier.

References

- [1] SKB, *Technical report TR 06-09*, Svensk Kärnbränslehantering AB (SKB), Stockholm, Sweden (2006).
- [2] Shelton et al., *Technical report TR-17-17*, Svensk Kärnbränslehantering AB (SKB), Stockholm, Sweden (2018).
- [3] Gribi et al., *Technischer Bericht NTB 08-05*, Nationale Genossenschaft für die Lagerung radioaktiver Abfälle (NAGRA) Wettingen, Switzerland (2008).
- [4] Bouby et al., *Applied Clay Science*, **198**, 105797, (2020).
- [5] Rinderknecht, Doctoral thesis, Karlsruhe Institute of Technology (KIT), Karlsruhe, Germany, (2017).

5.3 Colloid impact on radionuclide migration

M. Bouby, H. Geckeis, F. Geyer, S. Kraft, S. Kuschel, A. Lunz, A. Thumm

In co-operation with:

S. Brassines^a, J. Brendlé, O. Courson^b, S. Georg^b, M. Del Nero^b, G. Montavon^c

^aONDRAF/NIRAS, Belgian Agency for Radioactive Waste and Enriched Fissile materials, Geological Disposal, R&D, Avenue des Arts, 14, 1210 Bruxelles, Belgium

^bENSCMu - Université de Haute-Alsace, 3 rue Alfred Werner 68093 Mulhouse Cedex

^cInstitut Pluridisciplinaire Hubert Curien (IPHC), UMR 7178, Département de Recherches Subatomiques, Groupe de Radiochimie, 23 rue du Loess, BP 28, F-67037 Strasbourg cedex 2.

^dSUBATECH - UMR 6457, Groupe Radiochimie, IMT Atlantique, 4 rue Alfred Kastler, La Chantrerie BP 20722, 44307 Nantes cedex 3 - FRANCE

Introduction

The influence of colloidal/nano-scale phases on the radionuclide solubility and migration behavior is of concern for the safety assessment of a nuclear waste repository [1], [2] or for the assessment of environmental impacts of old nuclear-industrial sites after and during remediation or decommissioning activities. The long-term goal of our group, following a bottom-up approach, is:

- To identify the relevant repository-specific processes of colloid formation ("eigen" colloids, pseudocolloids from backfill material or host rock, pseudocolloids from secondary phase formation).
- To determine the stability of inorganic and organic colloids as a function of essential geochemical parameters (pH, Eh, ionic strength, DOC) on long time scales (> several years).
- To analyze the influence of colloidal phases on radionuclide migration in close to reality systems based on i) laboratory and underground laboratory experiments and ii) natural sample analysis.

The process understanding gained at the molecular and macroscopic level will be used to develop new geochemical models and to optimize existing models that allow a prediction of colloid stability and colloid-borne radionuclide migration under natural geochemical conditions. The final goal is to implement our experimental data into reactive transport modelling codes.

Our work requires accordingly the use and development of highly sensitive and sophisticated analytical techniques (see chapter 8 and hereafter).

Our present activities are conducted with the support and in close collaboration with international nuclear waste management agencies (ONDRAF / NIRAS, Belgium; NAGRA, Switzerland), in the framework of several projects like the BMWi project KOLLORADO-e3 (see chapter 5, §5.2). We are actively part of the European Campus EUCOR via the funding we received for a SEED Money project (<https://www.eucor.uni.org/en/research/networks-and-projects/c4-pon->) in collaboration with our partners from Strasbourg and Mulhouse (France). In addition, we are developing strong partnership and collaborative work with our

partners from Nantes (France) involved in activities devoted to the characterization of a former uranium-mining site (Rophin, Auvergne, France).

The collaboration with the ONDRAF/NIRAS agency is related to the characterization of natural organic matter (NOM) derived from different layers within the Belgian **Boom Clay (BC)** formation and their interaction with radionuclides [3].

Experiments performed in the framework of the BMWi project **KOLLORADO-e3** are closely related to the CFM (Colloid Formation and Migration) project performed in the Grimsel Test Site (GTS) in the frame of the Phase VI (www.grimsel.com/gts-phase-vi/cfm-section). Research on the stability of the geotechnical barrier under glacial melt water conditions and the potential release of bentonite colloids constitutes the scientific goal of the CFM project.

Our **EUCOR-SEED Money project** named **C4-PON** (Feb.2020-Jan.2022), consisted in the establishment of a Cross-border Competence Center for the Characterization of (micro) **POLL**utants and their (in)organic Nanovectors around decommissioning sites. We could start despite the COVID-19 by the collection and analysis of samples from the Grand Canal of Alsace and the Old Rhine, around the Fessenheim Nuclear power plant site, located in Alsace, France [4].

ROPHIN is one of the 17 storage sites for uranium mining residues produced in France during the 20th century. Between 1948 and 1957, the mechanical leaching of some 44,625 tons of ore produced 33.9 tons of uranium. About 30,000 tons of mine waste are now stored at the site of former Rophin mine and covered by vegetation [5]. Understanding the fate of radionuclides near a former uranium (U) mine is of great importance given both the potential enhancement of environmental dose rates and the transfer of radionuclides into ecosystems. All information on the geochemical speciation and dynamics of U in soils for regulating U transfer into other environmental compartment is therefore of major interest [6].

In this chapter, we report on 1) the finalization of a bentonite erosion study [7], 2) the acquisition and the use of a new and highly sophisticated analytical technique named LC-OCD-UVD-OND coupled to our new iCAP-ICPMS which is presently unique, to the best of our knowledge.

Bentonite clay erosion study [7]

Potential erosion processes of bentonite, planned to be used as a backfill material in some deep geological repositories (DGR) in argillaceous and crystalline host rocks, have to be clearly understood in order to properly assess its long-term barrier function for certain scenarios. The objective of this work was to determine the dynamic of bentonite erosion, which may occur during periods of glaciation [8]. Na-exchanged, Na-Ca-exchanged, Ca-exchanged and raw bentonite were studied, which cover different potential materials used for backfill and different stages of cation loading via cation exchange processes upon contact with groundwater of different composition. To this end, erosion experiments were carried out with highly compacted bentonite confined by a porous filter (20 μm) under dynamic conditions simulating the presence of a hydraulically active fracture filled with fault gouge and fracture filling minerals (Figure 1).

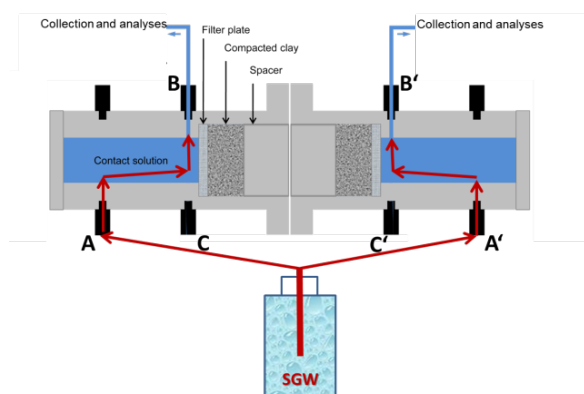


Fig.1: Scheme of a double-side reactor used for the erosion experiments with a synthetic ground water (SGW) [7].

The < 500 μm size fractions of untreated MX80 bentonite and after Na- or Ca-homoionization, were used. Two compacted clay pellets ($1.6 \pm 0.1 \text{ g/cm}^3$) of identical composition were placed in separate compartments of double-side reactors. Post-mortem visual inspection and the observed washout of water soluble MX80 components indicated full equilibration of the bentonite with simulated groundwater taking place during the experiment. The erosion was investigated by circulating a low ionic strength ($1.6 \cdot 10^{-3} \text{ M}$) water at pH 8.4. Bentonite swelling was confined by stainless steel filter plates.

The erosion (clay colloid detachment) via a low mineralized groundwater flow was quantified by determining an average eluted mass loss rate (AMLR). AMLR values integrated over 1466 days (4 years) erosion time for the raw MX80 bentonite, the Na-MX80 and the Na-Ca-MX80 are at $0.019 \pm 0.003 \text{ kg/y/m}^2$, $0.245 \pm 0.007 \text{ kg/y/m}^2$ and $0.10 \pm 0.02 \text{ kg/y/m}^2$, respectively. Only by the sensitive ICP-MS analysis of clay-bound Th and U a tiny detachment of particles from Ca-MX80 could be identified, which shows the highest resistivity against erosion ($0.004 \pm 0.002 \text{ kg/y/m}^2$). The experiments pointed to the swelling pressure as main driving force for colloid generation. A possible inhibiting effect of accessory minerals on erosion can also be deduced

from this study. Assuming erosion via a groundwater flow from a single fracture intersecting a deposition hole filled with raw MX80 bentonite at an angle of 90° and with a fracture aperture of up to 200 μm , the present estimations indicated that under the given scenario the mass loss limit of 1200 kg bentonite will not be reached during the first 10^6 years.

New experiments are on-going to examine in more details the role eventually played by the accessory minerals naturally present in the bentonite clay.

On our new LC-OCD-UVD-OND coupled to our new iCAP-ICPMS.

The LC-OCD-UVD-OND (Figure 2, right) is a liquid chromatography setup coupled on-line to an organic carbon detector (OCD), a UV-Vis detector (UVD) and an organic nitrogen detector (OND). This method is established for years [9] and with it, the pool of NOM is separated into major fractions of different sizes and chemical functions. It allows the identification of the class of compounds (biopolymers, humic substances (HS), low molecular weight compounds...) and the quantification of the (in)organically bound (e.g to biopolymer or HS, colloids or nanoparticles...) and of the inorganic (ammonium, nitrite, urea) nitrogen.



Fig.2: The hyphenated LC-OCD-UVD-OND equipment based on the liquid chromatography principle coupled to our new iCAP-ICPMS detector (KIT-INE, Status July 2021).

In brief (see www.doc-labor.de for all details), the first detector after chromatographic separation (column: 250 mm x 20 mm, TSK HW 50S) is the UV detector (UVD type S-200, Knauer, Berlin, Germany), non-destructive, measuring at a fixed wavelength (presently 225 nm). Afterwards the carbonates present initially in the solution are transformed into carbonic acid by acidification and then removed. The carbon detection is achieved by the use of a Grantzel thin-film reactor based on UV oxidation. For nitrogen detection, a side stream is diverted after UVD and enters a helical, fused silica capillary comprising an UV-emitting lamp. Organically and inorganically bound nitrogen are converted into nitrate while primary nitrate remains unaltered. Nitrate absorbs strongly in the deep UV-range. It

is detected at 220 nm by another UV detector (K-2001, Knauer, Berlin, Germany), named the OND. For data acquisition and data processing, a customized software program is used (ChromCalc, DOC - LABOR, Karlsruhe, Germany). The amount of samples injected may vary from 0.5 mL up to 6 mL at once. An on-line filtration at 450 nm is systematically done before each sample injection into the column. Measurements are usually done 3 to 6 times successively thanks to the use of an auto-sampler. The reported detection limit (LOD) lies in the range 0.5-50 $\mu\text{gC/L}$ (ppb), according to the compound analyzed. The use in parallel of an OCD and a UVD allows to determine the specific UV absorption (SUVA) of the fraction(s) analyzed at the wavelength selected (225 or 254 nm). The SUVA value is considered as a measure of the aromaticity of the fraction under interest considering that the response in the UVD reflects the presence of aromatic and unsaturated structures.

The additional coupling to an Inductively Coupled Plasma Mass Spectrometer (ICP-MS) allows the detection of the inorganic elements associated to the individual compounds (fractions), at trace levels. To the best of our knowledge, the hyphenation proposed nowadays at INE (Figure 2) is unique.

As requested by the ONDRAF/NIRAS agency, we are characterizing the natural organic matter (OM) present in Boom Clay pore water (BCPW). The BCPW were collected in the HADES underground laboratory (Mol, Belgium) from various piezometers, at different depths, in October 2019 (before COVID-19 events). Exemplarily here, we present (Figure 3) the mean LC-OCD-UVD-OND chromatograms obtained after three successive injections of each BCPW.

The chromatograms are very reproducible and strongly correlated. The first peak at 7' is the bypass peak (column by-passed). The working range of the LC column lies between 26' and 65'. It is calibrated 1) in molecular weight (MW) and in size via the use of humic substances (HS) standards from the International Humic Substances Society (IHSS, Saint Paul, USA) and polystyrene sulfonate sodium salts standards (Na-PSS, Polymer, Mainz, Germany); 2) in C and N concentration with potassium phthalate and nitrate solutions.

As calculated with the Chromcal software, the total NPOC content varies between the two BCPW (Table 1).

	NPOC _{TOT} (mgC/L)	NPOC _{HS} (mgC/L)	SUVA _{HS} (@ 225 nm)	DON _{HS} ($\mu\text{gN/L}$)
EGBS	87 ± 1	47 ± 3	6.2 ± 0.3	94 ± 1
SPRING	57 ± 1	36 ± 1	5.9 ± 0.3	80 ± 1

Table 1: Some results accessible after LC-OCD-UVD-OND analysis

Both BCPW contain HS-like fraction, i.e. eluted between 35' and 45' with a clear correlation between the OCD and the UVD signals. This fraction is rather similar from one BCPW to the other. It is below 3 kDa according to the calibration of the column. Interestingly it represents 65-70% of the total NPOC in SPRING and

50-55% of the total NPOC in EGBS (Table 1), in agreement with additional ultrafiltration results (data not shown). Nitrogen is clearly present on the HS-like fraction as seen by the good correlation between the OC and ON chromatograms. A similar N/C ratio is reported for the HS-like fractions present in SPRING or EGBS. The detection of an UV peak at the exclusion limit (~26') only in the case of the EGBS BCPW indicates the presence of bigger-sized particles like some inorganic colloids. A common OCD and UVD peak occurring at 53' indicates the presence of LMW compounds frequently observed in the presence of OM. It might reveal the occurrence of degradation products. This is plausible after a long storage time (more than 18 months) and consistent with the presence of OND peaks at ~80' and 87' corresponding to the elution of urea and ammonium.

The present equipment identifies and confirms [3] some singularities between the two BCPW. This has consequences on the radioelement migration statement in the BC formation as the BCPW are sampled at different depths. On-going activities concentrate on the Nb and Pa interaction and distribution with the BCOM.

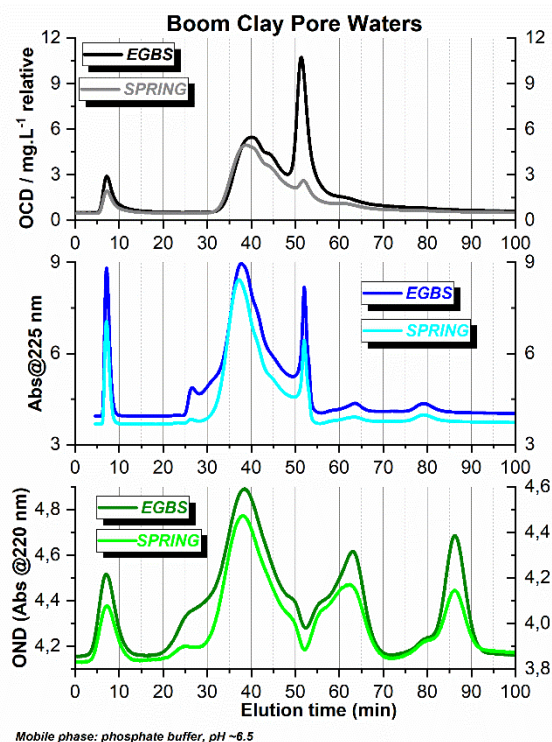


Fig.3: LC-OCD-OND-UVD chromatograms obtained for EGBS and SPRING BCPW, mean of 3 successive injections of 1 mL, dilution by 20 in NaHCO₃ 15 mM.

References

- [1] Geckeis, H., *Geological Society Special Publication*, **236**, 529-543, (2004)
- [2] Schäfer, Th. et al., *Appl. Geochem.*, **27**, 390-403, (2012)
- [3] Kaplan, U. et al., *KIT-Report*, 20004085, Karlsruhe Institute of Technology, Karlsruhe, (2018)
- [4] Thumm, A.K. *M.Sc. thesis*, Karlsruhe Institute of Technology, Karlsruhe, (2020)
- [5] Hassan Loni, Y. et al. *Spectrochimica Acta Part B*, **161**, 105709 (2019)

- [6] Martin, A. et al., *Chemosphere* **279**, 130526, (2021)
- [7] Bouby, M. et al., *App. Clay Sci.*, **198**, 105797 (2020)
- [8] SKB, *Main report of the SRSite project*. Updated 2012-12. Technical Report TR-11-01, Svensk Kärnbränslehantering AB, Stockholm (2011)
- [9] Huber, S.A. et al. *Wat.Res.*, *45*, 879-885, (2011)

5.4 Diffusion

D. Glückman, H. Geckeis, C. Joseph, S. Kraft, V. Metz, M. Plaschke, F. Quinto

In co-operation with:

I. Blechschmidt^a, T. Schäfer^b,

^aNAGRA (National Cooperative for the Disposal of Radioactive Waste), Wettingen, Switzerland; ^bFriedrich-Schiller-University (FSU), Institute for Geosciences (IGW), Applied Geology, Jena, Germany

Introduction

At KIT-INE, laboratory experiments with radiotracers and clays / clay rocks are conducted in order to determine diffusion parameters of safety-relevant radionuclides under a wide range of conditions. This applied research delivers transport parameters which contribute to safety assessment studies for nuclear waste repositories in argillaceous or crystalline host rocks. Additionally, fundamental processes underlying the interaction of ions with the porous material during diffusion are investigated.

Since July 2018, the Helmholtz Association is full partner of the underground rock laboratory (URL) in Mont Terri, Switzerland, in connection with the *Integrity of Nuclear Waste Repository Systems – Cross-Scale System Understanding and Analysis (iCROSS)* collaborative project. In addition, INE collaborates with international partners on field-scale diffusion experiments (DR-C) as well as initiated its own *in situ* diffusion experiment (DR-D) at the Mont Terri URL. One of the laboratory scale diffusion experiments is described in the next section.

Furthermore, INE contributes since 20 years to the research at the Grimsel Test Site (GTS), the URL located in the granodiorite rock of the Aar Massif in Switzerland and managed by NAGRA. As a partner of the international consortium of the CFM Project, INE is involved in the latest *in situ* radionuclide tracer test carried out at the GTS, the Long-term-In-situ-Test (LIT) to investigate diffusion of radionuclide tracers through compacted bentonite and their consecutive migration through water-conductive fissures and fractures in granodiorite rock. The breakthrough of the radionuclide tracers in the frame of the *in situ* LIT experiment is presented in the next section.

The results are also exchanged with other scientists working in the field of clay diffusion and transport in crystalline rocks in the EU Horizon 2020 project EURAD, work package *FUTURE* (Fundamental understanding of radionuclide retention).

Diffusion of U(VI) and Am(III) through Opalinus Clay studied down to ultra-trace levels

Laboratory scale in-diffusion experiments were conducted with samples of the shaly facies of Opalinus Clay (OPA; borehole BLT-14, drilled parallel to bedding), obtained from the Mont Terri URL. Two cylindrical OPA samples (length: 10 mm, diameter: 6 mm, Fig. 1), embedded in poly(methyl methacrylate) (PMMA) sample holders with epoxy resin and equilibrated with synthetic pore water [1] ($I = 0.22$ mol/L,

pH = 7.24) were immersed until 2 mm depth into a diffusion reservoir containing 400 mL of pore water spiked with $^{233}\text{U(VI)}$ and $^{243}\text{Am(III)}$ (5×10^{-9} mol/L, each). The diffusion reservoir was equilibrated with the spiked pore water for 56 days prior to the start of the diffusion experiment.

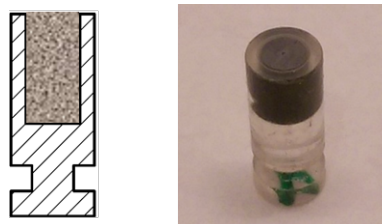


Fig. 1. Each cylindrical OPA sample was embedded in a PMMA sample holder using epoxy resin (EPOFIX, Struers). Illustration (left), photograph (right).

The first sample was removed after 126 d of diffusion and segmented into thin layers of 20–400 μm using abrasive peeling [2] proceeding backward to the direction of the proximal sample extremity immersed in the reservoir. The analysis of the segments indicated unexpectedly high actinide concentrations in the individual layers, especially for longer diffusion distances into the distal direction. Therefore, the processing procedure for the second OPA sample taken after 240 d was adjusted: prior to the segmentation, the external surface of the PMMA sample holder was removed to a depth of approximately 100 μm . This was necessary in order to prevent cross-contamination of the segmented layers by actinides sorbed on or incorporated into the PMMA. Furthermore, core segments were drilled from 3700 to 5500 μm depth with two corresponding rim segments (Fig. 2, dark and light blue segments, respectively) and from 5500 to 8220 μm with two corresponding rim segments (Fig. 2, red and purple segments, respectively). This allowed for the investigation of potential preferential pathways in the rim of the OPA sample. For sample depth ranges 0–3700 μm and 8220–8600 μm , the full segments were abraded (Fig. 2, green segments; Fig. 3, orange segments). Due to the expected ultra-trace concentration of ^{233}U and ^{243}Am in the clay segments, analysis was carried out with accelerator mass spectrometry (AMS) [3]. Details of the AMS analysis are given in sub-chapter 8.5.

Fig. 2 shows the concentration profile of $^{233}\text{U(VI)}$ determined down to 10^{-9} mol/m³ of clay and a distance of 8600 μm . Core and rim segments followed the general trend of decreasing ^{233}U concentrations with diffusion depth in the fully abraded segments, suggesting that no

preferential pathways along the rim of the OPA sample occurred. The parameters distribution coefficient, K_d , and effective diffusion coefficient, D_e , were obtained by fitting the concentration profile with COMSOL

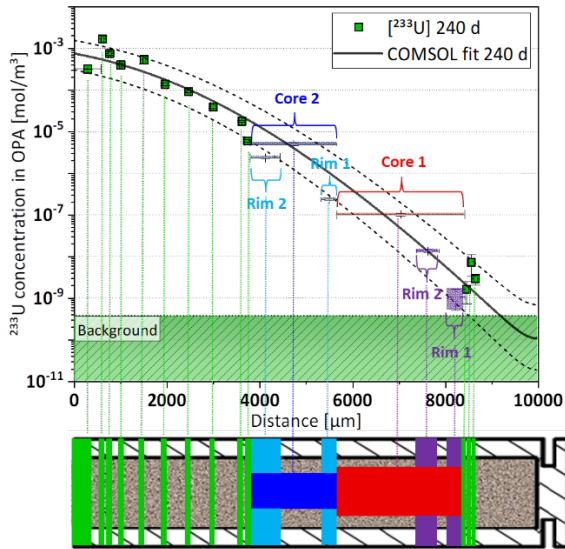


Fig. 2 Concentration profile of $^{233}\text{U(VI)}$ in OPA obtained with AMS after 240 d, comprising fully abraded segments (green), core segments (dark blue & red), and rim segments (light blue and purple).

Multiphysics (v. 5.6) and amounted to $K_d = 0.105 (+0.111/-0.065) \text{ m}^3/\text{kg}$; $D_e = 1.6 (+2.0/-1.1) \times 10^{-11} \text{ m}^2/\text{s}$. Joseph et al., (2013) reported a K_d of $0.025 \pm 0.003 \text{ m}^3/\text{kg}$ and a D_e of $1.9 \pm 0.4 \times 10^{-12} \text{ m}^2/\text{s}$ for U(VI) diffusing perpendicular to the bedding through shaly facies of OPA (BLT-14) [4]. Diffusion perpendicular to the bedding is known to be slower than parallel to the bedding with an anisotropy factor of 4–6 for HTO, Cl^- and Na^+ [5]. In the present study, this factor can be confirmed also for U(VI). The difference in K_d values can be explained by differences in the experimental setup (through-diffusion [4] vs. in-diffusion). Joseph et al., [4] applied a confining pressure of 5 MPa, while in the present study no confining pressure was applied which could have caused higher diffusion-accessible porosities.

For $^{243}\text{Am(III)}$, the concentration profile was determined down to ca. 10^{-6} mol/m^3 and a distance of about $4000 \mu\text{m}$ (Fig. 3). For longer distances, the determined ^{243}Am concentrations were consistent with the background (ca. $3 \times 10^{-7} \text{ mol/m}^3$). The profile of $^{243}\text{Am(III)}$ is featured by two different sections. The first section (about 0–1000 μm diffusion depth) exhibits a strong decrease in ^{243}Am concentration, while in the second section (about 1500–4000 μm), the concentration decrease is less distinct. There is currently no explanation for this “fast-runner” profile. However, such a diffusion behavior was also observed for Eu(III) diffusion in OPA [6]. For the first section of the profile, a K_d of $100 \pm 30 \text{ m}^3/\text{kg}$ was determined, which was fairly in agreement with literature data ($60 \text{ m}^3/\text{kg}$ [6]; $63 \text{ m}^3/\text{kg}$ [7]). The determined D_e value was equal to $2.4 (+2.1/-1.1) \times 10^{-10} \text{ m}^2/\text{s}$. With K_d and D_e , the apparent diffusion coefficient, D_a , can be calculated. It amounts

to $1 \times 10^{-15} \text{ m}^2/\text{s}$ for Am(III) diffusion parallel to the bedding through OPA. This is more than one order of magnitude higher than D_a for Eu(III) of $3.5 \times 10^{-16} \text{ m}^2/\text{s}$ diffusion through OPA [6] determined assuming a density of 2400 kg/m^3 and a porosity of 0.15. The actual D_a is however lower than D_a for Am(III) of $1.7 \times 10^{-14} \text{ m}^2/\text{s}$ diffusing through a sand-bentonite mixture [8]. This can be attributed to the lower density of the mixture with 1600 kg/m^3 compared to OPA with around 2400 kg/m^3 and differences in the main diffusing species, $[\text{Am}(\text{CO}_3)]^+$ in the present study vs. $[\text{Am}(\text{CO}_3)_3]^{3-}$ [8].

At next, diffusion experiments will be conducted for 20 to 60 d, in order to identify the nature of the “fast-runner” profile.

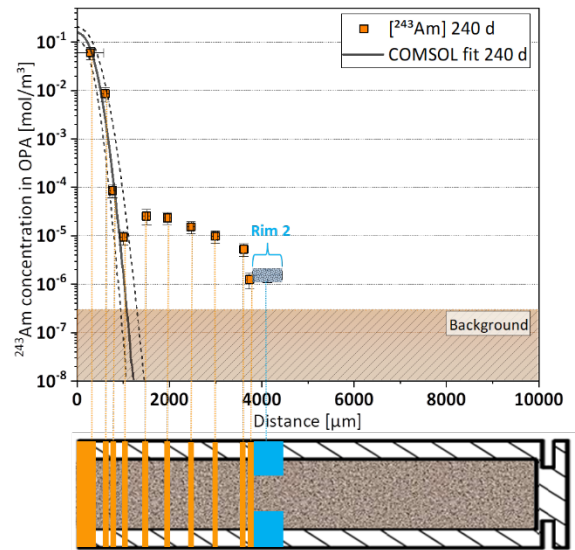


Fig. 3 Concentration profile of $^{243}\text{Am(III)}$ in OPA obtained with AMS after 240 d, comprising fully abraded segments (orange) and rim segment (light blue).

Breakthrough of ^{99}Tc and actinide tracers from the *in situ* LIT experiment

The LIT experiment consisted in a packer-system containing 16 Febex bentonite rings - four of them spiked with radionuclide tracers - emplaced in the crystalline rock intersecting a water-conducting shear zone at the Grimsel Test Site (GTS) [9]. The saturation of the bentonite with the Grimsel groundwater (GGW) from the shear zone, its consequent swelling with possible release of bentonite colloids and the diffusion of radionuclides through the bentonite followed by their transport/retention through the shear zone under advective conditions were investigated for a duration of 4.5 years.

Water samples were collected from two near field boreholes (5.6 cm from the bentonite source). In these samples, composed by bentonite porewater mixing with GGW from the shear zone, the concentration of the radioactive tracers ^{99}Tc , ^{233}U , ^{237}Np and ^{242}Pu , as well as that of the conservative fluorescent tracer Amino-G was analyzed. These radionuclides are strongly or relatively strongly sorbing elements from which a slow diffusion through bentonite is expected

and therefore ultra-trace levels in the LIT-GGW samples. Such analytical challenge was faced with AMS (as described in chapter 8.5 of this report) that provides extremely high sensitivity for ^{99}Tc [10] and actinide nuclides [3]. A further challenge consisted in the possible background of the shear zone from previous *in situ* radionuclide tracer tests [3, 11]. In order to estimate such shear zone background and identify radionuclides originating from the LIT, an analysis of the radionuclides originating from previous *in situ* radionuclide tracer tests was undertaken in GGW samples collected before the emplacement of LIT and from the tailing of the tests in 2012 and 2013 [3].

For both ^{233}U (Fig. 4) and ^{237}Np the highest breakthrough is observed in the early part of the experiment with concentrations above the estimated shear zone background within 600 days for ^{233}U and 300 days for ^{237}Np . Later, the concentration of ^{233}U decreases down to more than 3 orders of magnitude at the end of the experiment with values below the estimated range of shear zone background, whereas the concentration of ^{237}Np decreases by 2 orders of magnitude with values mostly consistent with the background. It is important to note that the signal of the conservative tracer was detected already after 20 days and reached the maximum between 400 and 750 days (indicated by the blue box in Fig. 4 and 5), and afterwards decreased by 60% due to the increase of the extraction rate of the water samples from 20 to 50 $\mu\text{l}/\text{min}$ (indicated by the purple star in Fig. 4 and 5). However, the decrease in the concentration of ^{233}U and ^{237}Np is much higher than 60% and cannot be explained with a dilution effect due to the mixing of bentonite porewater with a higher volume of GGW.

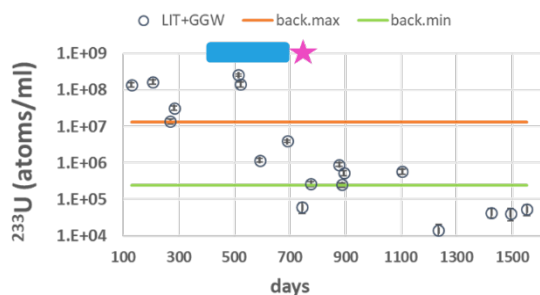


Fig. 4 Concentration of ^{233}U in LIT-GGW water samples. The horizontal lines indicate the maximum (orange) and minimum (green) of the estimated shear zone background. The blue box represents the maximum of the conservative tracer and the purple star the increase of the extraction rate of the water samples (see text).

Concentrations of ^{242}Pu had a different trend and were since the beginning mostly consistent with the shear zone background, with only a few data significantly higher especially at 900 days.

The breakthrough of ^{99}Tc (Fig. 5) was always above the estimated shear zone background with a maximum concentration at 200 days followed by a decrease down to 2 orders of magnitude towards the end, also in this case not explainable only with a dilution effect due to the increase of the extraction rate. Since all the ^{99}Tc data were above the estimated shear zone background

it is possible to estimate for ^{99}Tc the total number of atoms released from LIT during the test by summing up the number of atoms in the volume of the water samples collected between two consecutive experimental data. In this way, a possible release of ^{99}Tc from LIT equal to ca. 4×10^{12} ^{99}Tc atoms is estimated within the experimental time frame of 4.5 years and accounting for ca. 8.5×10^{-3} % of the inventory of ^{99}Tc in LIT.

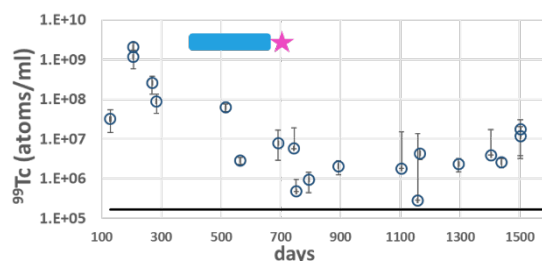


Fig. 5 Concentration of ^{99}Tc in LIT-GGW water samples. The horizontal line indicates the maximum of the estimated shear zone background. The blue box represents the maximum of the conservative tracer and the purple star the increase of the extraction rate of the water samples (see text).

While the obtained results suggest that ^{242}Pu release from the bentonite could not be detected above shear zone background, an unexpected early appearance of most of the radionuclide tracers - according to screening calculations with the transport code CLAYPOS [9] - was observed and cannot be interpreted as diffusion through the bentonite, except for Tc(VII) and Np(V).

Forthcoming research will focus on the post-mortem analysis of LIT (introduced in sub-chapter 5.2) that will allow for the investigation of the diffusion profiles of the radionuclide tracers through the bentonite, providing valuable experimental observation for the performance assessment of a bentonite engineered barrier system over the time span of 4.5 years.

References

- [1] T. Gimmi et al., *Geochim. Cosmochim. Acta* 2014, **125**, 373.
- [2] L. R. Van Loon, W. Müller., *Appl. Radiat. Isot.*, 2014, **90**, 197.
- [3] F. Quinto et al., *Anal. Chem.*, 2017, **89**, 7182.
- [4] C. Joseph et al., *Geochim. Cosmochim. Acta*, 2013, **109**, 74.
- [5] L. R. Van Loon et al., *Environ. Sci. Technol.*, 2004, **38**, 5721.
- [6] PSI Progress Report 2019; Laboratory for Waste Management (LES), Paul Scherrer Institut: Villigen-PSI, 2020.
- [7] M. H. Bradbury, B. Baeyens, PSI Technical Report 03-08, Paul Scherrer Institut, Villigen-PSI, 2003.
- [8] T. Sawaguchi, et al., *Clay Miner.*, 2013, **48**, 411.
- [9] Kollorado-e2 Final Report, KIT publications, 2019.
- [10] F. Quinto et al., *Anal. Chem.*, 2019, **91**, 4585.
- [11] H. Geckeis et al., *Radiochim. Acta*, 2004, **92**, 765

5.5 Reactive transport modelling

M.C. Chaparro, N. Finck, V. Metz, H. Geckeis

Introduction

The geological disposal in deep bedrock repositories is the preferred option for the management of high-level radioactive waste. In some of these multi-barrier concepts for argillaceous and crystalline host rocks, carbon steel is considered as potential canister material and bentonites are planned as backfill material to protect the canisters. Groundwater will saturate the bentonite, thus, reactive transport processes such as diffusion due to chemical gradients, mineral dissolution/precipitation and adsorption will occur, altering therefore the bentonite and the canister. Hence, deep understanding of reactive transport processes that will occur during the long-term disposal of the high-level radioactive waste disposal is imperative in order to proof the long-term safety of the final disposal system. To do so, reactive transport models have been performed in order to study canister-bentonite interactions at repository scale [1] and magnetite-montmorillonite interactions at laboratory scale.

The reactive transport modelling activities developed at KIT-INE during 2020-21 are in the framework of the collaborative *Integrity of Nuclear Waste Repository Systems – Cross-Scale System Understanding and Analysis* (iCROSS) project.

Modelling of long-term iron-bentonite interactions at repository-scale

The objective of this study is to better understand the reactive transport processes that will occur in the course of long-term iron-bentonite interactions in a (geo-)technical barrier sub-system of a repository in an argillaceous or crystalline host rock. Due to the lack of long-term experimental data, our results are compared with other published numerical studies on iron-clay / bentonite interaction [2,3,4].

The simulations were carried out using Retraso-CodeBright [5]. Our conceptual model considers a cylindrical carbon steel canister surrounded by bentonite (Figure 1). It assumes that the bentonite is fully water-saturated and the heat pulse of the high-level waste is already dissipated, therefore anaerobic conditions at a constant temperature of 25°C are considered. The model accounts for diffusion as transport mechanism, steel corrosion, aqueous complexation reactions, mineral dissolution/precipitation and cation exchange reactions. The mineral composition of the bentonite MX-80 and the volumetric fractions of each mineral were based on those reported in literature [6]. The primary phases considered are montmorillonite, quartz, muscovite, albite, illite, pyrite and calcite. We assume that carbon steel is composed only of iron, which is the main phase of carbon steel. Reported corrosion products that were found experimentally [7,8,9] are considered as potential secondary phases, consisting of

magnetite, greenatite, cronstedtite, Na-exchanged nontronite endmember, Mg-exchanged nontronite endmember and siderite. The initial porewater used in the numerical model corresponds to a clay groundwater [8] equilibrated with montmorillonite, because it is the main phase of the bentonite. The thermodynamic data is taken from the Geochemist's Workbench database thermo.com.V8.R6.full (generated by GEM-

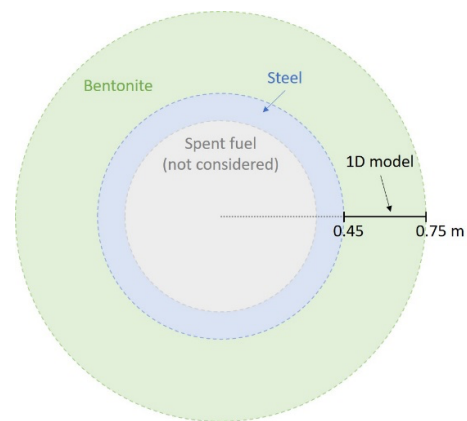


Fig. 1: Geometry and materials of the 1D radial model. The axisymmetric model only considers the steel-bentonite interface, at $X=0.45$ m, and a thickness of 0.3 m of bentonite (from $x=0.45$ to $x=0.75$ m).

BOCHS.V2-Jewel.src.R6) [10]. The kinetic data is the same used in other reported modelling works [2,3,4]. We consider a constant corrosion rate of 2 $\mu\text{m}/\text{year}$.

The numerical model results show that during the first 100 years, the Fe concentration in the porewater increases due to iron dissolution (Figure 2a). However, Fe is partly adsorbed by the montmorillonite and partly consumed by the secondary phases (e.g. nontronite). After 1000 years it decreases considerably in the porewater (below $1.6 \times 10^{-9} \text{ mol L}^{-1}$) because it is mainly consumed by the formation of secondary phases (e.g. magnetite, nontronite and greenalite) rather being adsorbed. The Si concentration increases in the short-term due to dissolution of bentonite, in the long-term it decreases because of the relatively rapid precipitation rate for Fe-silicates and the slow dissolution rate of montmorillonite. The Ca and HCO_3^- concentration decrease with time due to calcite precipitation. The pH of the porewater increases progressively from 7.5 to 10.9 because the dissolution of iron and bentonite minerals (such as montmorillonite and feldspar) consume protons (Figure 2b). This increase in pH has also been reported by other modellers [e.g. 1]. The model predicts dissolution of bentonite minerals that dissolve because the increase in pH makes the aluminosilicate unstable. Montmorillonite dissolution releases Ca yielding calcite precipitation, however, especially in the first 100 years, Ca in the montmorillonite interlayer can also be

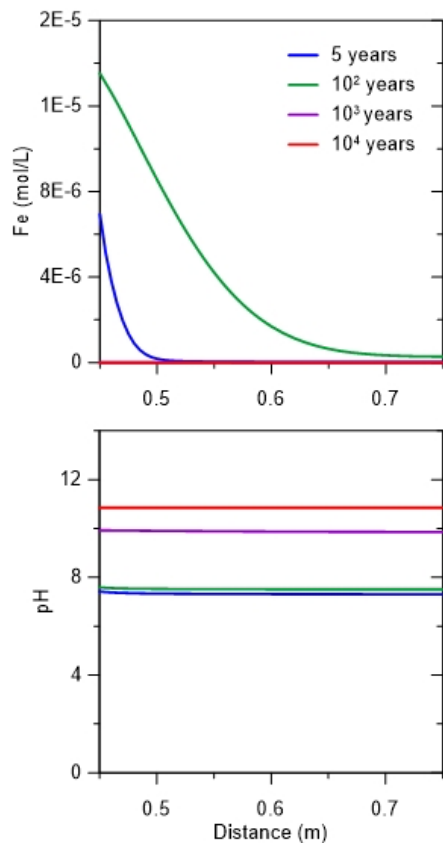


Fig. 2: Fe concentration and pH versus distance. Model results after 5, 100, 1000 and 10000 years are compared.

exchanged by Fe and thereby likewise induce calcite precipitation. Dissolution of the primary phases of the bentonite as well as precipitation of calcite are more important after 10000 years when the pH is higher. The corrosion products predicted by the numerical model are nontronite, magnetite and greenalite (Figure 3). After 5 years, especially Mg-nontronite but also Na-nontronite precipitate (2.5×10^{-5} and $3.8 \times 10^{-6} \text{ m}^3 \text{ m}^{-3}$ respectively) because there is available Fe and Si in the porewater due to iron and bentonite dissolution respectively. Magnetite starts precipitating after 100 years when enough Fe is available in the porewater. After 1000 years, Mg-nontronite ($5.8 \times 10^{-4} \text{ m}^3 \text{ m}^{-3}$) and magnetite are the principal corrosion products of the system. However, after 10000 years, magnetite and nontronite dissolve, then, Fe and Si are consumed by precipitation of greenalite, which is the main corrosion product after 10000 years. The secondary phases (nontronite, magnetite and greenalite) precipitate quite close to the iron-bentonite interface, and calcite also precipitates along the first 5 cm. The numerical model does predict neither precipitation of cronstedtite nor that of siderite. Precipitation of magnetite, calcite and greenalite has been recently found in the Iron Corrosion in Bentonite (IC-A) experiment in the Mont-Terri laboratory (Switzerland) [9], which supports our numerical results. Other experiments reported in literature [7,8], which were performed at 90°C with Callovo-Oxfordian clay, also found precipitation of siderite and cronstedtite. Thus, the temperature, bentonite and

porewater compositions could have a significant impact on the nature of formed corrosion products. In general, the model does not predict important changes in porosity, being unnoticeable after 5 years. At the end of the calculations, after 10000 years, there is a decrease in porosity right after the interface due to precipitation of greenalite, followed by an increase of porosity due to dissolution of montmorillonite. Dissolution of montmorillonite and precipitation of greenalite take place at the same time, both with similar pore volumes, therefore, not much changes on porosity are predicted.

A sensitivity analysis has also been performed to study the effect of selected parameters, such as corrosion rate, diffusion coefficient and composition of the porewater, on the corrosion products. Results from the sensitivity analysis show that larger corrosion rate would provoke a rapid precipitation of the greenalite due to the rapid Si supply from the dissolution of bentonite. On the contrary, when a lower corrosion rate is considered, the model predicts lower dissolution of bentonite, hence only nontronite and magnetite precipitate. When a larger diffusion coefficient is considered, the transport dominates, therefore, a larger thickness of the alteration is predicted, but with less mineral dissolution / precipitation. The composition of the porewater can affect the secondary phases forming during the iron-bentonite interaction, Fe-silicates being more relevant rather than magnetite.

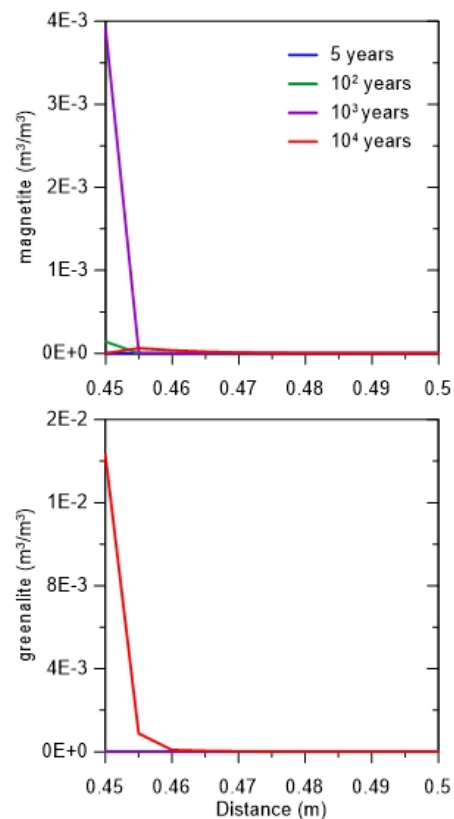


Fig. 3: Volumetric fraction of magnetite and greenalite against distance. The interface between steel and bentonite is at 0.45 m. Results after 5, 100, 1000 and 10000 years of interaction are plotted.

Overall, outcomes suggest that the predicted main corrosion products on the long-term are Fe-silicates minerals. Such phases thus should deserve further attention as chemical barrier in the diffusion of radionuclides to the repository far field. Our results can differ from other reactive transport calculations reported in literature [2,3,4] because of the assumptions considered in the conceptual model, such as selected secondary phases, considering the canister as porous material or the temperature of the system.

Modelling of short-term magnetite-montmorillonite interactions at lab-scale

The objective of this work is to perform scopus calculations in order to study the design of the diffusion experiments on magnetite-montmorillonite at laboratory scale. To do so, preliminary conservative and reactive transport models have been developed using the CodeBright [11] and the Retraso-CodeBright [5] codes, respectively.

The 1D numerical models consider a thickness of 5 mm of magnetite and 5 mm of montmorillonite. The models assume the same transport parameters for both magnetite and montmorillonite. The pore diffusion coefficient is $1.3 \times 10^{-10} \text{ m}^2 \text{ s}^{-1}$, which was determined by ab-initio calculations in montmorillonite at molecular scale. The porosity considered is 0.4 [3,4]. The models have been performed at 24°C and 85°C in order to study the effect of the temperature on the magnetite / montmorillonite interactions.

Results from the “conservative” transport models show total recovery of the conservative tracer after one week at 85°C, and after one month at 24°C. These values may differ from the reality if the transport parameters are different than the ones considered in the preliminary calculations.

Reactive transport models have been performed in order to study the effect of the solution composition on the magnetite-montmorillonite interactions. The conceptual model accounts for diffusion as transport mechanism, aqueous complexation reactions, mineral dissolution / precipitation, and cation exchange reactions. The potential secondary phases taken into account are Mg-nontronite, Na-nontronite, and cronstedtite. Different scenarios have been studied changing the

Table 1: Solution for each scenario studied.

Scenario	Magnetite	Montmorillonite
1	Water equilibrated with magnetite	Water equilibrated with magnetite
2	Water equilibrated with magnetite and montmorillonite	Water equilibrated with montmorillonite

solution composition at the magnetite side (Table 1).

In scenario 1, at 24°C, results show dissolution of magnetite and montmorillonite, and precipitation of Na-nontronite and Mg-nontronite (Figure 4). The precipitation of the secondary phases take place only at the interface. At, 85°C similar results are obtained, however there is only precipitation of Mg-nontronite. In

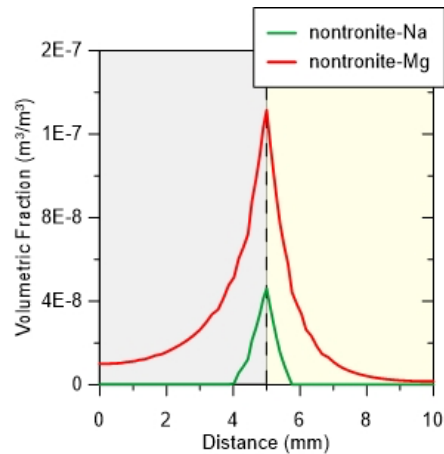


Fig. 4: Volumetric fraction of nontronite versus distance for the model considering the scenario 1 at 24°C after 60 days. The dashed line indicates the interface ($x=5\text{mm}$), the grey colour represents the magnetite (x from 0 to 5 mm) and the yellow one the montmorillonite (x from 5 to 10 mm).

scenario 2, there is dissolution of magnetite at the first node and at the interface, because the Si concentration in the solution makes magnetite unstable. At 24°C, nontronite precipitates not only at the interface but also at the first node. The dissolution of magnetite and precipitation of nontronite at the first node is higher than that at the interface. At 85°C, no precipitation is predicted, there is only dissolution of montmorillonite and magnetite. For all scenarios, and both temperatures, the models do not predict changes in porosity because the interactions with the porewater at the magnetite-montmorillonite interface does not result in extensive mineral alterations within the relatively short time span of 1 year.

References

- [1] M.C. Chaparro et al., *Minerals*, **11**, 1272, p. 1-20 (2021).
- [2] O. Bildstein et al., *Physics and Chemistry of the Earth, Parts A/B/C*, **31**, S306-S316, (2006).
- [3] J.C. Wilson et al., *Applied Geochemistry*, **61**, 10-28, (2015).
- [4] J. Samper et al., *Applied Geochemistry*, **67**, 42-51, (2016).
- [5] M.W. Saaltink et al., *Geologica Acta*, **2**, 235-251, (2004).
- [6] O. Karnland, *Technical Report TR-10-60, SKB*, (2010).
- [7] M.L. Schlegel et al., *Applied Geochemistry*, **23**, 2619-2633, (2008).
- [8] F. Martin et al., *Journal of Nuclear Materials*, **379**, 80-90, (2008).
- [9] N. Morelová et al., V.M. Goldschmidt Conference, *Goldschmidt Virtual*, July 2021, (2021).
- [10] J. Johnson and S. Lundeen, *Technical report, Yucca Mountain Laboratory. Milestone Report M0L72*, Lawrence Livermore National Laboratory, Livermore (1994).
- [11] S. Olivella et al., *Engineering Computations*, **13**, 87-112, (1996).

6 Coordination chemistry

We perform coordination chemistry studies in solution related to actinide separations by solvent extraction. These studies address the interactions and the speciation between actinide ions (and other ions) and ligands potentially useful for separating actinides. A closer look was taken on the complexation of Cm(III) and Eu(III) with diastereomers of a diglycolamide to explain their behaviour as extracting agents. We have also managed to identify a Cm(III)bis-triazinylpyridine complex with a tenfold coordination around the actinide ion in solution. To our knowledge, such has not unambiguously been reported before. Finally, the interaction of diglycolamides' O-donor atoms with Am(III) and several Ln(III) was investigated by NMR (see 8.4).

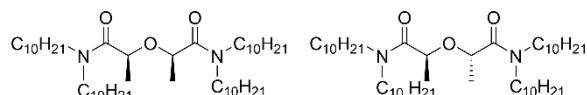
Complexation of Cm(III) and Eu(III) by diastereomeric diglycolamides, 2,2'-oxybis-(N,N-didecylpropanamide)

P. Weßling, M. Trumm, T. Sittel, A. Geist, P. J. Panak

Introduction

The ligand 2,2'-oxybis-(N,N-didecylpropanamide) exists in two diastereomeric forms (Scheme 1), each represented by two enantiomers:

1. *R,S* or *S,R* isomer (*cis*- or *meso*-mTDDGA)
2. *R,R* or *S,S* isomer (*trans*-mTDDGA)



Scheme 1: *cis*-mTDDGA (left) and *trans*-mTDDGA (right).

Both diastereomers extract trivalent actinides and lanthanides [1–2]. However, *cis*-mTDDGA is a stronger extracting agent, see also [1] for the respective 2,2'-oxybis-(N,N-dioctylpropanamide) compounds.

Time-resolved laser fluorescence spectroscopy (TRLFS) was employed to explain the difference. Stability constants for the complexation of Cm(III) and Eu(III) with both diastereomers were determined.

Results

Complexation of Cm(III)

Figure 1 shows the normalized Cm(III) fluorescence emission spectra in 2-propanol containing 5 vol.% H₂O and 10⁻² mol/L HClO₄ at varied *cis*-mTDDGA concentrations.

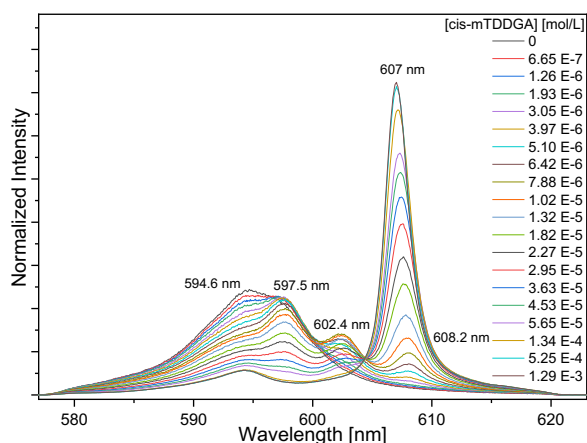


Fig. 1: Normalized Cm(III) fluorescence spectra in 2-propanol containing 5 vol.% H₂O and 10⁻² mol/L HClO₄ at increasing *cis*-mTDDGA concentrations.

The Cm(III) solvent spectrum shows two emission bands at 594.6 nm and 597.5 nm. With increasing *cis*-mTDDGA concentration three new emission bands at 597.5 nm, 602.4 nm and 607.0 nm are observed. These emissions bands are attributed to the [Cm(*cis*-mTDDGA)_n]³⁺ (*n* = 1–3) complexes by comparison other diglycolamide ligands [3–4]. Slope analysis further confirms the stoichiometries. Stability constants for the complexation of Cm(III) with *cis*-mTDDGA are given in Table 1.

The complexation of Cm(III) with *trans*-mTDDGA was studied accordingly. The respective stability constants are also given in Table 1.

Complexation of Eu(III)

Figure 2 shows normalized Eu(III) emissions spectra in 2-propanol containing 5 vol.% H₂O and 10⁻² mol/L HClO₄ as a function of the *cis*-mTDDGA concentration.

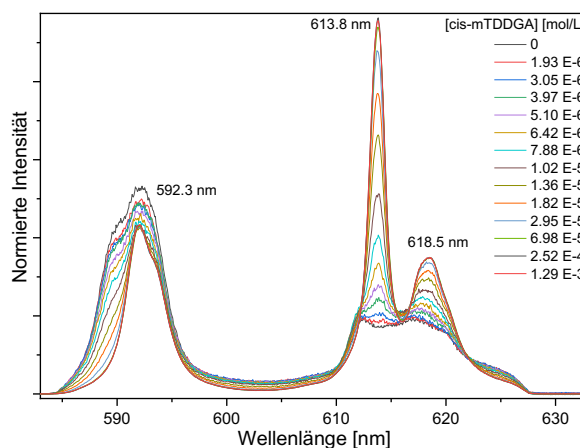


Fig. 2: Normalized Eu(III) fluorescence spectra in 2-propanol containing 5 vol.% H₂O and 10⁻² mol/L HClO₄ at increasing *cis*-mTDDGA concentrations.

In absence of *cis*-mTDDGA the Eu(III) solvent spectrum shows an intense ⁷F₁ and a weak ⁷F₂ emission band. With increasing *cis*-mTDDGA concentration the splitting and the intensity of the ⁷F₂ emission band strongly increases. Similar observations are made for the complexation of Eu(III) with *trans*-mTDDGA. Slope analysis confirms the 1:1 and 1:3 complexes for

both systems. No 1:2 complex is observed. Stability constants are given in Table 1.

In conclusion, *cis*-mTDDGA is the stronger ligand for both Cm(III) and Eu(III).

Table 1: Cm(III) and Eu(III) complex stability constants of *cis*-mTDDGA and *trans*-mTDDGA in 2-propanol containing 5 vol.% H₂O and 10⁻² mol/L HClO₄.

	<i>n</i>	Cm(III)	Eu(III)
<i>cis</i> -mTDDGA	1	5.4 ± 0.2	4.1 ± 0.2
	2	10.2 ± 0.3	–
	3	14.2 ± 0.4	13.7 ± 0.4
<i>trans</i> -mTDDGA	1	4.8 ± 0.2	3.9 ± 0.2
	2	9.5 ± 0.3	–
	3	13.1 ± 0.3	11.9 ± 0.4

Extraction of Cm(III) and Eu(III)

To study the speciation under extraction conditions Cm(III) and Eu(III) were extracted from 5 mol/L HNO₃ with 0.5 mol/L *cis*- or *trans*-mTDDGA in kerosene. The resulting organic phases were investigated by TRLFS. Figure 3 compares the respective emission spectra (“biphasic”) to the spectra of the 1:3 complexes from the titration experiments (“monophasic”).

With *cis*-mTDDGA both Cm(III) and Eu(III) show similar emission spectra in monophasic (blue lines) and biphasic (black lines) systems, confirming extraction as 1:3 complexes. In contrast, significant differences are observed between the monophasic (green lines) and biphasic (red lines) *trans*-mTDDGA systems. Cm(III) is predominantly extracted as the 1:3 complex. The shoulder at 606 nm indicates the presence of a further species, [Cm(*trans*-mTDDGA)₂(NO₃)_{*n*}(H₂O)_{*m*}]^{(3-*n*)+} is also extracted.

To verify the presence of coordinated nitrate, the nitrate concentration is gradually increased in a sample containing the 1:3 complex by addition of tetrabutylammonium nitrate (TBAN) (Figure 4).

Increasing the TBAN concentration leads to a hypsochromic shift of the emission spectrum. At 3.48 × 10⁻³ mol/L TBAN good agreement with the “biphasic”

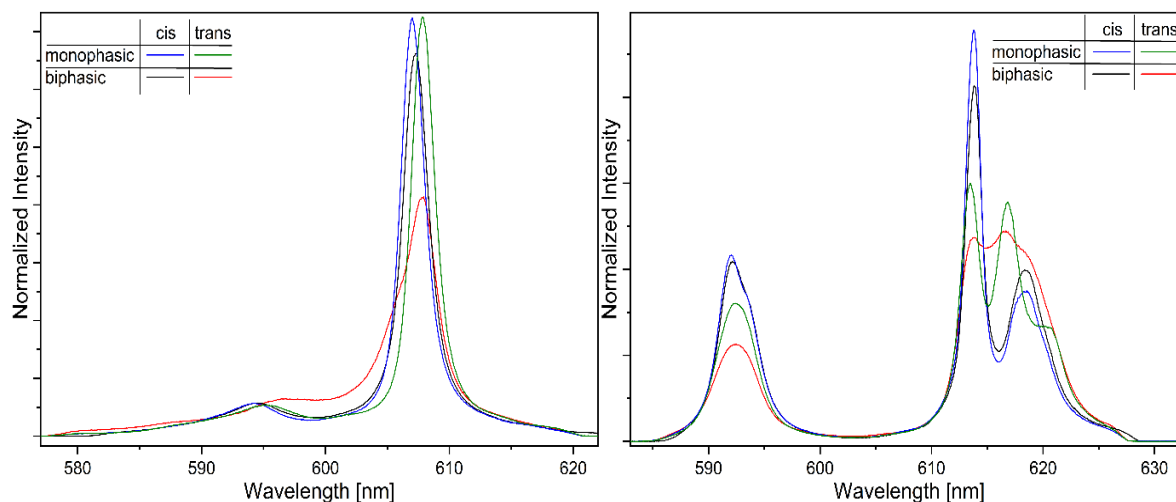


Fig. 3: Comparison of the Cm(III) (left) and Eu(III) (right) spectra of the organic phases after extraction (biphasic) and the emission spectra of the [ML₃]³⁺ complexes (M = Cm, Eu; L = *cis*-/*trans*-mTDDGA) in 2-propanol containing 5 vol.% H₂O and 10⁻² mol/L HClO₄ (monophasic).

spectrum is found, proving the presence of nitrate in the first coordination sphere.

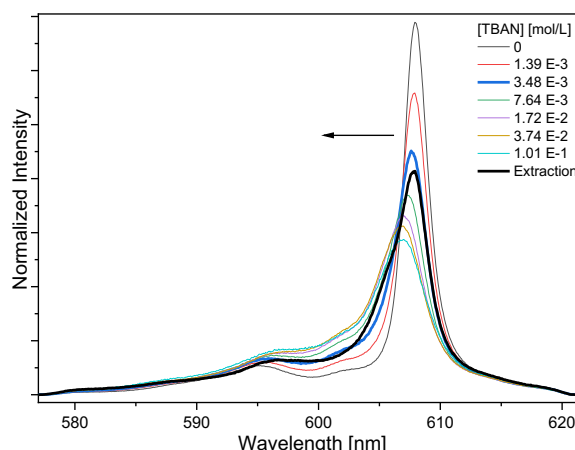


Fig. 4: Normalized Cm(III) fluorescence spectra with 5.73 • 10⁻³ mol/L *trans*-mTDDGA in 2-propanol with 5 Vol.% H₂O and 10⁻² mol/L HClO₄ at increasing TBAN concentration and Cm(III) emission spectrum in the organic phase after extraction with 0.5 mol/L *trans*-mTDDGA from 5 mol/L HNO₃.

DFT calculations of different ternary Cm(III) complexes show the species with a monodentate nitrate and two water molecules, [Cm(*trans*-mTDDGA)₂(κ¹-NO₃)(H₂O)₂]²⁺ to be the most stable species in solution. The number of water molecules is additionally supported by fluorescence lifetime measurements. Finally, the most stable stoichiometry is confirmed by comparing experimental and theoretical vibronic side-band spectra.

Conclusion

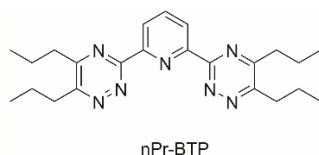
The complexation of Cm(III) and Eu(III) with the diastereomers *cis*- and *trans*-mTDDGA was studied using TRLFS, vibronic-sideband spectroscopy and DFT calculations. The stability constants of the 1:3 complexes with Cm(III) and Eu(III) show *cis*-mTDDGA to be the stronger ligand explaining the inferior extraction performance of the *trans*-isomer.

Trivalent actinide ions with tenfold coordination in solution

P. Weßling, T. Schenk, F. Braun, B. B. Beele, S. Trumm, M. Trumm, B. Schimmelpfennig, D. Schild, A. Geist, P. J. Panak

Introduction

2,6-Bis(5,6-dipropyl-1,2,4-triazin-3-yl)pyridine (nPr-BTP, Scheme 2) is a N-donor ligand known to form 1:3 complexes with trivalent actinides and lanthanides that are coordinated ninefold in solution [5–7].



Scheme 2: 2 nPr-BTP

Although coordination numbers greater 9 are reported for trivalent actinides in solution [8–10], unambiguous evidence has been missing so far.

Solutions of $[\text{An}(\text{nPr-BTP})_3]^{3+}$ (An = Am, Cm) in 2-propanol additionally containing nitrate were studied by time-resolved laser fluorescence spectroscopy (TRLFS), vibronic side-band spectroscopy (VSBS), density functional theory (DFT) and X-ray photo electron spectroscopy (XPS). This gave sound evidence for An(III) species with tenfold coordination in solution.

Results

Figure 5 shows normalized Cm(III) emission spectra with 1.58×10^{-5} mol/L nPr-BTP in 2-propanol as function of time after the addition of 4.03×10^{-5} mol/L tetrabutylammonium nitrate (TBAN).

An emission band at 617.2 nm is observed upon TBAN addition, disappearing within seven days in favour of an emission band at 613.1 nm. While the emission band at 613.1 nm represents the $[\text{Cm}(\text{nPr-BTP})_3]^{3+}$ complex [3], the band at 617.2 nm has not been observed before. Its bathochromic shift is due to a higher ligand field splitting potentially due coordination of a nitrate anion, forming $[\text{Cm}(\text{nPr-BTP})_3(\text{NO}_3)]^{2+}$ with a tenfold coordination.

To study the influence of the water concentration experiments are carried out in 2-propanol with 2.5 vol.% and 5 vol.% H₂O. $[\text{Cm}(\text{nPr-BTP})_3(\text{NO}_3)]^{2+}$ is observed in both systems, however with a bathochromically shifted emission band (2.5 vol.%, $\lambda_{\text{max}} = 616.4$ nm; 5 vol.%, $\lambda_{\text{max}} = 616.3$ nm). The molar fraction of $[\text{Cm}(\text{nPr-BTP})_3(\text{NO}_3)]^{2+}$ is shown in Figure 6 as a function of time after TBAN addition.

Three conclusions are evident:

1. A higher water content favours the formation of $[\text{Cm}(\text{nPr-BTP})_3(\text{NO}_3)]^{2+}$.
2. A higher water content leads to longer kinetics.
3. Different reaction mechanisms are observed with and without water.

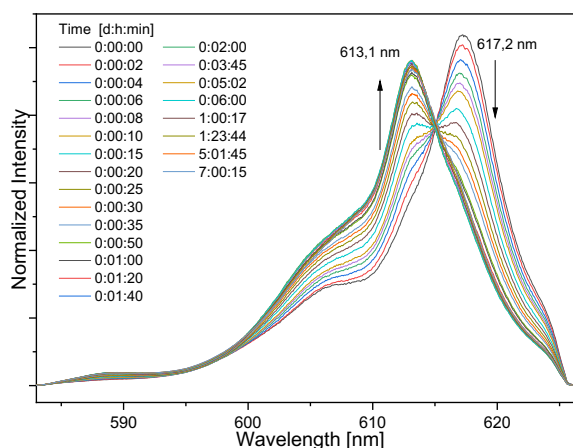


Fig. 5: Normalized Cm(III) fluorescence spectra in 2-propanol as a function of time after TBAN addition. $[\text{nPr-BTP}] = 1.58 \times 10^{-5}$ mol/L, $[\text{TBAN}] = 4.03 \times 10^{-5}$ mol/L.

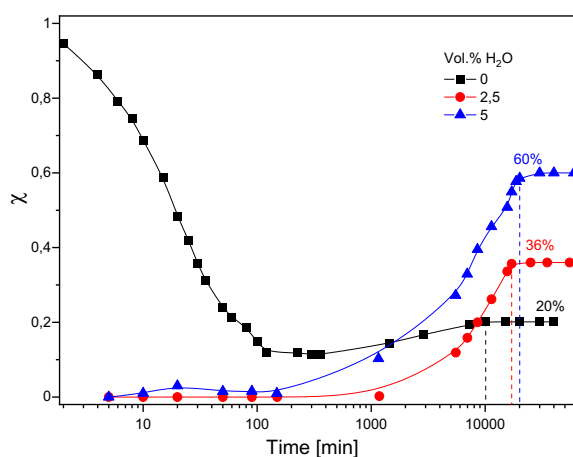


Fig. 6: Molar fraction of $[\text{Cm}(\text{nPr-BTP})_3(\text{NO}_3)]^{2+}$ in 2-propanol with 0, 2.5 and 5 vol.% H₂O as a function of time after TBAN addition. $[\text{nPr-BTP}] = 1.58 \times 10^{-5}$ mol/L.

The influence of the nitrate concentration is studied at a constant nPr-BTP concentration to further verify the formation of $[\text{Cm}(\text{nPr-BTP})_3(\text{NO}_3)]^{2+}$. Figure 7 shows the normalized Cm(III) emission spectra in 2-propanol with 2.5 vol.% H₂O as a function of the TBAN concentration.

A continuous shift of the Cm(III) emission band from 613.1 nm to 616.4 nm is observed with increasing nitrate concentration. Slope analysis (slope = 1.00 ± 0.04) verifies the formation of $[\text{Cm}(\text{nPr-BTP})_3(\text{NO}_3)]^{2+}$.

The nitrate anion seems to play a crucial role in the formation of the tenfold coordinated species as no evidence for such species is found in the presence of other small anions (e. g. NO_2^- , CN^- , OTf^-).

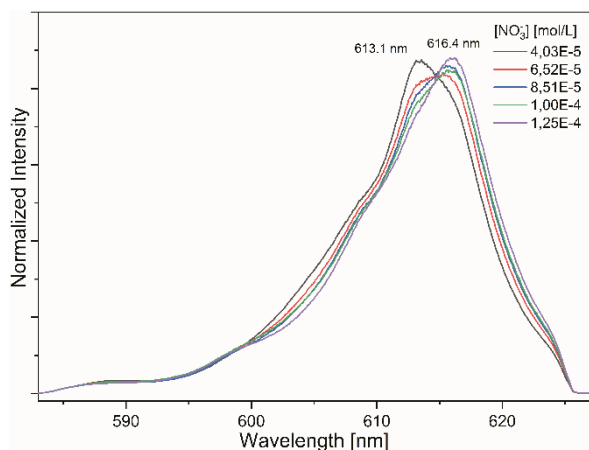


Fig. 7: Normalized Cm(III) fluorescence spectra in 2-propanol with 2.5 vol.% H₂O as a function of TBAN concentration. [nPr-BTP] = 1.58×10^{-5} mol/L.

Moreover, the influence of the nPr-BTP concentration at constant nitrate concentrations is studied. [Cm(nPr-BTP)₃(NO₃)₂]²⁺ is only found at free nPr-BTP concentrations smaller 10^{-4} mol/L. Higher nPr-BTP concentration seem to stabilize the nitrate anion in solution, hindering the formation of the tenfold coordinated species.

Further characterization by fluorescence lifetime measurements, DFT calculations, vibronic side-band spectroscopy (VSBS) and XPS verifies the formation of trivalent actinides with tenfold coordination in solution.

Conclusion

Combining results from TRLFS, VSBS, XPS, and DFT provides sound evidence for a unique tenfold coordinated Cm(III) complex in solution — a novelty in the solution chemistry of trivalent actinides [11].

References

- [1] A. Wilden et al., *Chem. Eur. J.*, **25**, 5507–5513 (2019).
- [2] R. Malmbeck et al., *J. Radioanal. Nucl. Chem.*, **314**, 2531–2538 (2017).
- [3] A. Wilden et al., *Solvent Extr. Ion Exch.*, **32**, 119–137 (2014).
- [4] L. Klab et al., *Solvent Extr. Ion Exch.*, **37**, 297–312 (2019).
- [5] P. J. Panak, A. Geist, *Chem. Rev.*, **113**, 1119–1236 (2013).
- [6] M. A. Denecke et al., *Inorg. Chem.*, **44**, 8418–8425 (2005).
- [7] S. Trumm et al., *Inorg. Chem.*, **19**, 3022–3028 (2010).
- [8] P. Allen et al., *Inorg. Chem.*, **39**, 595–601 (2000).
- [9] G. R. Choppin et al., *J. Alloys Compd.*, **223**, 174–179 (1995).
- [10] W. Runde et al., *J. Alloys Compd.*, **303–304**, 182–190 (2000).
- [11] P. Weßling et al., *Inorg. Chem.*, **59**, 12410–12421 (2020).

7. Deconstruction and decommissioning of conventional and nuclear buildings

Decommissioning of Nuclear Facilities and Power Plants is a multi-discipline mission. It involves a wide spectrum of technical and management tasks associated to terminate the operation of the nuclear installation and its subsequent dismantling. The objective of all steps is to perform them as safe as possible, generate the less possible waste that has to be stored in final storage facilities and finally being able to release the site from regulatory control. The need for a safe and economic decommissioning is worldwide. Due to the German decision to terminate the use of nuclear power in Germany by 2022, the need is more focused than in other countries, but the demand is also a worldwide one. By estimating a 50 years' time life for reactors, the number of nuclear facilities that are reaching their end of life time is increasing in the next second decade (2030 to 2040). This leads to increased awareness and interest among a variety of stakeholders, like decommissioning implementers, industry, operators, regulators, consultants, R&D organisations, universities, standardisation organisations, international organisations, waste management companies, and others. They all are in need to adopt adequate arrangements for implementing decommissioning programs globally and finding the solutions mutually.

7.1 Development of the department of deconstruction and decommissioning of conventional and nuclear buildings

S. Müller, N. Gabor, S. Gentes

A main goal of TMB's Department of Deconstruction and Decommissioning of Conventional and Nuclear Buildings in the last two years was to intensify targeted cooperation and input from other research and development (R&D) and industry groups nationally and internationally. One aspect for this intensification is the new deconstruction building information modelling (BIM) laboratory with acronym BIM D², planned within the framework of HOVER at the TMB. In order to ensure the laboratories high relevance at the time of its commissioning - several steps were taken: Already at the end of 2020, the new EU project PLEIADES on the topic of 'BIM in Nuclear Facility Deconstruction' was initiated, in which various partners from both industry and R&D are involved.

In 2021, there was also an exchange of several hours between the KIT (ITES, INR, TMB/deconstruction) and the internationally established Framatome GmbH on the topic of BIM. Framatome's potential needs in the area of virtual reality (VR) and BIM were presented, as well as an overview of the competences and research programmes at KIT in the area of "BIM and (partially) automated deconstruction of activated/ contaminated concrete structures". In addition to the work on deepening the promising research focus on BIM in deconstruction, the Department of Deconstruction and Decommissioning and Decommissioning of Nuclear Buildings at the TMB continues to focus on decontamination, in particular specializing on automation issues. Further developments of the Living Lab and the system developed in recent years in the area of "process chain digitalisation - decontamination - clearance measurement" were the focus here.

The goals of standardisation, performance enhancement and increasing the degree of automation

in decommissioning continued to be pursued by developing and refining various processes and technologies for the entire decontamination chain (e.g. regarding automated crack over-milling, inspection system for barrel containers, magnetic separation of grain mixtures to minimise secondary waste, and the development of a lightweight manipulator for ergonomic, mechanical surface removal of wall surfaces, especially of nuclear facilities).

In 2020 and 2021 several publications and conference talks were held or are going to take place. A highlight is the representation of the Decommissioning Department with 6 contributions in the DEM 2021 "International Conference on Decommissioning Challenges: Industrial Reality, Lessons Learned and Prospects" in Avignon, France.

Another highlight was the Week of the Environment, hosted by Federal President Frank-Walter Steinmeier and the Deutsche Bundesstiftung Umwelt (DBU). Here, selected exhibitors presented their innovative projects and concepts for a sustainable future. A jury of experts appointed by the Office of the Federal President selected the best projects from over 600 applications - the TMB's Department for the Demolition of Conventional and Nuclear Buildings was there with an innovation on the topic of "Resource conservation through innovative demolition and deconstruction methods and process procedures".

The TMB's Department of Deconstruction and Decommissioning of Conventional and Nuclear Buildings also works closely with the NEA. Currently, a report on robotics applications in the areas of decommissioning, contaminated site management and radioactive waste disposal is being prepared within the framework of the Expert Group on the Application of Robotics and Remote Systems in the Nuclear

Back-end (EGRRS), to which the TMB's Decommissioning Department is also contributing.

The Decommissioning Group of the Electric Power Research Institute (EPRI) will sponsor the demonstration of an autonomous wall survey system in the second half of 2021. Contact has already been made with EPRI in this regard, and a bid for the tender is already being prepared.

On the academic side, the two TMB scientists Madeleine Weber and Carla-Olivia Kraus successfully finished their PhD thesis [1], [2]. Birte Froebus, scientist in the Department of Deconstruction and Decommissioning of Conventional and Nuclear Buildings, was awarded the Women in Nuclear Germany Prize 2020/2021 for special achievements in

the field of nuclear research.. Currently, the Department of Deconstruction and Decommissioning of Conventional and Nuclear Buildings has 26 employees, 18 of whom are scientific staff financed exclusively by third-party funds. They are currently working on 12 research projects.

References

- [1] <https://publikationen.bibliothek.kit.edu/1000129619>
- [2] <https://publikationen.bibliothek.kit.edu/1000130768>

7.2 Robotic systems for decontamination in hazardous environments

S. Müller, A. Wernke, C. Li, Z. Chen, S. Kazemi, S. Gentes

In co-operation with:

Fraunhofer IOSB; DFKI; FZI; Götting KG; Kraftanlagen Heidelberg GmbH; KHG Kerntechnische Hilfsdienst GmbH; ICP Ingenieurgesellschaft Prof. Czurda und Partner mbH

Introduction

The use of autonomous and semi-autonomous robotic systems in the field of decontamination of hazardous environments reduces the risks for human workers. Therefore, the competence centre »Robotic systems for decontamination in hazardous environments« (ROBDEKON) aims to research and develop novel robotic systems for decontamination tasks. ROBDEKON is funded by the German Federal Ministry of Education and Research as part of the »Research for Civil Security« programme. The focus in this Project is the development of robust field usable robots. By creating a close expert network partnering members from science and the application side, a transfer and further development of science and research technologies to field applicable level can be achieved. The application requirements on autonomous systems in various hazardous application fields are related in many ways. Therefore, ROBDEKON concentrates on Decontamination of Plant Components and Waste, Remediation of Contaminated Sites and Decommissioning of Nuclear Facilities. [1]



Fig. 1: Living Lab for testing decontamination scenarios

Within this expert group, TMB decommissioning unit researches on the decommissioning process chain. Basis of the decommissioning process is the exploration of the facility in terms of radioactive inventory and actualisation on floor layout. In the next step surface decontamination can take place. For this tasks two new autonomous Systems, GammaBot and Manitou are being researched. To test this Systems a novel Lab, shown in Fig. 1, has been setup within the TMB facilities, providing a realistic testing environment for decontamination scenarios.

GammaBot

For autonomous exploration of indoor geometries and the mapping of local dose rates, the GammaBot platform shown in Fig. 2 has been set up. It generates a 3D point cloud and measures the local dose rates constantly. By over mapping data generated by the scintillator probe and the 3D point cloud, a detailed

decontamination plan can be generated. GammaBot manoeuvres autonomously through the building generating all scans and measurements that are needed to implement the 3D model of the floor and returns back to the starting point. The simulation of the surrounding is shown in Fig. 3. [2]



Fig. 2: Picture of GammaBot Platform

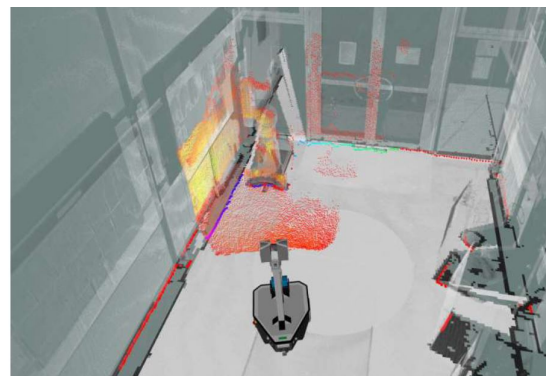


Fig. 3: Simulated surrounding area by GammaBot [3]

Manitou Manipulator

On the basis of GammaBot 3D mapping Manitou platforms continue the decontamination process chain. The Manitou shown in Fig. 4 is an autonomous aerial work platform with two tool heads. A working head with contamination sensor detecting β and γ radiation and a milling head to remove surface contamination. In a first working step the location, type and dose rate of the contamination is refined with the contamination sensors scanning the surfaces that were detected by GammaBot. In a second step, Manitou does a tool change for the milling operation. At spots where contaminated surfaces was detected

the milling head removes the surface. The depth of the milling is calculated according to the detected radiation. After the milling process, in a third step a scanning process is followed. If radiation is still detected, the milling head is applied at this spot again. Both working steps are continued until no radiation is detected anymore.

References

- [1] <https://robdekon.de/en/about-us/profile>
- [2] Project presentation at nuclear decommissioning lecture at TMB 27.01.2021
- [3] Distributed to ROBDEKON by KIT-IPR



Fig. 4: Manitou platform with shaver tool

7.3 Stakeholders based analysis of research for decommissioning

S. Müller, M. J. Chaudhry, S. Gentes

In co-operation with:

A. Bohnstedt^a, C. Georges^b, A. Fornier^b, R. Winkler^b, L. Aldave De Las Heras^c, E.G. Neri^d, A. Banford^e, K. Van Den Dungen^f

^a Karlsruhe Institute of Technology (KIT), Germany

^b Commissariat à l’Energie Atomique et aux Energies Alternatives (CEA), France

^c Joint Research Centre (JRC), European Commission

^d Empresa Nacional de Residuos Radiactivos (ENRESA), Spain

^e National Nuclear Laboratory (NNL), United-Kingdom

^f Centre d’étude de l’énergie nucléaire (SCK-CEN), Belgium

Introduction

The Coordination & Support Action project called “SHARE” (StakeHolders based Analysis of *¹ Research for decommissioning), is funded by EU-Horizon 2020 nuclear research program. The objective of this project is the development of a Strategic Research Agenda (SRA) associated with a Roadmap for the next 10-15 years, to increase confidence in the decommissioning process, it also aims to encourage the future coordination of research topics that are recommendable for financing in the next decade. Moreover, it will facilitate access to expertise and technology and maintain competences in decommissioning and environmental remediation for the benefit of Member states in Europe and beyond.

The Analysis

SHARE project intends to provide an inclusive roadmap for decommissioning research, in technical and non-technical areas, enabling stakeholders to jointly improve safety, reduce costs and minimise environmental impact in the decommissioning of nuclear facilities. It is based on a broad analysis of stakeholder needs including R&D, R&I, education, training, regulations, legislation, project management, costing and standardisation among others.

A detailed survey divided into different thematic areas of nuclear decommissioning (e.g. Safety and Radiological Protection aspects, Decommissioning material and radioactive waste management, Cost estimation and Benchmarking etc.) was sent to 650 stakeholders all over the value chain, to obtain their opinions about importance and urgency of their respective research needs. Similarly, an elaborate literature review was carried out, highlighting existing methodologies and techniques as well as international initiatives in these thematic areas. SHARE project is built on a consultation process including the needs and point of views of different stakeholders. In this regard, two online workshops were organised to receive stakeholders’ valuable

opinions by firstly investigating with them issues, challenges, and opportunities in research and secondly sharing status and results of ongoing developments [1][2].

A gap analysis between needs, identified in the survey and at the workshops, and existing solutions or on-going developments, drawn from the literature review, was carried out. The first outcome of the investigation was presented at DigiDecom 2021 conference, where again participants gave feedback [3]. The final analysis provided actions that can impact identified needs. The compiled actions will be further analysed and grouped as key research topics, which will be the basis for the SRA and the Roadmap. This may also lead to better future harmonisation in research of technological approaches used in decommissioning.

Conclusion

One of the main added value of SHARE project is to collect the opinion of the global stakeholders decommissioning community, in order to know and understand issues and challenges they are facing and lacks or opportunities they have in mind. As a result, SHARE will provide a Strategic Research Agenda and a Roadmap that will support policymakers in their choice of areas, eligible for financial contribution and for potential future collaborative research projects in R&D, R&I, methodologies, standardisation in technical and non-technical areas.

References

- [1] SHARE organized a 2-days workshop on international best-practices in nuclear Decommissioning - Share (share-h2020.eu)
- [2] <https://share-h2020.eu/2020/12/09/317-people-registered-to-the-public-online-workshop-organized-by-share-consortium-1-3-december-2020/>
- [3] Synergy with DigiDecom 2021 for a step further towards SHARE Strategic research agenda - Share (share-h2020.eu)

¹ R&D, R&I, methodologies, standardisation, etc. in technical and non-technical areas

8 Development of radionuclide speciation methods

Developing and maintaining a state-of-the-art portfolio of radionuclide speciation tools encompassing surface science and spectroscopy methods is an important R&D activity at INE, as these methods are indispensable for our understanding of actinide and radionuclide (geo)chemistry or the behavior of nuclear waste forms. Radionuclide speciation methods available at INE's controlled area laboratories and the ACT and INE-Beamline stations at the nearby KIT Light Source are continuously adapted to serve the requirements of in house and HGF/NUSAFE R&D programs or national and international cooperation partners. Recent technological developments at ACT-station have enabled high resolution X-ray absorption near edge structure (HR-XANES) spectroscopy for low radionuclide loading samples - encompassing the investigation of actinide elements down to 1 ppm concentration - combined with a cryogenic sample environment reducing beam induced sample alterations. A new setup for 'tender' X-ray spectroscopy ($\sim 2-5$ keV) in transmission or total fluorescence yield detection mode based on a He flow cell has been developed at the INE-Beamline. For the first time ever, Tc L_3 -edge XANES spectra of ^{99}Tc -species in liquid (aqueous) media were successfully recorded. In the reporting period, X-ray photoelectron spectroscopy (XPS) was successfully applied for the quantitative analysis of metal-organic complexes. The ability to determine accurate atomic concentrations and type and relative amounts of different bonding environments makes XPS a powerful speciation tool for, e.g., the analysis of radionuclide complexation by nPr-BTP / HNO_3 or adducts thereof. To enhance the energy resolution of X-ray spectroscopy in the scanning electron microscope (SEM), a wavelength dispersive X-ray spectrometer (WDS) was installed in addition to the existing energy dispersive (EDS) spectrometer. WDS resolves most of the spectral superpositions of element-specific X-ray lines, which is highly beneficial for the detection of trace elements, demonstrated, e.g., for Tc in spent fuel ϵ -particles. In the recent years the focus of NMR studies at INE was placed on bonding phenomena of trivalent f-elements complexed by N-donor ligands - probing the metal-nitrogen interaction. In the reporting period these studies were extended to the investigation of O-donor ligands such as tetraethyl diglycolamide (TEDGA). Besides the complex chemistry of the actinide ions and their fission products, the chemistry of cementitious phases or irradiated materials are important research topics with respect to the safety of nuclear waste disposal. ^{29}Si , ^{27}Al or ^9Be NMR spectroscopy available at INE is particularly well suited to investigate these topics, as the relevant elements are hard to address by X-ray based speciation methods. In the past two years, accelerator mass spectrometry (AMS) was used to investigate the long-term behavior of radionuclide tracers in the frame of the LIT experiment at the Grimsel Test Site as well as in laboratory scale diffusion experiments, obtaining results relevant for the safety assessment of nuclear waste disposal in crystalline and clay rock formations. Furthermore, AMS was applied to the analysis of Rhine River water samples from the vicinity of the Fessenheim NPP in France to gain initial radionuclide concentrations at the 'status-quo-ante' relative to the ongoing decommissioning activities. Ab initio computational chemistry methods are assisting and increasingly complementing experimental investigations at INE in the fields of nuclear waste disposal and fundamental radionuclide studies. In the reporting period, major breakthroughs were achieved for the systematic calculation of radionuclide (Tc L_3 -edge XANES) and actinide (uranyl M_4 -edge HR-XANES/RIXS) spectra, significantly contributing to the interpretation of recent experimental observations.

8.1 R&D projects conducted at the INE-Beamline and the ACT station of the KIT Light Source

K. Dardenne, S. Duckworth, X. Gaona, K. Hardock, V. Krepper, T. Prüßmann, J. Rothe, B. Schacherl, T. Vitova

Introduction

Synchrotron radiation (SR) based speciation techniques have become key methods in basic and applied radionuclide research. This development is primarily driven by the need to secure molecular-scale understanding of (geo-)chemical processes determining the mobility of safety relevant radionuclides (i.e., long-lived actinides, fission and activation products generated during nuclear reactor operation) which might be released into the geosphere from a breached repository for highly active, heat-producing nuclear waste.

The INE-Beamline for radionuclide science at the electron storage ring KARA (KArlsruhe Research Accelerator) became fully operational in 2005 as a flexible experimental platform for X-ray based radionuclide speciation investigations. The hard X-ray beamline 'CAT-ACT' for CATalysis and ACTinide research

was commissioned at an adjacent beam port in 2016. Both the INE-Beamline and the ACT laboratory for synchrotron based radionuclide studies are licensed to handle radioisotopes with activities up to one million times the (isotope specific) exemption limits, including 200 mg each of the fissile isotopes ^{235}U and ^{239}Pu . These experimental stations are the only facilities of their kind in Europe offering direct access to radiochemistry laboratories operating a shielded box-line in close proximity to the SR source on the same research campus [1]. They are continuously upgraded to adapt the portfolio of methods and instrumentation to the requirements set by the KIT-INE/NUSAFE R&D program in the topics nuclear waste disposal, pre-disposal / interim storage and fundamental investigations.

INE-Beamline and ACT operation in 2020/21

As in the previous years, INE in-house projects in the two year period 2020/21 covered the investigation of a broad range of materials containing actinides (*An*), their chemical homologues or possible fission products in the context of nuclear waste disposal safety research or basic actinide and radionuclide science. Besides others, studies at INE-Beamline included the solution chemistry of Tc in the presence of inorganic and organic ligands (sulphate and gluconate – s. the more detailed description below), Np L₃-edge XAFS for the speciation of neptunium after interaction with illite, XAFS, XRD and μ -XRF investigations of highly radioactive nuclear waste fragments (spent nuclear fuel, nuclear waste glass and zircaloy cladding segments), the characterization of bentonite in contact with corroding metallic coupons by μ -XRF and μ -XANES, an iodine L₃-edge investigation of iodate sorption on magnetite, the Pu L₃-EXAFS characterization of Ca-Pu(VI)-CO₃ species, X-ray spectroscopic investigations on the behaviour of volatile activation and fission products present in the fuel-cladding interaction layer of MOX fuel and vitrified HAWC, the long-term evolution of Pu(III/IV) solid phases under strongly reducing and alkaline conditions, the characterization of ZrO₂ solid phases equilibrated in alkaline solutions or the S K-edge speciation of sulphate moieties in new glass formulations as candidates for HAWC vitrification.

Experiments at the ACT station covered, e.g., the exploration of the electronic structure of bulk PuO₂ by Pu M₅-edge RIXS, *in situ* Pu M₅ HR-XANES studies of plutonium dioxide in aqueous environments (in search of Pu(V)), U M₄-edge HR-XANES of U in fullerene and waste encapsulation materials, Np M₅-edge HR-XANES/RIXS investigations of spent nuclear fuel fragments, Np M₅-edge HR-XANES measurements of Np/illite samples in search of the ‘detection limit’ for *An* sorption samples, Sm L₃-edge HR-XANES valence band X-ray emission of samarium compounds, an iodine K-edge study of iodide retention by Fe corrosion phases, an *in situ* Np M₅ RIXS investigation of aqueous Np(III/IV/V/VI) species stabilized in an electrochemical cell, the *An* M_{4,5}-edge HR-XANES/RIXS investigation of *An*O₂ nanoparticles (*An* = Th, U, Np, Pu), a Pu M₅ HR-XANES study of colloidal Pu at reducing conditions in the presence of hydrazine, single crystal polarization dependent measurements (PD-XANES) of uranyl halides, the investigation of long-term oxidation effects on a fuel pellet ‘footprint’ on adhesive tape or the investigation of *An* halide electronic structures from the metal and ligand point of view.

Several studies were conducted sequentially at both beamlines - benefitting from the complementary energy ranges or the adequate spectral and spatial resolution - e.g., the U L₃-edge XAFS / U M₄-edge HR-XANES investigation of U sorption on magnetite, U L₃- and M₄-edge (HR-)XANES measurements of U(VI)-, U(V)- and U(IV)-carbonate solids and solutions, Th L₃- and M₅-edge XAS of ThO₂ nanoparticles, *An* L₃-edge XAFS and M_{4,5}-edge HR-XANES studies

on homogeneous (U,Am)O₂ and (U,Pu,Am)O₂ solid solutions, the investigation of surface effects on the electronic and molecular structure of PuO₂ nanoparticles, the investigation of the valence state of the metals in PuBiO₄ compounds by Bi and Pu L₃-edge XAFS and Pu M_{4,5}-edge HR-XANES or a study of lanthanum and caesium interaction with DOTA as surrogates for radiopharmaceuticals.

Some of the aforementioned studies are presented in more detail elsewhere in this bi-annual report.

Although travel restrictions caused by the COVID-19 pandemic had significantly limited the external access to the KIT Light Source in the reporting period, researchers and cooperation partners from the following German and international research institutions conducted experiments at the INE-Beamline and ACT station in 2020/21:

- Helmholtzzentrum Dresden-Rossendorf, Germany
- Joint Research Center Karlsruhe, EU
- CEA Marcoule, France
- Leibniz Universität Hannover, Germany
- Forschungszentrum Jülich, Germany
- Universität Köln, Germany
- TU Delft, The Netherlands
- EPFL Lausanne, Switzerland
- SINAP Shanghai, PR China
- Sorbonne Université, France
- Université de Rennes 1, France
- Helsinki University, Finland

As in previous years, a considerable share of in-house beamtime was spent for experiments conducted by internship, master and graduate students in the frame of their thesis projects.

Implementation of ‘tender’ X-ray Tc L₃-edge XAFS at the INE-Beamline

⁹⁹Tc is one of the main fission products of ²³⁵U and ²³⁹Pu in nuclear reactors. Due to its long half-life ($t_{1/2} = 2.121 \cdot 10^5$ a) and large inventory in spent nuclear fuel, ⁹⁹Tc is of great relevance in the context of safety assessment of repositories for radioactive waste. ⁹⁹Tc is also a relevant contaminant associated with sites for plutonium production or nuclear fuel reprocessing such as the Hanford Site, Washington State, USA. Tc K-edge X-ray Absorption Fine Structure (XAFS) spectroscopy was frequently applied in the past decades to characterize ⁹⁹Tc species in solid specimen and liquid phases. Although ⁹⁹Tc is a radionuclide decaying by β -emission (~0.3 MeV), its relatively high exemption limit of 1E+7 Bq renders XAFS measurements with thoroughly encapsulated samples easily feasible at its K absorption edge (E_{1s} (Tc⁰): 21.044 keV) – even at X-ray Absorption Spectroscopy (XAS) beamline stations which are not specially equipped for radionuclide research. In contrast to the almost exclusively probed Tc K-edge (corresponding to dipole-allowed 1s \rightarrow 5p transitions), excitation of the shallower 2p_{3/2} core electrons ($E_{2p_{3/2}}$ (Tc⁰): 2.677 keV) probes the unoccupied 4d levels and – depending on the Tc bonding state and

symmetry – the corresponding crystal or ligand field splitting. The core-hole lifetime broadening at the Tc L_3 -level is only 1.91 eV compared to 4.91 eV at the K-level, enabling to detect subtle spectral differences between different oxidation states and bonding schemes. To the best of our knowledge, up to now (Dec. 2021) the only publications covering XANES measurements at the Tc L_3 absorption edge were presented by Blanchard et al. in 2014 [2], Bauters et al. in 2020 [3] and by us in Dardenne et al., 2021 [4]. In Ref. [2], Tc containing powder samples were embedded in epoxy resin and mounted in a windowless holder. Tc L_3 -edge spectra were collected at the Australian Synchrotron using the total electron (TEY) and total fluorescence yield (TFY) XAS detection modes with Tc samples held at UHV conditions. In Ref. [3], a comprehensive series of ^{99}Tc compounds, ranging from oxidation state I to VII, was measured at the Tc L_3 -edge applying our new approach to record ‘tender’ X-ray XANES spectra at ambient conditions [4].

A new setup for tender X-ray measurements at the INE-Beamline (currently applicable down to the phosphorus K-edge at ~ 2.14 keV) was developed and initially tested at the S K- and Mo L_3 -edge (~ 2.47 and ~ 2.53 keV, respectively). The system is based on a He-flow chamber comprising 1st ionization chamber (Oken, Japan, 5 cm length), bellows, sample chamber, bellows and 2nd ionization chamber (Oken, Japan, 19 cm length) – all connected without intersecting windows (Fig. 1).

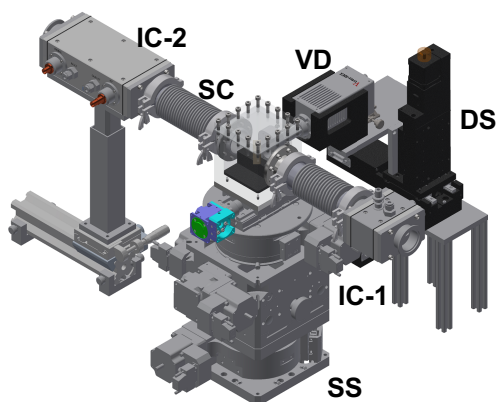


Fig. 1: New setup for ‘tender’ X-ray XAFS measurements - SS: sample stage, DS: detector stage, SC: sample chamber, VD: Vortex detector, IC-1: first ionization chamber, IC-2: second ionization chamber.

The sample chamber is mounted at a linear table on top of the multi-axis sample positioning stage (Huber, Germany) – allowing its lateral and vertical translation by each ± 6 mm. The 2nd IC is rigidly mounted at the X-95 rail carrying the downstream ionization chambers for conventional high-energy XAS measurements. A He-flow of 1 l/min (inlet at the 2nd IC, outlet at the 1st IC, exhausted via the ventilation system of the experimental hutch) is provided to constantly purge the chamber assembly. The sample chamber is manufactured as a transparent acrylic glass cube equipped with ISO-KF40 entrance and exit flanges and a sealed lid at the top, which can be opened to introduce various types

of sample cells, vials or holders. The major technical challenge was to position the Be entrance window of the solid-state detector for TFY measurements (Vortex 60EX, Hitachi, USA) close to the sample surface without directly exposing the detector snout to the He atmosphere in the sample chamber. This was solved by fitting the right-hand side (in beam direction) of the sample chamber with a sealed KAPTON® window (13 μm) on a frame protruding 20 mm into the chamber volume. The racetrack shape of the frame allows vertical sample positioning scans of the cell with inserted detector, while lateral positioning scans (at 90° relative to the impinging beam) are coupled to synchronous movements of the lateral detector positioning stage, keeping the sample to Be-window distance constant. Intensity losses due to the absorption of Tc L_α fluorescence (~ 2.42 keV) in the KAPTON® window and the remaining air gap amount to $\sim 30\%$. Standard (inactive) samples such as thin films or powders dusted to adhesive tape are attached to a stand inside the sample chamber held in position by magnets on a metallic base plate. Solution samples are investigated in PEEK (polyether ether ketone) cuvettes sealed by KAPTON films. This method was recently developed at KIT-INE for actinide M-edge high energy resolution X-ray emission spectroscopy (HR-XES) [5]. For the first time ever, with this setup we were able to collect ‘tender’ X-ray Tc L_3 -edge XANES spectra for liquid ^{99}Tc -samples [4]. All Tc L_3 -edge XAFS spectra were recorded in TFY mode detecting the Tc L_α -line, using the He-flushed 1st IC as I_0 monitor. The DCM was equipped with a pair of Si<111> crystals. The energy scale was calibrated by assigning the white line (sulphate) peak maximum in the sulphur K-edge spectrum of Na_2SO_4 to 2.477 keV, which was in turn calibrated against the $1s \rightarrow 4p$ Rydberg transition of Ar (3.20354 keV). PEEK cuvettes with 13 μm KAPTON windows were placed in the sample chamber with the surface of the window at 45° relative to the impinging beam.

Fig. 2a depicts the Tc L_3 -XANES of samples A and B, a Tc(V)-gluconate complex with distorted square-pyramidal oxygen coordination and a Tc(IV)-gluconate complex with presumably octahedral oxygen coordination of Tc, respectively, together with the liquid pertechnetate (Ref Tc(VII)) and the amorphous $\text{TcO}_2 \cdot x\text{H}_2\text{O}(\text{am})$ reference (vertically shifted for clarity). Pertechnetate and samples A and B exhibit a splitting of the most intense transition feature (white line, WL). In contrast to that, the WL observed for TcO_2 is more symmetric and less intense. The latter observation has to be attributed to the higher filling of the 4d-states in TcO_2 (d3), but might be as well affected by ‘self-absorption’ when recording the Tc L_α fluorescence from a concentrated bulk sample. The spectra have been further analysed by fitting two pseudo-Voigt (called peak 1 and peak 2) and an arc tangent function (representing the continuum transition above the edge). Fit results (positions of peak 1 and 2, the centre of mass of peaks 1 and 2 and the energy differences between peak 2 and peak 1) are plotted in Fig. 2b. As expected, the centre of mass and the energy positions of peak 1 and 2 are monotonously increasing with the formal Tc

oxidation state – a well-known phenomenon for transition metal XANES spectra due to the decreasing screening of the nuclear charge. Interestingly, the WL splitting exhibits the highest value for sample B (Tc(IV)-gluconate) and decreases via sample A (Tc(V)-gluconate) to pertechnetate. Generally, peaks 1 and 2 in L_3 -edges XANES spectra of 4d transition metals are associated with transitions to unoccupied, crystal-field split 4d levels, denoted according to the irreducible representations of the corresponding symmetry groups. This energy splitting depends on the ligand field strength, which typically increases as the oxidation state increases (with similar bond distances) or the bond length decreases. Thus, this observation is in agreement with the decreased Tc-O bond length obtained by Tc K-EXAFS [4] for sample B compared to $\text{TcO}_2 \cdot x\text{H}_2\text{O}(\text{am})$. Details of the quantum-chemical calculation of these spectra are given below in section 8.6.

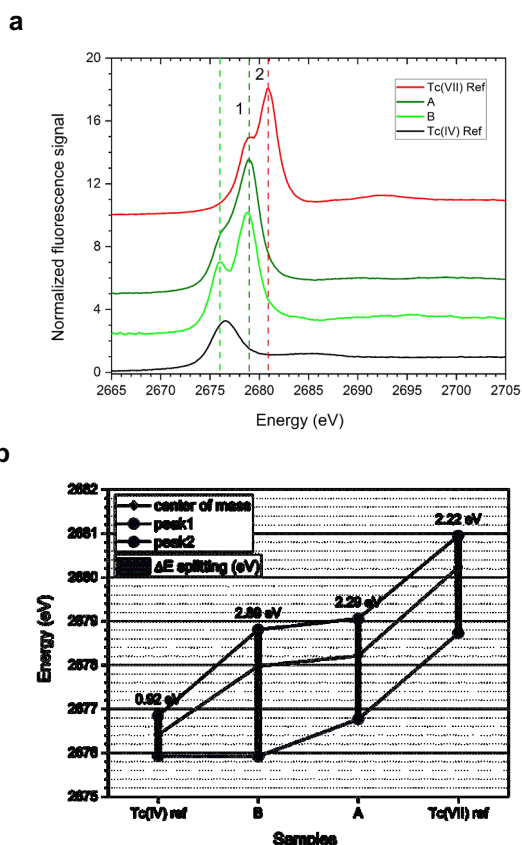


Fig. 2: a) Normalized Tc L_3 -XANES spectra of gluconate samples A and B and reference compounds. b) White line peak positions and energy splitting extracted by peak fitting of Tc L_3 -XANES spectra.

Cryogenic actinide M-edge HR-XANES spectroscopy at the ACT station of the CAT-ACT beamline

The Johann-type X-ray emission spectrometer at the ACT laboratory is routinely applied for HR-XES/HR-XANES and RIXS experiments in a broad energy range encompassing the actinide M- and L-edges (Th – Es feasible). The ‘tender’ X-ray range at ACT is accessible with a Si<111> crystal pair in the cryo-cooled

double crystal monochromator down to ~ 3.4 keV [1]. In this energy region, scattering and absorption of X-rays is efficiently minimized by enclosing all beam paths – i.e., that of the impinging beam and those between the sample, the analyzer crystals and the silicon drift detector entrance window arranged in a vertical Rowland circle geometry – in He atmosphere. A rigid plexiglass box housing the spectrometer components has been (re)designed and recently installed on the ACT experiment breadboard table (Fig. 3) [6].

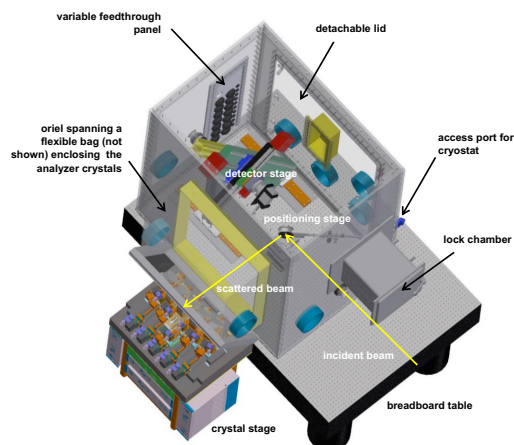


Fig. 3: 3D CAD model of the He box providing an improved concept with possibilities for several experiments, e.g., enabling in situ measurements and cryostat experiments at the M-edges of actinides at the ACT station.

The improved design allows to keep stable conditions with less than 150 ppm oxygen inside the box through a controlled He flow of ~ 5 l/min. The five crystal holders are placed inside a flexible polyvinyl chloride (PVC) bag clamped by the five crystal mounts and spanned by an oriel protruding from the left-hand side wall (in beam direction) of the He box. This setup allows for sufficient freedom of motion of the crystals along their individual Rowland circles. The He box is equipped with a spacious rectangular lock chamber for exchanging sample cells (e.g., in situ cells or combined UV-Vis/XES setups) and a panel at the back side (in beam direction) providing various media and power feedthroughs (e.g., He/N₂/Ar inert gas supply, cooling water, motor power/encoder/limit-switch lines, detector HV/power supply and signal lines, vacuum pump hose etc.). A special access port based on a gear stick sleeve at the front side, right-hand corner (in beam direction) of the box allows to insert the supply lines for the modified LN₂ cryostat which are bundled in a flexible stainless-steel tube. The plexiglass box is further equipped with a large detachable lid sealed by a PVC gasket at the wall opposite from the crystal stage (right-hand side in beam direction). The large opening provides inside access for installation of the standard transmission / fluorescence XAFS detection equipment with ionization chambers and the recently commissioned electrically cooled 8-element LGe detector (Mirion, France) or a Laue diffraction setup. Compared

to the original setup with a flexible top, the improved design of the box enclosing the HR-XES spectrometer offers the following advantages:

- the box remains permanently installed on top of the breadboard table, minimizing the time to switch between HR-XES and standard XAS experiments;
- the front and back side walls of the box are fitted with ISO-KF 50 flange feedthroughs, simplifying to switch between ACT and CAT stations by bridging the box with a vacuum pipe;
- significantly improved He gas purity – correspondingly higher photon flux;
- significantly reduced He consumption during ‘tender’ X-ray measurements;
- large lock chamber, e.g., for transfer of in situ sample cells.

A commercial flow-through cryostat primarily developed for microscopy applications (Oxford Instruments MicrostatHe, UK) – optionally operational with LHe or LN₂ as cryogenic coolant – was selected to be adapted to the HR-XES setup at ACT. It has been modified for tender X-ray (*An* M-edge) requirements while providing a special clamp mechanism enabling fast sample changes with the new cryo sample cells. The instrument was chosen based on the special vacuum chamber dimensions offering a large solid angle field of view (~140° opening angle) onto the sample(s) and a narrow gap of ~2 mm between the sample surface and the outer vacuum window (as required, e.g., for cryo-microscopy investigations). This in turn allows the X-rays isotropically emitted from the sample to be captured and diffracted by all five analyzer crystals in the 1 m Rowland circle arrangement.

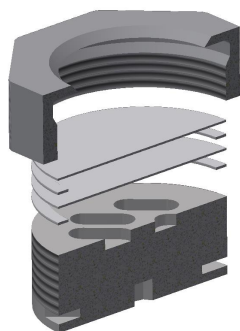


Fig. 4: Exploded view 3D CAD drawing of the sample cell assembly with –from top to bottom– cap nut, 2nd KAPTON window, 2nd TEFLON gasket, 1st KAPTON window, 1st TEFLON gasket, cell body with sample cavities.

A vacuum resistant sample cell (Fig. 4) – adhering to the double containment rule for radioactive samples – had to be designed and thoroughly tested. The loaded sample cells are pre-frozen in a LN₂ bath and introduced via the lock chamber into the dry He atmosphere inside the box. The cylindrical cryostat chamber is opened at cryogenic temperatures and the sample cell attached to a copper fork providing the heat exchange. The original quartz window of the sample chamber flange facing the top side of the sample cell has been replaced by an epoxy-glued 12.5 μm KAPTON disk.

Although already absorbing ~35 % of the photon intensity at the Np M₅-edge energy, the cryostat window thickness has been a necessary compromise between vacuum stability and X-ray transparency. The vacuum chamber attached to the flexible tube containing LN₂ supply and exhaust lines as well as thermal sensor (PT-100 type) and heater connections is mounted by a half-shell adapter on top of the sample positioning stage at 45° relative to the impinging beam. This setup enabled a sample temperature of approximately 141.2 ± 1.5 K at irradiation conditions with the heat exchange block cooled down and stabilized at LN₂ temperature (~77 K) [6].

Oxidation state changes of redox-sensitive *An* elements (primarily U, Np and Pu, which may exist (or even co-exist) at different oxidation states (IV – VI) at the relevant geochemical conditions), are not exclusively induced by redox partners such as Fe(II) in mineral surface reactions. These changes have been observed to occur for mostly wet samples in XAS based speciation experiments under inert gas conditions. It is suspected that water radicals formed in bright X-ray beams might interact with the *An* cations and change their oxidation state. Another conjecture are effects due to increased sample temperatures at X-ray irradiation conditions.

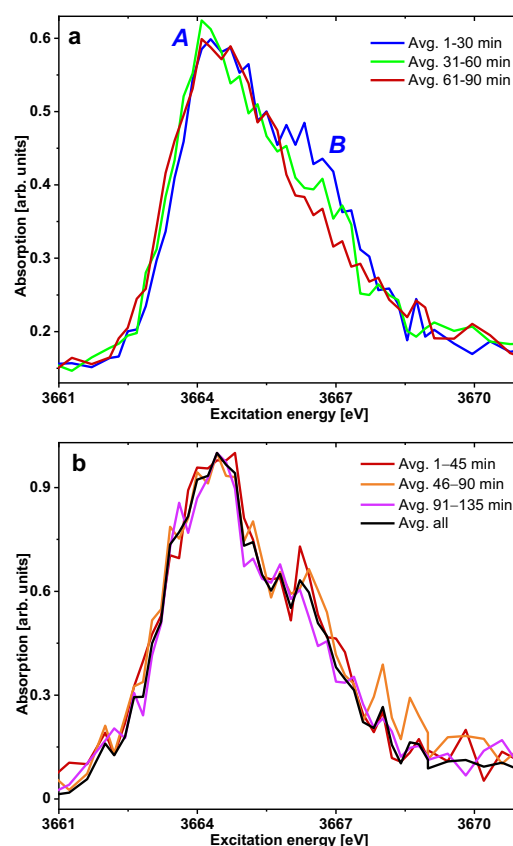


Fig. 5: a) Gradual change of Np M₅-edge HR-XANES spectra of a Np / illite sorption sample at 300.0 ± 1.5 K, changes in the shoulder denoted as feature B are visible with irradiation time. b) At cryogenic conditions (141.2 ± 1.5 K), no significant changes of the spectra are discernible within the noise level.

As an example to illustrate the performance of our improved cryogenic ‘tender’ X-ray emission spectroscopy setup, we have performed Np M_{5} -edge HR-XANES measurements of Np-237 sorbed on illite (Illite du Puy (6.94 % Fe_2O_3) contacted with Np at an initial concentration of $c_0(Np(V))=1\times 10^{-6}$ mol/L for 11 days at pH 9.2 with a solid to liquid ratio of 2 g/L and $I = 0.1$ mol/L NaCl, resulting in a sorbed Np loading on illite of 83 ± 2 ppm). A solid Np reference sample ($K_3Na[U,NpO_2(CO_3)_3]\times H_2O$) was used to calibrate the DCM for Np M_{5} -edge HR-XANES spectroscopy. The white line maximum of this sample was assigned to 3664 eV. The Np $M_{\alpha 1}$ fluorescence line was recorded with four Si<220> analyzer crystals, aligned at a Bragg angle of 81.92° . For the sample at room temperature, 9×10 min scans were recorded. For the sample mounted inside the cryostat at 141.2 ± 1.5 K, 9×15 min scans were recorded. The program OriginPro was used to calibrate the spectra using the reference scans recorded before and after each sample scan.

The higher photon flux achieved with the advanced He box setup, further optimization of the beamline optics alignment and recent improvements of the KARA storage ring operation has led to the observation of beam-induced alterations in hydrated samples such as wet Np-sorbed illite pastes. This is clearly shown in Fig. 5a, where the average of several Np M_{5} -edge HR-XANES scans of the Np / illite sample with the progression of irradiation time of a series of measurements performed at room temperature on the same sample

spot are depicted. Peak B – significant for the presence of Np(V) ‘neptunyl’ species – disappears after prolonged irradiation time, strongly suggesting reduction of Np(V) to Np(IV). Note that the white line maximum (peak A) position does not significantly change upon reduction of Np(V) to Np(IV) – a well-known anomaly for pentavalent ‘actinyl’ species upon the loss of the trans-dioxo conformation upon transition to the tetravalent state. In contrast to that, it becomes clearly evident from the comparison of scans averaged for different time intervals as depicted in Fig. 5b that beam-induced reduction is successfully suppressed when applying the cryostat setup stabilizing a sample temperature of 141.2 ± 1.5 K. Within the noise level, no significant changes in the spectra were detected when irradiating the same spot up to more than 130 min.

References

- [1] Rothe, J. et al., *Geosciences* **9**, 91 (2019).
- [2] Blanchard et al., *J. Synchrotron Radiat.* **21**, 1275 (2014).
- [3] Bauters, S. et al., *Chem. Commun.* **56**, 9608 (2020).
- [4] Dardenne, K. et al., *Inorg. Chem.* **60**, 12285 (2021).
- [5] Vitova, T. et al., *Chem. Commun.* **54**, 12824 (2018).
- [6] Schacherl, B. et al., *J. Synchrotron Radiat.* **29** (1), 80 (2022).

8.2 Development of a new software for LIBD analysis

T. Hippel, A. Skerencak-Frech

Due to its long service time, the equipment of the Laser Induced Breakdown Detection (LIBD) systems operated at INE required a renewal. A new camera including a new interface, the UI-3040SE-M-GL from IDS, was purchased. Instead of using separate PCI capture-cards, the camera signal is transferred to the data acquisition PC via USB 3.0. For the installation of this new equipment, a new software for the data analysis was required. In order to achieve a maximum of expandability and adaptability of the new experimental setup for upcoming scientific questions, the decision was made to develop a custom-made software in-house. The source code of the new software was written in C++, enabling an easy exchange of the graphical user-interface or implementation of new features.

The experimental principle of LIBD is based on a pulsed laser beam, which is focused into a cuvette containing nano-sized solid particles dispersed in a solution. Depending on the laser power and the target materials, within the focused area of the laser beam a light emitting plasma (breakdown event) is formed. The threshold for this plasma formation is lower for the dispersed solid materials compared to the solvent matrix. Thus, in a typical LIBD experiment a breakdown event occurs when a solid particle passes the area of highest photon density in the area of the laser focus. The breakdown events result in the emission of a flash of light detected by the camera, which takes a picture of the solution for every laser shot. An exemplary camera feed of breakdown events is shown in Fig. 1. The aim was to enable the newly established software to identify the size as well as the concentration of the nano-particles dispersed in a solution online during the LIBD measurement.



Fig. 1: Camera feed of breakdown events.

The software analyses the pictures for possible breakdown events. If no events are detected, the picture is discarded. If a breakdown event is observed, the software determines the position of the breakdown event in two dimensions. If multiple breakdown events occurred in one picture, all of them are taken into account. The position of each single breakdown event is plotted in a graph (s. Fig. 2).

From the distribution of the breakdown events along the x-axis, a histogram is generated. Currently, two different methods are implemented in the software to determine the particle size. The first method (method 1) is based on an algorithm to fit a Gaussian distribution curve to the histogram (s. Fig. 3). From this fit, the size and the concentration of the particles in the sample can

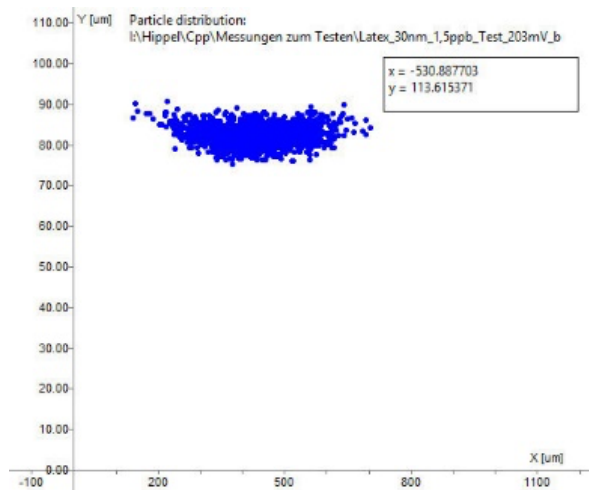


Fig. 2: Distribution of breakdown events, 30 nm particle size and 1.5 ppb concentration.

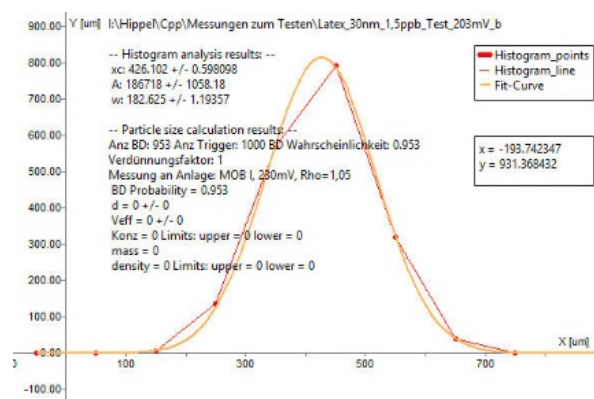


Fig. 3: Histogram analysis of 30 nm particles with 1.5 ppb concentration

be derived. The second method (method 2) also generates a histogram from the distribution of the breakdown events. From this, the length of the breakdown volume along the x-axis is calculated, which depends on the particle size. Therefore, the user receives two evaluations of the particle size.

One of the major advantages of the new software compared to the old setup is the fully automatic exportation of the breakdown distribution data and processing of the different calculation steps by the program within several seconds. The old software required all of these steps to be done manually, which took a considerable amount of time. Furthermore, the new software is compatible with data determined with the old setup. Hence, the former data can still be used if necessary.

Regarding the current development state, the software reads out image files taken by the old as well as the new

camera. Method 1 is fully operational and able to calculate the breakdown distribution as well as the Gaussian fit of the histogram on the fly. The only thing required is a new calibration measurement for the new camera. Method 2 is partially working, but requires further development. Furthermore, evaluation of data determined with the old software is also fully implemented and functional.

Current work in progress involves a modification of the software to capture the live feed from the camera

online during the measurement. Future development of the software aims at the installation of a control mechanism to stabilize the laser power during a measurement, or to change it over time if required for an analytical technique. In addition, a simplification of the calibration process for a specific system by automating the calculation of the calibration factors is under development.

8.3 Microscopy and surface analytics

D. Schild, O. Dieste Blanco, S. Duckworth, X. Gaona, A. Geist, M. Herm, T. König, P.J. Panak, E. Soballa, S. Trumm, A. Walschburger, M. Weigl, P. Weßling

Introduction

X-ray photoelectron spectroscopy (XPS) is successfully applied to the analysis of metal-organic complexes. The ability to determine atomic concentrations and type and amount of bonding states makes XPS a tool for characterization of such complexes. This is exemplified by analysis of Fe(II), Eu(III), and Am(III) complexation with nPr-BTP resulting in new insights into bonding properties.

To enhance energy resolution of X-ray spectroscopy in the scanning electron microscope (SEM), a wavelength dispersive spectrometer (WDS) was installed in addition to the existing energy dispersive X-ray spectrometer (EDS). Spectral superposition of characteristic X-ray lines using EDS are resolved in most cases by WDS, beneficial for example at multi-elemental samples consisting of transition elements.

Eu(III)- and Am(III)- nPr-BTP complexation by XPS

Trivalent actinides are separated from lanthanides by liquid-liquid extraction using suitable extracting agents. 2,6-Bis(5,6-dipropyl-1,2,4-triazin-3-yl)pyridine (nPr-BTP) is a tridentate ligand and forms nine-coordinate 1:3 complexes with the light trivalent actinides. Various analysis techniques indicated the formation of ten-fold coordinated species in non-aqueous solution [1]. To provide further evidence of a coordination number higher than nine, XPS is performed by a ULVAC-PHI VersaProbe II spectrometer by use of monochromatic Al K α (1486.7 eV) X-ray excitation. Survey spectra and narrow scans of elemental lines were acquired to characterize composition and bonding of the elements. The C 1s elemental line of nPr hydrocarbons is used as internal charge reference at 284.8 eV [2]. The error of binding energies of elemental lines is estimated to ± 0.2 eV. One microliter of solution with 1 mM of

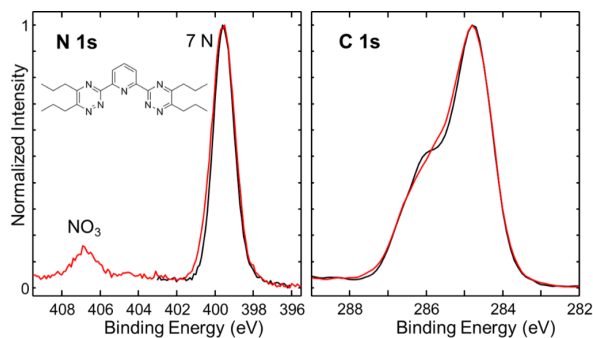


Fig. 1: Comparison of XP spectra of nPr-BTP (black curve, molecular structure) and nPr-BTP·HNO₃ (red curve) in 2-propanol with 0.15 M HNO₃. [nPr-BTP] = 3 mM.

complexes was spread onto aluminum foil, and the solvent was evaporated.

First, narrow scans of N 1s and C 1s elemental lines of nPr-BTP in the presence and absence of HNO₃ in 2-propanol were measured (Figure 1). nPr-BTP is known to form nPr-BTP·xHNO₃ (x = 1, 2) adducts [3,4]. The N 1s and C 1s main lines show little differences in the presence or absence of HNO₃. However, an additional peak at 406.8 eV in the N 1s spectrum of nPr-BTP containing HNO₃ indicates adduct formation. The peak area ratio of the N 1s BTP signal and the N 1s nitrate signal (after subtraction of a Shirley background) is 7:1, corroborating the formation of nPr-BTP·HNO₃ (seven N from BTP, one N from HNO₃).

Then, the [M(nPr-BTP)₃(NO₃)₂]²⁺ complexes (M = Am, Eu) (analogues for Cm(III)) were prepared in the presence of nitrate dissolved in 2-propanol and ana-

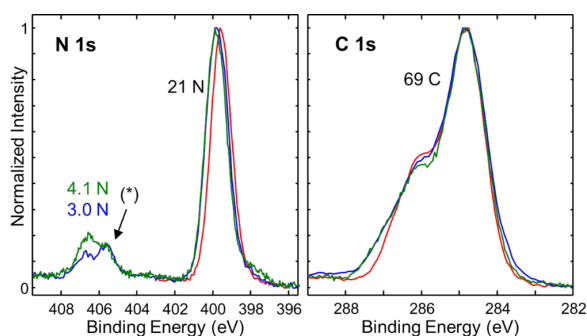


Fig. 2: X-ray photoelectron spectra of nPr-BTP (red curve) and [M(nPr-BTP)₃(NO₃)₂]²⁺ complexes (M = Eu, blue curve and Am, green curve) in 2-propanol (nPr-BTP and Eu(III) complex) or 2-propanol with 0.15 M HNO₃ (Am(III) complex). () denotes a constant fraction of two nitrate groups.*

lyzed by XPS. The narrow scans of N 1s and C 1s elemental lines are shown in Figure 2 together with elemental lines of nPr-BTP. Compared to the spectra of nPr-BTP, the N 1s spectrum and the aromatic region of the C 1s spectrum of the Am(III) and Eu(III) complexes are slightly shifted to higher binding energies. This indicates a decreased electron density in the aromatic system due to complexation with Am(III) or Eu(III). The N 1s and C 1s spectra of Am(III) and Eu(III) complexes show no significant differences.

The Am(III) and Eu(III) complexes show two additional lines assigned to nitrate at the N 1s spectrum: 405.6 eV (nitrate₁) and 406.7 eV (nitrate₂). The M(nPr-BTP)₃ : nitrate₁ : nitrate₂ peak area ratios after subtraction of a Shirley background are 21:2:1 for Eu(III) and 21:2:2 for Am(III). Two nitrate peaks with an intensity ratio of 2:1 are expected in a [M(nPr-BTP)₃(NO₃)₂](NO₃)₂ complex which coincides with the XPS result of the Eu(III) complex. However, the

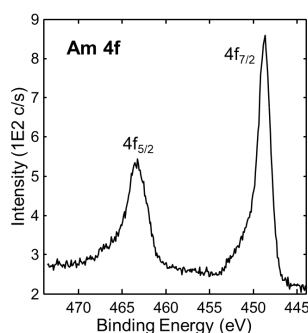


Fig. 3: Am 4f of $[Am(nPr-BTP)_3(NO_3)](NO_3)_2 \cdot HNO_3$. The binding energy of Am $4f_{7/2}$ is 448.7 eV (FWHM 1.74 eV) and the 4f spin-orbit splitting 14.6 eV.

Am(III) stock solution contained nitric acid. The observed 2:2 ratio of the lines assigned to nitrate of the Am(III) complex could be due to adduct formation, $[Am(nPr-BTP)_3(NO_3)](NO_3)_2 \cdot HNO_3$. The Am 4f spectrum is depicted in Figure 3.

The adduct formation was investigated by preparation of the $[Eu(nPr-BTP)_3(NO_3)](NO_3)_2$ complex in presence of increasing HNO_3 concentration. The N 1s and C 1s spectra are shown in Figure 4. The N 1s elemental line at 406.7 eV assigned to nitrate grows in intensity with increasing nitric acid concentration. According to the peak areas, the complexes are

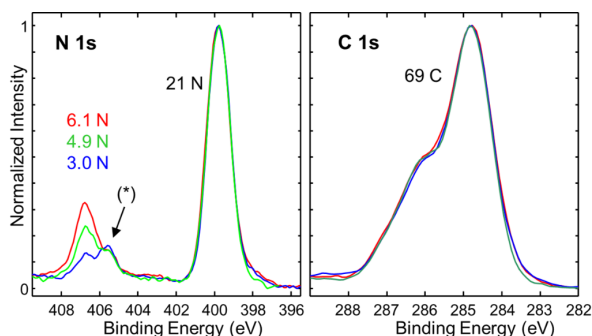


Fig. 4: XP spectra of $[Eu(nPr-BTP)_3(NO_3)](NO_3)_2 \cdot xHNO_3$ complexes in 2-propanol with 0 (blue curve, $x = 0$), 0.18 (green curve, $x = 2$), and 0.5 M HNO_3 (red curve, $x = 3$). (*) denotes a constant fraction of two nitrate groups.

$[Eu(nPr-BTP)_3(NO_3)](NO_3)_2 \cdot 2HNO_3$ and $[Eu(nPr-BTP)_3(NO_3)](NO_3)_2 \cdot 3HNO_3$. Thus, the N 1s elemental line of nitrate at 406.7 eV is assigned to one inner-sphere nitrate bound directly to the trivalent metal ion and to adduct HNO_3 molecules. The N 1s line at 405.6 eV corresponds to two outer-sphere nitrate anions. XPS measurements could confirm the formation of $[M(nPr-BTP)_3(NO_3)]^{2+}$ complexes ($M = Am, Eu$) with tenfold coordination.

Ferrous nPr-BTP 1:2 complex by XPS

The interaction of nitrate and nPr-BTP with iron was investigated since iron forms complexes with nPr-BTP solvent which damages stainless steel.

$Fe(III)(NO_3)_3$ and nPr-BTP were dissolved in 2-propanol resulting a dark colored solution which was stable in contact with air for one day. XPS of a dried sample shows that iron was reduced to Fe(II). The

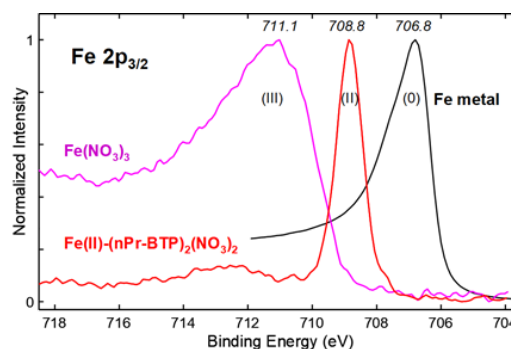


Fig. 5: Fe $2p_{3/2}$ spectrum of $Fe(II)(nPr-BTP)_2(NO_3)_2$ compared to Fe(III) nitrate and Fe(0) metal.

N 1s (nPr-BTP) main line has a binding energy of 400.0 eV, while the N 1s line at 405.7 eV corresponds to outer-sphere nitrate anions (NO_3^-). The molar ratios $[Fe]/[NO_3] = 1:2$ and $[N_{nPr-BTP}]/[NO_3]$ around 7:1 point to a $Fe(II)(nPr-BTP)_2(NO_3)_2$ complex. The Fe $2p_{3/2}$ line of the Fe(II) complex exhibits a narrow Gaussian, FWHM 0.98 eV. The absence of multiplet splitting indicates a low-spin Fe(II) complex with strong-field ligands (Figure 5).

Wavelength dispersive X-ray spectrometer for scanning electron microscopy

A wavelength dispersive X-ray spectrometer (WDS), model MagnaRay (Thermo Scientific), was installed in the SEM to overcome the limitation of EDS resolving peaks with close energies. In such cases the about ten times higher energy resolution of WDS in comparison with EDS supports the identification of X-ray lines and elements present in the sample. Acquisition, data processing and analyses are integrated into Pathfinder software (Thermo Scientific). In contrast to EDS, WDS is a crystal spectrometer and the X-ray energy range is scanned during the measurement which requires more time than EDS. The measured intensity of the X-ray lines is reduced for WDS, but detection limits are lower.

The WDS detector installed is a parallel beam spectrometer type with a polycapillary and grazing incidence optics. A scheme of the WDS spectrometer is

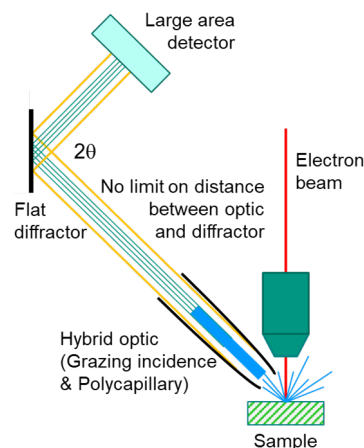


Fig. 6: Scheme of parallel beam wavelength dispersive X-ray spectrometer with hybrid optic. The angle 2θ is variable within 28° to 154° .

depicted in Figure 6. Divergent high energy X-ray fluorescence from the sample is converted into a parallel beam by a polycapillary optic located near to the sample surface to capture characteristic X-rays at a large solid angle. The polycapillary optics consist of thousands of parallel microcapillary glass tubes, diameter about 2 μm , each of which acts as a waveguide. Low energy X-rays up to about 2.2 keV are parallelized by a grazing incidence X-ray optic consisting of a paraboloidal hollow metallic tube with a highly polished internal surface which contains the polycapillary optic. The parallel X-ray beam is pointed to a flat diffractor. Different diffractors, e.g., crystals or multilayers, are mounted on a carousel and are selected automatically to cover the X-ray energy range of interest. A sealed large area Xe proportional counter tube detects the diffracted X-rays. Diffractor and counter tube are moved when scanning the selected energy range. The advantage of this design is that the diffractor is flat and can be placed at a convenient distance from the sample. Thus, no Rowland circle geometry or curved diffractors are required.

However, spectral artefacts are present at EDS and WDS spectra. Si-drift detectors cause additional lines in the X-ray spectrum like sum-peaks or escape peaks. With WDS such lines are not present but X-ray lines with low intensity from higher order reflections ($n = 2, 3, \dots$) according to Bragg's Law of diffraction ($n\lambda = 2d \sin\theta$) occur.

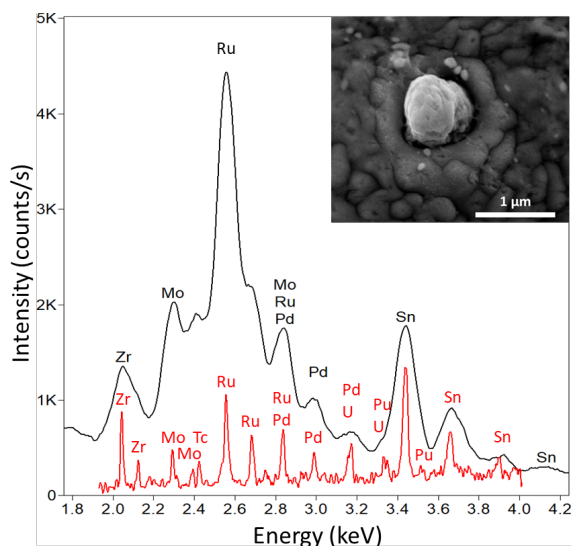


Fig. 7: Secondary electron image of an individual ϵ -particle analyzed by SEM-EDS (black curve) and -WDS (red curve), accelerating voltage 10 kV. The intensity of the WDS lines was enhanced by a factor of 20 for easier comparison.

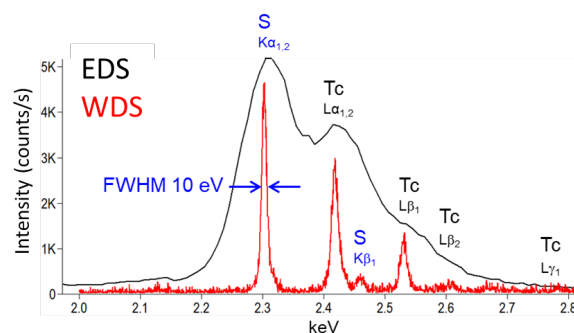


Fig. 8: SEM-EDS and -WDS spectra of S $K_{\alpha,\beta}$ and Tc $L_{\alpha,\beta,\gamma}$ X-ray lines of Tc-sulfide, accelerating voltage 10 kV. The intensity of the WDS lines was enhanced by a factor of 20 for easier comparison.

As an application example EDS and WDS spectra were recorded from a single ϵ -particle of about 1 μm in diameter (insert in Figure 7) located at the interaction zone between Zircaloy-4 cladding and a spent fuel UO_2 pellet (burn-up 50.4 GWD/tHM). Low amounts of Tc could be identified by WDS, but are not detectable by EDS (Figure 7). Regarding their catalytic effect in conjunction with the emitted β -radiation and the overall radiation field of spent nuclear fuel (SNF), ϵ -particles play an important role in local radionuclide immobilization mechanisms together with the elevated H_2 partial pressure generated in case of the SNF canister corrosion under repository conditions [5].

Another example is Tc(IV)-sulphide stabilized by $\text{Na}_2\text{S}_2\text{O}_4$. Sulfur K and technetium L lines are superimposed in the EDS spectrum but clearly resolved by WDS using a PET diffractor (Figure 8).

References

- [1] Weßling, P. et al.; *Inorg. Chem.* **59**, 12410 (2020).
- [2] Moulder, J.F. et al., *Handbook of X-ray Photoelectron spectroscopy*, ULVAC-PHI, Inc., Japan, (1995).
- [3] Kolarik, Z. et al.; *Solvent Extr. Ion Exch.* **17(5)**, 1155 (1999).
- [4] Weigl, M.; et al.; *Solvent Extr. Ion Exch.* **24(6)**, 845 (2006).
- [5] Cui, D.; et al.; *Hydrogen catalytic effects of nanostructured alloy particles in spent fuel on radionuclide immobilization*, *Appl. Catal. B-Environ.* **94**, 173, (2010).

8.4 NMR spectroscopy at INE

T. Sittel, U. Müllich, P. Weßling, N. Cevirim-Papaioannou, M. Böttle, D. Schild, C. Adam, X. Gaona, M. Altmaier, A. Geist, P. J. Panak

Introduction

NMR spectroscopy is a widely used spectroscopic method in organic and inorganic chemistry. A wide variety of experiments can be performed, yielding a wealth of chemical information (Figure 1). Experiments are feasible for substances in liquid or solid state and on a broad range of nuclei. This has led to applications of NMR in fields ranging from small molecule spectroscopy to geochemistry and even biomolecular NMR with its focus on protein molecules of several kilo daltons molecular weight.



Fig. 1: NMR spectroscopy, the chemist's Swiss army knife.

Insights on the M(III)-O interaction in Ln(III)- and An(III)-TEDGA complexes

In the recent years NMR studies of Ln(III) and An(III) complexes with N-donor ligands probed the metal-nitrogen interaction [1–2]. These studies showed that the

Am(III)-N interaction has a larger covalent contribution compared to the Ln(III)-N interaction.

Further NMR studies with hard and soft donor ligands are required to expand the understanding of these interactions. In addition to N-donor ligands, we studied the complexation of Ln(III) and Am(III,IV) with the O-donor ligand *N,N,N',N'*-tetraethyl diglycolamide (TEDGA).

NMR titration experiments show the formation of the 1:3 complexes $[M(\text{TEDGA})_3]^{3+}$ ($M = \text{La-Lu, Y, Am}$) in D_2O . In contrast, with tetravalent Pu(IV) and Th(IV), only the 1:2 complex $[\text{An}(\text{TEDGA})_2]^{4+}$ is observed in D_2O . A characteristic feature of all complexes is a fast ligand exchange rate, resulting in line broadening of all proton signals.

NMR spectra of paramagnetic compounds stand out due to the coupling of the electronic and nuclear spin. Since the electronic spin is significantly larger than the nuclear spin the coupling results in unique effects on the NMR spectrum. Mainly three effects are observed: a large chemical shift, line broadening of the signal and a temperature dependency of the chemical shift. In all cases, the effect decreases with the distance between the observed nuclei and the paramagnetic centre. Therefore, temperature dependent NMR spectra are an efficient tool to gather additional information on the structure and electronic properties of paramagnetic complexes.

As an example, Figure 2 features the ^1H NMR spectra of $[\text{Yb}(\text{TEDGA})_3](\text{NO}_3)_3$ ($[\text{Yb}] = 10 \text{ mmol L}^{-1}$) in D_2O between 300–350 K. As highlighted, the signals shift with increased temperature. Yet, the temperature effect is not pronounced equally throughout the proton spectra. Only minor temperature-dependent shifts are observed for H_5 and H_6 . In conclusion, these protons are

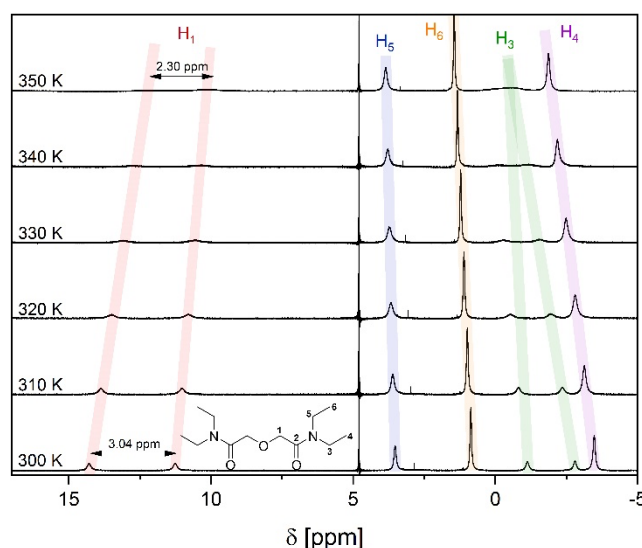


Fig. 2: Temperature dependent ^1H NMR spectra of $[\text{Yb}(\text{TEDGA})_3](\text{NO}_3)_3$ ($[\text{Yb}] = 10 \text{ mmol L}^{-1}$) recorded in D_2O [3].

located quite far away from the paramagnetic ion. In contrast, H₁ and H₃ show significant temperature-dependent shifts. They are located quite closely to the paramagnetic centre and as a result experience a strong paramagnetic influence.

In addition to the lanthanide complexes, [Am(TEDGA)₃]³⁺ was synthesized and characterized by NMR spectroscopy. The focus was on the americium-ligand interaction in direct comparison to the complexes of the trivalent lanthanides. Due to a low natural abundance of the NMR active isotope ¹⁷O the Am(III)- and Ln(III)-O bond was probed utilizing the unique electronic properties of the amide bond. In fact, the lone pair electrons of the amide nitrogen atom are delocalized in the C-O double bond, thus forming a mesomeric system [4]. Thus, information on the M(III)-O interaction can be gathered by collecting ¹³C and ¹⁵N data.

Table 1 shows the ¹⁵N and ¹³C NMR data of the amide nitrogen and carbon atoms, respectively. For both nuclei, similar chemical shifts are found for all M(III) ions studied. In conclusion, the Ln(III)-O and Am(III)-O bond show similar bonding properties, in agreement with the general observation that oxygen donors show similar complexation behaviour towards both An(III) and Ln(III).

Table 1: ¹³C and ¹⁵N chemical shifts of the amide group in [M(TEDGA)₃]³⁺ complexes (M = Am, Lu, Sm, La) in D₂O.

[M(TEDGA) ₃] ³⁺	δ ^{obs} (¹⁵ N)	δ ^{obs} (¹³ C)
Am	139	176.6
Lu	138	170.8
Sm	138	172.1
La	137	170.3

Be(II) speciation in alkaline solutions

Common NMR experiments on (in)organic compounds usually focus on the acquisition of ¹H, ¹³C, ¹⁹F and ³¹P data. Besides the complex chemistry of the actinide ions and their fission products, the chemistry of cementitious phases or irradiated materials are important research topics with respect to the safety of nuclear waste disposal. ²⁹Si, ²⁷Al or ⁹Be NMR spectroscopy are particularly well suited to investigate these topics.

Beryllium plays an important role in nuclear fission reactors due to its neutron multiplication properties, making it a useful neutron reflector. The production of ⁴He and ³H causes swelling of materials, requiring irradiated beryllium components to be replaced and disposed periodically [5,6].

Figure 3 shows the ⁹Be NMR spectra (300 K, 56.23 MHz) of a supernatant of a selected solubility sample

in 3.0 M NaCl solution at pH_m = 14.1. Compared to BeSO₄ (pH_m = 3.0) a shift of the ⁹Be signal of approx. 1.8 ppm is observed. Based on the sharp NMR signals it is concluded that in both cases a highly symmetric species is present. In conclusion, at pH_m = 14.1 the formation of Be(OH)₄²⁻ and pH_m = 3.0 the formation of [Be(H₂O)₄]²⁺ is observed.

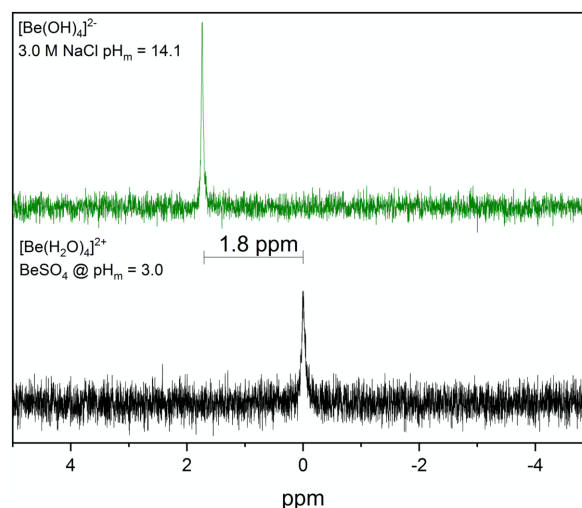


Fig. 3: ⁹Be NMR spectra (300 K, 56.23 MHz) of an acidic solution of BeSO₄ at pH_m = 3.0 and of the supernatant of a selected solubility sample in 3.0 M solution at pH_m = 14.1 [5].

Conclusion

Combined with further spectroscopic techniques available at INE (see the *Coordination Chemistry* chapter), the capability of performing NMR spectroscopy on radioactive samples provides an essential tool to study the coordination and bonding properties of actinide complexes in solution. Furthermore, ongoing studies related to the disposal of special wastes (such as beryllium containing wastes) are supported by NMR spectroscopy.

References

- [1] C. Adam et al., *Dalton Trans.*, **42**, 14068–14074 (2013).
- [2] C. Adam et al., *Chem. Sci.* **6**, 1548–1561 (2015).
- [3] T. Sittel, PhD thesis, Ruprecht-Karls-Universität Heidelberg (2021).
- [4] V. Pace et al., *Adv. Synth. Catal.*, **356**, 3697–3736 (2014).
- [5] N. Çevirim-Papaioannou et al., *Appl. Geochem.*, **117**, 104601 (2020).
- [6] G. R. Longhurst et al., *Nucl. Technol.*, **176**, 430–441 (2011).

8.5 Accelerator mass spectrometry (AMS)

F. Quinto, H. Geckeis, D. Glückman, S. Kraft, M. Plaschke, T. Roth

In co-operation with:

T. Faestermann^a, K. Hain^b, G. Korschinek^a, J. Pitters^a, G. Rugel^c, P. Steier^b

^aVERA Laboratory, Faculty of Physics, University of Vienna, Währinger Straße 17, A-1090 Vienna, Austria; ^bPhysics Department, Technical University of Munich (TUM), James-Frank-Straße 1, D-85748 Garching, Germany; ^cHelmholtz-Zentrum-Dresden-Rossendorf, Accelerator Mass Spectrometry and Isotope Research, Dresden, Germany

Introduction

AMS offers the analytical capability of determining ultra-trace levels of long-lived actinides and fission products in a variety of environmental samples. Detection efficiency for actinide nuclides and ⁹⁹Tc at the level of ca. 1×10^4 atoms (25 ag) and ca. 3×10^6 atoms (0.5 fg) in a sample, respectively [1, 2], can be reached allowing for experimental results at concentration levels that may not be obtained with more commonly used mass spectrometric techniques. This enables addressing certain scientific questions on the behavior of actinides and ⁹⁹Tc at the ultra-trace levels useful to several projects in the field of nuclear waste management, safety and radiation research. In the past two years, with the use of AMS we have investigated the long-term behavior of radionuclide tracers in the frame of the Long-Term-In-situ-Test (LIT) experiment at the Grimsel Test Site in Switzerland (CFM project), as well as in laboratory scale in-diffusion experiments through Opalinus (OPA) clay (iCross project), obtaining results relevant for the safety assessment of nuclear waste disposal in deep geological crystalline and clay host rock repositories (sub-chapter 5.4). Furthermore, we have applied AMS to the analysis of Rhine river water samples in the vicinities of the Fessenheim Nuclear Power Plant (NPP) in France, in a first attempt to gain information on the status-quo-ante relative to the ongoing decommissioning activities (EUCOR project).

Our analytical research focuses on the development of sample preparation methods enabling the concurrent determination of ultra-trace levels of several actinide nuclides and ⁹⁹Tc in clay rock, groundwater and surface water samples. In the following text, recent results concerning the analytical approach in the frame of the aforementioned projects, as well as the identification of the nuclear contamination source in the investigated Rhine River water samples are described. The actinide nuclides were analyzed at the 3 MV tandem accelerator of VERA, while ⁹⁹Tc was investigated at the 14 MV tandem accelerator of TUM.

Analysis of ⁹⁹Tc and actinide tracers in the frame of the LIT in-situ experiment

The concentration of radionuclide tracers ⁹⁹Tc, ²³³U, ²³⁷Np and ²⁴²Pu was determined in bentonite porewater mixing with Grimsel groundwater samples (LIT-GGW) from the LIT experiment. At the same time, in order to estimate a possible “shear zone” background

(sub-chapter 5.4), Grimsel groundwater samples (GGW) from the tailing of two previous in-situ radionuclide tracer tests were analyzed. Two different sample preparation approaches were applied for the two mentioned sample systems. The LIT-GGW samples (1.6 to 10 mL volume) were split in halves, each of them submitted to the sample preparation described in [2] for ⁹⁹Tc and in [3] for the actinide nuclides using a multi-actinide analysis method. A novel approach was employed for the GGW samples (500 mL volume), in which the group of actinide tracers were separated from ⁹⁹Tc with a TEVA® resin chromatographic column with a sample loading solution in 0.1 M HCl. For these samples, the lowest concentration of ⁹⁹Tc was expected and, therefore, instead of splitting the sample in halves, the tracers were extracted from the maximum available sample size. This procedure makes use of the pronounced difference in retention between Tc and the actinides from HCl media [4]. At low acidity, the high selectivity of quaternary ammonium salts of TEVA® for the pertechnetate anion TcO⁴⁻, over the acid anionic complexes of the actinides enables quantitatively retaining Tc on the column while eluting the group of the actinides. Then, the so-obtained Tc and actinides fractions were each submitted to the AMS sample preparation procedures described in [2] and [3], respectively. With these procedures, concentrations down to ca. 2×10^5 atoms/mL for ⁹⁹Tc and ca. 6×10^4 atoms/mL for ²³³U could be determined with AMS in the GGW and LIT-GGW samples (Fig. 4 and Fig. 5 in sub-chapter 5.4).

Multi-actinide analysis in clay rock and river water samples

In the frame of laboratory-scale experiments of ²³³U and ²⁴³Am in-diffusion through samples of OPA clay (sub-chapter 5.4), the multi-actinide analysis with AMS adapted to clay matrix samples was applied [5]. In this procedure, the actinide nuclides are co-precipitated as group with Fe(OH)₃ from a desorbing solution in 1M HNO₃. After co-precipitation, the so-obtained Fe(OH)₃ is converted to iron oxide at a T = 900° C and the embedded actinide nuclides are sputtered in the Cs negative ion source of AMS. During the analysis of the clay, clay porewater and 1 M HNO₃ standard samples, a decrease of the count rate of the actinide nuclide with the increase of the sample matrix was observed. In order to investigate this phenomenon, the efficiency of the

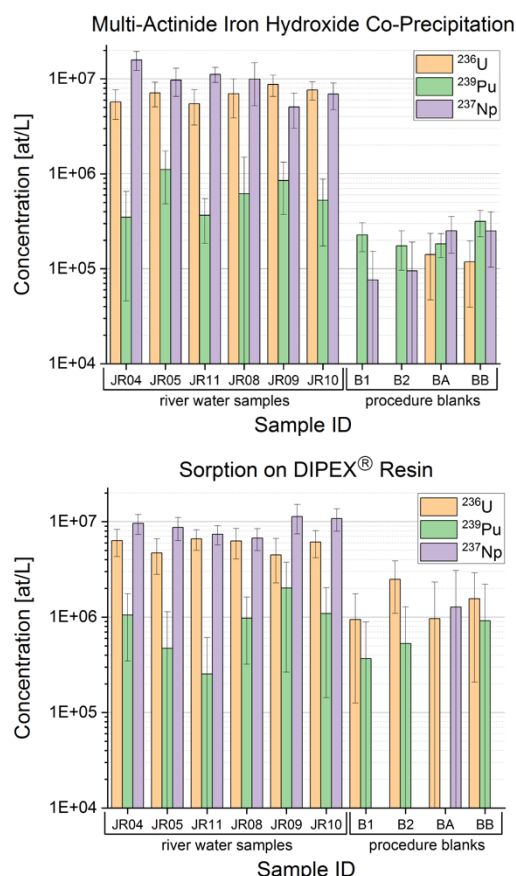


Fig. 1 Concentration of ^{236}U , ^{237}Np and ^{239}Pu in the six Rhine river water samples and four procedure blanks determined with AMS after $\text{Fe}(\text{OH})_3$ co-precipitation (above) and DIPEX sorption (below).

$\text{Fe}(\text{OH})_3$ co-precipitation for several matrix elements was determined with (SF) ICP-MS in four procedure blanks composed of clay desorbing solutions. First results show that the elements mostly contributing to the final AMS sample matrix are Al, Si and Ca. Comparing the obtained mass of the sample matrix of the clay samples with those estimated from clay porewater and standard samples, a negative exponential behavior of the count rate of the actinide tracers as function of the sample matrix was observed. Further tests are ongoing in order to validate this observation as well as to investigate possible mechanisms affecting the actinide count rate in addition to a likely dilution effect.

Maximizing the count rate of the investigated nuclide from an AMS sample is a crucial aspect for an efficient sample preparation and AMS analysis. To this purpose, we have tested a sample preparation procedure alternative to the $\text{Fe}(\text{OH})_3$ co-precipitation for multi-actinide analysis, which involves the group separation of the actinide with DIPEX® resin [6]. This resin shows a high affinity for tri-, tetra- and hexavalent actinides with the highest retention in 0.1 M HCl, but also the disadvantage that the actinides cannot be easily stripped from the extractant. However, it is possible to dissolve the extractant with the retained actinides from the resin substrate with isopropanol. We adapted this procedure

to AMS sample preparation and compared it to the $\text{Fe}(\text{OH})_3$ co-precipitation for Rhine river water samples (2 L volume, each) collected in the vicinities of the Fessenheim NPP [7]. Fig. 1 shows the concentration of ^{236}U , ^{237}Np and ^{239}Pu in six river water samples collected upstream (JR04 and JR05), in front of (JR10 and JR11) and downstream (JR08 and JR09) of the NPP, as well as four procedure blanks submitted to the two sample preparations, namely $\text{Fe}(\text{OH})_3$ co-precipitation (above) and sorption on DIPEX® resin (below) and determined with AMS. The results from all six water samples are consistent to each other, indicating repeatability of the AMS analysis between the two sample preparation procedures. We are further investigating the sorption efficiency of matrix elements, e.g., Al, Si and Ca on DIPEX® in order to verify whether this sample preparation can allow for a lower AMS sample matrix compared to the $\text{Fe}(\text{OH})_3$ co-precipitation and possibly adapt its application to other kinds of samples, i.e., clay and clay porewater specimens.

Concerning the origin of the determined anthropogenic actinides, since they show similar concentrations in all the samples, we deduce that there was no contribution of nuclear contamination from the NPP to the Rhine river water. The concentration of ^{239}Pu , which is the most abundant global fallout derived actinide nuclide [8], in the analyzed samples is on average mainly consistent to the blanks level and at least one order of magnitude lower than that of ^{236}U and ^{237}Np (Fig. 1). This can be explained with the lower solubility of Pu compared to U and Np in river water and its higher sorption onto particles undergoing sedimentation, being in this way subtracted from the river water [9]. The weighted mean of the atomic ratio $^{236}\text{U}/^{237}\text{Np}$ equal to 0.5 ± 0.1 and 0.6 ± 0.1 for the co-precipitation and resin sorption procedures, respectively, indicates a global fallout origin of the ^{236}U and ^{237}Np signals [8]. These results represent a first hint on the origin of the nuclear contamination in the vicinities of the Fessenheim NPP at the moment of sampling [7]. More conclusive results could be obtained with the analysis of river water sediment, possibly constituting a reservoir for past releases from the NPP, as well as the global fallout.

References

- [1] P. Steier et al., Nucl. Instrum. Methods Phys. Res., Sect. B, 2010, **268**, 1045.
- [2] F. Quinto et al., Anal. Chem., 2019, **91**, 4585.
- [3] F. Quinto et al. Anal. Chem., 2017, **89**, 7182.
- [4] E. P. Horwitz et al., Anal. Chim. Acta, 1995, **310**, 63.
- [5] Master Thesis Daniel Glückman (2018) KIT.
- [6] E. P. Horwitz et al., Reactive and Functional Polymers, 1997, **33**, 25.
- [7] Master Thesis Thomas Roth (2021) KIT.
- [8] M. A. Denecke et al., Experimental and Theoretical Approaches to Actinide Chemistry; Wiley, 2016, pp 378-444.
- [9] E. Klemm et al., Journal of Environ. Radioact., 2021, **232**, 106584.

8.6 Computational chemistry

R. Polly

Introduction

Computational Chemistry using *ab initio* methods at KIT-INE provides valuable fundamental insights on a molecular scale, greatly assisting, supporting and complementing experimental investigations in the field of nuclear waste disposal and fundamental radionuclide studies. There is a wide range of applications for Computational Chemistry at INE: from providing detailed structures of complex chemical systems including actinides and other radionuclides in solution, at surfaces or solid phases, to spectroscopic information reproducing the actual experimental spectra for EXAFS, (HR-)XANES or RIXS. Hence, the considered systems vary from molecular species in the gas phase over small complexes in solution to bulk phases or mineral/liquid interfaces at ambient conditions. The synergistic effects at INE from doing theoretical and experimental research together in one research institution are enormous. New theoretical methods and the constantly improving hardware allow a steady improvement of the description of actinide systems at the electronic structure level. These improvements also increase the accuracy and reliability of quantum chemistry as a predictive tool.

Quantum-chemical calculation of HR-XANES spectra and RIXS maps of actinide compounds

It is one of the main aims of the quantum chemical group to provide spectroscopic data in order to support the interpretation of experimental observations. 2020/21 was spent on systematic theoretical studies of radionuclides (Tc) and actinyl (UO_2^{2+} , NpO_2^{2+} , PuO_2^{2+}) ions to support relevant experimental X-ray studies. During the past decades, relativistic multireference *ab initio* quantum chemistry methods have developed into a powerful tool supporting X-ray spectroscopy techniques. Because of the complexity of the detected signals, theoretical calculations are mandatory for the interpretation of the experimental data.

Relativistic multireference *ab initio* calculations of Tc L_3 -edge X-ray absorption fine structure (HR-XANES) [1]

For all the relevant Tc species with different oxidation states either a molecule or a suitable model system was optimized without considering any hydration shell. All considered species have single reference ground states and therefore DFT can be applied. We optimized structures of $[\text{Tc(VII)O}_4]^-$, $[\text{Tc(V)O(OH)}_4]^-$, $[\text{Tc(IV)(GLU}_{-2\text{H}})_2(\text{OH})_2]^{4-}$ and $[\text{Tc(IV)(OH)}_6]^{2-}$ with TURBOMOLE on the RI-DFT level using the def2-TZVP basis set. The optimized structures are shown in Fig. 1 and the optimized bond lengths are included in Tab. 2.

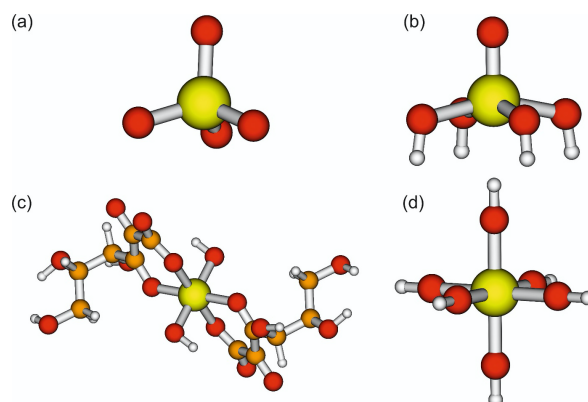


Fig. 1: DFT optimized structures for (a) tetrahedral pertechnetate $[\text{Tc(VII)O}_4]^-$, (b) square-pyramidal $[\text{Tc(V)O(OH)}_4]^-$, (c) $[\text{Tc(IV)(GLU}_{-2\text{H}})_2(\text{OH})_2]^{4-}$ (C_i symmetry) and (d) octahedral $[\text{Tc(IV)(OH)}_6]^{2-}$.

Table 1: Structural parameters (Tc-O) optimized by DFT

Tc(VII)O_4^-	Tc-O	4	1.79
$[\text{Tc(V)O(OH)}_4]^-$	Tc-O ₁	1	1.71
	Tc-O ₂	4	2.01
$[\text{Tc(IV)(OH)}_6]^{2-}$	Tc-O	6	2.01
$[\text{Tc(IV)(GLU}_{-2\text{H}})_2(\text{OH})_2]^{4-}$	Tc-O ₁	2	1.99
	Tc-O ₂	4	2.07
	average		2.04

The pertechnetate ion $[\text{Tc(VII)O}_4]^-$ has a well-defined tetrahedral structure (Fig. 1a) which we optimized by DFT. The Tc-O bond distances are 179 pm which compares very well with the available experimental data (for a detailed comparison with experimental data see [1]). For the Tc(V) species we optimized a pyramidal $[\text{Tc(V)O(OH)}_4]^-$ cluster in C_{4v} symmetry (Fig. 1b). The four dangling bonds at the oxygen atoms were saturated with hydrogen atoms. The two Tc-O bond lengths are 171 and 201 pm, respectively. The results agree very well with the experimental data of 164 and 197 pm. For the solid $\text{TcO}_2(\text{s})$ we optimized a $[\text{Tc(IV)(OH)}_6]^{2-}$ model system (Fig. 1d) in O_h symmetry and saturated the dangling oxygen bonds with hydrogen atoms. The corresponding Tc-O bonds are with 201 pm very close to the experimental results for Tc(IV) complexes, e.g., Tc(IV)-oxalate (199 pm average Tc-O distance). For the structure of the Tc(IV)-gluconate complex a model comprising two $(\text{OH})^-$ and two $(\text{GLU}_{-2\text{H}})^{3-}$ moieties was assumed. The corresponding Tc K-XANES spectrum lacks a $1s \rightarrow 4d/5p$ pre-edge feature, thus pointing to inversion symmetry in this structure. Accordingly, we optimized the $[\text{Tc(IV)(GLU}_{-2\text{H}})_2(\text{OH})_2]^{4-}$ structure in C_i symmetry (see Fig. 1c). The oxygen atoms forming bonds to Tc

are in an arrangement resembling very closely the octahedral symmetry. The corresponding bond lengths are 199 pm for Tc-O(H) and 207 pm for Tc-O(COH). Both average to 204 pm.

We tackled the calculation of the Tc L_3 -XANES spectra (corresponding to $2p_{3/2} \rightarrow 4d_{3/2,5/2}$ excitations) of the different Tc moieties applying relativistic multi-reference *ab initio* methods available in MOLCAS8.4. We used the restricted active space (RASSCF) method and for the inclusion of the dynamical correlation second-order perturbation theory RASPT2 with an IPEA shift of 0.0. Spin-orbit interactions were calculated in the restricted-active-space state-interaction (RASSI) scheme¹²⁷. For the RASSCF/RASPT2 calculations we subdivided the active space. The RAS1 space contains the core states (2p) and the 4d orbitals in the RAS2/3 space. In total we had six ($[\text{Tc}(\text{VII})\text{O}_4]^-$), eight ($[\text{Tc}(\text{V})\text{O}(\text{OH})_4]^-$) and nine ($[\text{Tc}(\text{IV})(\text{OH})_6]^{2-}$) active electrons distributed in the active space. There were no restrictions on the number of electrons in RAS1 for the ground state calculations, but for the excited state calculations the RAS1 space was restricted to contain only five electrons. Both scalar relativistic and spin-orbit coupling were accounted for in our calculations. For the spin-orbit interaction calculations all relevant spin states were included in the calculations. As basis sets we used the ANO basis sets (VDZ/VTZ and VQZ) available in MOLCAS. We performed the calculations using the full t_d $[\text{Tc}(\text{VII})\text{O}_4]^-$, C_{4v} $[\text{Tc}(\text{V})\text{O}(\text{OH})_4]^-$ and O_h $[\text{Tc}(\text{IV})(\text{OH})_6]^{2-}$ symmetry with the SUPERSYMMETRY option imposing higher supersymmetry by restricting rotations to irreducible representations in the RASSCF calculations. Experimental spectra were simulated by applying a Lorentzian profile at the calculated transition energies with the intensities given by the oscillator strengths with a full width at half maximum of $\gamma=1.2$ -2.5 for the different species.

We determined the excitation energies corresponding to the Tc L_3 -XANES of TcO_4^- with the ANO-VDZ/VTZ/VQZ basis sets. The results are summarized in Tab. 2. Both RASSCF and RASPT2 results are similar and in good agreement with experimental data. The RASPT2/ANO-VQZ results (transition energies and scaled oscillator strengths) are shown in the right panel of Fig. 2.

Table 2: Tc L_3 -XANES excitation energies of TcO_4^- . Comparison of calculated and experimental results. All energies in eV.

Method	Basis set	E ₁	E ₂	DE=E ₂ -E ₁
Exp		2678.7	2680.9	2.2
RASSCF	ANO-VDZ	2702.8	2705.7	2.9
RASPT2		2698.7	2700.2	1.5
RASSCF	ANO-VTZ	2698.9	2701.7	2.8
RASPT2		2694.0	2695.5	1.5
RASSCF	ANO-VQZ	2694.8	2697.7	2.9
RASPT2		2689.9	2691.4	1.5

Due to the ligand field splitting of the d-orbitals in the tetrahedron there are two lower lying states in the irreducible representation E of t_d and three higher lying states in T_2 . The two peaks visible in the spectrum (denoted as 1 and 2 in Tab. 2) can be assigned to excitations from $2p_{3/2} \rightarrow 4d_{xz}/4d_{x^2-y^2}$, $4d_{yz}/4d_{xy}$ (2678.7 eV, all 4d orbitals in E) and $2p_{3/2} \rightarrow 4d_{yz}/4d_{xy}$, $4d_{xz}/4d_{x^2-y^2}$, $4d_{z^2}$ (2680.9 eV, all 4d orbitals in T_2). The excited states are predominantly singlet states (S=0) with a small admixture of triplet states (S=1). Due to the orientation of one TcO bond along the z-axis the 4d orbitals mix strongly. The improvement of the results increasing the basis set from ANO-VDZ to ANO-VQZ can be clearly seen. The energy shift compared to the experimental spectra is significantly reduced with increasing basis set size. For all applied basis sets the RASPT2 results are closer to the experiment compared with the corresponding RASSCF result. The splitting between the two peaks is ~ 2.8 -2.9 eV for the RASSCF calculations and ~ 1.5 eV for the RASPT2 calculations. Therefore, the RASPT2 results are in slightly better agreement with experiment compared to the RASSCF results. It can be seen from Fig. 2 that the Tc L_3 -XANES spectrum of $[\text{Tc}(\text{VII})\text{O}_4]^-$ consist only of a few transitions.

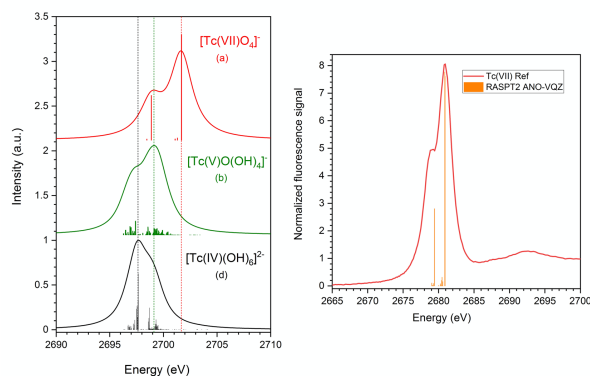


Fig. 2: Left panel: *Ab initio* Tc L_3 -XANES spectra of $[\text{Tc}(\text{VII})\text{O}_4]^-$, $[\text{Tc}(\text{V})\text{O}(\text{OH})_4]^-$ and $[\text{Tc}(\text{IV})(\text{OH})_6]^{2-}$ (vertically shifted for clarity) obtained by RASSCF/ANO-VTZ calculations based on DFT structure optimizations (cf. Fig. 1) – vertical bars representing transition energies and oscillator strengths of relevant Tc $2p_{3/2} \rightarrow 4d_{5/2}$ excitations and spectral envelopes (solid lines) obtained by convoluting bars with Lorentzians (cf. text for details). Right panel: *Ab initio* Tc L_3 -XANES spectra of $[\text{Tc}(\text{VII})\text{O}_4]^-$ (bars) obtained by RASPT2/ANO-VQZ calculations (shifted -4.57eV) compared to experimental spectrum (solid line).

For the calculations on $[\text{Tc}(\text{V})\text{O}(\text{OH})_4]^-$, $[\text{Tc}(\text{IV})(\text{OH})_6]^{2-}$ and $[\text{Tc}(\text{IV})(\text{GLU}_{-2\text{H}})_2(\text{OH})_2]^{4+}$ we applied only the RASSCF method with the ANO-VTZ basis set due to the very large number of involved excited states. The Tc L_3 -XANES spectrum of $[\text{Tc}(\text{V})\text{O}(\text{OH})_4]^-$ clearly shows two main peaks. The splitting of the 4d states in this pyramidal structure is similar as in the octahedral ligand field (Fig. 2). The 4d orbitals form two groups. In the first group are three 4d orbitals (irreducible representation E_g and B_{2g}). They have lower energies compared to the second group. Two are degenerate (d_{xz} and d_{yz} in E_g) and the third (d_{xy}

in B_{2g}) has slightly lower energy. In the second group (irreducible representation A_{1g} and B_{1g}) the orbital energies are significantly higher, but they are not degenerate. The orbital energy of d_{z^2} in A_{1g} is slightly lower than the orbital energy of $d_{x^2-y^2}$ in B_{1g} . The two peaks featured in the XANES spectrum can be assigned to excitations of an additional electron into one of these two groups, either d_{xy} , d_{xz} , d_{yz} or d_{z^2} , $d_{x^2-y^2}$ (see Fig. 3). The states with orbital occupations of both groups are exclusively triplet states ($S=1$). Fig. 2 also clearly shows that many closely spaced transitions contribute to this Tc L_3 -XANES spectrum.

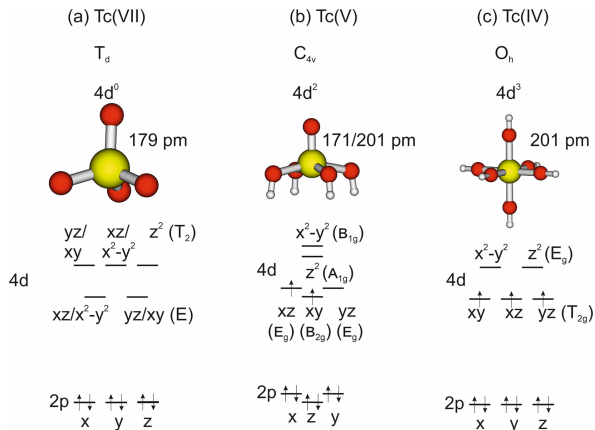


Fig. 3: Diagram of Energy levels for (a) tetrahedral pertechnetate $[Tc(VII)O_4]$, (b) square-pyramidal $[Tc(V)O(OH)_4]$, and (c) octahedral $[Tc(IV)(OH)_6]^{2-}$.

The experimental Tc L_3 -XANES spectrum of $[Tc(IV)(OH)_6]^{2-}$ shows only one main peak which we can very well reproduce with our RASSCF calculations. However, a small shoulder at the higher energy side is visible. In the octahedral ligand field the 4d orbitals form two groups, d_{xz} , d_{yz} , d_{xy} in T_{2g} and d_{z^2} , $d_{x^2-y^2}$ in E_g . In the ground state with $S=3/2$ all three orbitals in T_{2g} are occupied with parallel spin. The reason for the shape of the L_3 -XANES spectrum are excitations into these two groups (T_{2g} and E_g) as shown in Fig. 2. The two groups of transitions are hardly discernible in the final simulated spectrum (as in the experimental, nearly symmetric WL), because there are so many transitions close in energy. Both groups are a mixture of quartet ($S=3/2$) and doublet ($S=1/2$) states. As for $[Tc(V)O(OH)_4]$ the $[Tc(IV)(OH)_6]^{2-}$ Tc L_3 -XANES spectrum is again the sum of many transitions (Fig. 2). Although we were able to accurately reproduce the experimental Tc-O distances for Tc(IV)-gluconate applying the DFT optimized $[Tc(IV)(GLU_{-2H})_2(OH)_2]^{4-}$ structure, we failed to reproduce the distinct WL splitting into two clearly separated peaks obtained for the Tc L_3 -XANES. The calculated Tc L_3 -XANES spectrum based on the $[Tc(IV)Glu_2(OH)_2]^{4-}$ structure (not shown) only slightly differs from that obtained for $[Tc(IV)(OH)_6]^{2-}$, i.e., exhibits a broad, nearly symmetric WL resonance.

As mentioned above, the calculated $[Tc(IV)(OH)_6]^{2-}$ and the $[Tc(IV)(GLU_{-2H})_2(OH)_2]^{4-}$ Tc L_3 -XANES spectra are a convolution of many single transitions. The spectrum of $[Tc(IV)(OH)_6]^{2-}$ in Fig. 2 clearly

shows two distinct groups of transitions split by about 2 eV in energy forming the overall shape of the spectrum. The same is observed for the $[Tc(IV)(GLU_{-2H})_2(OH)_2]^{4-}$ spectrum (not shown), but the calculated splitting between the two groups is not large enough to reproduce the observed Tc L_3 -XANES. We conclude for now that in this case the Tc L_3 -XANES spectrum depends very critically on the per se unknown molecular structure of the Tc(IV) coordination. Thus, the DFT optimized $[Tc(IV)Glu_2(OH)_2]^{4-}$ structure might not be close enough to the ‘real’ structure to reproduce the Tc L_3 -XANES spectrum. Nevertheless, from the comparison of the three calculated Tc L_3 -XANES spectra of $[Tc(VII)O_4]$, $[Tc(V)O(OH)_4]$ and $[Tc(IV)(OH)_6]^{2-}$ in Fig. 2 (spectra not shifted with respect to experimental data) it can be clearly seen that the spectra obtained with RASSCF reproduce very well the experimental findings regarding the overall spectral shape and the relative WL positions. This very clearly demonstrates

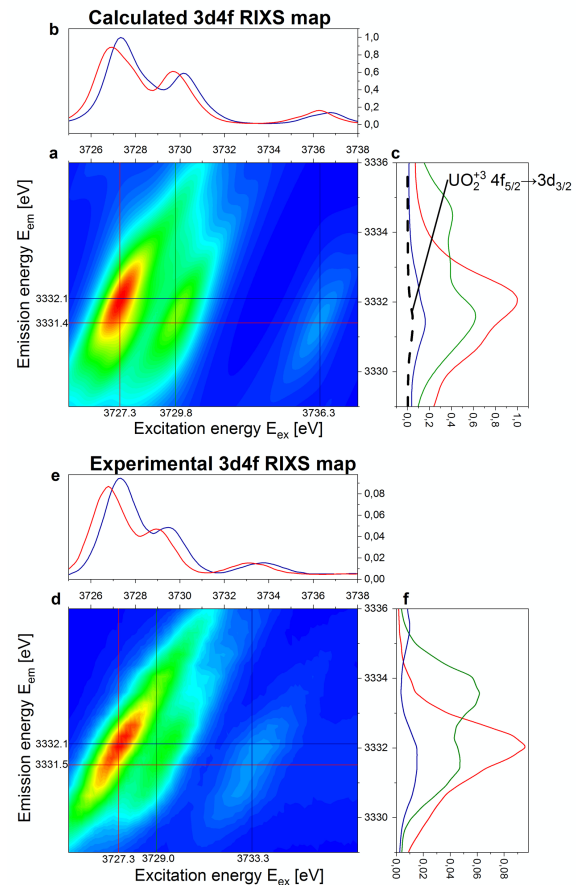


Fig. 4: RASPT2 calculated [2] and experimental [3] (see Fig. 3a therein) 3d4f RIXS maps of uranyl UO_2^{2+} depending on the excitation energy E_{ex} and emission energy E_{em} . (a) calculated and shifted ($E_{ex} = -13.6$ eV / $E_{em} = -21.2$ eV) 3d4f RIXS map (b) calculated HR-XANES spectra at the maximum of the resonant (3332.1 eV) and non-resonant (normal) emission (3331.4 eV). (c) RIXS emission lines calculated at the three peak maxima and calculated $4f_{5/2} \rightarrow 3d_{3/2}$ transitions of UO_2^{3+} (dashed black line). (d) experimental 3d4f RIXS map. (e) HR-XANES spectra measured at the maximum of the resonant (3332.1 eV) and non-resonant (normal) emission (3331.5 eV). (f) RIXS emission lines measured at the three peak maxima (all energies in eV).

the high quality of our relativistic multireference *ab initio* calculations and supports the assignment of the observed WL features in the experimental spectra to electronic transitions obtained by our *ab initio* calculations.

Relativistic multiconfigurational *ab initio* calculation of uranyl 3d4f Resonant Inelastic X-ray Scattering (RIXS) [2]

The main goal of this work is to show that relativistic multiconfigurational *ab initio* calculations of RIXS spectra can be applied to challenging chemical systems involving actinide (An) ions providing accurate results and reproduce the multiplet structure of the spectra. The calculations help to understand a complex RIXS map of An systems in a clear and transparent way. The results of our calculations allow to answer several open questions concerning some features of the 3d4f RIXS map observed by Vitova et al. [3]:

(1) clarification why the two peaks attributed to the excitation into $5f \pi^*$ and $5f \sigma^*$ are slightly red shifted (to lower energy) in emission compared to the $5f \delta\phi$ peak, (2) explanation why the maxima of the resonant and the non-resonant (normal) emission of the RIXS map do not coincide and

(3) understanding why the HR-XANES spectra measured by positioning the X-ray emission spectrometer at the maximum of the resonant or non-resonant (normal) emission line differ only slightly.

These calculations are, to our knowledge, the first application of relativistic multiconfigurational *ab initio* methods to RIXS maps of An systems.

As can be seen from Table 2 the calculated data [2] agrees very well with the experimental results [3]. The most pronounced feature in the RIXS map are the splittings of the 3 pronounced peaks in emission, which can be explained by the excitation into the non-bonding $5f \delta\phi$, and antibonding $5f \pi^*$ and $5f \sigma^*$ orbitals of uranyl. The reason of the splitting observed in emission between these three peaks was previously unknown and can be clearly explained with the help of the relativistic multiconfigurational *ab initio* calculations. The final states of the RIXS process possess a hole in the $4f \delta\phi$, $4f \pi$ and $4f \sigma$ core orbitals. The splitting of the states with different $4f$ orbital occupation is the reason for the splitting of the peaks in the emission energies. This excellent agreement between our theoretical data and the measurements shows that the approach using

the RASSCF/RASPT2 methods followed by the inclusion of SOC is applicable to the accurate calculation of An M_4 HR-XANES and $3d4f$ RIXS maps and reproduces the multiplet structure of the uranyl spectra faithfully.

We show that the multiconfigurational protocol which is nowadays applied as a standard tool to study X-ray spectra of transition metal complexes can be extended to the calculations of RIXS maps of actinide compounds. They have many intermediate- and final-state multiplets of the RIXS process with rather complicated electronic structures and they can be accurately described with our theoretical approach.

The calculations presented in this work establish relativistic multiconfigurational *ab initio* methods as a new powerful tool for the reproduction of resonant inelastic X-ray scattering maps involving actinides.

Table 2: Peak positions of the 3 d4f RIXS map of uranyl and positions of the maxima of the resonant and non-resonant (normal) emission (see Fig. 3 in [3]). All the calculated values are shifted by $E_{ex} = -13.6$ eV, $E_{em} = -21.2$ eV to align with the experimental data (energies in eV).

Theory: RASPT2 calculations				
	Excitation energy		Emission energy	
	E_{ex}		E_{em}	
$5f \delta\phi$	3727.3	-	3332.1	-
$5f \pi^*$	3729.8	+2.5	3331.5	+3.1
$5f \sigma^*$	3736.3	+9.0	3331.4	+9.7
Experiment [3]				
$5f \delta\phi$	3727,3	-	3332.1	-
$5f \pi^*$	3729,0	+1.7	3331.5	+2.3
$5f \sigma^*$	3733,3	+6.0	3331.6	+6.5

References

- [1] K. Dardenne, S. Duckworth, X. Gaona, R. Polly, B. Schimmelpfennig, T. Pruessmann, J. Rothe, M. Altmaier and H. Geckeis, *Inorg. Chem.* **60** (16), 12285 (2021)
- [2] R. Polly, B. Schacherl, J. Rothe, T. Vitova, *Inorg. Chem.*, online Nov. 2021
- [3] T. Vitova, I. Pidchenko, D. Fellhauer, P. Bagus, Y. Joly, T. Prüssmann, S. Bahl, E. Gonzalez-Robles, J. Rothe, M. Altmaier, M. Denecke, H. Geckeis, *Nature Commun.* **8**, 1-9 (2017).

9 (Radio-)chemical analysis

The business of the analytical team is the (radio-)chemical analysis for the INE R&D projects, analytical service for external clients, development and adaption of analytical methods, teaching and education, and, finally, support of the INE infrastructure. For these goals, a pool of instrumentation for the analysis of radioactive and non-radioactive samples as well as highly qualified personnel are available. Our special skills are in handling of radioactive material, separation procedures for element and isotope analysis, as well as operation and maintenance of glove box adapted instrumentation. Our analytical service for external clients is in the fields of decommissioning of nuclear installations, nuclear waste declaration, nuclear pharmacy and others. Many of the analytical instruments are operated both in cold and radioactive labs. We have a special focus on mass spectrometry for trace element analysis and speciation studies of actinides and fission products. Hyphenated techniques, like Sector Field or Quadrupole ICP-MS coupled to species sensitive methods, e.g., to capillary electrophoresis (CE) or ion chromatography (IC), are adapted and further developed. Another focus is Accelerator Mass Spectrometry (AMS) for the supersensitive determination of actinides below ppq levels and ^{99}Tc at the ppq levels, achieved in close cooperation with international AMS facilities.

M. Plaschke, M. Böttle, M. Bouby, D. Fellhauer, N. Finck, M. Fuss, A. Fried, X. Gaona, F. W. Geyer, T. Kisely, S. Kraft, S. Kuschel, M. Kuss, J. Lützenkirchen, C.M. Marquardt, R. Meier, S. Moisei-Rabung, A. Pfeil, F. Quinto, S. Ratnayake, D. Rehorn, J. Rentmeister, E. Rolgejzer, T. Roth, D. Schild, A. Seither, C. Walschburger, and H. Geckeis.

In co-operation with:

K. Hain^a, P. Steier^a, C.-O. Krauß^b, A. Heneka^b, S. Gentes^b, G. Roth^c, A. Salimi^c, M. Weiser^c, S. Weisenburger^c, C. Willberger^c

^aVERA Laboratory, Faculty of Physics, University of Vienna, Währinger Straße 17, A-1090 Vienna, Austria

^bDepartment of Deconstruction and Decommissioning of Conventional and Nuclear Buildings, Institute for Technology and Management in Construction (TMB), KIT Campus South, Germany

^cKraftanlagen Energies & Services GmbH, Ridlerstraße 31 c, D-80339 München, Germany

Instrumentation

The analytical instrumentation of INE is continuously modernised and supplemented. A state-of-the-art TripleQuad-ICP-MS (Thermo Scientific iCAP TQs) is installed in a non-radioactive lab. The triple-quadrupole technology is capable of analyzing trace elements in the ultra-trace range even in difficult matrices. Another new instrument is the Quantulus GCT 6220 liquid scintillation counter (Perkin Elmer) with unsurpassed performance for measuring radionuclides (RN). The Guard Compensation Technology (GCT) technology combined with Bismuth Germanium Oxide (BGO) guard background reduction accurately measures to near-background levels. Another new tool is a capillary ion chromatography (IC, Thermo Scientific) system providing intrinsic advantages for radioactive applications, such as improved productivity, less waste volume or measurement of small sample quantities. Table 1 presents the spectrum of analytical techniques available at INE.

External clients

Analytical service is offered to external clients, e.g. in the fields of nuclear waste declaration or nuclear pharmacy.

Nuclear pharmacy

In 2018 a co-operation in the field of nuclear pharmacy with the Norwegian company *Oncoinvent AS* (www.oncoinvent.com) started. Actually, several tenth of samples are analysed at INE per year with regard to

toxic heavy metal trace impurities. *Oncoinvent* is committed to developing new innovative products to provide better treatment options for cancer patients. The radiopharmaceutical Radspherin[®] is a novel alpha-emitting radioactive microsphere suspension designed for treatment of metastatic cancers in body cavities. The first clinical indication for Radspherin[®] will be treatment of peritoneal carcinomatosis (information taken from [1]). Clinical development will be conducted in collaboration with European and American clinical research centers.

Table 1: Analytical techniques available at INE

<p>Element and Isotope Analysis Universal Cell Inductively Coupled Plasma Mass Spectrometry (ICP-MS) Triple Quadrupole ICP-MS Sector Field (SF)-ICP-MS ICP Optical Emission Spectrometry (ICP-OES)</p>
<p>Nuclear Spectroscopic Methods Alphaspectrometry Liquid Scintillation Counting (LSC, conventional/high sensitivity) Gamma spectrometry (with auto-sampler)</p>
<p>Other Methods (Capillary) Ion Chromatography (IC) Gas Chromatography (GC) Carbon Analysis (TOC, DOC, TIC, NPOC) Specific Surface Area Analysis (BET) Differential Thermal Analysis (DTA) Dilatometry Fusion and Microwave Digestions</p>

The active component ^{224}Ra is incorporated in inorganic microparticles of Ca_2CO_3 acting as carriers in the human body. This allows for a relative slow degradation in the body and a regional retention of effective radiation dose. In addition, INE continued the longtime cooperation with the *Bayer* company (www.pharma.bayer.com) for the quality control analysis of Xofigo[®], also containing a short half-live and short range alpha emitter as active component, in this case ^{223}Ra .

Nuclear waste treatment and decommissioning of nuclear facilities (KTE)

Since more than 20 years, INE provides analytical service for KTE (Kerntechnische Entsorgung Karlsruhe GmbH). The origin of the samples are the different waste treatment facilities of KTE, mainly the incineration facility (producing ashes) and the evaporation plant (producing liquid waste concentrates). Annually averaged samples from the different waste treatment facilities as well as samples from decommissioning of nuclear facilities (e.g., demolition waste) and others (e.g., wipe tests) are analysed. At INE, isotope concentrations and nuclide vectors are determined by the combination of nuclear and mass spectrometry techniques. The main purpose of these determinations is the waste declaration according to the conditions of acceptance for the Konrad nuclear waste repository for low- and intermediate-level nuclear waste. The analysed RN include neutron activation and fission products (^{55}Fe , ^{63}Ni , ^{90}Sr), as well as actinides ($^{233,234,235,236,238}\text{U}$, $^{238,239,240,241,242}\text{Pu}$ and $^{242,243+244}\text{Cm}$).

In addition, the analysis of the fission product ^{99}Tc will become increasingly important in the dismantling of the former reprocessing and vitrification plants Karlsruhe (WAK and VEK). ^{99}Tc is analysed by ICP-MS on mass 99, but this can be interfered by natural ruthenium (Ru_{nat}). However, in samples from a nuclear facility the isotope composition of Ru may change from its natural abundance because of the contribution of fission-derived Ru (Ru_{sp}). In order to quantify the contribution of Ru_{nat} and Ru_{sp} , a chemical separation study of the Tc and Ru fractions in a wipe test sample was performed. It could be derived from the $^{101}\text{Ru}/^{102}\text{Ru}$ ratio, that the Ru-fraction contained almost only Ru_{sp} , which had no interference on the determination of ^{99}Tc [2]. From the determined isotope ratio of Ru_{sp} together with the known isotope ratio of Ru_{nat} a mathematical correction of mass 99 for an accurate determination of ^{99}Tc is possible (see Fig. 1).

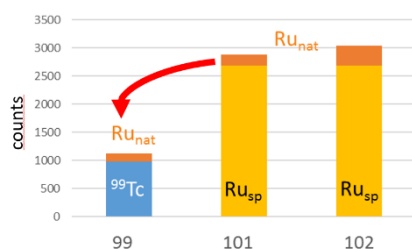


Fig. 1: Scheme of the mathematical correction for an accurate determination of ^{99}Tc (blue) on mass 99 using the known isotope ratio of Ru_{nat} (dark orange) and Ru_{sp} (light orange) on masses 101 and 102, see text.

Competence laboratory for glass development

In a collaboration between KIT and *Kraftanlagen Heidelberg* (KAH) a laboratory for waste-specific glass development including all necessary laboratory tests and the analysis is established at INE. The analytical team supports the glass laboratory by practical laboratory analysis, i.e. the analysis of the glass components or leachates. The glass composition is analysed by adapted digestion techniques, elemental analysis (ICP-OES) or chromatography (IC).

Two different types of waste glass have been developed, one for legacy waste and the other for pilot reprocessing plant waste. Major challenges associated with the legacy waste is the required high waste glass loading and the high concentration of sulfur (S) in this type of waste. A legacy waste glass (LWG) has been developed that can incorporate a maximum amount of S without phase separations between the glass and S containing compounds in the glass (yellow phase, dominated by SO_4^{2-} and other compounds). The requirements for this LGW is a 25 wt% waste loading and a 0.716 wt% nominal SO_3 content. Samples with a SO_3 target value of 2 wt% were prepared to explore the maximum S capacity of the LWG (to compensate for any S fluctuations during the plant operation). These glass samples were analysed by IC for S (determined as sulphate after KOH fusion melting of the glass).

Table 2: Analysis of LWG samples by IC to evaluate the S capacity of the waste glass, see text

sample No.	target value wt% SO_3	found by IC wt% SO_3	Δ wt% SO_3
1	2.0	2.0	0
2	2.0	1.6	-0.4
3	2.0	1.8	-0.2
4	2.0	1.2	-0.8
mean		1.7 ± 0.3	

From the IC results (see Table 2) one can conclude that the developed LWG can incorporate more than the nominal SO_3 content of 0.716 wt% in the waste without signs of phase separation. However, several issues still need to be addressed to confirm this conclusion, such as the fact that the mean value of SO_3 found by IC in the glass samples is lower than the target value.

Analysis for INE R&D

In the following, selected INE R&D topics are addressed from the analytical perspective.

Decommissioning

Monitoring of micro pollutants during the decommissioning of a nuclear power plant (NPP)

Within the Framework of ‘EUCOR – the European Campus’, the project ‘C⁴-PON’ strives to provide insight into the effect that the decommissioning process of a NPP may have on the environment [3]. The Fessenheim NPP is located in northeast France at the Grand Canal of Alsace, a man-made by-channel of the Rhine River. As of June 2020, both reactors are shut down and the power plant entered the decommissioning phase.



Fig. 2: Sampling locations and position of the Fessenheim Nuclear Power Plant at the Grand Canal of Alsace and the Old Rhine River, image adapted from "Google maps", see text.

As part of a master's thesis, six Rhine river water samples of three locations (named JR04 to JR11 as marked in Figure 2; samples taken upstream, at and downstream of the NPP) from the Grand Canal of Alsace and the Old Rhine River, respectively, were analysed, with the goal to establish a status quo of the RN content of the water before the start of the decommissioning phase. The samples were measured via AMS to determine the concentrations of the anthropogenic RN ^{236}U , ^{237}Np , ^{239}Pu and ^{240}Pu . All AMS measurements were performed by the staff of the VERA AMS facility at the University of Vienna. Samples were prepared via multi-actinide iron hydroxide co-precipitation of 2 L aliquots of river water [4]. All actinides were simultaneously separated from the sample solution by co-precipitation on iron hydroxide. The precipitate was combusted to iron oxide in an oven at 800 °C and subsequently analysed.

No significant differences between the six different sampling locations were detected and no influence of the NPP was found. The determined average concentrations for ^{236}U and ^{237}Np , $(5.8\pm 0.9)\cdot 10^6$ atoms/L and $(9.1\pm 1.8)\cdot 10^6$ atoms/L, respectively, and a $^{236}\text{U}/^{237}\text{Np}$ isotopic ratio of 0.519 ± 0.10^6 , indicate an origin from global fallout. No ^{239}Pu and heavier Pu isotopes above the background could be detected. Heavier Pu isotopes could be bound to the river sediment, which would be in agreement with literature studies dealing with the analysis of Pu in river water samples.

The determined $^{236}\text{U}/^{237}\text{Np}$ isotopic ratio was found to be similar to a literature value of 0.43 ± 0.05 , found for

a natural water sample located in a German natural reserve approximately 110 km to the northeast of Fessenheim [4]. The determined ^{236}U concentrations were compared to a literature value of $(2.5\pm 0.7)\cdot 10^7$ atoms/L for river water from the Danube River in Romania, close to the Black Sea, and found to be lower by one order of magnitude [5]. The calculated detection limit of $2.28\cdot 10^5$ atoms/L for the measurement of ^{239}Pu was compared and found to be similar to a literature value of $(2.1\pm 0.5)\cdot 10^6$ atoms/L for river water of the Danube River [5], indicating a lower concentration of ^{239}Pu for the Rhine River.

The present results will serve as a baseline measurement of the Rhine river water for further works in the $\text{C}^4\text{-PON}$ project that will accompany the Fessenheim NPP throughout its decommissioning process. Further discussion on sample preparation and results can be found in chapter 8.5.

Reduction of secondary waste produced during decommissioning of a NPP

A promising approach to reduce the amount of secondary waste produced by the waterjet abrasive suspension cutting technique (WASS) in the context of decommissioning of a NPP is represented by the joint KIT (INE and TMB) project "Magnet-Separation von Korngemischen zur Minimierung von Sekundärabfällen im Rückbau kerntechnischer Anlagen" (MaSK). Within this project, a multi-step mechanic and magnetic pilot separation device was constructed, successfully tested and further optimized [6]. It could be demonstrated that the separation of magnetic steel particles from the grain suspension can be markedly improved compared to a previous device. The separation efficiency is quantified at INE by the analysis of the steel fraction in the secondary waste by, i.e., ICP-OES. In a follow-up project, called NaMaSK, questions concerning the nuclear operation of the separation device and the use of corrosion inhibitors for low-alloy steels will be investigated. Actual developments aim at a continuous operation of the separation device.

Solubility studies in highly saline solutions

INE contributes to the activities of BGE (*Bundesgesellschaft für Endlagerung*) for emergency preparedness in particular by evaluating the geochemistry of RN in several potential scenarios for the future evolution of the Asse II salt mine. Important aspects are the estimation of robust RN source terms, and assessment of solubility limitations and retention processes within the emplacement chambers, amongst others. One part of the work for BGE focuses on the potential impact of organic compounds present in the waste forms on the solubility of specific elements and RN in highly saline solutions. In the present stage of the project, solubility studies with Pb, Nd, Th and U were performed in generic NaCl-, MgCl₂- and CaCl₂-dominated solutions in presence of various organic ligands. As a function of time, regular samplings of pH and quantification of the element and RN concentration by ICP-MS after 10 kD ultrafiltration were conducted. Works with highly concentrated salt solutions require large dilution steps of

the sample aliquots for the MS analysis. This increases the effective detection limit. In the present work, a successful determination of the RN concentration in samples with low solubility was, therefore, only possible by the use of the SF-ICP-MS. The application of highly sensitive analytical methods enables a realistic estimation of RN concentrations in saline solutions and a trustworthy evaluation of the potential impact of organic compounds on the solubility behavior.

Mobilization of RN from soil samples of Sri Lanka

Column experiments allow studying the mobility of trace elements for the large soil-to-liquid ratios that are more realistic in natural settings and can be viewed as “close-to-reality” mobilization tests. In our study, column experiments assist investigations of the vertical mobilization of Th, U, and La, by imposing a continuous and constant flow of a leaching solution of defined composition. The closest phenomenon to mimic this kind of column experiments is percolation, consisting in elemental leaching from topsoil into the groundwater. Studying the mobility of Th, U and La, here involves column leaching experiments with simulated rainwater (SRW) along with focus on some potential carrier phases such as silica nanoparticles (Si NPs – as a proxy for anthropogenic released NPs) and humic acids (HA – as a proxy for naturally occurring organic colloidal matter). Columns were leached with SRW and HA solution or in the case of soil with Si NPs initially homogenized and subsequently leached with a NP free solution. The determination of trace element concentrations (such as Th, U, and La) in the liquid phase for the investigated eluents from column experiments and groundwater samples was performed with ICP-MS, X-Series II and iCAP TQs (both Thermo Scientific).

Results from the columns corresponding to the three systems described above and their leaching patterns are shown in Figure 3. The vertical leachability as observed in column experiments with SRW suggests that trace elements show higher mobility during the first days of the experiment and eventually reach the independently measured groundwater levels (colored regions in Figure 3). Results from column experiments with HA and Si NPs indicate that colloidal species such as HA and Si NPs are not as mobile as assumed and

rather appear to be predominantly retained within the soil. Moreover, the column experiments (in the presence and absence of “mobile” colloidal species), representing potential transfer to underground water systems, yield lower mobile fractions of Th and U than synthetic rainwater only. For La, there is not an obvious trend.

Overall, this work highlights the need for comprehensive studies ideally including several environmental compartments in order to better understand the environmental dispersion, fate and impact of natural RN for risk assessment purposes.

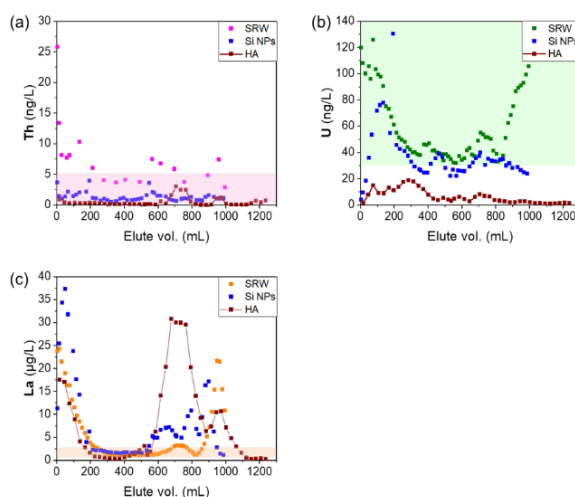


Fig. 3: Comparison of column experiments from simulated rainwater (SRW), mixed with Si NPs, and injected with HA for (a) Th, (b) U and (c) La, see text.

References

- [1] www.oncoinvent.com
- [2] H.J. Ache, L.H. Baestle, R.P. Bush, A.F. Nechaev, V.P. Popik, Y. Ying, Technical Reports Series - No. 308, IAEA, Vienna (1989).
- [3] <https://www.eucor-uni.org>
- [4] F. Quinto, R. Golser, M. Lagos, M. Plaschke, Th. Schäfer, P. Steier, and H. Geckeis, *Anal. Chem.* 87, 5766–5773 (2015).
- [5] R. Eigl, M. Srnecik, P. Steier, G. Wallner, *Journal of environmental radioactivity* 116, 54–58 (2013).
- [6] A. Heneka, C.-O. Krauß, S. Gentes, F. Becker, H. Geckeis, J. Lützenkirchen, M. Plaschke, D. Schild, W. Tobie, *ATW*, 66 (1), 34-40 (2021).

10. Radiation protection research

Fundamental studies on radionuclide chemistry and geochemistry ensure a detailed understanding and reliable quantitative prediction of aqueous chemistry. In order to allow a comprehensive assessment of radionuclide behaviour and mobility in aquatic systems relevant for nuclear waste disposal, studies with actinides and long-lived fission products are performed. The investigated aqueous systems cover from dilute solutions to highly saline salt brine systems and establish essential site-independent data and process understanding. Work is focussing both on detailed experimental investigations using the unique facilities available at KIT-INE and subsequently developing reliable chemical models and consistent thermodynamic data. This combined approach allows a systematic and reliable evaluation of key processes such as radionuclide solubility, radionuclide speciation, radionuclide retention and transport processes in relevant near- and far-field scenarios. The work summarized in this section is related to the (i) chemistry and thermodynamics of actinides and fission products in aqueous solution, (ii) radionuclide sorption on mineral phases, (iii) radionuclide diffusion in clays, and (iv) retention of radionuclides by secondary phase formation. The studies aim at identifying relevant radionuclide retention/retardation mechanisms on a molecular level and their robust thermodynamic quantification in support of the Nuclear Waste Disposal Safety Case. Fundamental studies on aqueous radionuclide chemistry are giving support to the applied studies (see Chapter 6) performed at KIT-INE.

10.1 Age-dating of young Cf sources by means of γ -spectroscopy

F. Becker, R. Dagan, K. Wu

Introduction

This study investigated the feasibility of combining high-resolution γ -ray spectroscopy with the simulation capabilities of the Nucleonica Nuclear Science Portal [1] with the aim to determine the age of a young Cf source. At the KIT-SUM calibration laboratory a new Cf source was purchased and we took the opportunity to investigate this source.

Experimental procedure

γ -ray spectra were measured at the KIT-SUM calibration laboratory using a coaxial HPGe Germanium detector. To account for the strong gamma and neutron emission of the Cf source, the detector was placed at a distance of 321 cm from the source to avoid high dead time and pile up effects as well as possible neutron induced damages in the detector. The measurement was carried out overnight in order to avoid disturbing the routine operation of the calibration laboratory during the day. The calibration of the detector itself was performed with a Eu-152 source in the control area of KIT-INE.

Theoretical investigation tool

The Nucleonica Nuclear Science Portal provides web-based nuclear science applications such as e.g. decay calculations, dosimetry and shielding. To obtain simulated spectra we employed Nucleonica's Decay Engine (DEC), the Gamma Spectrum Generator application (GSG) and the web-based Spectrum Analyser (WESPA).

For our investigation of the young Cf source, we used DEC to determine age dependent nuclide mixtures in a Cf source. In a next step, based on the simulated nuclide mixtures, we generated γ -ray spectra with GSG. GSG offers a basic geometric arrangement of the source, filters and detector in accordance with the

experimental set-up. The simulated spectra can be viewed and saved for further investigations. In addition, the contributions of individual nuclides to the full spectrum can be visualised. The γ -ray spectra were analysed with WESPA, which allows to determine the intensities of γ -ray peaks and to identify the nuclides in the spectra.

To get a suitable model in GSG, we matched the experimental Eu-152 spectra to the simulated ones. For our DEC and GSG calculations, a large number of nuclides had to be taken into account. As a result, we tested the employed Nucleonica tools at their limit and together with the programme developers, improvements and extensions were introduced into Nucleonica.

Results

Age-dating of older Cf sources, first proposed by Gehrke [2], calls for the fitting of the Cs-137 peak at 662 keV and the I-132 peak at 668 keV. The underlying idea is to assess their age dependent peak-intensity ratios according to the nuclide's different lifetimes. The calculated ratio of γ -ray emission rates of 662 keV to 668 keV plotted as a function of the age of the Cf source (age-determination curve, ADC) allows assessing the age of a Cf source from respective ratios determined in measured spectra.

However, in our measured spectra of the young source, the 662 keV peak could not be identified, as the build-up of Cs-137 was too small at this age.

Hence, we followed a new strategy. Using Nucleonica, γ -ray spectra were generated for the assumed age range of the investigated source from 2 to 24 months in steps of one month. In the spectra of the different source ages, we searched for peak pairs that showed a noticeable increase or decrease in intensity compared to each other. As a result, we found suitable pairs, a peak at 134 keV, together with the peaks at 724 or 497

keV. For this two peak pairs we plotted two ADCs. We used these two ADCs to determine the age of our source using the measured peak area ratios. The results for the 498 keV / 134 keV and 724 keV / 134 keV ADCs are 17-21 months and 17-24 months, respectively.

The advantage of this procedure is pronounced by the fact that beyond the individual γ -ray peaks, also multiplets can be used. Therefore, a nuclide assessment of different peak contributions is not necessary (as was the case in previous ADC investigations).

Conclusion

With an improved age-dating procedure, based on simulated γ -ray spectra, we could estimate the age of our investigated young Cf source to be around 20 months.

Even complex dense γ -ray spectra originating from many Cf source decay or fission products could be handled.

Finally, it was shown that Nucleonica's tools are well suited to investigate such a complex task.

Acknowledgement

The authors are grateful for the excellent support of the KIT-SUM calibration laboratory.

References

- [1] Nucleonica GmbH, 2017, Nucleonica Nuclear Science Portal (www.nucleonica.com), Version 3.0.269, Karlsruhe
- [2] R.J. Gehrke et al., *Nucl. Instr. and Meth. in Phys. Res. B*, **213**, 10–21, (2004).

10.2 Impact of neutron slowing down on radiation fields for spent nuclear fuel waste disposal

H. Wu, F. Becker, R. Dagan

Introduction

This investigation extends a former study of Suarez and Becker concerning the radiation field of spent nuclear fuel (SNF) disposal casks within a rock salt gallery compared to a SNF disposal cask free in air. The paper deals with geometrical improved configurations of light materials within the cask, which lead by means of neutron slowing down (thermalization) to enhanced absorption and in return to reduction of neutron exposure. The impact of neutron scattering from the specific walls in a gallery, subjected to the type of repository, is also considered. The study shows that by means of interactions with hydrogen in polyethylene, the neutron flux around the casks can be reduced by up to a factor 5. Moreover, scattering of neutrons in the gallery changes the distant dependent neutron flux considerably compared to the almost inverse-square law for the free in air case.

In the current study, the Monte-Carlo N-Particle code MCNP6 [1] was employed to obtain the information on scattered neutrons around a POLLUX-10 cask.

The ongoing discussion on the site selection process for a multi-barrier system for high level waste in Germany on one side and the existing interim storage of SNF in surface facilities on the other side increases the interest for reduction of the radiation dose in the surrounding of the spent nuclear fuel casks.

Suarez and Becker [2-3] have calculated the dose rate that a worker is exposed during emplacement of a SNF disposal cask in a repository within rock salt, considering salinar host rock as one of the three types of host rocks discussed in Germany for disposal of high level waste.

In contrast to multi-purpose casks for surface interim storage and transportation (e.g. CASTOR®), POLLUX casks were designed specifically for final disposal of SNF and vitrified high level waste in a deep geological repository in rock salt.

In the next section, the geometrical cross section of a POLLUX-10 cask is followed by postulated technical modifications, which lead to reduction in the neutron and photon flux. The study concentrates mainly on the polyethylene (PET) rods embedded in the POLLUX-10 on one side and the impact of the rock salt gallery in comparison to free air on the other side. Based on this type of calculation other temporary repository buildings could be similarly analyzed.

The POLLUX-10 cask

The POLLUX-10 cask was designed as part of the technical barrier of a potential multi-barrier system for high level waste in rock salt [4]. The cask has a double-layer structure, mmm the inner layer is made of stainless steel and outer layer is made of nodular cast iron. PET rods embedded in the outer layers of the cask forming two

rings; they serve as neutron moderator and absorber. The nuclear waste is stored in the center of the cask as shown in Fig. 1a as active fuel zone.

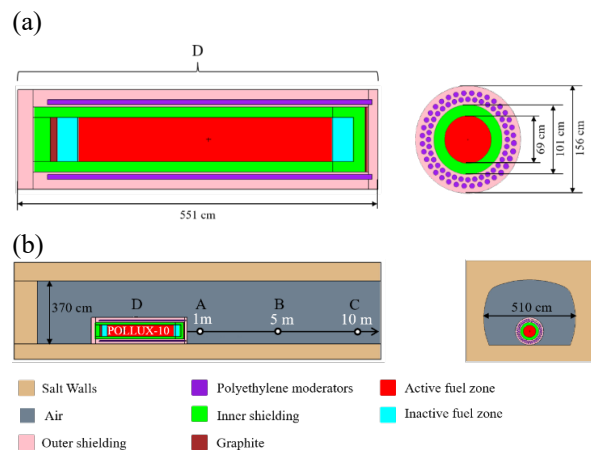


Fig. 1: MCNP6 model of the POLLUX-10 cask (a) and the horizontal emplacement drift (b). The side surface of the cask marked D was defined as a surface detector, as shown in (a). PET rods in the outer layer of the POLLUX-10 forms two rings, 36 PET rods for each ring. The radius of the rod is 3.75 cm. A, B, and C are the position of the point detectors, as shown in (b).

The MCNP code and modelling of the POLLUX-10 cask

Monte Carlo techniques are usually used to solve transport problems of neutrons and photons, including the interaction with matter. In this study, a POLLUX-10 cask shown in Fig. 1a, was modeled. In particular, the points A, B, and C indicate the position of point detector tallies (F5 tally) at 1 m, 5 m, and 10 m away from the cask, respectively (Fig. 1b). For improving computing efficiency and in accordance with the geometry of the rock salt gallery, the radius of the detectors tallied in this study is 10 cm. It should be mentioned that the detector's radius was tested with other radii and did not have significant influence on the results. To calculate the surrounding radiation field, the side surface from bottom to top of the (upright) POLLUX-10 was defined as a surface detector marked D, where F2 tally was applied (Fig. 1a).

Due to the geometrical complexity, the fuel-contents within the POLLUX-10 cask were simplified to a homogeneous mixture of 5.45 tons heavy metal, which consist of nine UOX fuel assemblies and one MOX fuel assembly (the red area in Fig. 1a), the clad, structural material and air were also taken into account within the homogenized mixture. Further, the definition of the source term in the simulation was taken from [5]. The neutron emissions in the active area (active fuel zone

indicated in red in Fig. 1) was mainly contributed by Cm-244 and Cm-246. To pass statistical checks, the MCNP simulation applied tracking history of 1×10^8 source particles.

Calculation results

1. Distance-dependent neutron flux

Surrounding rock salt walls have a significant influence on the scattered neutrons in the repository. The distance-dependent neutron fluxes were calculated at various positions, as shown in Fig. 1b, in order to estimate the rock salt wall's effect. The neutron flux of the casks "free in air", shown in Fig. 2a, served as reference.

In those cases of POLLUX-10 free in air, Fig. 2a shows the neutron flux spectra at detector positions A, B and C, at 1, 5, and 10 m, respectively. The total neutron flux is 1.86×10^{-8} , 9.59×10^{-10} , and 2.48×10^{-10} cm^{-2} source neutron $^{-1}$, respectively. The neutron flux is reduced by a factor 75 from detector position at 1 m compared to 10 m. This is quite in good agreement with the inverse-square law of a factor 100.

In Fig. 2b, the total neutron flux amounts to 2.74×10^{-8} , 6.32×10^{-9} , and 1.80×10^{-9} cm^{-2} source neutron $^{-1}$ at the detector positions A, B and C, respectively. Due to the enhanced neutron scattering in the rock salt gallery, the neutron flux is only reduced by a factor 15 from detector position at 1 m compared to 10 m. This is strongly different from the above-mentioned inverse-square law due to the back scattering of neutrons from the gallery walls. The simulation of the scattering was based on the

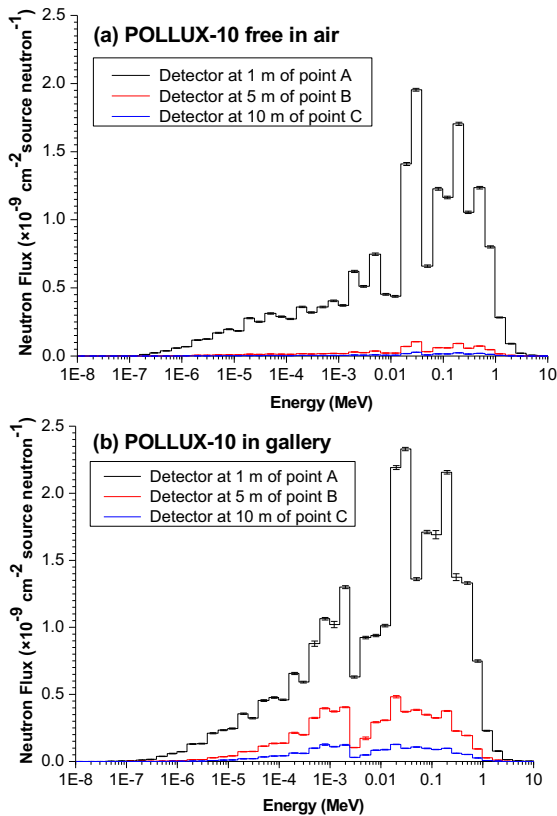


Fig. 2: Calculated neutron fluxes at various detector positions of the POLLUX-10 free in air (a) and in rock salt gallery (b). The point detectors are located at A, B, and C corresponding 1 m, 5 m, and 10 m away from the POLLUX-10, respectively (see Fig. 1b).

reference scattering model in MCNP6 known as the asymptotic scattering.

Comparing Fig. 2a and Fig. 2b, the neutron fluxes in Fig. 2b are 1.5, 6.6 and 7.3 times higher than the corresponding values in Fig. 2a. In other words, neutron scattering gives an important contribution to the total neutron flux with increasing detector distance to the cask. Consequently, radiation exposure due to neutron scattering at different positions in the gallery should be investigated in subsequent studies as the asymptotic scattering model excludes the temperature and energy dependent cross sections, which could have a considerable effect on the direction of the scattered neutron after interaction with the rock salt walls in the gallery.

2. Influence of the PET rods on the neutron moderation

Due to the high hydrogen component, PET is an important material for neutron moderation in the POLLUX-10. The shielding container includes two rings of PET moderator rods in the external layers. To study the impact of the PET moderator rods on the surrounding radiation field of the POLLUX-10, simulations were also performed with different PET moderator rod configurations.

As a first step, the POLLUX-10 was simulated free in air with and without PET rods of 3.75 cm radius. The neutron flux was counted at the side coating surface of the cask (see position D in Fig. 1). Fig. 3 shows that the total neutron flux at the side coating surface of the POLLUX-10 with and without PET rods is 2.08×10^{-8} and 6.12×10^{-7} cm^{-2} source neutron $^{-1}$, respectively. Embedding the PET rods reduces the total neutron flux at the side coating surface of the POLLUX-10 by a factor 29. This fact emphasizes the importance of optimizing the neutron thermalization feasibility as shown below.

3. Variation of the polyethylene rods

The shielding of the neutron radiation strongly depends on the quantity and position of the PET rods, which are used as neutron moderator [6]. The influence of different parameters of PET rods on the neutron flux spectra is studied in this section.

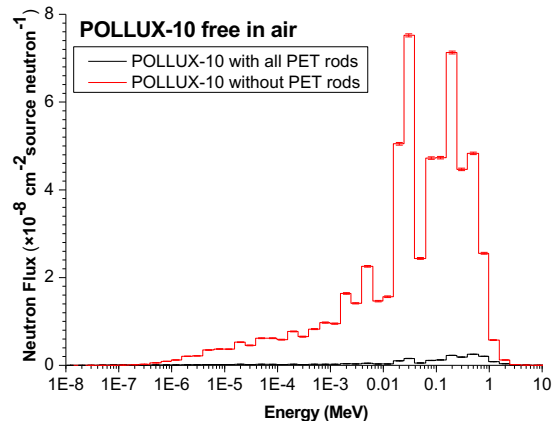


Fig. 3: Neutron flux spectrum at the side coating surface of the POLLUX-10 with and without PET rods. The original design of the POLLUX-10 includes two rings of PET rods serving as neutron moderator (see Fig. 1). The radius of each rod is 3.75 cm.

To calculate the side coating surface neutron flux of POLLUX-10, the radius of PET rods were set as 3.75 cm, 4.25 cm and 4.75 cm, respectively. The side coating surface flux was obtained as shown in Fig. 4.

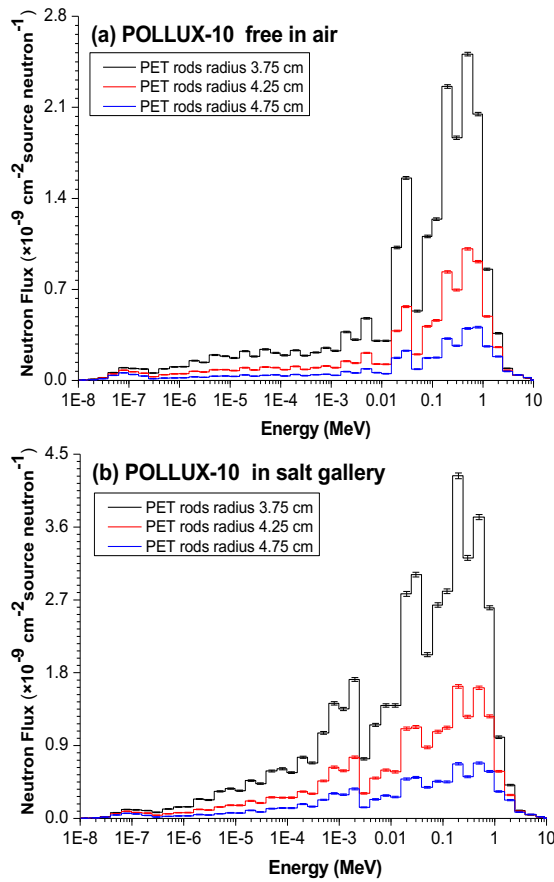


Fig. 4: Neutron flux spectrum at the side coating surface of the POLLUX-10 (see position D in Fig. 1a) for different radii of PET rods free in air (a) and in salt gallery (b).

In Fig. 4a, the total neutron flux at the side coating surface of the POLLUX-10 is 2.10×10^{-8} , 8.91×10^{-9} , and $3.97 \times 10^{-9} \text{ cm}^{-2} \text{ source neutron}^{-1}$, respectively. The neutron flux is reduced by a factor 5 when the PET rod radius is increased from 3.75 cm to 4.75 cm. In Fig. 4b, the total neutron flux at the side coating surface of the POLLUX-10 amounts to 4.53×10^{-8} , 1.95×10^{-8} , and $9.03 \times 10^{-9} \text{ cm}^{-2} \text{ source neutron}^{-1}$, respectively. The neutron flux in this case, is again reduced by a factor 5 with an increased radius from 3.75 cm to 4.75 cm.

Comparing Fig. 4a and Fig. 4b, the neutron fluxes in Fig. 4b are 2.2, 2.2 and 2.3 times higher than the corresponding values in Fig. 4a.

Another optimization concerns the complexity of two rings. For POLLUX-10 cask free in air, the neutron flux at the side coating surface of the cask was calculated with only the inner or outer ring of PET rods, which quantifies the impact of each ring on the outer exposure separately. In this way, the accumulated dose of workers in the gallery could be analyzed against the simplification of the POLLUX-10 structure. Fig. 5 shows the neutron flux calculated with only the inner ring of PET rods. The radii of PET rods were set as 3.75 cm and 4.75 cm.

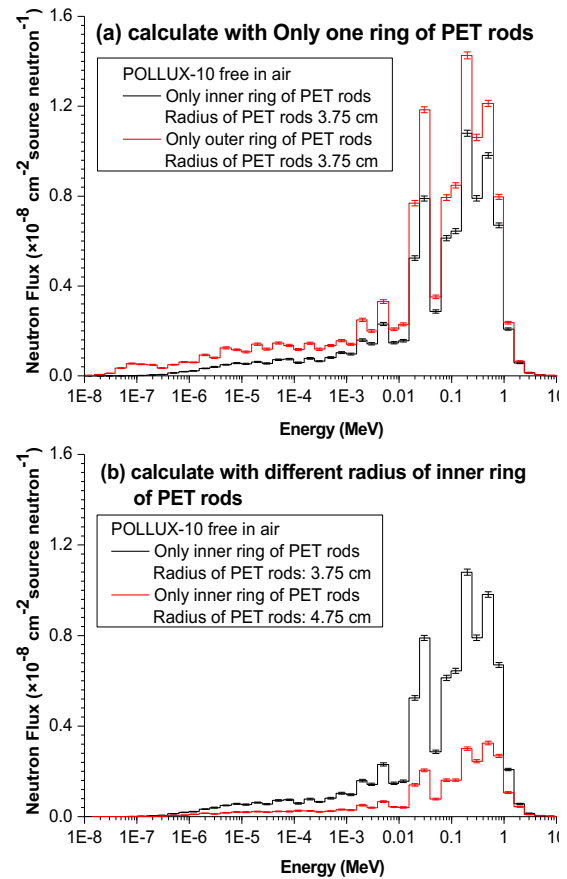


Fig. 5: POLLUX-10 free in air. Neutron fluxes were calculated at side coating surface of the POLLUX-10 (surface detector at D, see Fig. 1). (a) Calculation with only inner or outer ring of PET rods. (b) Calculation with only inner ring of PET rods but radius of the inner ring of PET rods were set as 3.75 cm and 4.75 cm, respectively.

The impact of the inner PET ring, shown in Fig. 5, is more pronounced than the outer one. This is due to the enhanced pathway of thermalized neutrons in the stainless steel. Strictly speaking, the enhanced capture cross section of thermalized neutrons in the low energetic zone indicates that it is better to first thermalize the neutrons in an inner ring than doing so in the outer ring (Fig. 5a) where the distance to the surface is too short, reducing the probability of the thermalized neutrons to be absorbed within the cask.

Therefore, the neutron flux at the side coating surface of the POLLUX-10 is strongly affected by changing shielding structure or material.

4. Neutron induced photons

To study the impact of the rock salt walls on neutron induced photon production, simulations were performed with MCNP6 to obtain the neutron induced photon flux at detector positions 1 m and 5 m (see Fig. 1, points A and B).

The spent nuclear fuel of the POLLUX-10 cask was used as neutron source to simulate the neutron-induced photons free in air and in gallery, i.e. only neutrons were considered to be emitted from the active fuel zone. As shown in Fig. 6, γ -ray lines stemming from the reactions with the gallery walls, $^{35}\text{Cl}(n,\gamma)^{36}\text{Cl}$ and

$^{37}\text{Cl}(n,\gamma)^{38}\text{Cl}$, as well as with the cask, $^{54}\text{Fe}(n,\gamma)^{55}\text{Fe}$ and $^{56}\text{Fe}(n,\gamma)^{57}\text{Fe}$ could be identified in the calculated neutron induced photon flux spectra. The comparison of the spectra free in air with the ones in the rock salt gallery clearly shows the newly occurring γ -ray lines caused by neutron interactions with materials of the rock salt walls. In addition, Compton scattering and pair production also contribute to an increased photon flux in the gallery.

Moreover, in view of calculated results at the detector positions A and B, respectively, Fig. 6 includes further the total neutron-induced photon flux for POLLUX-10 free in air and in rock salt gallery. For the POLLUX-10 free in air, the total photon flux at the detector positions A and B amounts to 1.94×10^{-9} and 1.11×10^{-10} cm^{-2} source neutron $^{-1}$, respectively. The photon flux is reduced by a factor 18. For the POLLUX-10 in gallery, the total photon flux at the detector positions A and B amounts to 6.93×10^{-9} and 2.28×10^{-9} cm^{-2} source neutron $^{-1}$, respectively. In this case, the photon flux is reduced only by a factor 3.

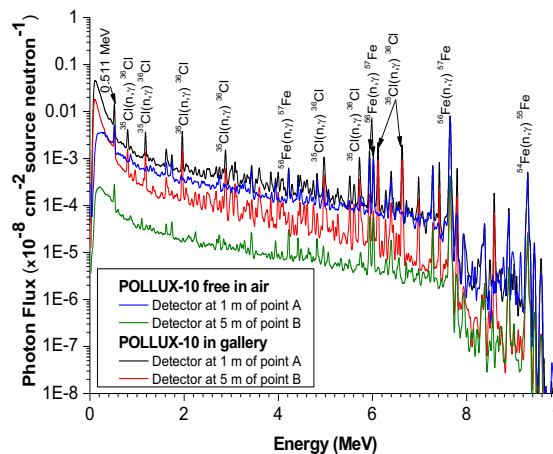


Fig. 6: Calculated neutron induced photon flux spectra at various positions for the POLLUX-10 free in air and in rock salt gallery. Some γ -ray lines stemming from neutron capture reactions are indicated.

Again, the scattering of photons and photon production in the gallery walls plays an important role. As visible in Figure 6, the background is enhanced below 7 MeV when comparing the spectra with and without gallery. At position A, the ratio of the total photon flux in the gallery to the one free in air amounts to 3.6, but at position B to 20.5. Hence, the relative photon flux is more pronounced with increased distance from the cask. Moreover, for the gallery spectra an increased photon flux is observed below 0.3 MeV attributed to Compton scattering of the photons produced.

Conclusion

Possible reduction of the exposure to neutron flux outside of a POLLUX-10 cask was demonstrated by different configuration of PET rods in the outer shielding layer. Increasing the radius of the PET rods from 3.75

to 4.75 cm reduces the exposure to neutron flux by almost a factor 5. Alternatively, and in view of the real exposure time of employees within the gallery, simple designs with only one PET rods inner ring could be considered as was shown in Fig. 5b. The different neutron exposure in a salt gallery compared to free in air points out the importance of reflections from the surrounding walls, namely the backscattering from salt, which in return depends on the model used in the simulating MCNP6 code. In this study, the approximated reference model known also as the asymptotic model was employed. The correct treatment of neutron scattering including temperature and energy dependent cross sections are beyond the scope of this study and should be further investigated.

Absorbing neutrons within the POLLUX calls for neutron-gamma reactions with eventually enhanced gamma doses. Suarez [2] and Poenitz [6] showed that neutron-induced γ -ray doses are by far lower than the neutron doses. The impact of several relevant interactions were shown in Fig. 6 to confirm those former works pointing out in addition the slightly increase of gamma dose in the 200 keV range. The amount of gammas produced mostly due to Compton scattering and pair production becomes relevant at lower energies at which hydrogen could be ionized (at about 20 eV and above).

References

- [1] T. Goorley et al., 2012. Initial MCNP6 release overview. Nucl. Technol. 180, 298–315 (2012)
- [1] H. Saurí Suárez et al., "Monte-Carlo based comparison of the personal dose for emplacement scenarios of spent nuclear fuel casks in generic deep geological repositories." Atw. Internationale Zeitschrift fuer Kernenergie 62, 384-390 (2017)
- [2] H. Saurí Suárez et al., "Monte-Carlo based comparison of the personal dose for emplacement scenarios of spent nuclear fuel casks in generic deep geological repositories." Atw. Internationale Zeitschrift fuer Kernenergie 62, 384-390 (2017)
- [3] H. Saurí Suárez et al., "Neutron flux measurements on a mock-up of a storage cask for high-level nuclear waste using 2.5 MeV neutrons." Journal of Radiological Protection 38, 881- 891 (2018)
- [4] H. Spilker, and R. Hüggenberg, "Description of the German concept of final storage cask." International Journal of Radioactive Materials Transport 2, 67-75 (1991)
- [5] H. Saurí Suárez, H., Individual dosimetry in disposal facilities for high-level nuclear waste, Ph.D. thesis, urn:nbn:de:swb:90-840326, KITopen ID: 1000084032 (2018)
- [6] E. Poenitz and C. Walther, "Calculation of Dose Rates at the Surface of Storage Containers for High-Level Radioactive Waste." Radiation protection dosimetry 177 361-372 (2017)

10 Geoenergy

The Karlsruhe Institute of Technology has defined a broad research program on Enhanced Geothermal Systems (EGS) technology development and high-temperature heat storage. Research activities cover the whole process chain of geothermal exploration, engineering and production including system integration and social acceptance and span from fundamental to applied research across scales. Compared to a nuclear waste disposal research, the conditions at a geothermal site are characterized by elevated temperature, flow rate and pressure conditions. In particular, the influence of hydraulic processes extends even further: not only the direct hydraulic observables like flow / pressure fields or tracer propagation is affected by the petrophysical setting, but the changes in the system setting due to mechanical and chemical interaction become important. In this context, the geoenergy research at INE concerns mainly physical and chemical processes in the surface and sub-surface thermal water circuit. The technical feasibility of EGS in fractured crystalline basement was demonstrated first at the Soultz-sous Forêts project, France. Major conclusion from this project are that effective enhancement of hydraulic yield under environmentally friendly condition, e.g., reducing induced seismicity, are technically feasible during reservoir engineering and operation. However, both was achieved by reducing the injection wellhead pressure at the expense of economic viability. For the further development of EGS, this learning curve needs to be continued in the field of controlled high-flowrate injection on existing fractures. For this purpose, KIT proposes the generic underground laboratory *GeoLaB* in the Black Forest/Odenwald complex. In the surface facilities, scaling and corrosion remains an issue. High-temperature heat storage, i.e. sub-surface heat storage at temperature > 100 °C, is a novel approach in sub-surface engineering technologies. Under the technical lead of INE, the new research infrastructure *DeepStor* is being prepared. Preparation includes planning, surface exploration, first modelling of operational scenarios and moreover interaction with public. Against this background the following major topics of geothermal research were covered at INE in 2020 and 2021.

F. Bauer, N. Cornejo, N. Haaf, F. Heberling, M. Pavez, K. Schätzler, E. Schill, U. Steiner

In co-operation with:

M. Frey^b, J. Grimmer^a, T. Kohl^a, I. Sass^b

^a AGW, Karlsruhe Institute of Technology, Germany

^b IAG, Technical University of Darmstadt, Germany

Introduction

Aiming at the utilization of subsurface thermal fluids to accomplish a drastic reduction in CO₂ emissions, KIT's geothermal research concentrates on geothermal utilization in the Upper Rhine Graben, i.e. a major geothermal resource in Germany. It intends to 1) increase the economics of operation, 2) increase the efficiency of thermal production for sector coupling, and 3) establish highly efficient thermal underground storage by applying high-temperature changes.

The importance of this base-load capable, steerable energy source for Germany is reflected by the expanding need of heat-storage systems in individual buildings and in heating grids.

It is envisaged to extend the current utilization through technological innovations, e.g. by establishing a scientific demonstrator on high-temperature underground storage measuring up to 170 °C. This facility should advance the technical and scientific topics necessary for seasonal, on-demand heat supply below e.g. KIT Campus North, situated on one of the most prominent geothermal anomalies.

Research on the environmentally friendly development of deep geothermal energy addresses key issues such as perceptible seismicity during enhancement of the

reservoir performance and operation, as well as partly NORM-bearing scaling.

Special focus is given to integrating the public into the project development and communication.

The research in the Helmholtz program *Renewable Energies* and since 2021 *Materials and Technologies for the Energy Transition (MTET)* at INE were completed among others by the *Helmholtz Climate Initiative (HI-CAM)*¹ and the GECKO² project.

In 2020 and 2021, INE has prepared the new research infrastructures *DeepStor* and *GeoLaB*³. Research at INE has contributed among others to the understanding of electric and electromagnetic signals during hydrofracturing and –shearing. To further investigate such phenomena a new experiment *RockBlockEx* is being installed at INE.

Geothermal Laboratory in the Crystalline Basement (GeoLaB)

The proposed new underground research laboratory *GeoLaB* addresses fundamental challenges of reservoir technology. The specific objectives of *GeoLaB* are 1) efficient and safe management of fractured reservoirs, 2) cutting-edge multi-disciplinary and multi-process research with visualization concepts, 3) developing

¹ <https://www.netto-null.org/>

² <https://www.gecko-geothermie.de/>

³ <https://www.geolab.kit.edu/>

new environmentally benign strategies for subsurface installations, and 4) transparent interaction with the public and decision makers. The planned experiments will significantly expand our fundamental understanding of processes associated with operational conditions in reservoir structures. The application and development of cutting-edge tools for the analysis and the monitoring of below-ground processes will yield fundamental findings, which are of major importance for a safe and ecologically sustainable usage of geothermal energy. It will also open up new perspectives for alternative ways to use the geological underground for energy purposes. Designed as an interdisciplinary and international research platform, GeoLaB will foster scientific cooperation among Helmholtz research centres, and with universities, industrial partners, and professional organizations, hence creating multiple synergies for advancing scientific insight and for boosting technological innovations.

For the envisaged target areas in the Black Forest and the Odenwald region the selection of the GeoLaB location will be based on predefined criteria and on innovative geoscientific exploration techniques. At the selected site, a two km long gallery will be excavated which will give access to individual caverns where controlled, high flow rate experiments will be conducted at greater depths (Fig. 1). The experiments will be monitored continuously from multiple wells, drilled either from the underground laboratory or from the surface. This will create a unique 4D-benchmark dataset of thermal, hydraulic, chemical and mechanical parameters.

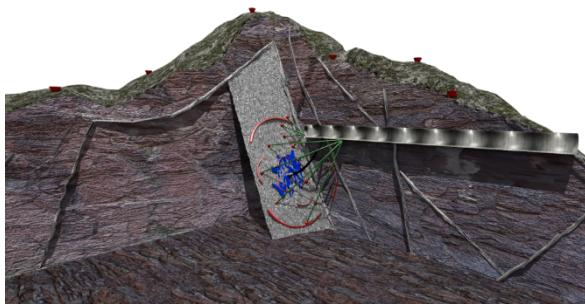


Fig. 1: Layout of the experimental studies enabled by GeoLaB from caverns connected to a central gallery.

GeoLaB allows for cutting-edge science, associating fundamental to applied research for reservoir technology and borehole safety, bridging laboratory to field scale experiments and connecting renewable energy research to social perception. With its novel approach, it will shape the research in earth sciences for the next generation of students and scientists.

For the site selection of GeoLaB after exploring favourable areas in the Black Forest, a complementary geophysical and geological exploration has been carried out in the Tromm granite of the Odenwald, located at the northeastern margin of the URG [1]. Here an outcrop analogue study was conducted to obtain the key characteristics of the fracture network. Based on this, discrete fracture network models were developed to

calculate equivalent permeability tensors under assumed reservoir conditions. The influence of different parameters, such as fracture orientation, density, aperture and mineralization was investigated. In addition, extensive gravity and radon measurements were carried out in the study area, allowing for more precise localization of fault zones with naturally increased porosity and permeability. Gravity anomalies served as input data for a stochastic density inversion, through which areas of increased open porosity were identified. A laterally heterogeneous fracture network characterizes the Tromm granite, with the highest natural permeabilities expected at the pluton margin, due to the influence of large shear and fault zones.

DeepStor

The worldwide unique infrastructure DeepStor aims at the development of high-temperature heat storage in the deep underground as a new element in the future CO₂-neutral global energy mix. HT-ATES (high-temperature aquifer thermal energy storage) systems are a future option to shift large amounts of high-temperature excess heat from summer to winter using the deep underground [2]. Among others, water-bearing reservoirs in former hydrocarbon formations show favourable storage conditions for HT-ATES locations. This study characterizes these reservoirs in the Upper Rhine Graben (URG) and quantifies their heat storage potential numerically. Assuming a doublet system with seasonal injection and production cycles, injection at 140 °C in a typical 70 °C reservoir leads to an annual storage capacity of up to 12 GWh and significant recovery efficiencies increasing up to 82% after ten years of operation. Our numerical modelling-based sensitivity analysis of operational conditions identifies the specific underground conditions as well as drilling configuration (horizontal/vertical) as the most influencing parameters. With about 90% of the investigated reservoirs in the URG transferable into HT-ATES, our analyses reveal a large storage potential of these well-explored oil fields. In summary, it points to a total storage capacity in depleted oil reservoirs of approximately 10 TWh a⁻¹, which is a considerable portion of the thermal energy needs in this area.

Raising the ATES temperature of max. 50 °C to temperatures up to 150 °C in high temperature systems involves considerable technology development such as optimal reservoir development, solutions to damage of the natural reservoir by thermo-hydro-chemical interaction, or materials sustaining chemically harsh condition of the thermal water.

To overcome current temperature limitation, the scientific infrastructure DeepStor has been designed. It allows for a number of cutting-edge experiments in transient hydraulic, thermal and chemical loading and de-loading of the underground that will have implications for the development of geothermal storage and energy in general.

Three overarching goals of the scientific investigations in DeepStor are defined:

- Suitability: The site investigations need to be appropriate to advance DeepStor to a full-developed

HT-ATES system. Therefore, various logging, testing and laboratory methods will be combined to quantify the site parameters as a whole. Results are compared to earlier data acquisition (e.g. 3-D seismics, hydrocarbon wells). This provides the base for novel drilling concepts adapted to storage.

- **Transferability:** The geological setting, formation and evolution will be identified from coring data supported by 3D seismics, logging or analogue locations. This will include sedimentological, petrologic and geochemical studies to examine alteration or water-rock interaction. Specific conditions, being most important for the further development of HT-ATES systems, will be classified and transferred to potential future sites.

- **Process recognition:** The chemo-physical processes are a basic requirement to ensure an economic efficient and environmental safe operation of the underground storage system. Forecasting the performance of the HT-ATES system requires necessary parameter sets for the calibration and benchmarking of numerical reservoir models. These parameter sets are gathered from the individual experiments that will be carried out in the infrastructure.

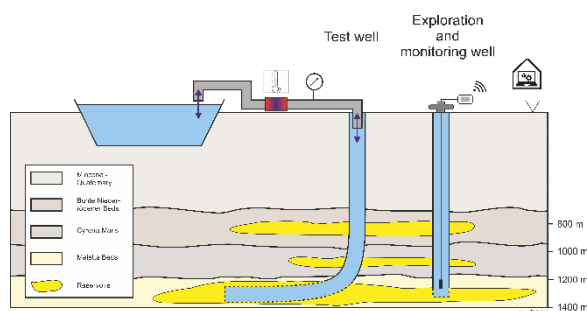


Fig. 2: Conceptual layout of the Helmholtz research infrastructure DeepStor including an exploration and monitoring as well as a test well

DeepStor is fully integrated in the Helmholtz Research Program “MTET” and contributes to the program overarching research within the “HI-CAM”, in particular to the climate neutral Helmholtz Association.

Thermodynamic equilibrium models for the DeepStor site

Upon successful demonstration of the technology in the Helmholtz research infrastructure DeepStor, the project may be prepared for integration into the KIT heat supply. Heat from different sources at the campus may be stored in an underground reservoir during the summer months, when the heat is not required. The stored heat will then be reproduced in the winter, when the campus’s thermal power demand is much higher. INE has carried out a preliminary geochemical risk assessment for the operation of this subsurface, seasonal geothermal energy storage system [3]. We used equilibrium thermodynamics to determine the potential phases and extent of mineral scale formation in the plant’s surface infrastructure, and to identify possible

precipitation, dissolution, and ion exchange reactions that may lead to formation damage in the reservoir. The reservoir in question is the calcareous fine grained Mettla sandstone layers of the Upper Rhine Graben’s Froidefontaine Formation. We modeled scale- and formation damage-causing reactions during six months of injecting 140 °C fluid into the reservoir during the summer thermal storage season and six months of injecting 80 °C fluid during the winter thermal consumption season. Overall, we ran the models for 5 years. Anhydrite and calcite are expected mineral scales during the thermal storage season (summer). Quartz is the predicted scale-forming mineral during the thermal consumption period (winter). Within ~20 m of the wellbores, magnesium and iron are leached from biotite; calcium and magnesium are leached from dolomite; and sodium, aluminum, and silica are leached from albite. These reactions lead to a net increase in both porosity and permeability in the wellbore adjacent region. At a distance of ~20–75 m from the wellbores, the leached ions recombine with the reservoir rocks to form a variety of clays, i.e., saponite, minnesotaite, and daphnite. These alteration products lead to a net loss in porosity and permeability in this zone. After each thermal storage and production cycle, the reservoir shows a net retention of heat, suggesting that the operation of the proposed DeepStor project could successfully store heat, if the geochemical risks described can be managed. This, thus, defines one research topic in DeepStor.

Magnetotelluric monitoring

To date, magnetotelluric monitoring of processes during reservoir engineering of geothermal systems have been carried out only at three sites world-wide. INE has added a new survey at the Reykjanes peninsular (Iceland) [4]. The MT data acquisition at RN-15/IDDP-2 covered the last third of the drilling period and thermo-hydraulic stimulation. Drilling was accompanied by temporal total fluid losses of up to 60 L/s as well as randomly distributed induced seismicity. The experimental results of a two-months magnetotelluric monitoring during the deepening of the RN-15/IDDP-2 well on the Reykjanes peninsular (Iceland) to 4’659 m are in line with earlier observations on decreasing resistivities at periods of a few s to about 20 s (or up to about 40 s) in conjunction with fluid injection. Simple models indicate however that it is not the fluid volume itself that causes the anomaly. Moreover, here, temporal decreases in the electric resistivities occur at 0.2-20 s with minima at periods of about 0.4 s 1-2 days ahead of clusters of seismic events with magnitudes up to ML < 2. Unlike in the previous studies, where resistivity decreases occur on the component that is parallel to Shmin, here they in both components (XY and YX) of the MT data. At the Reykjanes peninsular, Shmin is oriented N120°E off the XY component (N0°E). Therefore, if we rotate our data in Shmin direction, the difference between both components would be slightly smaller than that for the non-rotated ones. The decrease in resistivity (on both components) extends over > 1 order of magnitudes over a short period range and is thus considered noise induced in the subsurface. This

study aims at adding an essential dataset to the general discussion on MT monitoring of reservoir processes. The results show a temporal relation between decreasing apparent resistivity and (i) the geomagnetic field activity, (ii) the fluid losses up to 60 L/s, as well as (iii) mechanic processes occurring in the reservoir before clusters of induced seismicity on the other hand. The physical background of the correlation shall be further investigated at laboratory scale, in the new RockBlockEx.

Hydro-fracturing and reactive flow on meter-scale: a rock block experiment (RockBlockEx)

With the worldwide societal objective of net-zero CO₂-emissions in the next decades, new developments are required for extraction and storage of climate-neutral energy in form of heat and fluids. Major challenges with such technologies are the control of induced seismicity, leakage or scaling. A key to tackle them are comprehensive and cross-scale investigation of thermo-hydraulic-mechanic-chemical processes, which is as well a relevant topic in research towards the safe disposal of nuclear waste. While micro- and reservoir-scales are comparably well investigated, intermediate scale studies often lack in appropriate research facilities, although they allow for controlled experiments and high resolution monitoring. At the 10-100 m scale, KIT has proposed GeoLaB. The RockBlockEx addresses the cm-scale with a strong focus on electric potential and electromagnetic monitoring systems that are required upon mitigation of induced seismicity and for reactive transport.

Resistivity changes acquired during magnetotelluric monitoring were mainly related to fluid injection, but occur also contemporaneously with or prior to induced seismicity [4]. Although some theories were put forward, their seismo-electric origin is still a matter of debate. The RockBlockEx aims at investigating these effects under controlled laboratory condition. The set-up of RockBlockEx (Fig. 3) includes

- 1) an exchangeable block of rock (granite related to deep geothermal/GeoLaB, porous sandstone related to DeepStor, or basaltic rock related to mineralization of CO₂). A granite block from the Tegernau quarry is donated by Kimo GmbH.

- 2) The block is integrated in a steel frame, which allows for application of differential confining pressure using flat jacks. Pressure, temperature, pH, acoustic emission (AE), SP, and zeta-potential sensors are placed in wells and at the surface. Laser-induced breakdown-detection (LIBD) may be employed for colloid experiments

- 3) Existing electromagnetic sensors are placed outside of the block.

RockBlockEx is designed in particular for developing electric and electromagnetic monitoring. Techniques developed for different scales are employed and adapted here to this cm-m scale:

- 1) Zeta-potential detects processes at microscale involving charge changes (e.g. by chemical reactions).

- 2) SP typically detects charge accumulation at meso- to reservoir-scale.

- 3) Electromagnetic sensors detect signals in the 1-100 kHz range.

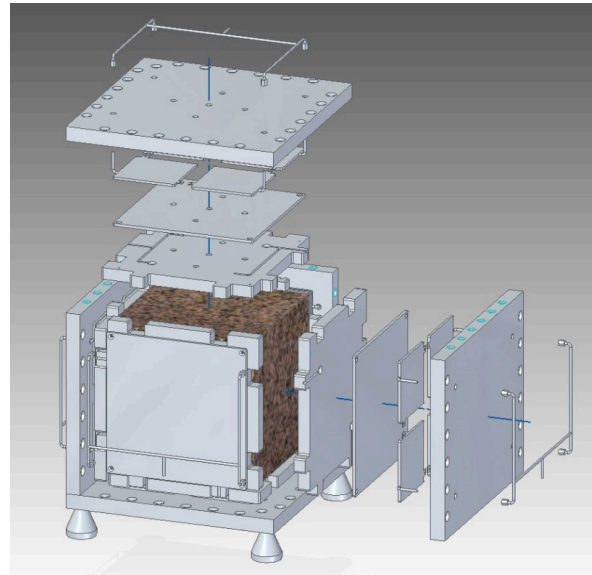


Fig. 3: Design of the steel frame and position of flatjacks of the RockBlockEx.

GECKO

The geothermal development faces a number of drawbacks resulting from immature technological development in early prototypes. Although major technological developments have been made, the related major setback, the low acceptability of deep geothermal technology by the society, remains. This is where the inter- and transdisciplinary project GECKO comes in. GECKO aims at involving the public in a co-design process that is linked to the establishment of deep geothermal infrastructures for heat production and storage at the KIT Campus North.

At INE, different scenarios of utilization and their respective consequences will be established using numerical modelling to provide the co-design process with the consequences of criteria decisions and alternatives in the design.

The co-design process includes a criteria and a scenario workshop for the exchange with public: "Join us in shaping the regional heat transition!" This was the invitation that more than 60 participants accepted for the criteria workshops in October 2020. The core of the workshops was a discussion round in small groups with the aim of identifying concerns and expectations about the infrastructure project in their living and working environment. The participants were able to openly voice their concerns and thus became active advocates for their interests.

In the criteria workshop, more than 250 comments from citizens were collected. The evaluation showed that about 150 of these comments could be related to

technical aspects. Not surprisingly, there is a strong interest in information with regard to the assessment of various risks. Induced seismicity, increased emissions or drinking water pollution are some of such possible risks. In order to monitor them and be able to intervene in time, fully comprehensive safeguarding and preventive measures as well as continuous monitoring have been called for. This also includes measures such as insurance to cover financial and legal risks. The citizens also wanted a comparison of heat generation through geothermal energy with other technologies such as solar thermal energy or the increased use of photovoltaics with regard to economic efficiency, but above all also with regard to the potential for CO₂ savings. The participants most frequently mentioned aspects of transparency. This includes open and honest communication of information as well as its independent and neutral development in order to enable all interested parties to have a say.

In 2021, the GECKO project integrated the comments received from the citizens into the scenarios for the use of geothermal energy at KIT Campus North.

Some of the citizens' comments refer to the extraction of heat from the underground or its CO₂-saving potential. Other comments, however, refer to the safety concept, for example, for monitoring the groundwater.

It was our task at INE to complement the interdisciplinary creation of the scenarios with the numerical modelling and to examine the different technical implementations.

Three scenarios were bundled and presented to the citizens in the scenario workshop in October 2021. The results of the discussions and evaluations will be incorporated into the utilisation concept representing the citizens' wishes and needs. In addition, GECKO is going to formulate conditions that contribute to the success of the construction of renewable energy plants.

References

- [1] Frey, M., et al., *Solid Earth* (in review).
- [2] Stricker, K., et al., *Energies* (2020).
- [3] Banks et al., *Energies* (2021).
- [4] Haaf and Schill, *Geothermics* (2021).

12 Publications

2020

ISI/SCOPUS

1. Abdelmonem, A.; Ratnayake, S.; Toner, J. D.; Lützenkirchen, J., Cloud history can change water-ice-surface interactions of oxide mineral aerosols: A case study on silica. *Atmospheric chemistry and physics* **2020**, *20* (2), 1075-1087.
2. Abdollahpour, M.; Rahnamaie, R.; Lützenkirchen, J., The vulnerability of calcareous soils exposed to Mg-enriched irrigation water. *Land degradation & development* **2020**, *31* (16), 2295-2306.
3. Altmaier, M.; Lothenbach, B.; Metz, V.; Wieland, E., Preface / Special Issue “Geochemistry Research for Cement-based materials in nuclear waste disposal applications”. *Applied geochemistry* **2020**, *123*
4. Apostolidis, C.; Kovács, A.; Walter, O.; Colineau, E.; Griveau, J. C.; Morgenstern, A.; Rebizant, J.; Caciuffo, R.; Panak, P. J.; Rabung, T.; Schimmelpfennig, B.; Perfetti, M., Tris-hydridotris(1-pyrazolyl)boratoactinide Complexes: Synthesis, Spectroscopy, Crystal Structure, Bonding Properties and Magnetic Behaviour. *Chemistry - a European journal* **2020**, *26* (49), 11293-11306.
5. Bae, S.; Yoon, S.; Kaplan, U.; Kim, H.; Han, S.; Lee, W., Effect of groundwater ions (Ca²⁺, Na⁺, and HCO₃⁻) on removal of hexavalent chromium by Fe(II)-phosphate mineral. *Journal of hazardous materials* **2020**, *398*
6. Bauer, F.; Hadidi, A.; Tügel, F.; Hinkelmann, R., Flash Flood Investigations in El Gouna, Northern Red Sea Governorate. In *Flash Floods in Egypt. Ed.: Abdelazim M. Negm*, Springer International Publishing: 2020; pp 61-81.
7. Bauters, S.; Scheinost, A. C.; Schmeide, K.; Weiss, S.; Dardenne, K.; Rothe, J.; Mayordomo, N.; Stedtner, R.; Stumpf, T.; Abram, U.; Butorin, S. M.; Kvashnina, K. O., Signatures of technetium oxidation states: a new approach. *Chemical communications* **2020**, *56* (67), 9608-9611.
8. Becker, F.; Köhnke, D.; Reichardt, M.; Budelmann, H., Investigation of various concrete compositions with respect to gamma-radiation transmission properties of Cs-137. *Radiation physics and chemistry* **2020**, *171*
9. Bogner, A.; Link, J.; Baum, M.; Mahlbacher, M.; Gil-Diaz, T.; Lützenkirchen, J.; Sowoidnich, T.; Heberling, F.; Schäfer, T.; Ludwig, H.-M.; Dehn, F.; Müller, H. S.; Haist, M., Early hydration and microstructure formation of Portland cement paste studied by oscillation rheology, isothermal calorimetry, ¹H NMR relaxometry, conductance and SAXS. *Cement and concrete research* **2020**, *130*
10. Bouby, M.; Kraft, S.; Kuschel, S.; Geyer, F.; Moisei-Rabung, S.; Schäfer, T.; Geckeis, H., Erosion dynamics of compacted raw or homoionic MX80 bentonite in a low ionic strength synthetic water under quasi-stagnant flow conditions. *Applied clay science* **2020**, *198*
11. Çevirim-Papaioannou, N.; Gaona, X.; Böttle, M.; Bethune, E. Y.; Schild, D.; Adam, C.; Sittel, T.; Altmaier, M., Thermodynamic description of Be(II) solubility and hydrolysis in acidic to hyperalkaline NaCl and KCl solutions. *Applied geochemistry* **2020**, *117*
12. Darnet, M.; Wawrzyniak, P.; Coppo, N.; Nielsson, S.; Schill, E.; Fridleifsson, G. Ó., Monitoring geothermal reservoir developments with the Controlled-Source Electro-Magnetic method - A calibration study on the Reykjanes geothermal field. *Journal of volcanology and geothermal research* **2020**, *391*
13. Dubos, J. L.; Orberger, B.; Milazzo, J. M.; Blancher, S. B.; Wallmach, T.; Lützenkirchen, J.; Banchet, J., Agglomeration potential evaluation of industrial Mn dusts and sludges based on physico-chemical characterization. *Powder technology* **2020**, *360*, 1079-1091.
14. Duro, L.; Altmaier, M.; Holt, E.; Mäder, U.; Claret, F.; Grambow, B.; Idiart, A.; Valls, A.; Montoya, V., Contribution of the results of the CEBAMA project to decrease uncertainties in the Safety Case and Performance Assessment of radioactive waste repositories. *Applied geochemistry* **2020**, *112*, Art.Nr.:104479.
15. Eibl, M.; Shaw, S.; Prieur, D.; Rossberg, A.; Wilding, M. C.; Hennig, C.; Morris, K.; Rothe, J.; Stumpf, T.; Huittinen, N., Understanding the local structure of Eu³⁺- and Y³⁺-stabilized zirconia: insights from luminescence and X-ray absorption spectroscopic investigations. *Journal of materials science* **2020**, *55* (23), 10095-10120.
16. Ekeröth, E.; Granfors, M.; Schild, D.; Spahiu, K., The effect of temperature and fuel surface area on spent nuclear fuel dissolution kinetics under H₂ atmosphere. *Journal of nuclear materials* **2020**, *531*
17. Epifano, E.; Prieur, D.; Martin, P. M.; Guéneau, C.; Dardenne, K.; Rothe, J.; Vitova, T.; Dieste, O.; Wiss, T.; Konings, R. J. M.; Manara, D., Melting behaviour of uranium-amerium mixed oxides under different atmospheres. *The journal of chemical thermodynamics* **2020**, *140*
18. Ferrari, P.; Jovanovic, Z.; Bakhanova, E.; Becker, F.; Krstic, D.; Jansen, J.; Principi, S.; Teles, P.; Clairand, I.; Knezevic, Ž., Absorbed dose in the operator’s brain in interventional radiology practices: evaluation through KAP value conversion factors. *Physica medica* **2020**, *76*, 177-181.

19. Finck, N., Iron speciation in Opalinus clay minerals. *Applied clay science* **2020**, 193
20. Gabor, N., Beeinflussbarkeit einer Staubentwicklung bei der maschinellen Rückholung tiefengelagerter Abfallgebinde. *Bautechnik* **2020**, 97 (11), 802-808.
21. Geist, A.; Berthon, L.; Charbonnel, M.-C.; Müllich, U., Extraction of Nitric Acid, Americium(III), Curium(III), and Lanthanides(III) into DMDOHEMA Dissolved in Kerosene. *Solvent extraction and ion exchange* **2020**, 38 (7), 681-702.
22. Gentes, S.; Gabor, N., Actual research and development activities in the field of dismantling. *Atw* **2020**, 65 (8/9), 394-396.
23. Gil-Díaz, T.; Heberling, F.; Keller, V.; Fuss, M.; Böttle, M.; Eiche, E.; Schäfer, J., Tin-113 and Selenium-75 radiotracer adsorption and desorption kinetics in contrasting estuarine salinity and turbidity conditions. *Journal of environmental radioactivity* **2020**, 213
24. Grambow, B.; López-García, M.; Olmeda, J.; Grivé, M.; Marty, N. C. M.; Grangeon, S.; Claret, F.; Lange, S.; Deissmann, G.; Klinkenberg, M.; Bosbach, D.; Bucur, C.; Florea, I.; Dobrin, R.; Isaacs, M.; Read, D.; Kittnerová, J.; Drtinová, B.; Vopálka, D.; Cevirim-Papaioannou, N.; Ait-Mouheb, N.; Gaona, X.; Altmaier, M.; Nedyalkova, L.; Lothenbach, B.; Tits, J.; Landesman, C.; Rasamimanana, S.; Ribet, S., Retention and diffusion of radioactive and toxic species on cementitious systems: Main outcome of the CEBAMA project. *Applied geochemistry* **2020**, 112, Art.Nr.:104480.
25. Hain, K.; Steier, P.; Froehlich, M. B.; Golser, R.; Hou, X.; Lachner, J.; Nomura, T.; Qiao, J.; Quinto, F.; Sakaguchi, A., ²³³U/²³⁶U signature allows to distinguish environmental emissions of civil nuclear industry from weapons fallout. *Nature Communications* **2020**, 11 (1), 1275.
26. Held, S.; Stricker, K.; Fuchs, S.; Gaucher, E.; Bremer, J.; Schill, E.; Kohl, T., Tiefengeothermie : Ein wichtiger Beitrag zur Energiewende. *Geowissenschaftliche Mitteilungen* **2020**, (82), 8-19.
27. Hinz, K.; Fellhauer, D.; Gaona, X.; Vespa, M.; Dardenne, K.; Schild, D.; Yokosawa, T.; Silver, M. A.; Reed, D. T.; Albrecht-Schmitt, T. E.; Altmaier, M.; Geckeis, H., Interaction of Np(v) with borate in alkaline, dilute-to-concentrated, NaCl and MgCl₂ solutions. *Dalton transactions* **2020**, 49 (5), 1570-1581.
28. Huang, L.-Z.; Wei, X.; Gao, E.; Zhang, C.; Hu, X.-M.; Chen, Y.; Liu, Z.; Finck, N.; Lützenkirchen, J.; Dionysiou, D. D., Single Fe atoms confined in two-dimensional MoS₂ for sulfite activation: A biomimetic approach towards efficient radical generation. *Applied catalysis / B* **2020**, 268
29. Idiart, A.; Laviña, M.; Kosakowski, G.; Cochepein, B.; Meeussen, J. C. L.; Samper, J.; Mon, A.; Montoya, V.; Munier, I.; Poonosamy, J.; Montenegro, L.; Deissmann, G.; Rohmen, S.; Damiani, L. H.; Coene, E.; Naves, A., Reactive transport modelling of a low-pH concrete / clay interface. *Applied geochemistry* **2020**, 115
30. Ilić, K.; Selmani, A.; Milić, M.; Glavan, T. M.; Zapletal, E.; Ćurlin, M.; Yokosawa, T.; Vrček, I. V.; Pavičić, I., The shape of titanium dioxide nanomaterials modulates their protection efficacy against ultraviolet light in human skin cells. *Journal of nanoparticle research* **2020**, 22 (3), 71.
31. Kalt, J.; Sternik, M.; Krause, B.; Sergueev, I.; Mikolasek, M.; Bessas, D.; Sikora, O.; Vitova, T.; Göttlicher, J.; Steininger, R.; Jochym, P. T.; Ptok, A.; Leupold, O.; Wille, H.-C.; Chumakov, A. I.; Piekarz, P.; Parlinski, K.; Baumbach, T.; Stankov, S., Lattice dynamics and polarization-dependent phonon damping in α -phase FeSi₂ nanostructures. *Physical review / B* **2020**, 101 (16)
32. Kalt, J.; Sternik, M.; Krause, B.; Sergueev, I.; Mikolasek, M.; Merkel, D.; Bessas, D.; Sikora, O.; Vitova, T.; Göttlicher, J.; Steininger, R.; Jochym, P. T.; Ptok, A.; Leupold, O.; Wille, H.-C.; Chumakov, A. I.; Piekarz, P.; Parlinski, K.; Baumbach, T.; Stankov, S., Lattice dynamics of endotaxial silicide nanowires. *Physical review / B* **2020**, 102 (19)
33. Kauric, G.; Walter, O.; Beck, A.; Schacherl, B.; Dieste Blanco, O.; Vigier, J.-F.; Zuleger, E.; Vitova, T.; Popa, K., Synthesis and characterization of nanocrystalline U_{1-x}Pu_xO_{2(+y)} mixed oxides. *Materials today advances* **2020**, 8
34. Klose, T.; Chaparro, M. C.; Schilling, F.; Butscher, C.; Klumbach, S.; Blum, P., Fluid Flow Simulations of a Large-Scale Borehole Leakage Experiment. *Transport in porous media* **2020**.
35. Kölbel, L.; Kölbel, T.; Sauter, M.; Schäfer, T.; Siefert, D.; Wiegand, B., Identification of fracture zones in geothermal reservoirs in sedimentary basins: A radionuclide-based approach. *Geothermics* **2020**, 85
36. Kutus, B.; Gaona, X.; Pallagi, A.; Pálkó, I.; Altmaier, M.; Sipos, P., Recent advances in the aqueous chemistry of the calcium(II)-gluconate system – Equilibria, structure and composition of the complexes forming in neutral and in alkaline solutions. *Coordination chemistry reviews* **2020**, 417
37. Li, W. B.; Belchior, A.; Beuve, M.; Chen, Y. Z.; Di Maria, S.; Friedland, W.; Gervais, B.; Heide, B.; Hocine, N.; Ipatov, A.; Klapproth, A. P.; Li, C. Y.; Li, J. L.; Multhoff, G.; Poignant, F.; Qiu, R.; Rabus, H.; Rudek, B.; Schuemann, J.; Stangl, S.; Testa, E.; Villagrasa, C.; Xie, W. Z.; Zhang, Y. B., Intercomparison of dose enhancement ratio and secondary electron spectra for gold nanoparticles irradiated by X-rays calculated using multiple Monte Carlo simulation codes. *Physica medica* **2020**, 69, 147-163.

38. Li, W. B.; Beuve, M.; Di Maria, S.; Friedland, W.; Heide, B.; Klapproth, A. P.; Li, C. Y.; Poignant, F.; Rabus, H.; Rudek, B.; Schuemann, J.; Villagrasa, C., Corrigendum to "Intercomparison of dose enhancement ratio and secondary electron spectra for gold nanoparticles irradiated by X-rays calculated using multiple Monte Carlo simulation codes" [Phys. Med. 69 (2020) 147–163]. *Physica medica* **2020**, *80*, 383-388.
39. Link, J.; Sowoidnich, T.; Pfitzner, C.; Gil-Diaz, T.; Heberling, F.; Lützenkirchen, J.; Schäfer, T.; Ludwig, H.-M.; Haist, M., The influences of cement hydration and temperature on the thixotropy of cement paste. *Materials* **2020**, *13* (8)
40. Lützenkirchen, J.; Darbha, G. K.; Chakravadhanula, V. S. K.; Redel, E.; Selmani, A.; Vayssières, L., Interaction of Polyoxometalates and Nanoparticles with Collector Surfaces—Focus on the Use of Streaming Current Measurements at Flat Surfaces. *Colloids and interfaces* **2020**, *4* (3), Art.-Nr.:
41. Maiwald, M. M.; Dardenne, K.; Rothe, J.; Skerencak-Frech, A.; Panak, P. J., Thermodynamics and Structure of Neptunium(V) Complexes with Formate. Spectroscopic and Theoretical Study. *Inorganic chemistry* **2020**, *59* (9), 6067-6077.
42. Maiwald, M. M.; Müller, K.; Heim, K.; Trumm, M.; Banik, N. L.; Rothe, J.; Dardenne, K.; Skerencak-Frech, A.; Panak, P. J., Determination of thermodynamic functions and structural parameters of NpO_2^+ lactate complexes. *New journal of chemistry* **2020**, *44* (39), 17033-17046.
43. Maiwald, M. M.; Skerencak-Frech, A.; Panak, P. J., Spectroscopic characterisation and thermodynamics of the complexation of Np(V) with sulfate up to 200°C. *Spectrochimica acta / A* **2020**, *240*, Art.-Nr.
44. Maiwald, M. M.; Trumm, M.; Dardenne, K.; Rothe, J.; Skerencak-Frech, A.; Panak, P. J., Speciation, thermodynamics and structure of Np(V) oxalate complexes in aqueous solution. *Dalton transactions* **2020**, *49*, 13359-13371.
45. Mayordomo, N.; Rodríguez, D. M.; Schild, D.; Molodtsov, K.; Johnstone, E. V.; Hübner, R.; Shams Aldin Azzam, S.; Brendler, V.; Müller, K., Technetium retention by gamma alumina nanoparticles and the effect of sorbed Fe^{2+} . *Journal of hazardous materials* **2020**, *388*, Article-No.122066.
46. Morelová, N.; Finck, N.; Lützenkirchen, J.; Schild, D.; Dardenne, K.; Geckeis, H., Sorption of americium / europium onto magnetite under saline conditions: Batch experiments, surface complexation modelling and X-ray absorption spectroscopy study. *Journal of colloid and interface science* **2020**, *561*, 708-718.
47. Mossini, E.; Macerata, E.; Wagner, C.; Boubals, N.; Panak, P. J.; Geist, A.; Charbonnel, M.-C.; Mariani, M., Radiolytic effects on actinide(III) complexation with a hydrophilic PyTri ligand. *Il nuovo cimento della Società Italiana di Fisica / C* **2020**, *43* (6), 148.
48. Pavez, M.; Schill, E.; Held, S.; Díaz, D.; Kohl, T., Visualizing preferential magmatic and geothermal fluid pathways via electric conductivity at Villarrica Volcano, S-Chile. *Journal of volcanology and geothermal research* **2020**, *400*, Art.-Nr.:
49. Prieur, D.; Bonani, W.; Popa, K.; Walter, O.; Kriegsman, K. W.; Engelhard, M. H.; Guo, X.; Eloirdi, R.; Gouder, T.; Beck, A.; Vitova, T.; Scheinost, A. C.; Kvashnina, K.; Martin, P., Size Dependence of Lattice Parameter and Electronic Structure in CeO_2 Nanoparticles. *Inorganic chemistry* **2020**, *59* (8), 5760-5767.
50. Rodríguez, D. M.; Mayordomo, N.; Scheinost, A. C.; Schild, D.; Brendler, V.; Müller, K.; Stumpf, T., New Insights into $^{99}\text{Tc(VII)}$ Removal by Pyrite: A Spectroscopic Approach. *Environmental science & technology* **2020**, *54* (5), 2678-2687.
51. Schätzler, K.; Bremer, J.; Schill, E.; Kohl, T.; Kühn, M.; Kolditz, O.; Sass, I., GeoLaB – Das geowissenschaftliche Zukunftsprojekt für Deutschland. *Mining report* **2020**, *156* (6).
52. Seher, H.; Geckeis, H.; Fanghänel, T.; Schäfer, T., Bentonite nanoparticle stability and the effect of fulvic acids: Experiments and modelling. *Colloids and Interfaces* **2020**, *4* (2)
53. Stricker, K.; Grimmer, J. C.; Egert, R.; Bremer, J.; Gholami Korzani, M.; Schill, E.; Kohl, T., The Potential of Depleted Oil Reservoirs for High-Temperature Storage Systems. *Energies* **2020**, *13* (24)
54. Vehmas, T.; Montoya, V.; Alonso, M. C.; Vašiček, R.; Rastrick, E.; Gaboreau, S.; Večerník, P.; Leivo, M.; Holt, E.; Fink, N.; Ait Mouheb, N.; Svoboda, J.; Read, D.; Červinka, R.; Vasconcelos, R.; Corkhill, C., Characterization of Cebama low-pH reference concrete and assessment of its alteration with representative waters in radioactive waste repositories. *Applied geochemistry* **2020**, *121*
55. Vettese, G. F.; Morris, K.; Natrajan, L. S.; Shaw, S.; Vitova, T.; Galanzew, J.; Jones, D. L.; Lloyd, J. R., Multiple Lines of Evidence Identify U(V) as a Key Intermediate during U(VI) Reduction by MR1. *Environmental science & technology* **2020**, *54* (4), 2268-2276.
56. Vilas, V. V.; Millet, S.; Sandow, M.; Iglesias Pérez, L.; Serrano-Purroy, D.; Van Winckel, S.; Aldave de las Heras, L., An Automated SeaFAST ICP-DRC-MS Method for the Determination of ^{90}Sr in Spent Nuclear Fuel Leachates. *Molecules* **2020**, *25* (6)
57. Vitova, T.; Pidchenko, I.; Schild, D.; Prüßmann, T.; Montoya, V.; Fellhauer, D.; Gaona, X.; Bohnert, E.; Rothe, J.; Baker, R. J.; Geckeis, H., Competitive Reaction of Neptunium(V) and Uranium(VI) in Potassium–Sodium Carbonate-Rich Aqueous Media: Speciation Study with a Focus on High-Resolution X-ray Spectroscopy. *Inorganic chemistry* **2020**, *59* (1), 8-22.

58. Weßling, P.; Müllich, U.; Guerinoni, E.; Geist, A.; Panak, P. J., Solvent extraction of An(III) and Ln(III) using TODGA in aromatic diluents to suppress third phase formation. *Hydrometallurgy* **2020**, *192*
59. Weßling, P.; Schenk, T.; Braun, F.; Beele, B. B.; Trumm, S.; Trumm, M.; Schimmelpfennig, B.; Schild, D.; Geist, A.; Panak, P. J., Trivalent Actinide Ions Showing Tenfold Coordination in Solution. *Inorganic chemistry* **2020**, *59* (17), 12410-12421.
60. Wilden, A.; Kreft, F.; Schneider, D.; Paparigas, Z.; Modolo, G.; Lumetta, G. J.; Gelis, A. V.; Law, J. D.; Geist, A., Countercurrent Actinide Lanthanide Separation Process (ALSEP) Demonstration Test with a Simulated PUREX Raffinate in Centrifugal Contactors on the Laboratory Scale. *Applied Sciences* **2020**, *10* (20)
61. Yu, J.; Yang, M.; Zhang, J.; Ge, Q.; Zimina, A.; Pruessmann, T.; Zheng, L.; Grunwaldt, J.-D.; Sun, J., Stabilizing Cu⁺ in Cu/SiO₂ Catalysts with a Shattuckite-Like Structure Boosts CO₂ Hydrogenation into Methanol. *ACS catalysis* **2020**, *10* (24), 14694-14706.
62. Zaytsev, A. V.; Bulmer, R.; Kozhevnikov, V. N.; Sims, M.; Modolo, G.; Wilden, A.; Waddell, P. G.; Geist, A.; Panak, P. J.; Weßling, P.; Lewis, F. W., Exploring the Subtle Effect of Aliphatic Ring Size on Minor Actinide-Extraction Properties and Metal Ion Speciation in Bis-1,2,4-Triazine Ligands. *Chemistry - a European journal* **2020**, *26* (2), 428-437.

Oral and poster presentations

63. Cakir-Wuttke, P.; Finck, N., Electrochemical investigations of steel corrosion in saline media. Annual Congress of the European Federation of Corrosion (EUROCORR 2020), Online, 7.–11. September 2020: **2020**.
63. Heberling, F., Electrostatics of Mineral-Water-Interfaces, and the Reactivity of Calcite close to Equilibrium. Winterschool: Investigating Solid-Liquid Interfaces: The Calcite-Water Interface at the Molecular Level (2020), Bielefeld, Deutschland, 2.–6. März 2020: **2020**.
64. Polly, R.; Platte, T.; Heberling, F.; Finck, N.; Geckeis, H., Incorporation of iodide in hydroxychloride green rust. International Workshop on Theory Frontiers in Actinide Sciences: Chemistry and Materials (2020), Santa Fe, NM, USA, 2.–5. Februar 2020: **2020**.
65. Popa, K.; Walter, O.; Dieste Blanco, O.; Beck, A.; Vitova, T., Reduction-precipitation of U(VI) by Fe(II)-oxalate. 5th World Congress on Recent Advances in Nanotechnology (RAN 2020), Lissabon, Portugal, 12.–14. April 2020: **2020**.
66. Stricker, K. R.; Grimmer, J.; Egert, R.; Bremer, J.; Gholami Korzani, M.; Schill, E.; Kohl, T., The potential of high-temperature storage systems in depleted oil reservoirs in the Upper Rhine Graben. 1st Geoscience & Engineering in Energy Transition Conference (GET 2020), Online, 16.–18. November 2020: **2020**.
67. Stricker, K. R.; Grimmer, J.; Egert, R.; Bremer, J.; Gholami Korzani, M.; Schill, E.; Kohl, T., Wärmespeicherung in ehemaligen Kohlenwasserstofflagerstätten des Oberrheingrabens. Der digital Geothermiekongress (DGK 2020), Essen, Deutschland, 9.–13. November 2020: **2020**.
68. Stricker, K. R.; Grimmer, J.; Egert, R.; Bremer, J.; Gholami Korzani, M.; Schill, E.; Kohl, T., Potential für Wärmespeicherung in ehemaligen Kohlenwasserstofflagerstätten des Oberrheingrabens. 25. Dresdner Fernwärme-Kolloquium (2020), Online, 27.–28. Oktober 2020: **2020**.
69. Stricker, K. R.; Grimmer, J.; Egert, R.; Bremer, J.; Gholami Korzani, M.; Schill, E.; Kohl, T., Heat storage in depleted hydrocarbon reservoirs of the Upper Rhine Graben. 8th European Geothermal Workshop (EGW 2020), Online, 7.–8. Oktober 2020: **2020**.
70. Stricker, K. R.; Grimmer, J.; Meixner, J.; Dashti, A.; Egert, R.; Gholamikorzani, M.; Schaetzler, K.; Schill, E.; Kohl, T., Utilization of abandoned hydrocarbon reservoirs for deep geothermal heat storage. EGU General Assembly - Sharing Geoscience Online (EGU 2020), Wien, Österreich, 4.–8. Mai 2020: **2020**.

Proceedings

71. Platte, T.; Finck, N.; Polly, R.; Mangold, S.; Geckeis, H., Interaction of Iodide with Green Rust and Magnetite. In *Goldschmidt Abstracts*, Geochemical Society: **2020**; p 2093.

Reports

72. Altmaier, M.; Cevirim-Papaioannou, N.; Dardenne, K.; Fellhauer, D.; Gaona, X.; Lee, J.-Y.; Yalcintas, E. *Entwicklung und Durchführung experimenteller Methoden zur verbesserten Modellierbarkeit uranhaltiger salinärer Lösungen (EDUKEM): Abschlussbericht Teilprojekt C, KIT-INE*; **2020**.

73. Britz, S.; Flügge, J.; Garcia-Perez, C.; Götz, R.; Heck, S.; Holl, F.; Huber, F.; Mattick, F.; Montoya, V.; Noseck, U.; Quinto, F.; Reiche, T.; Rinderknecht, F.; Schäfer, T.; Stoll, M. *Integrity of the bentonite barrier for the retention of radionuclides in crystalline host rocks - experiments and modeling (Project KOLLORADO-e2; Final Report)*; **2020**.

Dissertations

74. Morelová, N., *Steel corrosion and actinide sorption by iron corrosion products under saline conditions*. Ph.D. thesis, Karlsruher Institut für Technologie (KIT), **2020**.
75. Schepperle, J., *Löslichkeit von Plutonium und Neptunium in An- und Abwesenheit von Carbonat*. Ph.D. thesis, Karlsruher Institut für Technologie (KIT), **2020**.
76. Weßling, P., *Extraktions- und Speziationsuntersuchungen zur Optimierung des EURO-GANEX-Prozesses*. Ph.D thesis, Universität Heidelberg, **2020**.

1. Abdelmonem, A.; Morelová, N.; Finck, N.; Schild, D.; Lützenkirchen, J., Unexpected behavior of sodium sulfate observed in experimental freezing and corrosion studies. *Journal of Raman spectroscopy* **2021**, *52* (9), 1499-1506.
2. Adam, N.; Hinz, K.; Gaona, X.; Panak, P. J.; Altmaier, M., Impact of selected cement additives and model compounds on the solubility of Nd(III), Th(IV) and U(VI): screening experiments in alkaline NaCl, MgCl₂ and CaCl₂ solutions at elevated ionic strength. *Radiochimica acta* **2021**, *109* (6), 431-443.
3. Adam, N.; Reitz, C. Y.; Ditter, A.-L.; Panak, P. J., Complexation of Cm(III) with blood serum proteins: Recombinant human serum albumin (rHSA). *Radiochimica Acta* **2021**.
4. Águila, J. F.; Montoya, V.; Samper, J.; Montenegro, L.; Kosakowski, G.; Krejci, P.; Pflingsten, W., Modeling cesium migration through Opalinus clay: a benchmark for single- and multi-species sorption-diffusion models. *Computational Geosciences* **2021**, *25* (4), 1405-1436.
5. Bagus, P. S.; Schacherl, B.; Vitova, T., Computational and Spectroscopic Tools for the Detection of Bond Covalency in Pu(IV) Materials. *Inorganic chemistry* **2021**, *60* (21), 16090-16102.
6. Ban, M.; Luxbacher, T.; Lützenkirchen, J.; Viani, A.; Bianchi, S.; Hradil, K.; Rohatsch, A.; Castelvetro, V., Evolution of calcite surfaces upon thermal decomposition, characterized by electrokinetics, in-situ XRD, and SEM. *Colloids and Surfaces A: Physicochemical and Engineering Aspects* **2021**, *624*, 126761.
7. Banks, J.; Poulette, S.; Grimmer, J.; Bauer, F.; Schill, E., Geochemical Changes Associated with High-Temperature Heat Storage at Intermediate Depth: Thermodynamic Equilibrium Models for the DeepStor Site in the Upper Rhine Graben, Germany. *Energies* **2021**, *14* (19), 6089.
8. Börsig, N.; Scheinost, A. C.; Schild, D.; Neumann, T., Mechanisms of selenium removal by partially oxidized magnetite nanoparticles for wastewater remediation. *Applied geochemistry* **2021**, *132*, 105062.
9. Bouty, O.; Ramond, L.; Dardenne, K.; Rothe, J., Two-dimensional Wide-Angle X-ray Scattering on a Cm-doped borosilicate glass in a beryllium container. *Journal of synchrotron radiation* **2021**, *28* (1), 214-223.
10. Brouwer, S. M.; Lindqvist-Reis, P.; Persson, D. P.; Marttila, S.; Grenville-Briggs, L. J.; Andreasson, E., Visualising the ionome in resistant and susceptible plant-pathogen interactions. *Plant Journal* **2021**, *108* (3), 870-885.
11. Çevirim-Papaioannou, N.; Androniuk, I.; Han, S.; Mouheb, N. A.; Gaboreau, S.; Um, W.; Gaona, X.; Altmaier, M., Sorption of beryllium in cementitious systems relevant for nuclear waste disposal: Quantitative description and mechanistic understanding. *Chemosphere* **2021**, *282*, 131094.
12. Çevirim-Papaioannou, N.; Han, S.; Androniuk, I.; Um, W.; Altmaier, M.; Gaona, X., Uptake of Be(II) by cement in degradation stage I: Wet-chemistry and molecular dynamics studies. *Minerals* **2021**, *11* (10), 1149.
13. Chaparro, M. C.; Finck, N.; Metz, V.; Geckeis, H., Reactive transport modelling of the long-term interaction between carbon steel and MX-80 bentonite at 25°C. *Minerals* **2021**, *11* (11), 1272.
14. Chaparro, M. C.; Klose, T.; Hirsch, A.; Schilling, F.; Butscher, C.; Blum, P., Modelling of wellbore cement alteration due to CO₂-rich brine interaction in a large-scale autoclave experiment. *International Journal of Greenhouse Gas Control* **2021**, *110*, 103428.
15. Chevreux, P.; Tissandier, L.; Laplace, A.; Vitova, T.; Bahl, S.; Guyadec, F. L.; Deloule, E., Uranium solubility and speciation in reductive soda-lime aluminosilicate glass melts. *Journal of nuclear materials* **2021**, *544*, 152666.
16. Dardenne, K.; Duckworth, S.; Gaona, X.; Polly, R.; Schimmelpfennig, B.; Pruessmann, T.; Rothe, J.; Altmaier, M.; Geckeis, H., A Combined Study of Tc Redox Speciation in Complex Aqueous Systems: Wet-Chemistry, Tc K-/L-Edge X-ray Absorption Fine Structure, and Ab Initio Calculations. *Inorganic chemistry* **2021**, 12285–12298.
17. Dávila, G.; Cama, J.; Chaparro, M. C.; Lothenbach, B.; Schmitt, D. R.; Soler, J. M., Interaction between CO₂-rich acidic water, hydrated Portland cement and sedimentary rocks: Column experiments and reactive transport modeling. *Chemical Geology* **2021**, *572*, 120122.
18. DiBlasi, N. A.; Tasi, A. G.; Gaona, X.; Fellhauer, D.; Dardenne, K.; Rothe, J.; Reed, D. T.; Hixon, A. E.; Altmaier, M., Impact of Ca(II) on the aqueous speciation, redox behavior, and environmental mobility of Pu(IV) in the presence of EDTA. *The science of the total environment* **2021**, *783*, 146993.
19. Dixit, R.; Gupta, A.; Jordan, N.; Zhou, S.; Schild, D.; Weiss, S.; Guillon, E.; Jain, R.; Lens, P., Magnetic properties of biogenic selenium nanomaterials. *Environmental science and pollution research* **2021**, *28*, 40264-40274.
20. Dubos, J.-L.; Orberger, B.; Banchet, J.; Milazzo, J.-M.; Blancher, S. B.; Wallmach, T.; Lützenkirchen, J., Binder-free tableting experiments on manganese oxides and industrial mineral powders. *Powder technology* **2021**, *377*, 194-211.

21. Duckworth, S.; Gaona, X.; Castaño, D.; Park, S.; Altmaier, M.; Geckeis, H., Redox chemistry, solubility and hydrolysis of Re in reducing aquatic systems. Thermodynamic description and comparison with Tc. *Applied geochemistry* **2021**, *132*, 105037.
22. Duckworth, S. B.; Gaona, X.; Baumann, A.; Dardenne, K.; Rothe, J.; Schild, D.; Altmaier, M.; Geckeis, H., Impact of sulfate on the solubility of Tc(IV) in acidic to hyperalkaline aqueous reducing systems. *Radiochimica acta* **2021**, *109* (9), 681–697.
23. Fernández-Rojo, L.; Soler, J. M.; Dávila, G.; Chaparro, M. C.; Queralt, I.; Cama, J., Flow and reaction along the interface between hydrated Portland cement and calcareous rocks during CO₂ injection. Laboratory experiments and modeling. *International Journal of Greenhouse Gas Control* **2021**, *108*, 103331.
24. García, D.; Lützenkirchen, J.; Huguenel, M.; Calmels, L.; Petrov, V.; Finck, N.; Schild, D., Adsorption of strontium onto synthetic iron(III) oxide up to high ionic strength systems. *Minerals* **2021**, *11* (10), 1093.
25. Geist, A.; Panak, P. J., Recent progress in trivalent actinide and lanthanide solvent extraction and coordination chemistry with triazinylpyridine N donor ligands. *Solvent extraction and ion exchange* **2021**, *39* (2), 128-151.
26. Gil-Díaz, T.; Jara-Heredia, D.; Heberling, F.; Lützenkirchen, J.; Link, J.; Sowoidnich, T.; Ludwig, H.-M.; Haist, M.; Schäfer, T., Charge regulated solid-liquid interfaces interacting on the nanoscale: Benchmarking of a generalized speciation code (SINFONIA). *Advances in colloid and interface science* **2021**, *294*, 102469.
27. Haaf, N.; Schill, E., “Noise” during long-term continuous magnetotelluric monitoring of RN-15/IDDP-2 well engineering (Reykjanes peninsular, Iceland): A geogenic origin? *Geothermics* **2021**, *96*, 102192.
28. Heberling, F.; Klačić, T.; Raiteri, P.; Gale, J. D.; Eng, P. J.; Stubbs, J. E.; Gil-Díaz, T.; Begović, T.; Lützenkirchen, J., Structure and Surface Complexation at the Calcite(104)-Water Interface. *Environmental Science and Technology* **2021**, *55* (18), 12403-12413.
29. Heneka, A.; Geckeis, H.; Gentes, S.; Becker, F.; Krauß, C. O.; Lützenkirchen, J.; Plaschke, M.; Schild, D.; Tobie, W., A new technical approach for the minimization of secondary waste produced by water abrasive suspension cutting during disassembling of nuclear facilities. *Atw* **2021**, *66* (1), 34-40.
30. Huber, F. M.; Leone, D.; Trumm, M.; Moreno, L. R.; Neretnieks, I.; Wenka, A.; Schäfer, T., Impact of rock fracture geometry on geotechnical barrier integrity – A numerical study. *International journal of rock mechanics and mining sciences* **2021**, *142*, 104742.
31. Jungcharoen, P.; Pédrot, M.; Choueikani, F.; Pasturel, M.; Hanna, K.; Heberling, F.; Tesfa, M.; Marsac, R., Probing the effects of redox conditions and dissolved Fe²⁺ on nanomagnetite stoichiometry by wet chemistry, XRD, XAS and XMCD. *Environmental Science: Nano* **2021**, *8* (7), 2098-2107.
32. Kaiser, M.; Göttlicher, J.; Vitova, T.; Hinz, A., Towards Heteroleptic Dicoordinate Cu(II) Complexes. *Chemistry - a European journal* **2021**, *27* (30), 7998-8002.
33. Kegler, P.; Pointurier, F.; Rothe, J.; Dardenne, K.; Vitova, T.; Beck, A.; Hammerich, S.; Potts, S.; Faure, A.-L.; Klinkenberg, M.; Kreft, F.; Niemeyer, I.; Bosbach, D.; Neumeier, S., Chemical and structural investigations on uranium oxide-based microparticles as reference materials for analytical measurements. *MRS advances* **2021**, *6*, 125–130.
34. Kobayashi, T.; Fellhauer, D.; Sasaki, T., Solubility of PuO₂(am,hyd) and the Formation of Pu(IV) Carbonate Complexes in Carbonate Solutions Containing 0.1–5.0 mol·dm⁻³ NaNO₃. *Journal of Solution Chemistry* **2021**, *50* (4), 443-457.
35. König, T.; Dagan, R.; Dardenne, K.; Herm, M.; Metz, V.; Pruessmann, T.; Rothe, J.; Schild, D.; Walschburger, A.; Geckeis, H., Spectroscopic and chemical investigations on volatile fission and activation products within the fuel-cladding interface of irradiated pressurised water reactor fuel rod segments. *Safety of Nuclear Waste Disposal* **2021**, *1*, 5-6.
36. Loqman, A.; El Bali, B.; El Gaidoumi, A.; Boularbah, A.; Kherbeche, A.; Lützenkirchen, J., The First Application of Moroccan Perlite as Industrial Dyes Removal. *Silicon* **2021**.
37. Lyseid Authen, T.; Adnet, J.-M.; Bourg, S.; Carrott, M.; Ekberg, C.; Galán, H.; Geist, A.; Guilbaud, P.; Miguiritchian, M.; Modolo, G.; Rhodes, C.; Wilden, A.; Taylor, R., An overview of solvent extraction processes developed in Europe for advanced nuclear fuel recycling, Part 2 — homogeneous recycling. *Separation Science and Technology (Philadelphia)* **2021**.
38. Molinas, M.; Faizova, R.; Brown, A.; Galanzew, J.; Schacherl, B.; Bartova, B.; Meibom, K. L.; Vitova, T.; Mazzanti, M.; Bernier-Latmani, R., Biological Reduction of a U(V)-Organic Ligand Complex. *Environmental Science and Technology* **2021**, *55* (8), 4753-4761.
39. Montoya, V.; Noseck, U.; Mattick, F.; Britz, S.; Blechschmidt, I.; Schäfer, T., Radionuclide geochemistry evolution in the Long-term In-situ Test (LIT) at Grimsel Test Site (Switzerland). *Journal of Hazardous Materials* **2021**, 127733.
40. Morelová, N.; Dardenne, K.; Finck, N.; Heberling, F.; Metz, V.; Schild, D.; Geckeis, H.; Diomidis, N., Anaerobic corrosion of carbon steel in compacted bentonite exposed to natural Opalinus clay porewater: Bentonite alteration study. *Safety of Nuclear Waste Disposal* **2021**, *1*, 103-104.

41. Neumann, J.; Brinkmann, H.; Britz, S.; Lützenkirchen, J.; Bok, F.; Stockmann, M.; Brendler, V.; Stumpf, T.; Schmidt, M., A comprehensive study of the sorption mechanism and thermodynamics of f-element sorption onto K-feldspar. *Journal of colloid and interface science* **2021**, *591*, 490-499.
42. Ocádiz-Flores, J. A.; Gheribi, A. E.; Vlieland, J.; Dardenne, K.; Rothe, J.; Konings, R. J. M.; Smith, A. L., New insights and coupled modelling of the structural and thermodynamic properties of the LiF-UF₄ system. *Journal of molecular liquids* **2021**, 115820.
43. Ocádiz-Flores, J. A.; Gheribi, A. E.; Vlieland, J.; De Haas, D.; Dardenne, K.; Rothe, J.; Konings, R. J. M.; Smith, A. L., Examination of the short-range structure of molten salts: ThF₄, UF₄, and related alkali actinide fluoride systems. *Physical Chemistry Chemical Physics* **2021**, *23* (18), 11091-11103.
44. Pang, B.; Becker, F.; Metz, V., Monte-Carlo based investigation of individual dosimetry in deep geological repository for high-level nuclear waste with consideration of realistic body postures. *Annals of nuclear energy* **2021**, *161*, 108414.
45. Platte, T.; Finck, N.; Mangold, S.; Polly, R.; Geckeis, H., Retention of Iodide and Chloride by Formation of a Green Rust Solid Solution GR-Cl_{1-x}I_x: A Multiscale Approach. *Inorganic chemistry* **2021**, *60* (14), 10585-10595.
46. Polly, R.; Schacherl, B.; Rothe, J.; Vitova, T., Relativistic Multiconfigurational Ab Initio Calculation of Uranyl 3d4f Resonant Inelastic X-ray Scattering. *Inorganic chemistry* **2021**.
47. Prieur, D.; Desagulier, M.-M.; Neuville, D. R.; Guéneau, C.; Epifano, E.; Dardenne, K.; Rothe, J.; Martin, P., A spectroscopic hike in the U–O phase diagram. *Journal of synchrotron radiation* **2021**, *28* (6), 1684-1691.
48. Prieur, D.; Vigier, J.-F.; Popa, K.; Walter, O.; Dieste, O.; Varga, Z.; Beck, A.; Vitova, T.; Scheinost, A. C.; Martin, P. M., Charge Distribution in U_{1-x}Ce_xO_{2+y} Nanoparticles. *Inorganic Chemistry* **2021**, *60* (19), 14550-14556.
49. Rabus, H.; Li, W. B.; Nettelbeck, H.; Schuemann, J.; Villagrasa, C.; Beuve, M.; Di Maria, S.; Heide, B.; Klapproth, A. P.; Poignant, F.; Qiu, R.; Rudek, B., Consistency checks of results from a Monte Carlo code intercomparison for emitted electron spectra and energy deposition around a single gold nanoparticle irradiated by X-rays. *Radiation Measurements* **2021**, *147*, 106637.
50. Rodríguez, D. M.; Mayordomo, N.; Schild, D.; Brendler, V.; Müller, K.; Stumpf, T.; Azzam, S. S. A., Reductive immobilization of ⁹⁹Tc(VII) by FeS₂: The effect of marcasite. *Chemosphere* **2021**, *281*, 130904.
51. Singh, N.; Khandelwal, N.; Tiwari, E.; Naskar, N.; Lahiri, S.; Lützenkirchen, J.; Darbha, G. K., Interaction of metal oxide nanoparticles with microplastics: Impact of weathering under riverine conditions. *Water research* **2021**, *189*, 116622.
52. Sittel, T.; Trumm, M.; Adam, C.; Geist, A.; Panak, P. J., Impact of Solvent Polarity on the Ligand Configuration in Tetravalent Thorium N-Donor Complexes. *Inorganic chemistry* **2021**, *60* (2), 1092-1098.
53. Suksi, J.; Tullborg, E.-L.; Pidchenko, I.; Krall, L.; Sandström, B.; Kaksonen, K.; Vitova, T.; Kvashnina, K. O.; Göttlicher, J., Uranium remobilisation in anoxic deep rock-groundwater system in response to late Quaternary climate changes – Results from Forsmark, Sweden. *Chemical Geology* **2021**, *584*, 120551.
54. Tasi, A.; Gaona, X.; Rabung, T.; Fellhauer, D.; Rothe, J.; Dardenne, K.; Lützenkirchen, J.; Grivé, M.; Colàs, E.; Bruno, J.; Källstrom, K.; Altmaier, M.; Geckeis, H., Plutonium retention in the isosaccharinate – cement system. *Applied geochemistry* **2021**, *126*, 104862.
55. Townsend, L. T.; Morris, K.; Harrison, R.; Schacherl, B.; Vitova, T.; Kovarik, L.; Pearce, C. I.; Mosselmans, J. F. W.; Shaw, S., Sulfidation of magnetite with incorporated uranium. *Chemosphere* **2021**, *276*, 130117.
56. Uzunidis, G.; Schade, O.; Schild, D.; Grunwaldt, J. D.; Behrens, S., Design of bimetallic Au/Cu nanoparticles in ionic liquids: Synthesis and catalytic properties in 5-(hydroxymethyl)furfural oxidation. *ChemNanoMat* **2021**, *7* (10), 1108-1116.
57. Zegke, M.; Grödler, D.; Roca Jungfer, M.; Haseloer, A.; Kreuter, M.; Neudörfl, J. M.; Sittel, T.; James, C. M.; Rothe, J.; Altmaier, M.; Klein, A.; Breugst, M.; Abram, U.; Strub, E.; Wickleder, M. S., Ammonium Pertechnate in Mixtures of Trifluoromethanesulfonic Acid and Trifluoromethanesulfonic Anhydride. *Angewandte Chemie / International edition* **2021**.

Oral and poster presentation

58. Fellhauer, D.; Gaona, X.; Altmaier, M.; Geckeis, H., Radionuclide geochemistry: solubility and thermodynamics in a HLW repository. Interdisziplinäres Forschungssymposium für die Sicherheit der nuklearen Entsorgung (safeND 2021), Berlin, Germany, **2021**.
59. Fellhauer, D.; Kuzenkova, A.; Schramm, T.; Schepperle, J.; Schorer, M.; Gaona, X.; Romanchuk, A.; Kalmykov, S.; Altmaier, M.; Geckeis, H., Pu(VI) solubility and hydrolysis in NaCl and CaCl₂ solutions. 19th International Symposium on Solubility Phenomena and Related Equilibrium Processes (ISSP 2021), Online, **2021**.

60. Geist, A.; Adnet, J.-M.; Bourg, S.; Ekberg, C.; Galán, H.; Guilbaud, P.; Miguiditchian, M.; Modolo, G.; Rhodes, C.; Taylor, R., An overview of solvent extraction processes developed in Europe for heterogeneous recycling of nuclear fuels. 9th Biennial Symposium on Emerging Trends in Separation Science and Technology (e-SESTEC-2020) (2021), Online, **2021**.
61. Mayordomo, N.; Rodríguez, D. M.; Schild, D.; Rossberg, A.; Scheinost, A. C.; Brendler, V.; Müller, K., Technetium retention by green rust chloride. Goldschmidt (2021), Online, **2021**.
62. Morelová, N.; Schild, D.; Heberling, F.; Finck, N.; Dardenne, K.; Metz, V.; Geckeis, H., Anaerobic corrosion of carbon steel in compacted bentonite exposed to natural opalinus clay porewater: bentonite alternation study. Goldschmidt (2021), Online, **2021**.
63. Stricker, K. R.; Egert, R.; Gholami Korzani, M.; Bauer, F.; Schill, E.; Kohl, T., Thermisch-Hydraulisch-Mechanische (THM) Modellierung von Hochtemperatur-Wärmespeicherung am Fallbeispiel DeepStor. Der Geothermiekongress (DGK 2021), Essen, Germany, **2021**.
64. Stricker, K. R.; Grimmer, J.; Egert, R.; Bremer, J.; Gholami Korzani, M.; Schill, E.; Kohl, T., Numerische und chemische Modellierung der Speicherstrukturen im tiefen Tertiär / Numerical and chemical modeling of the deep tertiary reservoir structures. GeoTHERM - expo & congress (2021), Offenburg, Germany, **2021**.
65. Stricker, K. R.; Grimmer, J.; Egert, R.; Bremer, J.; Gholami Korzani, M.; Schill, E.; Kohl, T., THM modeling of former hydrocarbon reservoirs for high-temperature heat storage. Der Geothermiekongress (DGK 2021), Essen, Germany, **2021**.
66. Stricker, K. R.; Grimmer, J. C.; Egert, R.; Bremer, J.; Gholamikorzani, M.; Schill, E.; Kohl, T., Utilization of Former Hydrocarbon Reservoirs for High-temperature Heat Storage. DGMK/ÖGEW Frühjahrstagung "Shaping the Energy Transition with Upstream and Storage Technologies" (2021), Online, **2021**.
67. Taylor, R.; Adnet, J.-M.; Bourg, S.; Carrott, M.; Ekberg, C.; Galán, H.; Geist, A.; Guilbaud, P.; Miguiditchian, M.; Modolo, G.; Rhodes, C., Development of a Grouped Actinide Extraction process for Advanced Nuclear Fuel Recycling. 9th Biennial Symposium on Emerging Trends in Separation Science and Technology (e-SESTEC-2020) (2021), Online, **2021**.

Proceedings

68. Krauß, C. O.; Becker, F.; Chaudhry, M. J.; Geckeis, H.; Gentes, S.; Heneka, A.; Plaschke, M.; Schild, D., Separation System for the Treatment of Secondary Waste from the Waterjet-Abrasive-Suspension-Cutting. In *Proceedings of the International Conference on Decommissioning Challenges: Industrial Reality, Lessons learned and Prospects (DEM 2021)*, Avignon, Frankreich, **2021**; p 8.

Reports

69. Altmaier, M.; Colas, E.; Endrizzi, F.; Fellhauer, D.; Gaona, X.; Hagemann, S.; Kiefer, C.; Kulik, D. A.; Lee, J.-Y.; Miron, G. D.; Thoenen, T. *Abschlussbericht ThermAc: Untersuchungen zur aquatischen Chemie und Thermodynamik von Actiniden bei erhöhten Temperaturen*; **2021**.
70. Finck, N.; Morelová, N.; Cakir-Wuttke, P.; Polly, R.; Schild, D. *Korrosions- und Sorptionsprozesse an Stahloberflächen bei hohen Temperaturen und Drücken im anaeroben salinaren Milieu (KORSO): Abschlussbericht Teilprojekt B, KIT-INE*; **2021**.
71. Kienzler, B. *Thermomechanische Modellrechnungen zur Endlagerung im KIT-INE*; **2021**.

Dissertations

72. Platte, T., *Rückhaltung von Iod durch die Eisen-Sekundärphasen Grünrost und Magnetit*. Ph.D. thesis, Karlsruher Institut für Technologie (KIT), **2021**.
73. Ratnayake, S. Y., *Assessment of the fate and behavior of naturally occurring thorium and uranium in the environment of central Sri Lanka*. Ph.D. thesis, Karlsruher Institut für Technologie (KIT), **2021**.
74. Sittel, T., *Spektroskopische Untersuchung zur Komplexbildung von Actiniden & Lanthaniden mit organischen Liganden*. Ph.D. thesis, Universität Heidelberg, **2021**.

INE Scientific Working Documents
ISSN 2701-262X
www.kit.edu